UNIVERSITAT DE BARCELONA

Theoretical reaction and relaxation dynamics in superfluid helium nanodroplets

Miquel Blancafort Jorquera

Theoretical reaction and relaxation dynamics in superfluid helium nanodroplets

Miquel Blancafort Jorquera

UNIVERSITAT DE BARCELONA

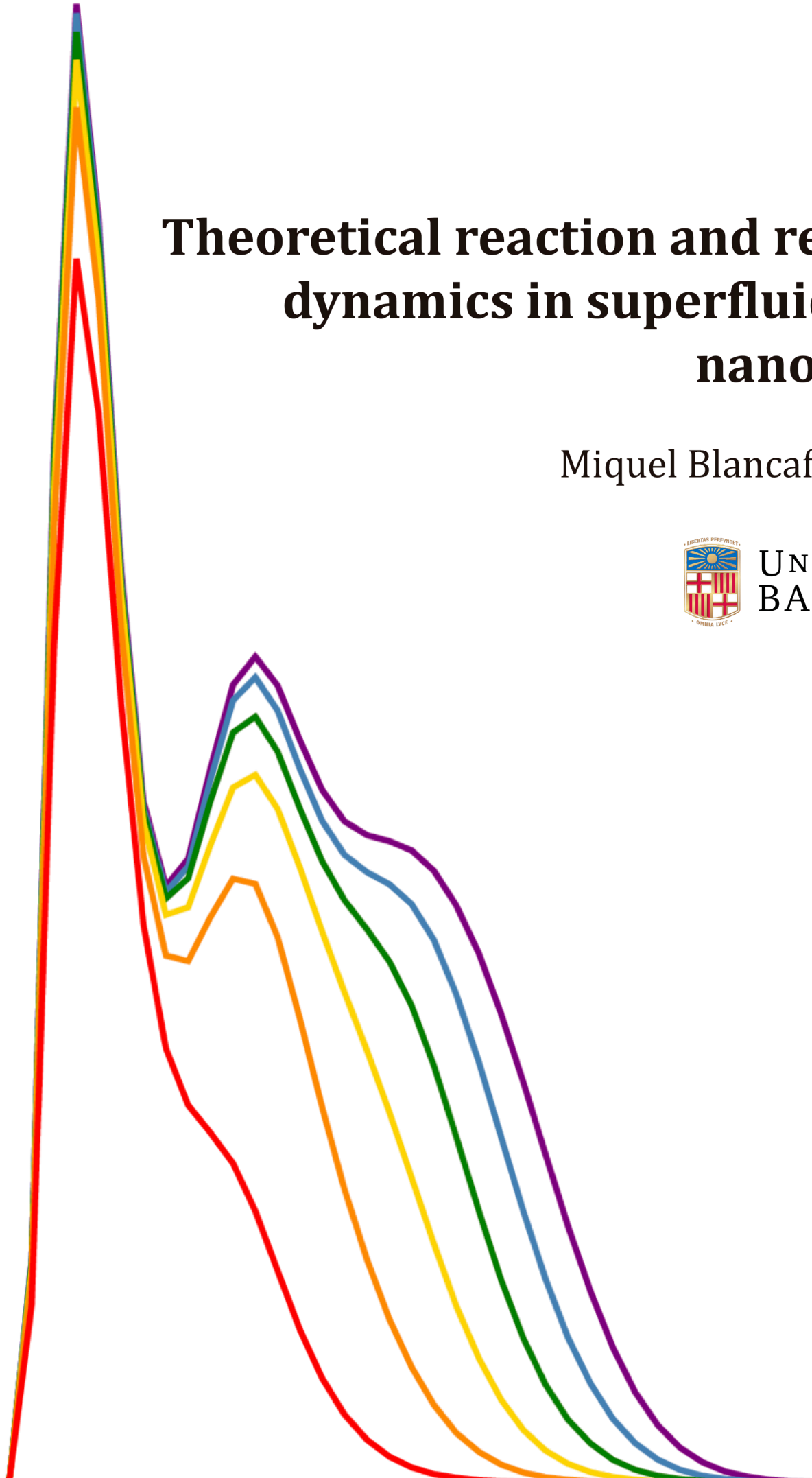

Universitat de Barcelona

Facultat de Química

Departament de Ciència de Materials i Química Física

Secció de Química Física

Programa de doctorat de Química Teòrica i Modelització Computacional

Theoretical reaction and relaxation dynamics in superfluid helium nanodroplets

Tesi presentada per optar al grau de doctor per la Universitat de Barcelona

Miquel Blancafort Jorquera

Setembre de 2019

Director:

Prof. Dr. Miguel González Pérez

Catedràtic del Departament de Ciència de Materials i Química Física, Secció de Química Física

Facultat de Química, Universitat de Barcelona

Que no et facis vella sense fer-te gran
que no et facis gran sense créixer,
que no perdis la inèrica del somriure,
que no oblidis la urgència del moment,
que sentis que formes part d'una tribu
i que respectis el teu cos
però vegis que només és una canoa.

Que no et senti dir mai:
"sí, sóc aquesta mandrosa acumulació d'errors",
i que entenguis que estimar
és estimar involuntàriament, imperfectament, inevitablement
i que si t'enamores d'algú
t'entrebanquis contínuament amb el seu nom
i que et digui:
"t'estimo però no ho sé escriure"
[…]
que si plores notis que el torrent de llàgrimes et neteja
que si t'en vas, sentis a dir-te:
"quan me mori enyoraré enyorar-te"
[…]
Que un dia un noi o una noia et digui:
"estic enamorat de la imperfecció del teu cos"
[…]
i que estimis i et deixis estimar
que sovint és la lliçó més difícil d'aprendre
[…]
Sigues només un infant que fa gargots
mantingues la teva innocència lluny de l'abast dels adults
[…]
Procura mantindre algun desig incomplert
[…]
I estigues contenta

Orchestra Fireluche i Pau Riba, "Nina de Miraguano", *Tants Caps, Tants Joguets* , 2013.

La tesi que teniu a les mans no hauria estat possible sense tot un seguit de persones que han estat o estan al meu volant

- A en Miguel González pel coneixement que m'ha transmès, les hores al despatx 441 de la quarta planta discutint sobre la ciència i la societat, les estones, de vegades frustrants, intentant entendre i raonar de manera sòlida alguns resultats que aquí es presentaran i sobretot per ensenyar-me com és el món de la investigació.
- A l'Arnau Vilà pels seus coneixements, disponibilitat, ganes d'ajudar i passió pel tema.
- A l'Arturo, que m'ha acompanyat i après amb mi durant l'agonia del màster i els primers anys d'aquest doctorat al despatx.
- Als amics del màster que han suposat un parèntesi molt necessari d'humor, festa i viatges a Santiago de Compostela, Toulouse, Saragossa, Luchon, Berlin, Amsterdam... On anem aquest any?
- A tothom dels màsters de natació del Medi i dels Castellers de la Vila de Gràcia: sense aquestes dues aficions, no seria qui soc i la meva quotidianitat seria feixuga.
- A en Iago, que duran l'últim tram m'ha acompanyat i donat recolzament com ningú i sempre troba com fer-me relativitzar i veure que res és tan dràstic ni extrem; t'estimo.
- Als de Vic i els companys de pis, que sempre hi són, ja sigui des de Vic, Lausanne, Los Angeles, Edimburg o Londres; sobretot a en Jordi, que sempre ho qüestiona tot i et força a veure-ho tot d'una manera diferent i que et plantegis perquè fas el que fas.
- Als membres de la meva família, estiguin aquí o no, que sempre creuen que el que fas és molt difícil, que ets el millor en tot i t'animen a continuar vivint fort.
- A algú a qui no vaig conèixer massa, però, pel que m'han explicat, admiro i dec molt del que soc; a qui m'agradaria haver pogut ensenyar aquest llibre que teniu a les mans i dir-li que sense ell, res del que conec existiria per mi.
- Però sobretot, sobretot, a la meva mare i la meva germana, que han fet que jo sigui; han aguantat els meus rampells i m'han sabut posar a lloc en èpoques dures; si no hagués estat per la seva severa intervenció, hauria abandonat el doctorat abans de poder dipositar aquesta tesi.

The development of the present Ph.D. thesis has been possible thanks to the financial support provided by:

Predoctoral research grants:

University of Barcelona grant (ADR) (2015-2018)

Research projects:

The main support to the research developed here has been provided by

National projects

Spanish Ministry of Science and Innovation, ref. CTQ2011-27857-C02-01

Spanish Ministry of Science, Innovation and Universities, ref. MDM-2017-0767

and some support has been provided by the

Autonomous Government projects

Catalan Autonomous Government, refs. 2014SGR 25, 2017SGR 348 and XRQTC.

Contents

Preface

The study of the properties of superfluid helium has been carried out mainly by physicists during many years. In more recent years, taking advantage of the potentialities presented by superfluid helium nanodroplets (HeNDs) as inert matrix at very low temperature (0.37 K), the chemical community became involved in its application to the study of the high-resolution spectroscopy of molecules. More recently (early 2000s), after verifying that HeNDs could also be good nanoreactors, this community began to be involved in research using HeNDs to investigate chemical reactivity in this quantum solvent. The interest of the chemists in the applications of HeNDs has been growing since then and, probably, it has grown more after discovering that these nanodroplets could also be useful in chemical synthesis. As for the theoretical studies on the dynamics of physicochemical processes in HeNDs, they have been possible about five years ago and up to now the number of theoretical dynamics studies carried out in the chemical context, despite their interest, is very scarce. The main objective of this thesis is to contribute to the development of the research in this area.

This thesis is structured in seven chapters and a summary in Catalan (last chapter). The first chapter gives an introduction into the field of study and the second one presents the theoretical methods used to perform the studies detailed in the following chapters. Chapters 3 and 4 report two studies (atomic capture and dimer or adduct formation reaction, respectively) where the impurities (atoms) are described using classical mechanics. Moreover, Chapters 5 and 6 report the studies of two kinds of molecular energy relaxation (rotational and vibrational, respectively), and the main conclusions obtained are presented in Chapter 7.

In order to introduce the reader into the topic, Chapter 1 is divided into four sections: the first one describes the properties of helium, the second one considers the

history of the discovery and research carried out on the superfluidity phenomenon, the third one outlines the properties of superfluid helium nanodroplets, and the last one gives an overview of the applications and fields of study implying HeNDs.

Afterwards, in order to understand how the calculations have been performed, the theoretical and numerical methods used to describe superfluid liquid helium are detailed in Chapter 2. In the first section particular attention has been paid on the density functional theory (DFT) and its extension for real-time simulations (time dependent DFT (TDDFT)). The second section describes the main density functionals used in this context. The third section is aimed to present the numerical methods used to perform the TDDFT calculations.

The following chapters contain the original studies carried out in this thesis. The study of the capture process of a Ne atom by a HeND (Ne + HeND → Ne@HeND' …) can be found in Chapter 3. Here, the atom is treated using classical mechanics and the influence of energy and angular momentum is examined for a wide set of initial conditions. The microscopic mechanism, energy and angular momentum exchanges and vortex formation have been extensively analysed. This work complements and extends a previous study of our group where the Ne atom was treated using standard quantum mechanics at zero angular momentum. Moreover, the present contribution corresponds to the first systematic analysis of the influence of angular momentum in the capture process and vortex formation.

Chapter 4 represents a natural evolution from Chapter 3 and reports what happens if a second Ne atom is captured by a doped nanodroplet (Ne@HeND). Thus, it describes the formation of a neon dimer or neon adduct inside a superfluid helium nanodroplet, treating both atoms classically. Analogously as in the previous chapter, angular momentum has also been taken into consideration and the mechanism, energy an angular momentum exchanges and vortex formation are analysed. This work complements and extends a previous investigation of our group where the Ne atoms were treated using standard quantum mechanics at zero angular momentum. Moreover, the contents of this chapter correspond to the second theoretical investigation of bimolecular reaction dynamics in HeNDs.

The following chapters use a full quantum hybrid approach to explore rotational and vibrational energy relaxation dynamics. Chapter 5 corresponds to the first theoretical study reported so far on the rotational energy relaxation dynamics of molecules in HeNDs. This process has been studied using several isotopes of the H_2 molecule (fast rotors) and considering a set of initial excitations and nanodroplet sizes.

The last investigation (Chapter 6) is centred on the study of the vibrational energy relaxation in HeNDs. Thus, the influence of the energy gap between the vibrational levels, molecule-helium interaction energy and nanodroplet size on the vibrational relaxation dynamics has been analysed, taking as a reference the $I_2@(^4He)_{100}$ doped HeND which was recently studied in our group. To the best of our knowledge it is the first time that the influence of these factors has been examined.

As indicated above, in Chapters 7 and 8 the main conclusions and a summary in Catalan are presented.

From the work developed here two papers have been already published:

- M. Blancafort-Jorquera, A. Vilà and M. González, Quantum-classical dynamics of the capture of neon atoms by superfluid helium nanodroplets, *Phys. Chem. Chem. Phys.,* 2018, **20,** 29737-29753. DOI: 10.1039/c8cp05140b.

- M. Blancafort-Jorquera, A. Vilà and M. González, Rotational energy relaxation quantum dynamics of a diatomic molecule in a superfluid helium nanodroplet and study of the hydrogen isotopes case, *Phys. Chem. Chem. Phys.,* 2019 (available online). DOI: 10.1039/c9cp00952c.

In addition, an article corresponding to Chapter 4 has been submitted (16th August): M. Blancafort-Jorquera, A. Vilà and M. González, Quantum-classical approach to the reaction dynamics in a superfluid helium nanodroplet. The Ne_2 dimer and Ne-Ne adduct formation reaction Ne + $Ne@(^4He)_N$. Besides, an article is in preparation on the vibrational energy relaxation (Chapter 6)

1. Introduction

1.1. Liquid helium

Helium has two stable isotopes, ^{3}He and ^{4}He, the later being $7.25 \cdot 10^5$ times more abundant than the former.[1] Helium is a closed shell electronic system (electronic configuration $1s^2$) and, thus, it is chemically inert. Moreover, due to their small radius and number of electrons the helium atom has a very low polarizability. The He-He interaction is of van der Waals type (vdW; instantaneous dipole-instantaneous dipole interaction) with a potential energy well of around 10 K. This interaction potential can be fitted to a Lennard-Jones potential with parameters $\epsilon = 10.22\ K$ and $\sigma = 2.556$ Å.

$$V(r) = 4\epsilon\left[\left(\frac{\sigma}{r}\right)^{12} - \left(\frac{\sigma}{r}\right)^{6}\right] \tag{1.1}$$

There are other potentials, e.g., the so-called Aziz potential[2] and the *ab-initio* one of Cybulski and Toczylowski[3] that are more accurate (Figure 1.1). However, the Lennard-Jones one is mathematically simpler and accurate enough for the applications considered here.

In the present thesis only ^{4}He nanodroplets are used (bosonic system). For this reason the properties of ^{4}He will be detailed. Its phase diagram shows a critical temperature at 5.2 K and 2.3 atm[4] and no triple point exists (Figure 1.2). At atmospheric pressure ^{4}He is liquid below 4.21 K and solidification is not achievable unless high pressures are applied (around 20 atm)[5]. The helium atom is the only one that shows this behaviour owing to its light mass and the weak helium-helium interaction. Solidification happens when temperature is low enough so that the interaction energy between atoms is larger (in absolute value) than their kinetic energy and due to this they stay in defined

sites. Kinetic energy cannot decrease below a value imposed by the Heisenberg uncertainty principle, the zero-point energy (ZPE).

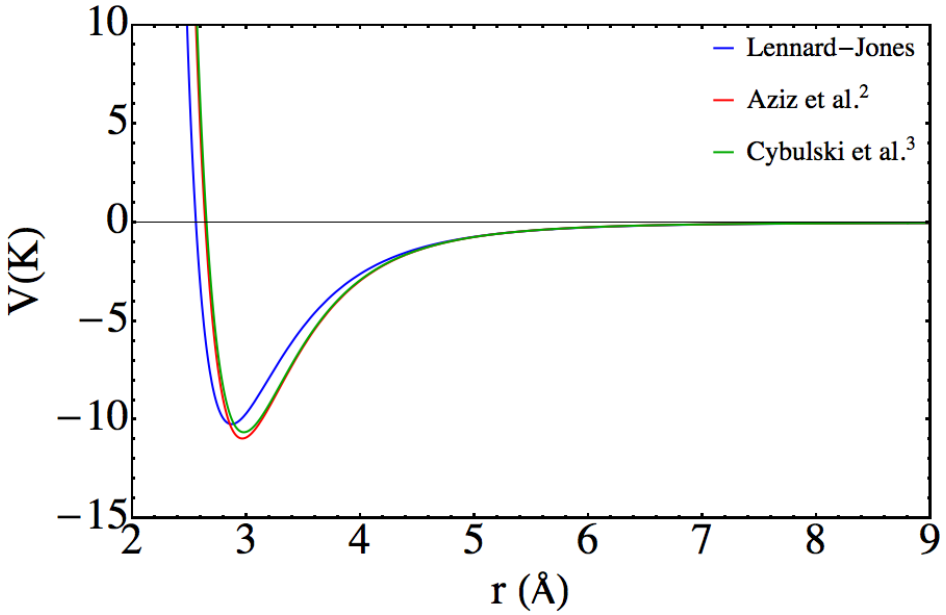

Figure 1.1 Potential energy curves for the He-He interaction.[6]

Probably the most interesting feature of ^{4}He is the phase change at 2.17 K and 1 atm from the normal liquid phase (Helium-I) to the superfluid phase (Helium-II). The superfluid phase arises from the collapse of the system at low temperatures into a collective macroscopic wave function (individual particle identities are lost) owing to the bosonic character of ^{4}He atoms.[4,5] The surprising properties of this phase include vanishing viscosity, very large thermal conductivity and new thermal waves called second sound, which make Helium-II a particularly important quantum liquid. Conversely, ^{3}He (which is a fermion) becomes superfluid at extremely low temperatures (below 0.003 K) when atoms pair to form bosons,[5] and for this reason ^{3}He is of less interest than ^{4}He.

Due to the superfluid character of liquid Helium-II it is an irrotational fluid[4]. This means that superfluid helium does not undergo rotation of the bulk fluid when subjected to a rotational torque, in contrast to normal fluids. If superfluid helium carries angular momentum it does it in the form of the rotation of the surface or quantum vortices. The axis running through the vortex core is a line of zero helium density about which the helium circulates, and its angular momentum around this vortex line is quantised. This behaviour is well known in superfluid helium as well as in weakly interacting Bose-Einstein condensates[4]. Another feature of liquid helium is that it is completely transparent

to photons below 20 eV[7] which is interesting for high resolution spectroscopy, one of the main applications of helium nanodroplets.

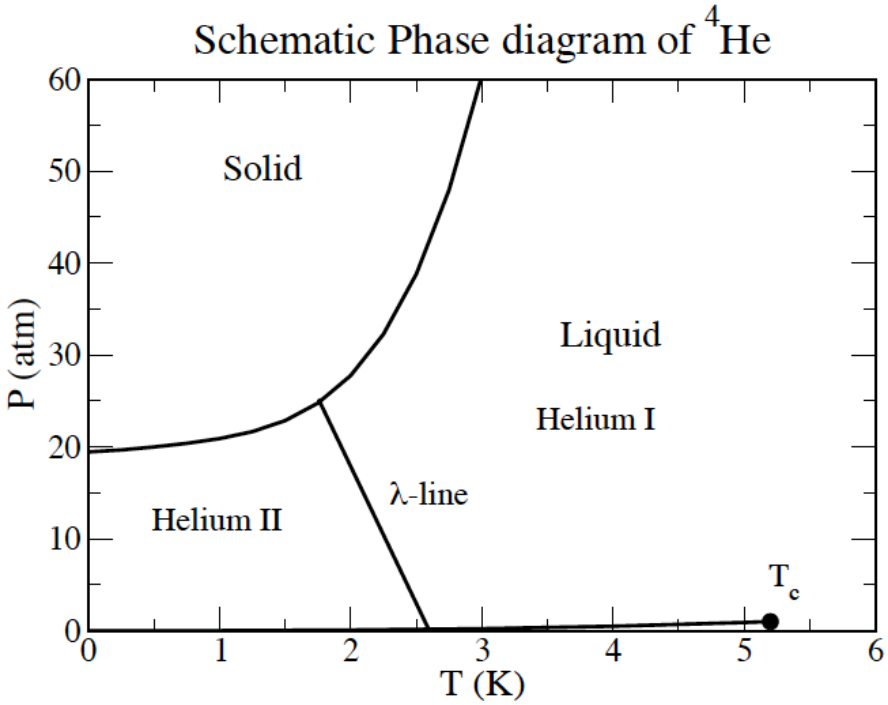

Figure 1.2 Phase diagram (P, T) of ^{4}He at low temperatures.[8]

1.2. History of superfluidity

Helium was discovered in the spectrum of Sun during an eclipse in 1868[9]. This is the reason for its name that comes from the Greek word *helios* which means Sun. It was not until 1908 that helium was liquified for the first time by H. K. Onnes[10] and he also tried to solidify it afterwards with no success. Fifteen years later, Danna and Onnes measured the latent heat and found a non-typical discontinuity around 2.2 K whose shape resembled a Greek letter lambda[11]. This temperature is known as the lambda-point, T_λ.

In 1932, Keesom and co-workers published a paper entitled "Two different liquid states of helium"[12] where they present the existence of a phase change in the liquid ^{4}He at the lambda-point (lambda transition)[13]. The two phases where named Helium-I (above T_λ) and Helium-II (below T_λ) and have different behaviours. In 1937, Allen and Misener[14] at the Royal Society Laboratories in Cambridge on one hand and Kapitza[15] in the Soviet Academy of Sciences on the other, independently found a frictionless flow for the Helium-II phase (both papers were published in *Nature* the 8 of January of 1938[16]). The only

difference is that Kapitza measured the viscosity of helium-II through channels while Misener used concentric cylinders. This behaviour was called *superfluidity* and implies the absence of viscosity, "free" rotation (Andronikashvili experiment), formation of quantised vortices and the fountain effect.

This phenomena also attracted the interest of theorists. Months after the discovery of superfluidity London proposed that it could be related to the Bose-Einstein condensates,[17,18] and that it could also be related to superconductivity. Tisza proposed the *two-fluid model*[19] which considers the fluid as a mixture of a normal liquid and a condensate part flowing under different dynamics.

In 1941 Landau found elementary excitations during the quantisation of the hydrodynamics of fluids and divided them in two groups: phonons, which are excitations of low angular momentum with linear dispersion (sound quanta), and rotons, which are high angular momentum excitations of quadratic dispersion (elementary vortices). Considering this approach the superfluid part of the two-fluid model can be considered as the ground state of the liquid helium and the normal part as the elementary excitations. It is worth noting that Landau never related superfluidity with Bose-Einstein condensates.

Probably the most remarkable contribution of Landau in this context was the rationalisation of the frictionless flow of liquid helium. He imposed the balance between energy and momentum transfer considering the dispersion relation and found a limiting velocity up to which superfluidity (ground state) happens and no elementary excitations ocurr, the *Landau's critical velocity* (58 m s^{-1})[20,21]:

$$v_c = Min_p \frac{\varepsilon(p)}{p} \tag{1.2}$$

where p is the momentum and $\varepsilon(p)$ is the energy associated to this momentum excitation. In 1947 Bogoliubov proved[22] that in a degenerate non-ideal (low-interacting) boson gas there exists Bose-Einstein condensation and that superfluidity appears at low temperatures when single particles collapse into collective modes.

In 1952 Penrose[23] generalised the Bose-Einstein condensate concept in terms of the "off-diagonal long-range order" (ODLRO). In 1956 he extended these considerations

together with Onsager,[24] allowing the Bose-Einstein condensate phase fraction to be significantly smaller than the normal one (at $T = 0$ K 10% of liquid helium is a Bose-Einstein condensate).

1.3. Helium nanodroplets

Helium nanodroplets (HeND) are aggregates of ~100 to 10^7 helium atoms. H. K. Onnes detected the formation of droplets when he was trying to liquefy helium, but he did not pay much attention to them[25]. They were not studied until Karlsruhe started studying the dependence of their properties with their size, but this was reported for the first time by Becker (1961).[26] During the late 1980's and early 1990's, the Toennies' group in Göttingen discovered that helium nanodroplets have the ability to capture chemical species.[27,28] Using electron impact mass-spectroscopy as detection technique and properly tuning the experimental conditions they obtained helium nanodroplets doped with just one impurity. Combining this pick-up technique with laser induced evaporation spectroscopy, Scoles and co-workers obtained the IR spectrum of SF_6 in HeND in 1992.[29] In 1994 Toennies and Vilesov measured for the first time the high-resolution spectrum of the same molecule in HeNDs, which was like the one in the gas phase and showing the superfluid character of liquid helium. These discoveries woke the interest of both physicists and chemists in these systems.

Helium nanodroplets are obtained using free jet supersonic expansions of pure helium gas (or liquid in few occasions) at 20-100 bar and 5-20 K through a micrometric nozzle[30]. During the expansion, the temperature decreases approximately adiabatically and atoms group together forming clusters of 100 to 10^4 atoms. Afterwards, several clusters get together and form droplets of 10^6 to 10^7 helium atoms. When droplets enter the vacuum chamber, nanodroplets release the excess of energy by evaporating helium atoms until a steady temperature of 0.37 K is reached, and nanodroplets end up being formed by 10^3 to 10^4 atoms. The nanodroplet size and size distribution (which is of the order of the mean value of the distribution) can be controlled by appropriately modifying the pressure, temperature and nozzle diameter. The experimental setup is shown in Figure 1.3.

When ^{4}He is used in the generation of nanodroplets the steady temperature reached is 0.37 K and, as it is below the superfluid transition temperature, ^{4}He nanodroplets are superfluid. However, if ^{3}He is used, the steady temperature is 0.15 K, which is above the ^{3}He superfluid transition and due to this ^{3}He nanodroplets are not superfluid. Mixed nanodroplets are composed by a core of ^{4}He atoms surrounded by ^{3}He atoms and their temperature is 0.15 K, because the outer ^{3}He atoms evaporate until this steady temperature is reached. Regardless of their superfluid character or not, the nanodroplets of both isotopes are low temperature matrices which attracts the attention of both theoreticians and experimentalists (physicists and chemists).

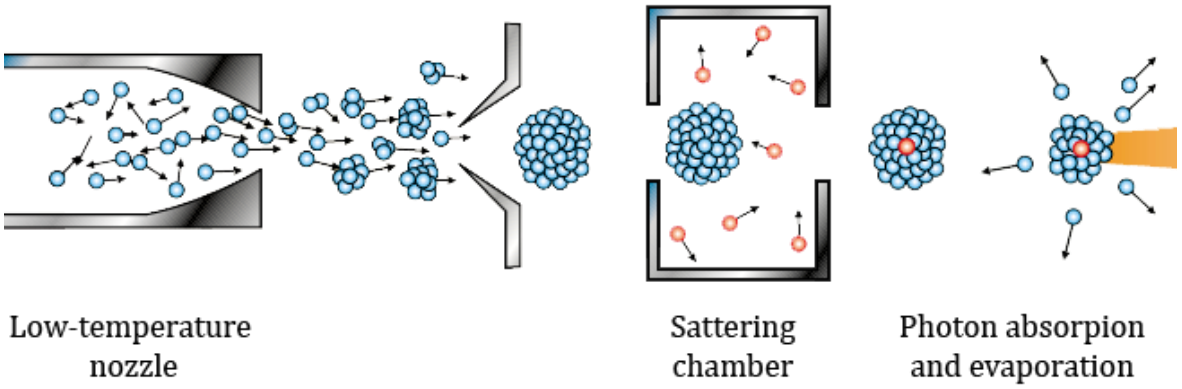

Figure 1.3 Schematic representation of the helium nanodroplets experimental setup.[25]

Concerning the energetics, the ^{4}He nanodroplets are saturating systems, i. e. , the density and binding energy per particle take an asymptotic value when the number of atoms increase. Taking the extreme cases, the He_2 dimer, which was detected experimentally by diffraction from a transmission grating[31], has a binding energy of $1.1(+0.3/-0.2)\cdot 10^{-3}$ K (and an internuclear distance of 52 ± 4 Å!); while the bulk value is 7.2 K. Ground state nanodroplets are spherical and for this reason the liquid drop model can be used to estimate the energy per helium atom as a function of the number of atoms of the nanodroplet,

$$e_{gs}(N) \equiv \frac{E_{gs}(N)}{N} = a_v + a_s N^{-\frac{1}{3}} + a_c N^{-\frac{2}{3}} + a_d N^{-1} \qquad (1.3)$$

where a_v, a_s, a_c and a_d correspond to the volume energy, surface energy, curvature energy and correction parameters (to include small nanodroplets in the fitting),

respectively. For liquid ^{4}He nanodroplets, $a_v = -7.156\ K$, $a_s = 17.47\ K$, $a_c = 4.027\ K$ and $a_d = -26.33\ K$ [6]. The thickness of the helium nanodroplets surface has been determined theoretical[32,33,34] and experimentally[33,35] and is rather large, about 6 Å. The surface of the nanodroplet is defined as the region where the helium density varies from 90 to 10% of the bulk value (0.022 atoms/Å^3). Besides, calculations showed that the Bose-Einstein condensate fraction in the surface is close to one.

As nanodroplets are finite size systems they have a discrete excitation spectrum. [35] There are two types of excitations: (a) compressional modes (or phonons) which are like the bulk helium ones but in HeND are discrete; and (b) rotons which are related with the superfluidity of the nanodroplets. Besides, there are multipolar surface modes (or ripplons) which have low energy values (below the threshold energy needed to evaporate an atom) and are long-lived.

Liquid helium is a very poor solvent because solutes interact stronger with the walls of the container than with helium. However, as nanodroplets do not interact with anything, as they isolated systems, the preference for impurities in general is to be captured by the nanodroplets. Not all impurities are placed in the centre of the nanodroplets. For very strong interacting dopants (such as, e. g., cations) snowball-like structures in the surrounding helium are formed. These structures are like a solid as the helium atoms are placed in fixed positions. The strongly heliophilic impurities (such as closed-shell atoms and molecules) are placed in the centre of the nanodroplet, while ^{3}He and alkali atoms and clusters of alkali atoms are placed on the surface forming dimples. After the pick-up (capture) impurities can cross the nanodroplet surface back and forth and the turning points can be placed outside or inside the nanodroplet, depending on the mass (for atoms heavier than Au turning points tend to lay outside and for atoms lighter than Cu they lay inside[4]) and the initial velocity at which impurities are captured by the nanodroplet[36].

The position of an impurity in a helium nanodroplet depends on the balance between the HeND-impurity interaction energy and the energy needed to create the cavity inside the nanodroplet, which depends on the He-He interaction. Ancilotto et. al.[37] achieved a remarkably good estimation on this question, obtaining the following expression:

$$\lambda_A = \frac{\rho \varepsilon r_{min}}{2^{1/6}\sigma} \tag{1.4}$$

where λ_A is an adimensional parameter, ρ is the saturation density, ε and r_{min} are the depth and the equilibrium distance of the impurity-helium interaction potential energy and σ is the helium surface tension. If λ_A is greater than 1.9 the impurity is placed in the centre of the nanodroplet, while if it is smaller than this value the surface is the favourable place for the impurity. When λ_A is close to this value, which is the case of the alkali earth atoms,[38] it is not clear what happens, and more accurate calculations or experiments are needed. When more than one impurity are present, different structures can be formed: cluster-like or foam-like structure[39]. Moreover Mg foam structures (vdW interaction) can collapse into clusters (metallic binding) by ionisation[40,41].

1.4. Applications of helium nanodroplets

The properties of helium nanodroplets have encouraged many applications implying them, from the most fundamental studies such as the study of their properties to the most applied ones such as high-resolution spectroscopy and the synthesis of metastable chemical species. An overview of them is given in this section.

From the fundamental physics point of view these systems possess fascinating properties which come from the quantum nature of the liquid. They derive from quantum statistics, as a macroscopic part of helium atoms are in the same quantum state. One of the main goals here is to study how properties vary with the nanodroplet size, in order to check to what extent the quantum nature of the liquid and its properties are a macroscopic phenomenon. These investigations have been carried using both pure and ^{3}He/^{4}He mixed nanodroplets.

Impurities act as sensitive probes to investigate properties of the liquid. In 1998 Grebenev, Toennies and Vilesov[42], using the Andronikashvili microscopic experiment, proved superfluidity by studying the OCS rovibrational spectrum using pure and mixed ^{3}He/^{4}He nanodroplets (progressively increasing the amount of ^{4}He), and they found that 60 helium atoms are present in the solvation layer. For pure ^{4}He nanodroplets the spectrum was well defined suggesting the free rotation of the OCS molecule, while for

pure ^{3}He nanodroplets the spectrum showed a single wide band[25]. For mixtures, a progressive transition was found. Therefore, spectroscopy can be used to retrieve information from liquid helium.

The pick-up process has been studied theoretical and experimentally. Theoretically, e.g., in our group we have used a hybrid approach based on the TDDFT (time dependent density functional theory) for liquid helium to study the dynamics of the Ne atom pick up, he first system for which it was found that helium clusters can capture chemical species[43]. On the other hand, another group investigated the capture of heliophobic Cs[44] and the capture of Xe and Ar atoms by helium nanodroplets with vortexes and estimated how impurities interact with vortices[36]. Besides, impurities in mixed nanodroplets can be placed in the centre of the nanodroplet, in its surface or in the ^{3}He/^{4}He interface[45].

Another proof that impurities can help determining liquid helium properties comes from the discovery of the Landau's critical velocity in the nanodroplets (above a given size)[46] and the excitation spectra of the nanodroplet and vortex nucleation[30,35]. The detection of vortexes in helium nanodroplets is related with the formation of nanowires and nanochains. Gomez et. al. used ultrafast X-ray diffraction to study atoms inside the nanodroplets and detected highly oval nanodroplets with high angular momentum[47]. The diffraction spots show that xenon clusters had been formed in the vortices of the nanodroplets. The capacity of these vortices to capture species comes from their short-range interactive force[4,36]. Furthermore, the presence of a branched structure in the TEM images indicate a variety of vortex geometries from curved lines to rings and parallel vortices in ordered lattices[47].

Apart from their interest in physics, helium nanodroplets have also drawn the attention of the chemistry community as ideal cryogenic matrices to study a wide variety of phenomena, related to atoms, complexes (Cu-H_2O complexes were studied for catalytic reasons[48]) and molecules of all sizes (low temperature chemistry[49,50,51]) including C_{60}[52]. These cryogenic matrices are interesting as they combine characteristics of both the gas phase and matrix isolation techniques[25].

Quantum effects are enhanced when temperature decreases. This can be easily interpreted in terms of the de Broglie wavelength ($\lambda = h/p$). Besides, at low temperatures only a few quantum states are occupied and less transitions are available[4,5]. This is very

important for spectroscopy as spectra are simplified in a significant way. Superfluidity also decreases the band broadening, due to the matrix effect, and the essentially negligible reactivity of helium provides a chemically stable system. These two facts combined increase the spectroscopic resolution. This was first reported by Scoles et. al.[29] when they studied the IR spectra of SF_6 embedded in helium nanodroplets.

In rotational spectroscopy molecular symmetry is unchanged and small changes in the rotational parameters due to the solvent are evident. Hence, this technique allows the determination of the rotational parameters and behaviour of large molecules that would not be possible or very difficult in gas phase or solid matrices. Even though spectroscopic experiment in helium nanodroplets permit to achieve high resolution, it has been seen that the individual rovibrational transitions are never as sharp as those measured with gas phase direct absorption methods, as seen for the methyl radical[53].

There has been considerable discussion regarding a number of potential sources of inhomogeneous and homogeneous broadening related to the finite size of the droplet and the broad statistical distribution of droplet sizes produced, and the relative importance of some of these has been quantitatively estimated[54]. For vibrational spectra, perturbations are very weak (line-shifts of about $2\ cm^{-1}$) due to the weak dispersive attractive interactions between the impurity and the liquid, so that they can be directly compared with the theoretical results for fully isolated molecules[25]. Furthermore, rotation can be hidden from the spectrum by aligning molecules with an electric field[25] or a laser pulse[55,56]. After aligning molecules, rotational revivals can be observed[57] showing that the liquid helium allows almost free rotation of impurities. Besides, isolating molecules in helium nanodroplets allows to carry out investigations which are not possible in other media, such as, e. g., the dynamics of organic molecules dimers[58].

A cryogenic not reactive and superfluid matrix is an ideal system[5,25,30] for the synthesis of a wide variety of chemical species, from small metastable molecules or radicals to metal clusters or nanowires,[59] for several reasons. Firstly, the nanodroplets stabilise the chemical species by removing kinetic energy excess from the pick-up process through the evaporative cooling. Secondly, as most dopants reside in the centre of the nanodroplet binary encounters of the impurities are easier. And, finally, the energy resulting from the synthetic process is released from the nanodroplet by evaporative

cooling, hence stabilising the products. For these reasons, helium nanodroplets have often been called *flying nano-cryo-reactors*[4].

Examples of this application are the formation of water solvated salts or molecules[60], dissociation and recombination of molecules[61], metal complexes[62,63], metal clusters[64], nanoparticles[65,66,67,68] (which are useful for catalytic purposes[69] and their size can be controlled by modifying the species' vapour pressure in the pick-up chamber), and nanowires[59], radical-radical reactions[70], hydrocarbon cations[71], organic molecules[50,72], inorganic reactions[73,74], reactions involving C_{60}[75,76,77,78,79], and complexes of polar molecules[80]. For the later, it has been seen that the preferred configuration is lineal as, at low temperatures, added molecules prefer to follow the electric field lines instead of forming compact complexes via stronger electrostatic interactions[80]. These kind of configuration helium nanodroplet mediated selectivity is also seen in the formation of the $O(^3P)$-HCN complex where only the N-bound complex is experimentally formed due the relatively big interconversion barrier[81]. It has also been seen that helium nanodroplets can be ionised and affect the dopants. Thus, alkali metals are efficiently Penning ionised which indicates rapid migration of the excitation to the droplet surface, followed by relaxation, and eventually energy transfer to the alkali dopants[79].

Another interesting application of helium nanodroplets in chemical reactivity is the formation of Cs_2-C_{60} complex through a direct harpoon-type electron transfer leading to Cs_2^+ and C_{60}^-, which is only possible when the reactants are close enough inside the nanodroplet[78,82]. When a chemical species is solvated in the centre of the nanodroplet and a second one prefers to be placed on surface, the chemical reaction between them is more difficult and, in some cases, their encounter can only be possible by photoinduction[83]. Furthermore, it has been shown that the addition of a carbon atom to a benzene molecule leads to a seven-membered ring without hydrogen release[84]. Reactions of this kind could be responsible for the low abundance of small polycyclic aromatic hydrocarbon molecules in the interstellar medium.

After synthesising any desired species in helium nanodroplets, it must be extracted from without modifying its structure. This is achieved using a substrate on which nanodroplets must land or impact[85] with a lower energy than the threshold for impurity restructuration (velocity ~200-300 m/s). This is the so-called *soft landing* and using this

procedure it has been possible, e.g., to deposit gold nanoparticles on a silica substrate. This process has also been studied theoretically for Ag clusters using molecular dynamics[86] and for Au@$^4He_{300}$ atoms on a TiO_2 surface using *ab initio*-assisted and time-resolved density functional simulations[87].

The last paragraphs in this section present the application of helium nanodroplets in the reaction dynamics context. To the best of our knowledge, in reaction dynamics there are few experimental studies on the photodissociation of alkyl iodides[88,89,90], fs photoexcitation dynamics (In)[91], fs solvation (In_2) dynamics[92], reactions involving metals, Mg + O_2[74], Al + O_2, H_2O[49], Ba + N_2O[93], etc. From the theoretical side, in this context the photodissociation of Cl_2(B) in non-superfluid[94] (hybrid method quantum packet/path integral centroid molecular dynamics) and a hybrid path integral molecular dynamics/bosonic path integral Monte Carlo[95] has been recently proposed for the study of molecules solvated in superfluid helium.

Several theoretical studies have also been performed in our group using a hybrid quantum approach combining standard quantum dynamics for the impurities and TDDFT for the helium nanodroplet. These studies include pick-up,[43] photodissociation,[96,97,98] nanodroplet relaxation,[99] vibrational energy relaxation[100] and dimer formation[101] inside a helium nanodroplet (in most cases these problems have been studied theoretically for the first time in helium nanodroplets). The main features of gas phase reaction dynamics are well stablished, and nowadays progressively more attention is being paid to the study of reaction dynamics in the liquid phase, in order to deepen into the microscopic reaction mechanism and dynamic properties in a more common situation in a chemical laboratory.

The study of the chemical reaction dynamics in helium nanodroplets provides deeper insight into these fundamental processes at very low temperatures and in a quantum fluid. Besides, it provides rich dynamics information about this important liquid. The main goal of this thesis is to broaden our understanding of these processes at a theoretical level, considering also the dynamics of a selection of interesting physico-chemical processes.

1.5. References

[1] Physics/nist.gov/PhyRefData/Handbook/Tables/heliumtable1.htm.

[2] R. A. Aziz, F. R. W. Mc Court and C. C. K. Wong, A new determination of the ground state interatomic potential for He_2, *Mol. Phys.,* 1987, **61,** 1487.

[3] S. M. Cybulski and R. R. Toczylowski, Ground state potential energy curves for He2, Ne2, Ar2, He-Ne, He-Ar and Ne-Ar: A coupled-cluster study, *J. Chem. Phys.,* 1999, **111,** 10520.

[4] A. Mauracher, O. Echt, A.M. Ellis, S. Yang, D.K. Bohme, J. Postler, A. Kaiser, S. Denifl and P. Scheier, Cold physics and chemistry: collisions, ionization and reactions inside helium nanodroplets close to zero K, *Phys. Rep.*, 2018**, 751**, 1.

[5] S. Yang and A. M. Ellis, Helium droplets: a chemistry perspective, *Chem. Soc. Rev.,* 2013, **42**, 472.

[6] A. Vilà, Quantum dynamics of physicochemical processes in superfluid ^{4}He nanodroplets, PhD thesis, University de Barcelona, July 2015.

[7] M. Y. Choi, T. M. Douberly, T. M. Falconer, W. K. Lewis, C. M. Lindsay, J. M. Merrit, P. L. Stiles and R. E. Miller, Infrared spectroscopy of helium nanodroplets: novel methods for physics and chemistry, *Int. Rev. Phys. Chem.,* 2006, **25,** 15.

[8] J. Navarro, *Density Functional Theory of Liquid Helium.* Lectures given at the Jyväskylä Summer School, Finland, August 2003.

[9] W. H. Keesom, *Helium,* Elsevier, 1942.

[10] H. K. Onnes, Experiments on the condensation of helium by expansion, *Commun. Phys. Lab. Univ. Leiden,* 1908, **105,** 744.

[11] R. Donnelly, The discovery of superfluidity, *Physics Today,* 1995, **48,** 30.

[12] W. H. Keesom and M. Wolfke, *Two different liquid states of helium*, Communications from the Physical Laboratory of the University of Leiden 219e (1932): 15-22.

[13] M. Wolfke and W.H. Keesom, On the change of the dielectric constant of liquid helium with the temperature. Provisional measurements, *Proc. Acad. Sci. Amst.,* 1927, **31,** 81.

[14] J. F. Allen and A. D. Misener, Flow of liquid helium II, *Nature,* 1938, **141,** 75.

[15] P. Kapitza, Viscosity of liquid helium below the λ-point, *Nature*, 1938, **141,** 74.

[16] S. Balibar, The discovery of superfluidity, *J. Low. Temp. Phys,* 2007, **146,** 441.

[17] F. London, The λ-phenomenon of liquid helium and the Bose-Einstein degeneracy, *Nature,* 1938, **141,** 643.

[18] F. London, On the Bose-Einstein condensation, *Phys. Rev.,* 1938, **54,** 947.

[19] L. Tisza, Transport phenomena in helium II, *Nature,* 1938, **141,** 913.

[20] I. M. Khalatnikov, *An introduction to the theory of superfluidity*. Advanced Books Classics*,* 1965.

[21] D. R. Tilley and J. Tilley, *Superfluidity and superconductivity*, Institute of Physics Publishing, 1974.

[22] N. N. Bogoliubov, On the theory of superfluidity, *J. Phys. USSR,* 1947, **11,** 23.

[23] O. Penrose, On the quantum mechanics of helium II, *Phil. Mag.,* 1951, **42,** 1373.

[24] O. Penrose and L. Onsager, Bose-Einstein condensation and liquid helium, *Phys. Rev.,* 1956, **104,** 576.

[25] J. P. Toennies, A. Vilesov and K. Whaley, Superfluid helium droplets: an ultracold nanolaboratory, *Physics Today,* 2011, **54,** 31.

[26] E. W. Becker, On the history of cluster beams *Z. Phys. Chem. D,* 1986, **3,** 101.

[27] A. Scheidemann, J. P. Toennies and J. A. Northby, Capture of neon atoms by ^{4}He clusters, *Phys. Rev. Lett.,* 1990, **64,** 1899.

[28] A. Scheidemann, B. Schilling, J. P. Toennies and J. A. Northby, Capture of foreign atoms by helium clusters, *Physica B,* 1990, **165,** 135.

[29] S. Goyal, D. L. Schutt and G. Scoles, Vibrational spectroscopy of sulfur hexafluoride attached to helium clusters, Phys. Rev. Lett., 1992, 69, 933.

[30] J. P. Toennies and A. Vilesov, Superfluid Helium Droplets: A Uniquely Cold Nanomatrix for Molecules and Molecular Complexes, Angew. *Chem. Int. Ed.,* 2004, **43,** 2622.

[31] R. E. Grisenti, W. Schölkopf, J. P. Toennies, G. C. Hegerfeldt, T. Köhller and M. Stoll, Determination of the bond length and binding energy of the helium dimer by diffraction from a transmission grating, *Phys. Rev. Lett.,* 2000, **85,** 2284.

[32] M. Barranco and E. S. Hernandez, Response of doped ^{4}He droplets *Phys. Rev. B,* 1994, **49,** 12078.

[33] J. Harms, J. P. Toennies and F. Dalfovo, Density of superfluid helium droplets, *Phys. Rev. B,* 1998, **58,** 3341.

[34] F. Dalfovo, A. Lastri, L. Pricaupenko, S. Stringari and J. Treiner, Structural and dynamical properties of superfluid helium: a density functional approach, *Phys. Rev B. Condens. Matter,* 1995, **52,** 1193.

[35] M. Barranco, R. Guardiola, S. Hernández, R. Mayol, J. Navarro and M. Pi, Helium nanodroplets: an overview, *J. Low. Temp. Phys.,* 2006, **142,** 1.

[36] F. Coppens, F. Ancilotto, M. Barranco, N. Halberstadt and M. Pi, Capture of Xe and Ar atoms by quantised vortices in ^{4}He nanodroplets, *Phys. Chem. Chem. Phys.,* 2017, **19,** 24805.

[37] F. Ancilotto, P. B. Lerner, and M. W. Cole, Physics of solvation, *J. Low. Phys.,* 1995, **101,** 1123.

[38] A. Hernando, R. Mayol, M. Pi, M. Barranco, F. Ancilotto, O. Buenerman and F. Stienkemeier, The structure and energetics of ^{3}He and ^{4}He nanodroplets doped with alkaline earth atoms, *J. Phys. Chem. A,* 2007, **111,** 7303.

[39] J. Eloranta, Theoretical study of quantum gel formation in superfluid ^{4}He, *J. Low Temp. Phys.,* 2011, **162,** 718.

[40] Andreas Przystawik, Sebastian Göde, Tilo Döppner, Josef Tiggesbäumker, and Karl-Heinz Meiwes-Broer, Light-induced collapse of metastable magnesium complexes formed in helium nanodroplets, *Phys. Rev. A,* 2008, **78,** 021202.

[41] S Göde, R Irsig, J Tiggesbäumker and K-H Meiwes-Broer, Time-resolved studies on the collapse of magnesium atom foam in helium nanodroplets, *New J. Phys.,* 2013, **15,** 015026.

[42] S. Grebenev, J. P. Toennies and A. Vilesov, Superfluidity within a small helium-4 cluster: the microscopic Andronikashvili experiment, *Science,* 1998, **279,** 2083.

[43] A. Vilà, M. González and R. Mayol, Quantum dynamics of the pick up process of atoms by superfluid helium nanodroplets: the Ne + $(^4He)_{1000}$ system, *Phys. Chem. Chem. Phys.,* 2016, **18,** 2006-2014.

[44] A. Leal, D. Mateo, A. Hernando, M. Pi and M. Barranco, Capture of heliophobic atoms by ^{4}He nanodroplets: the case of cesium, *Phys. Chem. Chem. Phys.,* 2014, **16,** 23206.

[45] F. Ancilotto, M. Barranco, François Coppens, J. Eloranta, N. Halberstadt, A. Hernando, D. Mateo, and M. Pi, Density functional theory of doped superfluid liquid helium and nanodroplets, *Int. Rev. Phys. Chem.,* 2017, **36,** 621.

[46] N. B. Brauer, S. Smolarek, E. Loginov, D. Mateo, A. Hernando, M. Pi, M. Barranco, W. J. Buma and M. Drabbels, Critical Landau velocity in helium nanodroplets, *Phys. Rev. Lett.,* 2013, **111,** 153002.

[47] L. F. Gomez, K. R. Ferguson, J. P. Cryan, C. Bacellar, R. M. P. Tanyag, C. Jones, S. Schorb, D. Anielski, A. Belkacem, C. Bernando, R. Boll, J.Bozek, S. Carron, G. Chen, T. Delmas, L. Englert, S. W. Epp, B. Erk, L. Foucar, R. Hartmann, A. Hexemer, M. Huth, J. Kwok, S. R. Leone, J. H. S. Ma, F. R. N. C. Maia, E. Malmerberg, S. Marchesini, D. M. Neumark, B. Poon, J. Prell, D. Rolles, B. Rudek, A. Rudenko, M. Seifrid, K. R. Siefermann, F. P. Sturm, M. Swiggers, J. Ullrich, F. Weise, P. Zwart, C. Bostedt, O. Gessner and A. F. Vilesov, Shapes and vorticities of superfluid helium nanodroplets, *Science,* 2014, **345,** 6199.

[48] S. Raggl, N. Gitzl, P. Martini, P. Scheier and O. Echt, Helium nanodroplets doped with copper and water, *Eur. Phys. J. D,* 2018, **72,** 130.

[49] S. A. Krasnokutski and F. Huisken, Low-temperature chemistry in helium droplets: reactions of aluminum atoms with O_2 and H_2O, *J. Phys. Chem. A,* 2011, **115,** 7120.

[50] S. A. Krasnokutski, M. Goulart, E. B. Gordon, A. Ritsch, C. Jäger, M. Rastogi, W. Salvenmoser, Th. Henning, and P. Scheier, Low-temperature condensation of carbon, *Astrophys. J.,* 2017, **847,** 89.

[51] S. A. Krasnokutski and F. Huisken, Oxidative reactions of silicon atoms and vlusters at ultralow temperature in helium droplets, *J. Phys. Chem.,* 2010, **114,** 13045.

[52] M. Kuhn, M. Renzler, J. Postler, S. Ralser, S. Spieler, M. Simpson, H. Linnartz, A. G. G. M. Tielens, J. Cami, A. Mauracher, Y. Wang, M. Alcamí, F. Martín, M. K. Beyer, R. Wester, A. Lindinger and P. Scheier, Atomically resolved phase transition of fullerene cations solvated in helium droplets, *Nat. Commun.,* 2016, **7,** 13550.

[53] A. M. Morrison, P. L. Raston and G. E. Douberly, Rotational dynamics of the methyl radical in superfluid ^{4}He nanodroplets, *J. Phys. Chem. A,* 2013, **117,** 11640.

[54] S. Fuchs, J. Fischer, A. Slenczka, M. Karra and B. Friedrich, Microsolvation of phthalocyanine molecules in superfluid helium nanodroplets as revealed by the optical line shape at electronic origin, *J. Chem. Phys.,* 2018, **148,** 144301.

[55] J. D. Pickering, B. Shepperson, B. A. K. Hübschmann, F. Thorning and H. Stapelfeldt, Alignment and imaging of the CS_2 dimer inside helium nanodroplets, *Phys. Rev. Lett.,* 2018, **120,** 113202.

[56] B. Shepperson, A. A. Søndergaard, L. Christiansen, J. Kaczmarczyk, R. E. Zillich, M. Lemeshko and H. Stapelfeldt, Laser-induced rotation of iodine molecules in He-nanodroplets: revivals and breaking-free, *Phys Rev Lett.,* 2017, **118,** 203203.

[57] B. Shepperson, A. S. Chatterley, L. Christiansen, A. A. Søndergaard and H. Stapelfeldt, Observation of rotational revivals for iodine molecules in helium droplets using a near-adiabatic laser pulse, *Phys. Rev. A,* 2018, **97,** 013427.

[58] M. Briant, E. Mengesha, M.-A. Gaveau, B. Soep, J.-M. Mestdagh and L. Poisson, Dynamics of acetylene dimers hosted in helium droplets, *Phys. Chem. Chem. Phys.,* 2018, **20,** 2597.

[59] E. Latimer, D. Spence, C. Feng, A. Boatwright, A. Ellis and S. Yang, Preparation of ultrathin nanowires using superfluid helium droplets, *Nano Lett.,* 2014, **14,** 2902.

[60] D. Leicht, M. Kaufmann, N. Pal, G. Schwaab and M. Havenith, From the tunneling dimer to the onset of microsolvation: Infrared spectroscopy of allyl radical water aggregates in helium nanodroplets, *J. Chem. Phys.,* 2017, **146,** 114306.

[61] A. Kautsch, M. Koch and W. E. Ernst, Photoinduced molecular dissociation and photoinduced recombination mediated by superfluid helium nanodroplets, *Phys. Chem. Chem. Phys.,* 2015, **17,** 12310.

[62] M. Gatchell, M. Goulart, L. Kranabetter, M. Kuhn, P. Martini, B. Rasulac and P. Scheier, Complexes of gold and imidazole formed in helium nanodroplets, *Phys. Chem. Chem. Phys.,* 2018, **20,** 7739.

[63] S. A. Krasnokutski and F. Huisken, Reactivity of iron atoms at low temperature, *J. Phys. Chem. A,* 2014, **118,** 2612.

[64] M. Ratschek, M. Koch and W. E. Ernst, Doping helium nanodroplets with high temperature metals: formation of chromium clusters, *J. Chem. Phys.,* 2012, **136,** 104201.

[65] A. Boatwright, C. Feng, D. Spence, E. Latimer, Chris Binns, A. M. Ellis and Shengfu Yang, Helium droplets: a new route to nanoparticles, *Faraday Discuss.,* 2013, **162,** 113.

[66] S. Yang, A. Ellis, C. Feng, A. Boatwright, E. Latimer and C. Binns, Growing metal nanoparticles in superfluid helium, *Nanoscale,* 2013, **5,** 11545.

[67] F. Lindebner, A. Kautsch, M. Koch and W. E. Ernst, Laser ionisation and spectroscopy of Cu in superfluid helium nanodroplets, *Int. J. Mass Spectrom.,* 2014, **365-366,** 255.

[68] A. W. Hauser, A. Volk, P. Thaler and W. E. Ernst, Atomic collisions in suprafluid helium-nanodroplets: timescales for metal-cluster formation derived from He-density functional theory, *Phys. Chem. Chem. Phys.,* 2015, **17,** 10805.

[69] Q. Wu, C. J. Ridge, S. Zhao, D. Zakharov, J. Cen, X. Tong, E. Connors, D. Su, E. A. Stach, C. M. Lindsay and A. Orlov, Development of a new generation of stable, tunable, and catalytically active nanoparticles produced by the helium nanodroplet deposition method, *J. Phys. Chem. Lett.,* 2016, **7,** 2910.

[70] D. Habig, D. Leicht, M. Kaufmann, G. Schwaab and M. Havenith, IR-spectroscopic study of the allyl + NO reaction in helium nanodroplets, *J. Chem. Phys.,* 2014, **141,** 044312.

[71] S. A. Krasnokutski, M. Kuhn, M. Renzler, C. Jäger, Th. Henning and P. Scheier, Ultra-low-temperature reactions of carbon atoms with hydrogen molecules, *Astrophys. J. Lett.,* 2016, **818,** L31.

[72] C. P. Moradi, A. M. Morrison, S. J. Klippenstein, C. F. Goldsmith and G. E. Douberly, Propargyl + O_2 reaction in helium droplets: entrance channel barrier or not?, *J. Phys. Chem. A,* 2013, **117,** 13626.

[73] J. M. Merritt, G. E. Douberly, P. L. Stiles and R. E. Miller, Infrared spectroscopy of prereactive aluminum-, gallium-, and indium-HCN entrance channel complexes solvated in helium nanodroplets, *J. Phys. Chem. A,* 2007, **111,** 12304.

[74] S. A. Krasnokutski and F. Huisken, Ultra-low-temperature reactions of Mg atoms with O_2 molecules in helium droplets, *J. Phys. Chem. A,* 2010, **114,** 7292.

[75] S. Denifl, F. Zappa, I. Mähr, F. F. da Silva, A. Aleem, A. Mauracher, M. Probst, J. Urban, P. Mach, A. Bacher, O. Echt, T. D. Märk and P. Scheier, Ion–molecule reactions in helium nanodroplets doped with C_{60} and water clusters, *Angew. Chem. Int.,* 2009, **48,** 8940.

[76] S. A. Krasnokutski, M. Kuhn, A. Kaiser, A. Mauracher, M. Renzler, D. K. Bohme and P. Scheier, Building carbon bridges on and between fullerenes in helium nanodroplets, *J. Phys. Chem. Lett.,* 2016, **7,** 1440.

[77] H. Schöbel, C. Leidlmair, P. Bartl, S. Denifl, T. D. Märk, O. Echt and P. Scheier, Electron ionization of superfluid helium nanodroplets doped with C_{60} and small molecules, *J. Phys. Conf. Ser.,* 2012, **388,** 012044.

[78] M. P. Lara-Castells, A. W. Hauser and A. O. Mitrushchenkov, Ab initio confirmation of a harpoon-type electron transfer in a helium droplet, *J. Phys. Chem. Lett.,* 2017, **8,** 4284.

[79] D. Buchta, S. R. Krishnan, N. B. Brauer, M. Drabbels, P. O'Keeffe, M. Devetta, M. Di Fraia, C. Callegari, R. Richter, M. Coreno, K. C. Prince, F. Stienkemeier, R. Moshammer and M. Mudrich, Charge transfer and Penning ionization of dopants in or on helium nanodroplets exposed to EUV radiation, *J. Phys. Chem. A,* 2013, **117,** 4394.

[80] K. Nauta and R. E. Miller, Nonequilibrium self-assembly of long chains of polar molecules in superfluid helium, *Science,* 1999, **283,** 1895.

[81] J. T. Brice, P. R. Franke and G. E. Douberly, Sequential capture of O(^{3}P) and HCN by helium nanodroplets: infrared spectroscopy and ab initio computations of the $^3\Sigma$ O−HCN complex, *J. Phys. Chem. A,* 2017, **121,** 9466.

[82] A. W. Hauser and M.P. Lara-Castells, Spatial quenching of a molecular charge-transfer process in a quantum fluid: the Cs_x–C_{60} reaction in superfluid helium nanodroplets, *Phys. Chem. Chem. Phys.,* 2017, **19,** 1342.

[83] F. Lackner and W. E. Ernst, Photoinduced molecule formation of spatially separated atoms on helium nanodroplets, *J. Phys. Chem. Lett.,* 2018, **9,** 3561.

[84] S. A. Krasnokutski and F. Huisken, Ultra-low-temperature reactions of C($^3P_0$) atoms with benzene molecules in helium droplets, *J. Chem. Phys.,* 2014, **141,** 214306.

[85] M. P. Lara-Castells, H. Stoll, B. Civalleri, M. Causà,E. Voloshina, A. O. Mitrushchenkov and M. Pi, A combined periodic density functional and incremental wave-function-based approach for the dispersion-accounting time-resolved dynamics of ^{4}He nanodroplets on surfaces: ^{4}He/Graphene, *J. Chem. Phys.,* 2014, **141,** 151102.

[86] P. Thaler, A. Volk, M. Ratschek, M. Koch and W. E. Ernst, Molecular Dynamics simulation of the deposition process of Ag-clusters under different landing conditions, *J. Chem. Phys.,* 2014, **140,** 044326.

[87] M. P. Lara-Castells, N. F. Aguirre, H. Stoll, A. O. Mitrushchenkov, D. Mateo and M. Pi, Unraveling the ^{4}He droplet-mediated soft-landing from ab initio-assisted and time-resolved density functional simulations: Au@$^4He_{300}$/ TiO_2(110), *J. Chem. Phys.,* 2015, **142,** 131101.

[88] A. Braun and M. Drabbels, Photodissociation of alkyl iodides in helium nanodroplets. I. Kinetic energy transfer, *J. Chem. Phys.,* 2007, **127,** 114303.

[89] A. Braun and M. Drabbels, Photodissociation of alkyl iodides in helium nanodroplets. II. Solvation dynamics, *J. Chem. Phys.,* 2007, **127,** 114304.

[90] A. Braun and M. Drabbels, Photodissociation of alkyl iodides in helium nanodroplets. III. Recombination, *J. Chem. Phys.,* 2007, **127,** 114305.

[91] B. Thaler, S. Ranftl, P. Heim, S. Cesnik, L. Treiber, R. Meyer, A. W. Hauser, W. E. Ernst and M. Koch, Femtosecond photoexcitation dynamics inside a quantum solvent, *Nat. Commun.,* 2018, **9,** 4006.

[92] B. Thaler, M. Meyer, P. Heim and M. Koch, Long-lived nuclear coherences inside helium nanodroplets, *arXiv*: 1907.04157 v1 [physics. chem-ph].

[93] E. Lugovoj, J. P. Toennies and A. F. Vilesov, Manipulating and enhancing reactions in helium droplets, *J. Chem. Phys.,* 2000, **112,** 8217-8220.

[94] T. Takayanagi and M. Shiga, Photodissociation of Cl_2 in helium clusters: an application of hybrid method of quantum wavepacket dynamics and path integral centroid molecular dynamics *Chem. Phys. Lett.,* 2003, **372,** 90.

[95] L. Walewski, H. Forbert and D. Marx, Reactive path integral quantum simulations of molecules solvated in superfluid helium *Comp. Phys. Comm.,* 2014, **185,** 3, 884.

[96] A. Vilà, M. González and R. Mayol, Photodissociation dynamics of homonuclear diatomic molecules in helium nanodroplets. The case of $Cl_2@(^4He)_N$, *J. Chem. Theory Comput.,* 2015, **11,** 899.

[97] A. Vilà, M. González and R. Mayol, Quantum interferences in the photodissociation of Cl_2(B) in superfluid helium nanodroplets $(^4He)_N$, *Phys. Chem. Chem. Phys.,* 2015, **17,** 32241.

[98] A. Vilà and M. González, Mass effects in the photodissociation of homonuclear diatomic molecules in helium nanodroplets: inelastic collision and viscous flow energy exchange regimes, *Phys. Chem. Chem. Phys.,* 2016, **18,** 27630.

[99] A. Vilà, M. González and R. Mayol, Relaxation dynamics of helium nanodroplets after photodissociation of a dopant homonuclear diatomic molecule. The case of $Cl_2@(^4He)_N$, *Phys. Chem. Chem. Phys.,* 2016, **18,** 2409.

[100] A. Vilà, M. Paniagua and M. González, Vibrational energy relaxation dynamics of diatomic molecules inside superfluid helium nanodroplets. The case of the I_2 molecule, Phys. *Chem. Chem. Phys.,* 2018, **20,** 118.

[101] A. Vilà and M. González, Reaction dynamics inside superfluid helium nanodroplets: the formation of the Ne_2 molecule from Ne + $Ne@(^4He)_N$, *Phys. Chem. Chem. Phys.,* 2016, **18,** 32869.

2. Methodology

The specific theoretical methods applied in each study of this thesis are presented in the corresponding chapters (Chapters 3 to 6), but the different theoretical approaches available (Section 2.1), the superfluid liquid helium density functionals (Section 2.2) and numerical methods (Section 2.3) used to describe liquid helium nanodroplets are explained with some detail in this chapter.

2.1. Theoretical approaches to liquid helium

Here are presented the methodologies used to describe liquid helium in general and the ones used in this thesis in particular: the density functional theory (DFT) for static (structure) calculations and the time dependent functional theory (TDDFT) for time evolutions (dynamics).

Since in this thesis nanodroplets composed of ^{4}He atoms are used, only the methods employed to describe bosonic systems are taken into account. Conventional molecular dynamics is not valid in this case due to the quantum behaviour of liquid helium.

A wide range of approximations have been developed for the of study liquid helium and in all of them helium atoms are treated as rigid spheres without internal structure, owing to the very low polarizability and chemical activity[1]. This approaches can be classified in two main groups: microscopic and phenomenological theories. While microscopic methods are addressed to obtain the full wave function (at zero temperature) or density matrix (at finite temperatures) of the system, phenomenological methods only consider the one body density (*density functional theory,* DFT). The method

chosen in this thesis is the DFT one and it will be detailed below, while microscopic methods will be only briefly described.

Microscopic theories involve dealing with a huge number of degrees of freedom (3 for each particle). This means that for calculations implying liquid helium Monte Carlo algorithms must be used, in order to calculate the required multidimensional integrals. These methods can be classified in two different types: *Variational Monte Carlo* (VMC) and *Quantum Monte Carlo* (QMC)[1] methods. For the VMC approach an ansatz form of the wave function is proposed and a variational principle is employed to determine the best values of the parameters that characterise the wave function. In the QMC framework the Schrödinger equation is directly integrated so as to obtain the wave function, and there are different approaches based on how the Schrödinger equation is presented. For the *Diffusion Monte Carlo* (DMC) uses a time dependent Schrödinger equation written in terms of an imaginary time and it looks like a diffusion equation. This method and an adequate initial guess lead to the exact ground state of the system in the infinite time limit. The *Green's Function Monte Carlo* method (GFMC)[2] is similar to DMC but the differential equation is converted to an integral one. To describe liquid helium at finite temperatures the *Path Integral Monte Carlo* method (PIMC) is used, which arises from the path integral formulation of the quantum mechanics. For a detailed description of the microscopic theories describing both liquid Helium-I and II see ref. 1.

Although microscopic theories can provide the exact solution, their very large computational cost and the fact that they do not allow to perform real time simulations made it necessary to develop phenomenological theories. DFT methods are *mean field* theories that allow to convert a many-body problem into an effective one-body problem. To study the reaction and relaxation dynamics of the selected systems, real-time simulations have been carried out using the time dependent DFT method. Besides, to extract information about the observables the full wave function is not always needed and the one-body density can be used as a fundamental variable in quantum mechanics, as stated by the Hohenberg-Kohn and Runge-Gross theorems.

2.1.1. Density Functional Theory

The Density Functional Theory is based on the Hohenberg-Kohn theorem,[3] which shows that given a potential energy operator, the wave function (and so the density) are completely determined for a non-degenerate ground state: $V_{ext} \Leftrightarrow \Psi \Leftrightarrow \rho$. The density is the fundamental entity to describe the system and for a system composed by N particles it is defined as:

$$\rho(\boldsymbol{r}) = |\Psi(\boldsymbol{r_1}, \boldsymbol{r_2}, \dots, \boldsymbol{r_N})|^2 \tag{2.1}$$

The energy can be written as a functional of the density ($E[\rho]$). For a given functional the ground state is obtained from the density that minimises the energy value for a constant number of atoms (using a Lagrange multiplier), which leads to the Euler-Lagrange equation:

$$\frac{\delta(E[\rho] - \mu_{He}N)}{\delta\rho(\boldsymbol{r})} = 0 \tag{2.2}$$

From Eq. (2.2) a Schrödinger-like equation is derived:

$$\left[-\frac{\hbar^2}{2m_{He}}\boldsymbol{\nabla}^2 + \int d\boldsymbol{r}\frac{\delta\varepsilon_c}{\delta(\boldsymbol{r})}\right]\sqrt{\rho(\boldsymbol{r})} = \mu_{He}\sqrt{\rho(\boldsymbol{r})} \tag{2.3}$$

where the first term is the kinetic energy operator and the second one is an effective potential that depends on the density functional, and it can be proven that μ_{He} is the chemical potential of the system. From Eq. (2.3) the density that represents the ground state of the system can be obtained.

2.1.2. Time Dependent Density Functional Theory

The time dependent density functional theory (TDDFT) lays on the Runge-Gross theorem[4] that states that there exists a one to one relationship between the density of the system at any time $\rho(\boldsymbol{r}, t)$ and the time-dependent external potential, $V_{ext}(\boldsymbol{r}, t)$, under which the system evolves.

The derivation of the equations to study the real time dynamics of liquid helium generally starts from an action principle using the quantum action (or Dirac action):

$$\mathcal{A}[\phi] = \int dt \left\langle \phi(t) \middle| i\hbar \frac{\partial}{\partial t} - \hat{H}(t) \middle| \phi(t) \right\rangle \tag{2.4}$$

where $|\phi(t)\rangle$ is the quantum many-body ket vector and $\hat{H}(t)$ the time-dependent Hamiltonian operator of the system. The minimisation of Eq. (2.4) with respect to $|\phi(t)\rangle$ leads to a Schrödinger-like equation.

Runge and Gross also stated that the action integral (Eq. (2.4)) can be expressed as a density functional $\mathcal{A}[\phi] = \mathcal{A}[\rho(\boldsymbol{r}, t)]$. However, when DFT is applied to liquid helium the corresponding effective complex wave function, $\Psi(\boldsymbol{r}, t)$, is replaced by the density. These two terms are related by

$$|\Psi(\boldsymbol{r}, t)|^2 \equiv \rho(\boldsymbol{r}, t). \tag{2.5}$$

Considering all the above the action integral for liquid helium has the following typical form:

$$\mathcal{A}[\Psi(\boldsymbol{r}, t)] = \int dt \left\{ \Psi^*(\boldsymbol{r}, t) i\hbar \frac{\partial}{\partial t} \Psi(\boldsymbol{r}, t) - E[\Psi(\boldsymbol{r}, t)] \right\} \tag{2.6}$$

Minimising Eq. (2.6) with respect to the effective wave function of helium leads a Schrödinger-like equation of motion for $\Psi(\boldsymbol{r}, t)$:

$$i\hbar \frac{\partial}{\partial t} \Psi(\boldsymbol{r}, t) = \left[-\frac{\hbar^2}{2m_{He}} \boldsymbol{\nabla}^2 + \int d\boldsymbol{r} \frac{\delta \varepsilon_c}{\delta \Psi^*} \right] \Psi(\boldsymbol{r}, t) \tag{2.7}$$

Eq. (2.7) has been deduced expressing the functional in terms of $\Psi(\boldsymbol{r}, t)$ which is not what the Runge-Gross theorem considers. The following will show why this is possible, which is related to the fourth theorem af Runge and Gross:

The exact time-dependent density of the system can be computed from:

$$\rho(\boldsymbol{r}, t) = \sum_j \varphi_j^*(\boldsymbol{r}, t) \varphi(\boldsymbol{r}, t) \tag{2.8}$$

where the single-particle orbitals $\varphi(r, t)$ fulfil the time-dependent Schrödinger equation

$$i\hbar\frac{\partial}{\partial t}\varphi_j(\boldsymbol{r},t)=\left[-\frac{\hbar^2}{2m_{He}}\nabla^2+V_{eff}[\boldsymbol{r},t;\rho(\boldsymbol{r},t)]\right]\varphi_j(\boldsymbol{r},t) \tag{2.9}$$

with an effective one-particle potential given by

$$V_{eff}[\boldsymbol{r},t;\rho(\boldsymbol{r},t)]=V_{ext}(\boldsymbol{r},t)+\int d\boldsymbol{r}'\rho(\boldsymbol{r}',t)V_{int}(\boldsymbol{r},\boldsymbol{r}')+\frac{\delta\varepsilon_c}{\delta\rho}(\boldsymbol{r},t) \tag{2.10}$$

For the time-independent case and for bosons the system is in its ground state, where all particles occupy the lowest energy single-particle wave function ($\varphi_0(\boldsymbol{r},t)$):

$$\rho(\boldsymbol{r},t=0)=N|\varphi_0(\boldsymbol{r},t=0)|^2 \tag{2.11}$$

The complex effective wavefunction is the same as this single-particle wave function but with a global phase (θ) and the $1/\sqrt{N}$ factor:

$$\Psi(\boldsymbol{r},t=0)=\frac{1}{\sqrt{N}}\varphi_0(\boldsymbol{r},t=0)e^{i\theta}. \tag{2.12}$$

This also applies to the time evolution case of Eqs. (2.7) and (2.9).

2.2. Density functionals for liquid ^{4}He

Several functionals have been proposed for liquid Helium-II through history, where the bulk liquid helium is taken as a reference in order to develop the functional. Then several extensions have been added so as to allow studying non-uniform systems (films, nanodroplets, etc…). As ^{4}He nanodroplets are at 0.37 K it is very reasonable to study them using a zero temperature DFT (ground state).

All functionals employed to describe liquid helium have the same general expression:

$$E[\rho_{He}]=\frac{\hbar^2}{2m_{He}}\int d\boldsymbol{r}\left(\boldsymbol{\nabla}\sqrt{\rho}\right)^2+\int d\boldsymbol{r}\varepsilon_c[\rho] \tag{2.13}$$

The first term is the kinetic energy functional for a non-interacting system of bosons at zero temperature in which all particles are in the same quantum single particle state

$\phi_0(\boldsymbol{r}) = \sqrt{\rho(\boldsymbol{r})/N}$, corresponding to an effective complex wave function $\Psi(\boldsymbol{r}) = \sqrt{\rho(\boldsymbol{r})}$ [5]. The kinetic energy term can be obtained from the:

$$\Psi(\boldsymbol{r_1}, \dots, \boldsymbol{r_N}) = \prod_{i=1}^{N} \phi_0(\boldsymbol{r_i}) \tag{2.14}$$

Then, the kinetic energy is expressed as:

$$\langle \Psi | \hat{T} | \Psi \rangle = \int d\boldsymbol{r_1} \dots d\boldsymbol{r_N} \Psi^* \left(\sum_i -\frac{\boldsymbol{\nabla}_i^2}{2m_{He}} \right) \Psi = -\frac{N}{2m_{He}} \int dr \phi_0^*(\boldsymbol{r}) \nabla^2 \phi_0(\boldsymbol{r})$$

$$= -\frac{1}{2m_{He}} \int d\boldsymbol{r} \left(\nabla \sqrt{\rho} \right)^2 \tag{2.15}$$

The second term in Eq. (2.13) ($\varepsilon_c[\rho]$) represents the potential and exchange-correlation energy densities.

The only difference among the proposed functionals is in the form of the second term, which is the one that contains the physics of liquid helium. In 1987[5] Stringari and Treiner adapted a Skyrme-like functional used in nuclear physics to make the first Helium-II functional. In this case the energy density only depends on the local density and the $\varepsilon_c[\rho]$ term reads:

$$\varepsilon_c[\rho] = \frac{1}{2} b \rho^2(\boldsymbol{r}) + \frac{1}{2} c \rho^{2+\gamma}(\boldsymbol{r}) + d |\boldsymbol{\nabla} \rho(\boldsymbol{r})|^2 \tag{2.16}$$

where b accounts for the attractive atomic interaction ($b < 0$), c is involved in the repulsion at short distances ($c > 0$), and d represents the repulsion energy due to the liquid-vapor interphase.

Finite range potentials represent an improvement in the description of the atom-atom interaction (vdW interaction), thanks to the introduction of an asymptotic r^{-6} behaviour via a Lennard-Jones potential and a strong repulsion at short distances which is different for each functional.

In 1990 Dupont-Roc et al proposed the first non-local energy density functional (Orsay-Paris (OP) functional)[6]. In this functional the quadratic term in Eq. (2.16) is replaced by a Lennard-Jones potential:

$$V_l(r) = \begin{cases} 4\epsilon\left[\left(\frac{\sigma}{r}\right)^{12} - \left(\frac{\sigma}{r}\right)^{6}\right] & r \geq h_0 \\ \begin{cases} V_0 r^4 & Orsay - Paris \\ 0 & Orsay - Trento \end{cases} & r \leq h_0 \end{cases} \tag{2.17}$$

with $\epsilon = 10.22\ K$, $\sigma = 2.556$ Å and h_0 depends on the functional. The term with the power of γ is the coarse-grained density, $\bar{\rho}_r$, which represents the density averaged on a sphere of atomic size and is defined by:

$$\bar{\rho}_r \equiv \int d\boldsymbol{r}' \Pi_{h_l}(|\boldsymbol{r} - \boldsymbol{r}'|)\rho(\boldsymbol{r}') \qquad \Pi_{h_l} \equiv \begin{cases} \frac{3}{4\pi h_l^3} & |r| \leq h_l \\ 0 & |r| > h_l \end{cases} \tag{2.18}$$

Considering all that has been exposed above, the potential plus exchange-correlation energy density of the OP functional has the following form:

$$\varepsilon_c[\rho] = \frac{1}{2}\rho(\boldsymbol{r}) \int d\boldsymbol{r}' V_l(|\boldsymbol{r} - \boldsymbol{r}'|)\rho'(\boldsymbol{r}') + \frac{c}{2}\rho^2(\boldsymbol{r})\bar{\rho}_r(\boldsymbol{r})^{\gamma} \tag{2.19}$$

Some years later (1995) Dalfovo et al. developed the Orsay Trento (OT) functional[7] which is the most commonly used nowadays. They introduced two new terms to better describe the properties at atomic level: the first is a non-local term considering the gradients of the density and the second one vanishes for the ground state calculations and will be discussed after. The OT functional has the following expression:

$$\begin{aligned} \varepsilon_c[\rho] = {} & \frac{1}{2}\rho(\boldsymbol{r}) \int d\boldsymbol{r}' V_l(|\boldsymbol{r} - \boldsymbol{r}'|)\rho(\boldsymbol{r}') + \frac{c_2}{2}\rho^2(\boldsymbol{r})(\bar{\rho}_r)^2 + \frac{c_3}{3}\rho(\boldsymbol{r})\left(\bar{\rho}_r(\boldsymbol{r})\right)^3 \\ & - \frac{1}{4m_{He}}\alpha_s \int d\boldsymbol{r}' F\left(|\boldsymbol{r} - \boldsymbol{r}'|\right)\left(1 - \frac{\ddot{\rho}(\boldsymbol{r})}{\rho_{os}}\right)\boldsymbol{\nabla}\rho(\boldsymbol{r})\boldsymbol{\nabla}\rho(\boldsymbol{r}')\left(1 - \frac{\ddot{\rho}(\boldsymbol{r}')}{\rho_{os}}\right) \end{aligned} \tag{2.20}$$

where another coarse-grained density (exponential weighted) is introduced and defined by:

$$\ddot{\rho}(\boldsymbol{r}) = \int d\boldsymbol{r}' F(|\boldsymbol{r} - \boldsymbol{r}'|)\rho(\boldsymbol{r}')\,, \qquad F(r) = \frac{l^3}{\pi^{\frac{3}{2}}} e^{\left(-\frac{r^2}{l^2}\right)}. \tag{2.21}$$

The parameters are determined from a fitting procedure based on the reproduction of some measured properties of liquid helium (bulk).

The second new term introduced in the OT functional helps describing the phonon-roton part of the excitation curve of bulk helium, taking into consideration the local variations of the velocity field (back-flow)[7]. With the introduction of this new term the functional not only depends on the density but also on the velocity, $E[\rho, \boldsymbol{v}]$. From the complete form of the wave function

$$\Psi(\boldsymbol{r}, t) = \sqrt{\rho(\boldsymbol{r}, t)} e^{\frac{i}{\hbar} S(\boldsymbol{r}, t)}, \tag{2.22}$$

in the OT functional, the velocity field is defined using the usual prescription for a macroscopic and hydrodynamic interpretation:

$$\boldsymbol{v}(\boldsymbol{r}, t) \equiv \frac{1}{m_{He}} \boldsymbol{\nabla} S(\boldsymbol{r}, t) \tag{2.23}$$

Considering all the above the new term (backflow term) consists in a velocity dependent effective potential which is a function of local variations in the velocity field and reads:

$$E_{backflow}[\rho, \boldsymbol{v}] = -\frac{m_{He}}{4} \int d\boldsymbol{r} \int d\boldsymbol{r}' V_J(|\boldsymbol{r} - \boldsymbol{r}'|) \rho(\boldsymbol{r}) \rho'(\boldsymbol{r}) \big(v(\boldsymbol{r}) - v(\boldsymbol{r}')\big)^2 \tag{2.24}$$

Finally, the OT functional is completely defined and its accuracy is rather good. In the studies presented in this thesis the terms related with the density gradients and the velocity field are not included, due to excessive computational cost in comparison with the small gain in accuracy.

2.3. Numerical methods

The methods used to perform the calculations concerning the liquid helium will be presented here for both the static and dynamic calculations. The methods used to describe the impurities (atoms or molecules) will be detailed in the corresponding chapters, as they vary depending on the impurity and kind of process studied.

The numerical methods for the integration of the equations which rule the statics and dynamics calculations are explained at the beginning of this section. Then it will be explained how the code deals with the spatial distribution of the helium density and calculates the convolution integrals involved, using fast Fourier transforms (FFT). Finally, the negative imaginary potential is presented.

2.3.1. Imaginary time step method

To determine the density in the context of DFT a Schrödinger-like equation, which comes from the minimisation of the functional $E[\rho]$ (ensuring the number of particles constant) must be solved. A way to do this is by means of the so-called imaginary time step method. This method is based on the time propagation of the wave function using an imaginary time step. This propagation is not really a dynamic propagation and leads to the ground state of the system.

In the development presented here the equation considered is the Schrödinger one and we make use of the wave function instead of the square root of the density. Anyway, this method works for any kind of Schrödinger-like equation. Starting from the time-dependent Schrödinger equation,

$$i\hbar\frac{\partial\Psi}{\partial t}=\widehat{H}\Psi, \tag{2.25}$$

and defining an imaginary time step, $\tau\equiv it$, Eq. (2.25) transforms into:

$$\hbar\frac{\partial\Psi}{\partial\tau}=-\widehat{H}\Psi \tag{2.26}$$

As the Hamiltonian operator does not depend explicitly on time, the solution for this equation, given an initial condition $\Psi(\tau)$ (initial guess), can be expressed in terms of the temporal propagation operator:

$$\Psi(\tau+\Delta\tau)=e^{-\frac{\widehat{H}\Delta\tau}{\hbar}}\Psi(\tau) \tag{2.27}$$

Introducing this expression to Eq. (2.26). leads to:

$$\hbar\frac{\partial\Psi(\tau+\Delta\tau)}{\partial\tau}=\hbar\left(-\frac{\widehat{H}}{\hbar}e^{-\frac{\widehat{H}\tau}{\hbar}}\right)\Psi(\tau)=-\widehat{H}\Psi(\tau+\Delta\tau) \tag{2.28}$$

If small imaginary time steps are considered and the temporal propagation operator is expanded in power series truncated to first order in $\Delta\tau$, the following equation is obtained

$$\Psi(\tau+\Delta\tau)=\left(1-\frac{\widehat{H}\Delta\tau}{\hbar}\right)\Psi(\tau) \tag{2.29}$$

Repeating this procedure the wave function of the ground state can be reached. As once the temporal propagation operator is expanded and truncated to first order it is no longer unitary, the wave function must be renormalized after each propagation step. Finally, it must be noted that for this method to be successful the initial wave function guess must have a non-zero projection on the ground state, $\langle\Psi_0|\Psi(\tau)\rangle\neq 0$, where Ψ_0 is the ground state wave function.

2.3.2. Predictor-Corrector method

Eq. (2.7) has been integrated in time using the so-called Predictor-Corrector method which is a numerical method to determine the solution of a system of N ordinary differential equations

$$\frac{dy}{dx}=f(x,y) \tag{2.30}$$

with the initial conditions $y(x_0)=y_0$, where y, y_0 and f are column vectors of N components. This method enables computers to calculate y at a sequence of values $x_i > x_0$, $i=1,2,\ldots$ by evaluating $f(x,y)$ only at the x_i points, and has been used in this thesis because it has a great accuracy-computational cost compromise[8].

The general form of the numerical integration formula is

$$y_{n+1}=a_0y_n+a_1y_{n-1}+\cdots+a_py_{n-p}+h\left(b_{-1}y'_{n+1}+b_0y'_n+\cdots+b_py'_{n-p}\right)+E_n \tag{2.31}$$

where $b_{-1}=0$ for forward integration formulae and where some of the other coefficients may be postulated to be equal to zero. The error E_n is the error incurred at the $(n+1)st$ step of the integration assuming that all the y_i and y'_i on the right-hand side of Eq. (2.31)

are known without error. Predictor-Corrector methods are iterative methods and they have smaller error terms than their analogous forward integration formulae. To use them it is necessary to perform the following steps:

I. Guess of the predicted value of y at $x = x_{n+1}$, call it $\tilde{y}_{n+1}$.
II. Using the differential equation calculate $\tilde{y}'_{n+1} = f(x_{n+1}, y_{n+1})$.
III. Using the iterative formula calculate a new y_{n+1}.
IV. Repeat steps 2 and 3 until the difference between successive values of y_{n+1} is within some predetermined limit.

A way of avoiding the iteration is to accept the first value of the corrector as y_{n+1}. This is more accurate than using forward integration formulas but not as accurate as iterating to convergence. This can be compensated by modifying the predicted and corrected values by an estimation of the truncation error caused by not iterating. Hamming developed a Predictor-Modifier-Corrector method that is stable. The expression of the generalised corrector is

$$y_{n+1} = a_o y_n + a_1 y_{n-1} + a_2 y_{n-2} + h(b_{-1} y'_{n+1} + b_0 y'_n + b_1 y'_{n-1}) \tag{2.32}$$

Using a Taylor series expansion we determine the six coefficients so that all powers of h through h^4 vanish. Therefore, the accuracy is of the order of h^5. Hamming chooses $a_0 = 0$:

$$y_{n+1} = \frac{1}{8}[9y_n - y_{n-2} + 3h(y'_{n+1} + 2y'_n - y'_{n-1})] - \frac{1}{40} h^5 y^v(\xi) \tag{2.33}$$

Then, the whole Hamming Predictor-Corrector method is:

Predictor:
$$p_{n+1} = y_{n-3} + \frac{4h}{3}(2y'_n - y'_{n-1} + 2y'_{n-2})$$

Modifier:
$$m_{n+1} = p_{n+1} - \frac{112}{121}(p_n - c_n)$$

$$m'_{n+1} = f(x_{n+1}, m_{n+1})$$

Corrector:
$$c_{n+1} = \frac{1}{8}[9y_n - y_{n-2} + 3h(m'_{n+1} + 2y'_n - y'_{n-1})]$$

Final value:

$$y_{n+1} = c_{n+1} + \frac{9}{121}(p_{n+1} - c_{n+1}) \tag{2.34}$$

where $c_{n+1} - p_{n+1}$ is the truncation error in Eq. (2.33). The initial $c_3 + p_3$ value is equal to zero.

This method is not self-starting and apart from the initial $c_{n+1} - p_{n+1}$ value, the first four y_0, y_1, y_2 and y_3 values are needed. These are obtained using the Runge-Kutta method which is explained in the following section.

2.3.3. Runge-Kutta method

The purpose of the Runge-Kutta method is to obtain numerical solutions for ordinary differential equations[9]. The difference between these methods and the ones explained above is that it not only uses the evaluation of successive x_i but of points in between these ones as well. In this thesis the Runge-Kutta method is used to provide the first four solutions of the equations as input for the Predictor-Corrector method with comparable accuracy than the ones obtained using this method.

Given a system of first-order ordinary differential equations:

$$\frac{\partial y_i}{\partial x} = y_i' = f_i\big(x, y_1(x), y_2(x), \dots, y_n(x)\big) \tag{2.35}$$

with the initial conditions:

$$y_i(x_0) = y_{i0} \tag{2.36}$$

we are looking for the values:

$$y_i(x_0 + ih) \tag{2.37}$$

where h is an increment of the independent variable x and $i = 1,2, \dots, n$. The input needed for such method consists of:

1. A sequence of instructions to evaluate $y_i'(x) = f_i\big(x, y_0(x), y_1(x), \dots, y_n(x)\big)$.
2. h, an arbitrary but small enough increment in x.
3. $y_i(x)$, the initial values.

The output consists of approximations $\tilde{y}_i(x_0 + h)$ to the true values $y_i(x_0 + h)$.

The Runge-Kutta method approximates the Taylor series solution:

$$y_i(x_0 + h) = y_i(x_0) + hy_i'(x_0) + \frac{h^2}{2!}y_i''(x_0) + \cdots \tag{2.38}$$

where $y' = f(x, y) \equiv f$.

Unlike the Taylor series the Runge-Kutta method does not need to explicitly calculate the derivatives of higher order than the first, but it approximates them using the first derivative. It is a fourth order method, which means that first derivatives must be evaluated to obtain agreement with the Taylor series solution through terms of order h^4. This means that this method has four internal steps for each iteration. Runge-Kutta has many variants. One of them yields great accuracy by compensating for some of the round-off errors accumulated at each evaluation. This refinement is achieved without increasing the complexity of the method. This is the Runge-Kutta-Gill method and it is expressed as:

$$k_1 = hf(x_0, y_0) \qquad y_1 = y_0 + \frac{1}{2}(k_1 + 2_{q_0})$$

$$k_2 = hf(x_0 + h/2, y_1) \qquad y_2 = y_1 + \left(1 - \sqrt{\frac{1}{2}}\right)(k_2 - q_1)$$

$$k_3 = hf(x_0 + h/2, y_2) \qquad y_3 = y_2 + \left(1 + \sqrt{\frac{1}{2}}\right)(k_3 - q_2)$$

$$k_4 = hf(x_0 + h/2, y_3) \qquad y_4 = y_3 + \frac{1}{6}(k_4 - 2_{q_3})$$

$$q_1 = q_0 + 3\left[\frac{1}{2}(k_1 - 2q_0)\right] - \frac{1}{2}k_1$$

$$q_2 = q_1 + 3\left[\left(1 - \sqrt{\frac{1}{2}}\right)(k_2 - q_1)\right] - \left(1 - \sqrt{\frac{1}{2}}\right)k_2$$

$$q_3 = q_2 + 3\left[\left(1 + \sqrt{\frac{1}{2}}\right)(k_3 - q_2)\right] - \left(1 + \sqrt{\frac{1}{2}}\right)k_3$$

$$q_4 = q_3 + 3\left[\frac{1}{6}(k_4 - 2q_3)\right] - \frac{1}{2}k_4 \tag{2.39}$$

where $q_0 = 0$. If these evaluations were to be made with infinite precision (i.e., with no round-off errors) q_4 would also be zero. To compensate for the error in y_4 accumulated during the evaluations q_4 is used as q_0 in the next iteration; y_1, y_2, y_3 and y_4 are not the solutions at each iteration, they are the solutions of each internal step in the method. The output at each iteration is then y_4.

Evaluating the derivatives four times may be time consuming, but the Runge-Kutta method is a stable and self-starting method, which makes it profitable for starting other methods.

2.3.4. Discretisation of space and Fourier transforms

To numerically solve the DFT and TDDFT equations for the helium nanodroplet effective wave function, the real space is discretised in a Cartesian grid of points according to:

$$x_i = i\Delta x = i\frac{L_x}{N_x}$$

$$y_j = j\Delta y = j\frac{L_y}{N_y}$$

$$z_k = k\Delta z = k\frac{L_z}{N_z} \tag{2.40}$$

where L_x, L_y and L_z are the lengths of the grid in the x, y and z axes; N_x, N_y and N_z are the number of points, and i, j, and k are the integer numbers. $\Omega = L_x L_y L_z$ is the volume of the simulation cell. Using this method the function is defined in all points of the grid and is represented using a multidimensional array:

$$f(x, y, z) \to f(x_i, y_j, z_k) = f_{ijk} \tag{2.41}$$

Then the integral of a function in the entire simulation cell is derived as:

$$\int d\boldsymbol{r} f(\boldsymbol{r}) \to \frac{\Omega}{N_x N_y N_z} \sum_{ijk} W_{ijk} f_{ijk} \tag{2.42}$$

where W_{ijk} is the weight of the point $(i\Delta x, j\Delta y, k\Delta z)$. In the present thesis the Simpson rule has been used:

$$W_{ijk} = 1 \tag{2.43}$$

Solving these equations implies calculating many convolution integrals which is significantly easier using Fourier transforms.

Convolution integrals take the general form:

$$h(\boldsymbol{r}) = \int_{-\infty}^{\infty} d\boldsymbol{r}' f(\boldsymbol{r}') g(\boldsymbol{r} - \boldsymbol{r}') \tag{2.44}$$

These integrals are computationally expensive. However, the convolution theorem states that the Fourier transform of a convolution of two functions is the product of the Fourier transforms of both functions[10]:

$$\mathcal{F}[h](\boldsymbol{p}) = \mathcal{F}[f](\boldsymbol{p}) \mathcal{F}[g](\boldsymbol{p}) \tag{2.45}$$

The Fourier transform and Fourier anti-transform are defined as:

$$\mathcal{F}[f](\boldsymbol{p}) = \int d\boldsymbol{r} e^{-2\pi i p r} f(\boldsymbol{r})$$

$$\mathcal{F}^{-1}[\mathcal{F}[f](\boldsymbol{p})](\boldsymbol{r}) = \int d\boldsymbol{p} e^{-2\pi i p r} \mathcal{F}[f](\boldsymbol{p}) = f(\boldsymbol{r}) \tag{2.46}$$

As the space in which the calculations take place is a discrete grid of points, these Fourier transforms cannot be calculated analytically, so, numerical Fourier transforms must be used. These transforms are similar to the previous ones but using summations instead of integrals:

$$\mathcal{F}_i[f_n] = \frac{1}{\sqrt{N}} \sum_{n=-\frac{N}{2}+1}^{N/2} f_n \exp\left(-i \frac{2\pi}{N} jn\right) \tag{2.47}$$

$$\mathcal{F}_n^{-1}\left[\mathcal{F}_j[f_n]\right] = \frac{1}{\sqrt{N}} \sum_{n=-\frac{N}{2}+1}^{N/2} \mathcal{F}_j[f_n] \exp\left(i\frac{2\pi}{N}jn\right) = f_n\,,$$

where N is the total number of points and the wave number values of the points the grid are limited to $k = \pi/\Delta x$. Using this discretisation means that the Fourier transform of a function defined in the interval $(-L/2 + \Delta x, L/2)$ in points equidistant at Δx will be defined in the wave vectors grid in the interval $\left(-\frac{\pi}{\Delta x} + \frac{2\pi}{N\Delta x}, \frac{\pi}{\Delta x}\right)$. Then, the discrete Fourier transform is defined as:

$$\mathcal{F}[f](k_j) = \mathcal{F}[f]_j = \frac{1}{\sqrt{2\pi N}} L\mathcal{F}_j \tag{2.48}$$

Evaluating these Fourier transforms requires N^2 operations per dimension because functions must be calculated at each point of the real space grid and the momentum grid. The computational cost is high but there is an algorithm called "Fast Fourier Transform" that reduces the number of operations to $Nlog_2N$ and then is much more efficient.

2.3.5. Negative imaginary potential

In quantum dynamics, wave functions may leave the simulation cell for different physical reasons. In the cases studied in this thesis some helium atoms may be evaporated from the nanodroplet because of the energy transfer between the impurities and the nanodroplets.

Once a fraction of the wave function arrives at the edges of the simulation cell, there may be unphysical reflections due to an undefined potential out of these points. A way to prevent this phenomenon is by defining a negative imaginary potential (NIP) at the edges of the simulation cage that absorbs the fraction of the wave function that reaches the limits of the cell.

The quartic NIP used here is described in ref. 11 and takes the following form:

$$V(\bar{x}) = -iA_4\left[\frac{5}{2}\bar{x}^4\right] \tag{2.49}$$

where $\bar{x} = x/L$ and L is the width of the region where the NIP is defined. As the space is discretised, the imaginary potential takes the following expression:

$$V(x) = \begin{cases} -iA_4 \left[\frac{5}{2} \left(\frac{x_i - (x_{min} + L)}{L} \right)^4 \right] & x_i \leq x_{min} + L \\ -iA_4 \left[\frac{5}{2} \left(\frac{(x_{max} - L) - x_i}{L} \right)^4 \right] & x_i \geq x_{max} - L \end{cases} \quad (2.50)$$

These potentials are shown to absorb up to a fraction of 10^{-12} per unit basis of the transmitted and reflected waves. They are applied to all edges in all three directions of the simulation cell.

2.4. References

[1] E. Krotscheck and J. Navarro, *Microscopic Approaches to Quantum Liquids in Confined Geometries. Series on Advances un Quantum Many-Body Theory*, Vol. 4, Ed. World Scientific, 2002.

[2] D. M. Ceperley, M. H. Kalos, *Monte Carlo Methods in Statistical Physics,* Ed. Springer, 1979.

[3] P. Hohenberg and W. Kohn, Inhomogeneous electron gas, *Phys. Rev. B.,* 1964, **136,** 864.

[4] E. Runge and E. K. U. Gross, Density-funtional theory for time-dependent systems, *Phys. Rev. Lett.,* 1984, **52,** 997.

[5] S. Stingari and J. Treiner, Surface properties of liquid ^{3}He and ^{4}He: a density functional approach, *Phys. Rev. B.,* 1987, **36,** 8369.

[6] J. Dupont-Roc, M. Himbert, N. Pavloff and J. Treiner, Inhomogeneous liquid ^{4}He: a density functional approach with a finite-range interaction *J. Low Temp. Phys.,* 1990, **81,** 31.

[7] F. Dalfovo, A. Lastri, L. Pricaupenko, S. Stringari, J. Treiner, Structural and dynamical properties of superfluid helium: a density-functional approach *Phys. Rev. B,* 1995, **52,** 1193.

[8] A. Ralston, *Mathematical Methods for Digital Computers*, eds. A. Ralston an H.S. Wilf, John Willey & Sons, New York, 1960, vol. 1, pp. 95-109.

[9] R. J. Thomson, Improving round-off in Runge-Kutta computations with Gill's method, *Commun. ACM,* 1970, **13,** 739.

[10] M. Figo and S. G. Johnson, The design and implementation of FFTW3, *IEE Proceedings,* 2005, **93,** 216.

[11] Á. Vibok and G. G. Balint-Kurti, Parametrization of complex absorbing potentials for time-dependent quantum dynamics, *J. Phys. Chem.,* 1992, **96,** 8712.

3. Quantum-classical dynamics of the capture of neon atoms by superfluid helium nanodroplets

3.1. Abstract

The capture of a Ne atom by a superfluid helium nanodroplet, Ne + $(^4He)_N \rightarrow Ne@(^4He)_{N'}$ + (N-N')^{4}He, was studied using a hybrid quantum (helium)-classical (Ne) approach and taking into account the angular momentum. The atom is captured by $(^4He)N$ and follows elliptical rotating trajectories, and large energy and angular momentum transfer from the atom to the nanodroplet occur. Helium atoms evaporation from $(^4He)N$ allows to remove the excess of energy and angular momentum of the doped nanodroplet. The behaviours observed for angular momentum different from zero are similar to the zero angular momentum case. The angular momentum of the Ne atom can induce vortex nucleation for high enough initial angular momentum values ($\sim$176.3-220.3 $\hbar$). Vortices arise from collapse of the surface excitations (ripplons) and are long-lived for some initial conditions. Comparison with a previous quantum dynamics study of our own at zero angular momentum shows that quantum effects are not important under the initial conditions examined here. Besides, a comparison with the scarce information available on other systems has been performed, showing the rich variety of behaviours that can be observed in the solvation of impurities by superfluid helium. More efforts are welcome in order to obtain a deeper insight into the dynamics of the capture process, especially in the vortex formation context.

3.2. Introduction

The study of superfluid helium nanodroplets (structure, energy and dynamics), $(^4He)_N$, $T = 0.37$ K, is an already rooted research area in physics.[1,2,3] Their intermediate size allows the researchers to investigate the properties of quantum fluids and how they change with the size of the system, from clusters to the bulk liquid. Besides, one of the features attracting more attention is the fact that, due to the inert character of He and the superfluidity of liquid ^4He below T=2.17 K, ^4He nanodroplets can be used as low temperature matrices for high resolution spectroscopy.[4,5,6]

From the initial study of chemical reactivity in helium nanodroplets,[7] the evolution of this field of study has been significant.[8,9,10,11,12,13,14,15,16] Interest in chemistry has increased in recent times due to the possibility of synthesizing new chemical species using these nanodroplets; as they are able to stabilize species which are not stable in gas phase such as metallic nanoclusters[17,18,19] and nanowires.[20,21] In terms of chemical reaction dynamics in the $(^4He)_N$ quantum fluid several reactions have been studied,[1,22] experimentally (photodissociation of alkyl iodides,[23,24,25] bimolecular reactions involving metals, Mg + O_2,[26] Al + O_2, H_2O,[9] Ba + N_2O,[7] *etc.*) and theoretically (photodissociation of Cl_2(B) in superfluid[11,12] and non-superfluid[27] helium nanodroplets; and Ne_2 formation[16]).

Even though our group is mainly interested in the study of reaction[11,12,15,16] and relaxation[14,28] dynamics inside helium nanodroplets, the pickup (capture) process of atomic or molecular species by $(^4He)_N$ is, of course, an important and related process as it precedes any chemical reactions and other processes that may occur inside the nanodroplets (see, e.g., refs. 13, 16). On the other hand, the impurities (atomic or molecular) can be considered as probes to investigate $(^4He)_N$.

The first time helium clusters were proved to have the ability to capture chemical species was in molecular beam experiments with neon atoms.[29] There is a wide variety of atomic and molecular species that can be captured by helium nanodroplets: Ar, Kr, Xe, H_20, and SF_6,[30] Ar_n,[31] Kr_n,[32] transition metal atoms (Cr_n,[33] Cu_n[34]), organic radicals (ethyl radicals),[35] aromatic organic molecules and related species (anthracene, pyrromethene, porphyrin derivatives),[36] fullerene with small molecules ($C_{60}(H_20)_n$, $C_{60}(NH_3)_n$ and $C_{60}(CO_2)_n$),[37] *etc*.

Even though a lot of experimental effort has been made (see, e.g., refs. 29, 28 and 38), information about the dynamics of the pickup process is still limited. The first attempt to study the quantum scattering dynamics of helium nanodroplets dates back to 1988,[39] and the first quantum analysis of the motion of particles inside nanodroplets was made in the late 1990s.[40,41] Further detailed many-body quantum studies of the scattering of atoms from helium nanodroplets and surfaces have been performed lately.[42,43,44] But it has not been until very recently that a few realistic theoretical studies of the pickup process and motion of the impurity inside the nanodroplet have been reported.[12,45,46,47,48]

In the present work we have theoretically investigated, using a quantum (helium)-classical (neon atom) hybrid approach, the dynamics of the pickup process of a Ne atom by a superfluid helium nanodroplet of 500 atoms, $Ne + (^4He)_N \rightarrow Ne@(^4He)_{N'} + (N\text{-}N')^4He$ (N=500). To do this we have considered four representative velocities of those typical in a pickup experimental chamber ($T \approx 300$ K) and a wide set of atom impact parameters, in order to take into account the angular momentum. Particular attention has been payed to the dynamics of the pickup microscopic mechanism and to the energy and angular momentum exchange processes. This quantum-classical study complements and extends a previous quantum dynamics investigation on the $Ne + (^4He)_N$ pickup process at zero angular momentum carried out by our group.[13]

This Chapter has the following structure: the theoretical methods are explained in Section 3.3; the description and analysis of the most important results is given in Section 3.4; and to finish the summary and conclusions are reported in Section 3.5. Additional useful information is provided in the appendices: Sections 3.6 and 3.7.

3.3. Theoretical methods

The theoretical study of the $Ne + (^4He)_N$ pickup dynamics has been carried out following a "divide and conquer" (hybrid) strategy. Thus, the superfluid helium nanodroplet has been modelled using one of the main procedures employed to describe large systems of bosonic liquid ^4He (time dependent density functional theory (TDDFT)) and the Ne atom has been described using classical mechanics (CM). In this case, differing from ref. 13, where a similar approach was used but the Ne atom was treated quantum

mechanically, the angular momentum of the attacking atom has been taken into account. The quantum-classical treatment of the pickup dynamics used here has also been applied to other atom + $(^4He)_N$ systems (see, e.g., refs. 45, 46).

To describe the helium system, we have used the Orsay-Trento (OT) phenomenological density functional.[49] The non-local contributions to the helium correlation energy and the back-flow term have been neglected for computational reasons and the major numerical complications arising from the second term. Besides, a modification has been added to the OT density functional that avoids unphysical helium density values, when the interaction between the impurity and helium is strong.[50] The theoretical investigation of the dynamics of chemical and physical processes involving $(^4He)_N$ has only been possible recently[11,12,13,14,15,16,28,45,46,51,52] and in all cases the approach indicated above has been used. On the other hand, when it has been possible to make the comparison between theory and experiment, a satisfactory agreement has been obtained by using such simplification in the OT functional[51,52,53] and, in addition, some satisfactory tests have been reported in the context of the $(^4He)_N$ relaxation.[14]

The helium wave function is propagated in time using the TDDFT method. Here we will only show the main equations used in the present study. To model the helium the quantum-classical action, in terms of the effective complex wave function of $(^4He)_N$, $|\Psi_{He}(\boldsymbol{R_{He}}, t)|^2 \equiv \rho_{He}(\boldsymbol{R_{He}}, t)$, reads:

$$\mathcal{A}[\Psi_{\mathrm{He}}(\mathbf{R_{He}}), \mathbf{R_{Ne}}] = \int \mathrm{d}t \left\{ \mathrm{E}[\Psi_{\mathrm{He}}(\mathbf{R_{He}}), \mathbf{R_{Ne}}] - \mathrm{i}\hbar \int \mathrm{d}\mathbf{R_{He}} \Psi^*_{\mathrm{He}}(\mathbf{R_{He}}) \frac{\partial}{\partial \mathrm{t}} \Psi_{\mathrm{He}}(\mathbf{R_{He}}) - \frac{1}{2} \mathrm{m_{Ne}} \left(\frac{\mathrm{d}\mathbf{R_{Ne}}}{\mathrm{dt}} \right)^2 \right\} \quad (3.1)$$

where E is the total energy of the system, that is given by:

$$E[\Psi_{He}(\mathbf{R_{He}}), \mathbf{R_{Ne}}] = \frac{\hbar^2}{2m_{He}} \int d\mathbf{R_{He}} |\boldsymbol{\nabla}\Psi_{He}|^2 + \int d\mathbf{R_{He}} \varepsilon_c[\rho_{He}] + \int d\mathbf{R_{He}} \rho_{He} V_{He-Ne}(|\mathbf{R_{He}} - \mathbf{R_{Ne}}|) + \frac{1}{2} m_{Ne} \left(\frac{d\mathbf{R_{Ne}}}{dt}\right)^2 \quad (3.2)$$

and $\varepsilon_c[\rho_{He}]$ is the density functional for liquid helium. The He-Ne diatomic potential energy used, $V_{\text{He-Ne}}$, corresponds to the *ab initio* coupled-cluster quantum chemical calculations with a large basis set reported in ref. 54. The nanodroplet-neon atom interaction has been calculated using the pairwise approach.

To obtain the equations for the time evolution of the Ne + $(^4He)_N$ system, where N=500 has been used, the quantum-classical action must be minimised by making variations on $\Psi_{He}(\boldsymbol{R_{He}})$ and $\boldsymbol{R_{Ne}}$. The resulting expressions correspond to a non-linear time-dependent Schrödinger-like equation for the helium and to the classical laws of motion for the propagation of the position and the velocity of the Ne atom (that occurs in the xy-plane):

$$i\hbar \frac{\partial}{\partial t} \Psi_{He}(\mathbf{R_{He}}) = \left[-\frac{\hbar^2}{2m_{He}} \boldsymbol{\nabla}^2 + \frac{\delta \varepsilon_c[\rho_{He}]}{\delta \rho_{He}} + V_{He-Ne}(|\mathbf{R_{He}} - \mathbf{R_{Ne}}|) \right] \Psi_{He}(\mathbf{R_{He}}) \quad (3.3)$$

$$m_{Ne} \ddot{\mathbf{R}}_{\mathbf{Ne}} = -\boldsymbol{\nabla}_{Ne} \left[\int d\mathbf{R_{He}} \rho_{He} V_{He-Ne}(|\mathbf{R_{He}} - \mathbf{R_{Ne}}|) \right] \quad (3.4)$$

Equation (3.3) has been solved using a discretization procedure (Cartesian grid) while no grid has been used for Eq. (3.4). The helium grid depends on the initial Ne velocity, being the grids denser the higher the velocity is Table s3.1. The numerical integration (time propagation) of these equations has been performed using a fourth order Adams predictor-corrector-modifier method,[55] initialised by a fourth order Runge-Kutta method.[56] The time step used in the numerical integration also depends on the initial velocity of Ne considered (Table s3.1). The derivatives involved in the calculations have been calculated in momentum space using a Fourier transform as implemented in the FFTW package.[57] To avoid possible unphysical reflections of the helium effective wave function at the edges of the grids, a quartic negative imaginary potential (NIP)[58] has been placed 1 Å before the minimum and maximum limits of the x, y, z axis (Table s3.1),

employing the same absorption strength and length as in ref. 13 (3315.0 K Å^4 and 1 Å, respectively).

The initial positions of the Ne atom considered in order to explore the influence of angular momentum on the pickup process are the following: -25.0 Å for the x-axis and 0, 7, 14, 17, 20, 27 and 34 Å for the y-axis. Moreover, the Ne and $(^4He)_N$ initial energies, considering a nanodroplet of 500 helium atoms, are given in Table 1 and the total simulation times are reported in

Table **s3.2**.

Table 3.1 Initial values of the energies involved in the Ne + (^{4}He)500 pickup process. a

v_0 Ne (m s^{-1})	E_{kin} Ne (K)
90.0	9.74
210.0	53.02
500.0	300.6
800.0	769.4

[a] E_{kin}, $E_{pot+corr}$ and E_{tot} helium are equal to 79.99, -2552.4 and -2472.3 K, respectively.

3.4. Results and discussion

The process of capturing a neon atom by a superfluid helium nanodroplet, Ne + $(^4He)_N \rightarrow Ne@(^4He)_{N'}$ + (N-N') ^{4}He with N=500 has been studied at several initial velocities of Ne (v_0 = 90, 210, 500 and 800 m s^{-1} (along the x-axis)) and several impact parameters to account for several angular momenta (b = 0, 7, 14, 17, 20, 27 and 34 Å). These velocities have been chosen in order to have a good representation of the Maxwell-Boltzmann velocity distribution of the Ne atoms at T= 300 K (Figure s3.1), which is the typical experimental condition in pickup chambers. The selected impact parameters allow us to examine the different possible situations that can be found (captured, tangential to the nanodroplet surface and non-captured trajectories).

Before carrying out the dynamics calculations and in order to define the initial conditions, the helium density of $(^4He)_{N=500}$ has been optimised using static DFT calculations with different grids, depending of the Ne atom initial velocity considered (Table s3.1). The radial distribution of the helium density obtained can be seen in Figure s2. The helium density strongly decreases near its surface and near its centre the density is constant (saturation density value (ρ_0) of 0.0224 Å^{-3}; where the helium DFT functional

has been fitted in order to reproduce the experimental value of 0.02184 $Å^{-3}$). Surface atoms have the tendency to migrate to the centre of the nanodroplet in order to minimise their energy, and this leads to the strong decrease of density observed at the HeND surface. The surface thickness is defined as the distance in which the density varies from 90% to 10% and a value of 5.2 Å has been obtained. The initial energies of the dynamic calculation are gathered in Table 3.1.

3.4.1. Case 1: zero angular momentum

Here we present the main results obtained from the calculations with b=0 Å and v_0=90, 210, 500, 800 m s^{-1}. In addition to the figures given here, additional material can be found in the ESI document and, in particular, in Movie 3.1 and Movie 3.2 the time evolution of the helium density and helium wave function phase in the xy-plane for v_0=500 m s^{-1} and two representative cases (b=0 and 14 Å, respectively) is shown. This initial velocity corresponds to the most probable velocity of neon at T=300 K. Snapshots of the helium density in the xy-plane and in the x- and y-axes for v_0=500 m s^{-1} and b=0 Å at illustrative times are shown in Figure 3.1. Moreover, the evolution of the position and velocity of the Ne atom in the x-axis as a function of time and the velocity as a function of the position (i.e., phase-space like diagram) are shown in Figure 3.2.

These figures and Movie 3.1 allow us to elucidate the capture process mechanism, which can be described considering three steps. Firstly, during the Ne atom approach a deformation of the helium nanodroplet density towards the Ne atom appears, due to the Ne-helium interaction potential energy. At this point, a waving pattern in the approaching direction appears in the HeND density, due to the excitation introduced by the atom and its velocity is increased. Secondly, once the Ne atom reaches the surface of the nanodroplet its velocity rapidly (~5 ps) decreases and, in some cases, it reaches negative values (the atom bounces back at some extent, as it can be seen in the position evolution; Figure 3.2). In addition, the waves formed due to the collision have already reached the opposite surface of the nanodroplet, colliding against it and going backwards. Finally, the helium density surrounds the Ne atom and drags it to the inside of the nanodroplet (and leading to capture), where the returning waves create interference patterns with the newly created ones.

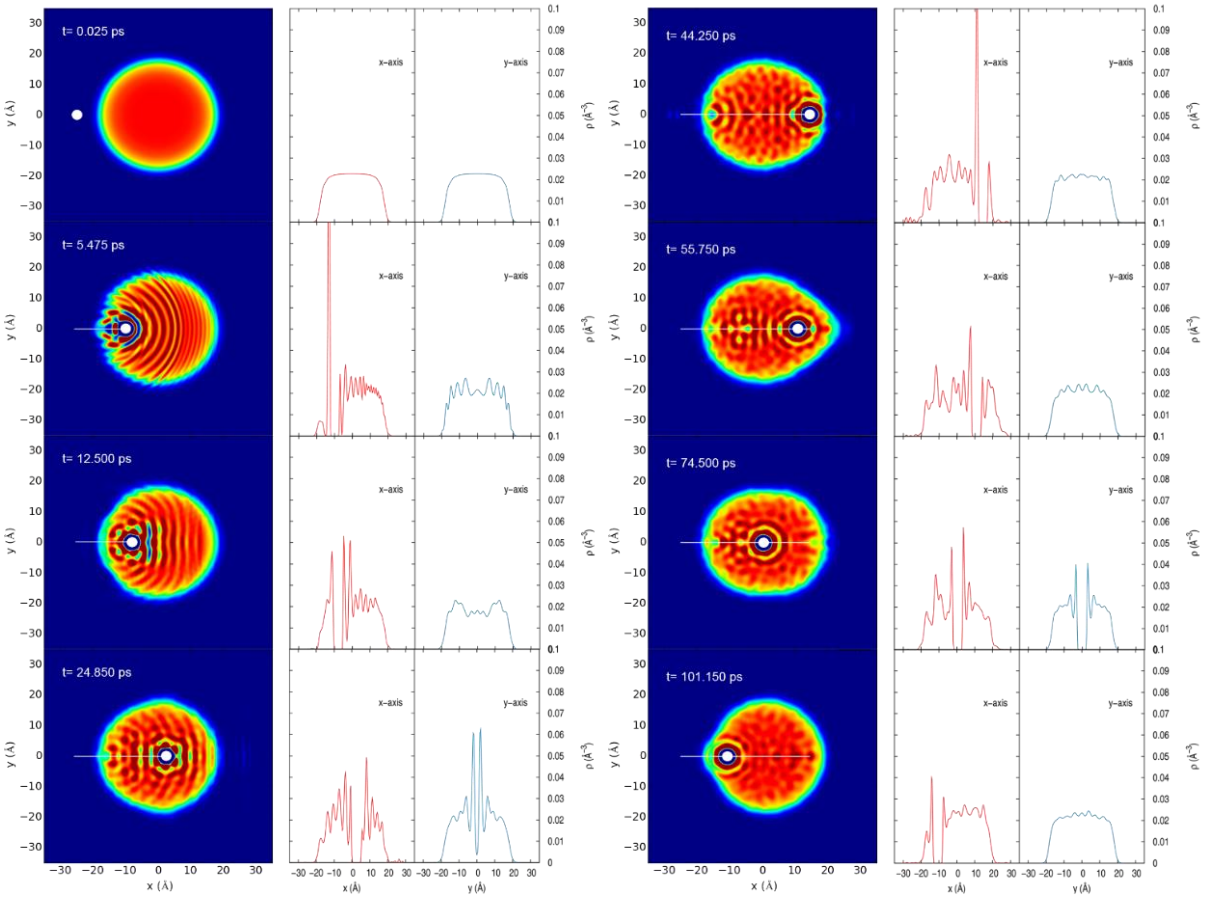

Figure 3.1 Time evolution of the helium density in the xy-plane and in the x- and y-axes for v_0=500 m s-1 and b=0 Å at representative times.

Once the Ne atom is located inside the HeND and the perturbation in the helium density is weaker, a solvation layer is formed around the atom. Then, in the bulk-like region of the HeND the atom reaches the Landau's critical velocity (v_L≈58 m s^{-1} in superfluid liquid helium (bulk)).[59,60] This velocity has been reported experimental and theoretically (TDDFT (helium) + classical mechanics (Ag)) in HeNDs with a thousand or more helium atoms.[51] We have also found the existence of this critical velocity in quantum dynamics studies (TDDFT (helium) + quantum mechanics (dopants); angular momentum equal to zero) on the Ne + $(^4He)_{1000}$ capture[13] and Ne + Ne@$(^4He)_{500}$ reaction[16] processes. Probably, this behaviour should be expected in superfluid helium nanodroplets that include a bulk-like zone.

This critical velocity reached by the atom, that when using the present method to describe the helium is ≈90 m s^{-1} [51] [due to the reasonable approximations made in the helium functional (the non-local contributions to the helium correlation energy and the back-flow term have been neglected), in order to make possible the dynamic calculations;

cf. Section 3.3], remains constant unless the atom approaches the surface of the HeND, where it bounces back. The asymmetric helium density distribution pushes the atom back and forward preventing it from staying in the centre of the nanodroplet, even though this is the most stable geometrical arrangement. Under these conditions the Ne atom is moving inside the HeND without friction, due to the superfluid character of helium below 2.17 K. In all cases examined the behaviour of Ne atom inside the nanodroplet is similar, this showing the great efficiency of the nanodroplet to accommodate the atom, even at the higher initial velocities studied.

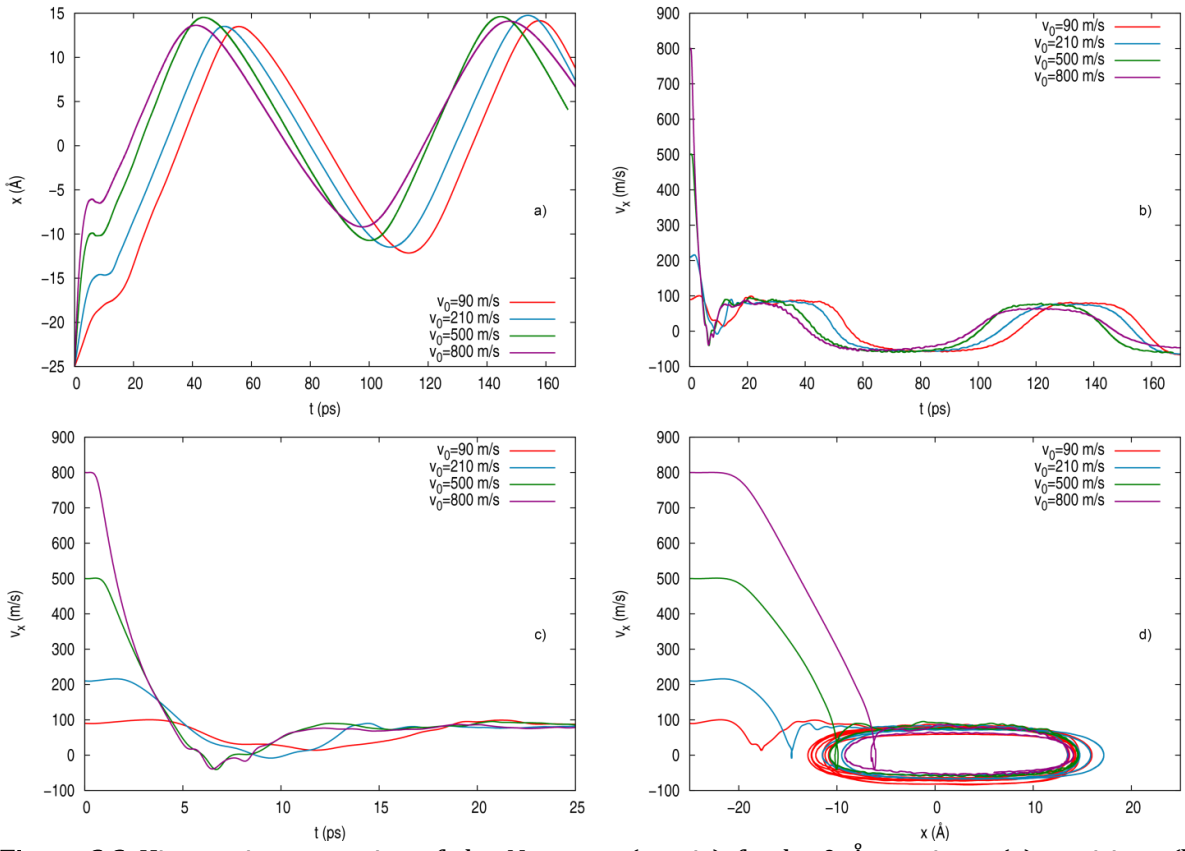

Figure 3.2 Kinematic properties of the Ne atom (x-axis) for b=0 Å vs. time: (a) position; (b) velocity; (c) velocity at short times; (d) phase-space like diagram.

The Ne atom kinetic, potential (Ne-helium) and total (kinetic + potential) energies as a function of time are given in Figure 3.3 for all the initial velocities investigated. In general terms, all energies experience a decrease when the atom is captured by the nanodroplet, i.e., the atom is stabilised by the capture. Then, there are oscillations arising from the collisions of the atom against the nanodroplet surface. Besides, for all initial velocities there is a small increase in the Ne kinetic energy at initial times, due to the Ne atom-helium interaction potential energy, and it sharply decreases as the atom reaches

the inside of the HeND. There is a clear correspondence between the kinetic energy of Ne and the Ne-helium potential energy: the minima in the kinetic energy correspond to maxima in the potential energy and vice versa.

The kinetic energy of Ne, the Ne-helium potential energy and the total energy of the HeND (without considering the previous term) *vs.* time is given in Figure 3.4 for the v_0=500 m s^{-1} case. The larger variations in the energies arise within the first 15 ps, being particularly strong the changes that occur below $t\approx$5 ps, when the capture takes place. At first, the kinetic energy of the atom strongly decreases and is mainly transformed into excitation energy of the nanodroplet.

After around 20 ps only small oscillations of the energies occur. When the Ne atom is well inside the nanodroplet, its kinetic energy and the Ne-helium interaction energy are almost constant and the HeND total energy has a slight decreasing tendency. The HeND decreases its energy by evaporation of some density (helium atoms) in order to reach the ground state density of the doped nanodroplet, Ne@(^{4}He)$_{N'}$, according to the process Ne + (^{4}He)$_N$ → Ne@(^{4}He)$_{N'}$ + (N-N')^{4}He.

The helium density is considered to correspond to evaporated density, i.e., it is not a part of the nanodroplet, when it is absorbed by the NIPs placed at the edges of the Cartesian grid of helium (cf. Section 3.3), as we have also considered in other studies.[11,12,13,14,15,16,28] Moreover, the evaporated helium density is integrated in time in order to obtain the number of evaporated He atoms, as usual.

In terms of the time derivatives of the energies, three strong peaks are evident at about 1.4 ps, when the atom reaches the surface of the nanodroplet, which are followed by small peaks and oscillations that show the existence of small energy exchanges between the atom and the HeND, with the system being not far from stability (cf. Figure 3.4).

The time evolution of the total energy of the system (without considering the energy of the evaporated He atoms) is shown in Figure 3.5. The energy is constant at the initial times and then it monotonically decreases with an asymptotic tendency (approx. -2480 K). This decrease does not occur until the Ne atom has been captured ($t\approx$5 ps for v_0=500 m s^{-1}; and at t=6.0 ps the neon velocity is equal to zero for the first time) and it arises from

the evaporation of some helium density, which allows the system to evolve towards the ground state structure of the resulting doped nanodroplet.

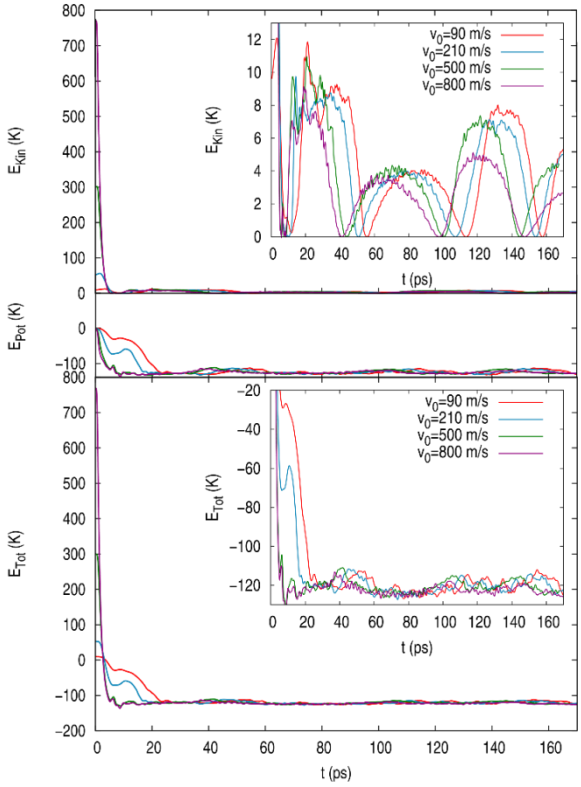

Figure 3.3 Neon kinetic energy (top), Ne-helium potential energy (middle) and the sum of both energies (bottom) for b=0 Å *vs.* time.

The number of helium atoms of the HeND and the corresponding energy per helium atom *vs.* time are given in Figure 3.6. The initial decrease of both properties is close to the moment when the neon velocity is equal to zero for the first time. Indeed, thanks to helium evaporation the nanodroplet energy per helium atom decreases to reach similar values in all cases (≈-4.8 K), even though the perturbation induced by the impurity is stronger for higher velocities.

Figure 3.7 shows how the He atoms evaporation releases the excitation energy introduced in the HeND by the collision with the Ne atom, presenting both the time interval (Δt) and energy released for each atomic evaporation. The initial evaporations are the faster ones and it is increasingly more difficult for the system to evaporate atoms, as the HeND becomes gradually less excited. Besides, the initial evaporated atoms take substantially more energy of the HeND with them that the other ones and the energy released per atom diminishes as the HeND becomes less excited. Hence, at the beginning

the HeND relaxation through He evaporation is particularly efficient, because the atoms evaporate in a faster way and remove significantly more excitation energy of the nanodroplet than the remaining evaporated atoms.

The comparison of the present quantum-classical results for b=0 Å with the quantum results at zero angular momentum previously obtained for Ne + $(^4He)_{1000}$ [13] shows that they are quite similar. Regarding the properties involving helium, we should be aware than the present nanodroplet, $(^4He)_{500}$, has half helium atoms than the nanodroplet used in ref. 13. Thus, e.g., if we consider the main peaks of the energy per He atom representation for v_0=500 and 800 m s^{-1}, increments of ≈1.53 and 0.68 K have been obtained here (Figure 3.6) with respect to the corresponding asymptotic values (final simulation times). The quantum values are ≈0.79 and 0.34 K, respectively, and this is consistent with the ratio of He atoms of the two nanodroplets. Also, if we consider the number of evaporated He atoms very close results have been obtained here and in the quantum study,[13] showing that this number only depends on the HeND excitation energy. Hence, we can conclude that for the initial conditions explored quantum effects are not very important in the Ne + HeND system, which is the lighter one of the Rg + HeND family (Rg: He, Ne, Ar, Kr, Xe, Rn), with the only exception of the Rg=He case.

Some theoretical information has been provided on the capture of a Xe or an Ar atom by $(^4He)_{1000}$ (for Xe: v_0=200, 300, 400 and 600 m s^{-1} with b=0 Å, and v_0=200 m s^{-1} with b=20.3 and 22.2 Å; for Ar: v_0=360 m s^{-1} and b=0 Å), in a TDFFT-CM study that was mostly centred on the capture of Xe and Ar atoms by HeNDs hosting quantized vortices.[47] These results are in qualitative agreement with the results obtained here for Ne, where these and other issues have been investigated in much more detail than in the previous reference: (a) most of the energy is transferred from the atom to the nanodroplet in the initial times of the collision; (b) the nanodroplet experiences large deformations; (c) at low-moderate initial velocities of the atom it moves back and forth inside the nanodroplet. Analogous trends have also been observed in the quantum dynamics studies at zero angular momentum carried out on the Ne atom capture by $(^4He)_{1000}$[13] and by the Ne@$(^4He)_{500}$ doped nanodroplet,[16] in this last case leading to the formation of the Ne_2 dimer.

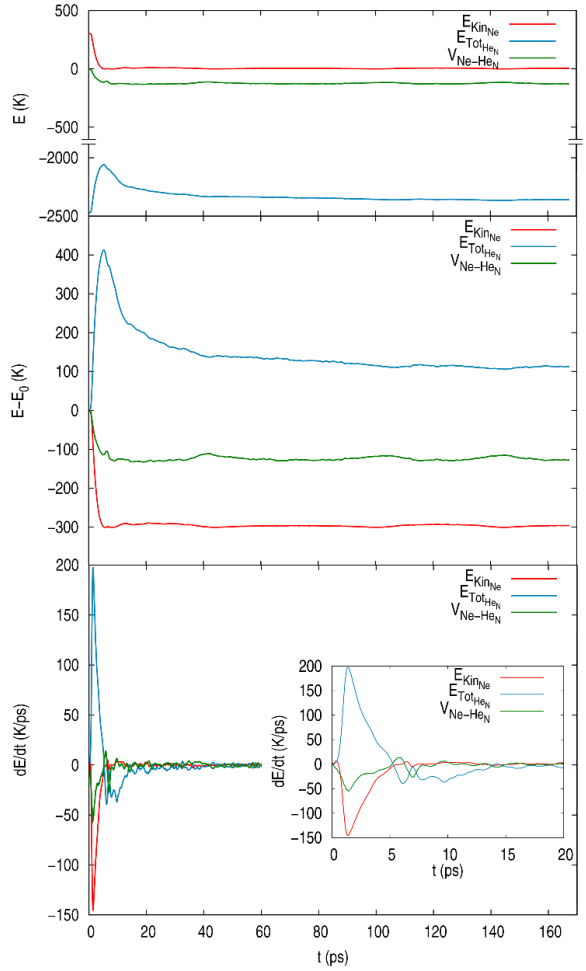

Figure 3.4 Energies (up), differences of energies, taking as a reference the respective initial values (middle), and time derivatives of the energies (bottom) including their values at short times (inset in the bottom panel), for v_0=500 m s^{-1} and b=0 Å *vs*. time.

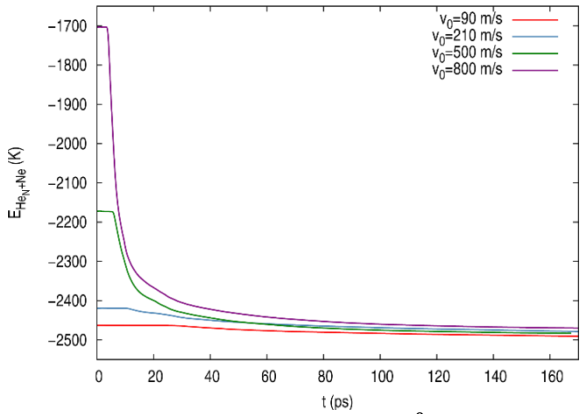

Figure 3.5 Total energy of the system *vs*. time for b=0 Å. The total energy changes due to the evaporation of some He atoms until the resulting doped HeND stabilizes.

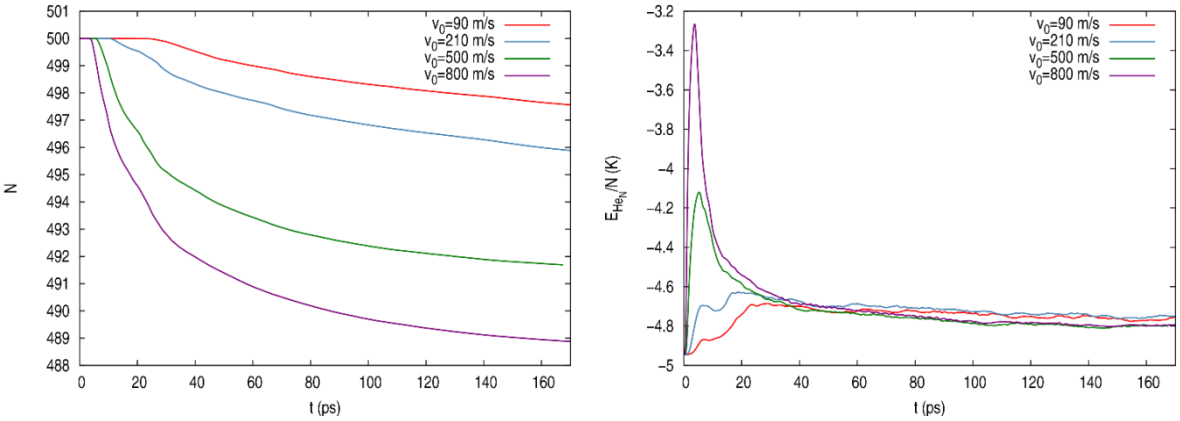

Figure 3.6 Number of helium atoms (left) and energy per helium atom of the HeND (right) for b=0 Å *vs.* time.

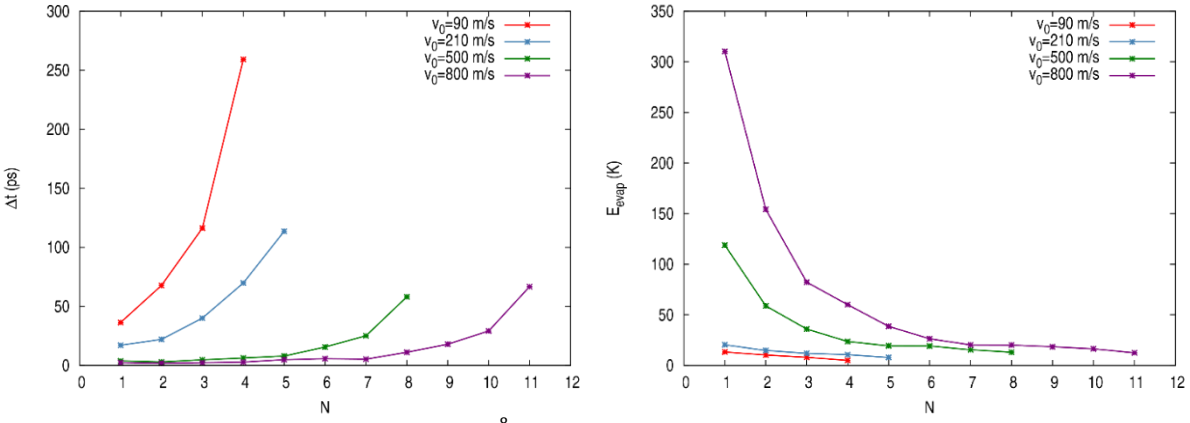

Figure 3.7 He atom evaporation for b=0 Å: time interval needed (left) and energy released (right) in each atomic evaporation.

Although strictly speaking it does not correspond to a capture process (as capture has really happened previously, once the heliophobic species Rb, Cs and Ba have been captured by the HeND and located on its surface forming a dimple), it is interesting to consider here the solvation process that occurs after photoionization of the Rb, Cs and Ba atoms, producing the Rb^+, Cs^+ and Ba^+ cations, respectively;[61] although the initial conditions are, of course, very different from those of the Ne capture. Even though at the beginning the cations move towards the centre of the nanodroplet they exhibit a large variety of behaviours. The TDDFT-CM comparative study of ref. 61 shows that after forming the Rb^+ snowball (i.e., a solid-like helium solvation structure) the cation remains essentially stationary and the helium rearranges around it; while after the formation of the Cs^+ snowball it does not penetrate the nanodroplet and, in around 90 ps, it desorbs from the HeND. The solvation of the cations initially located in the nanodroplet surface not only depends on the energy balance but also on the finer details of these systems.

In the case of Ba^+, once the snowball has been formed, it performs an almost undamped oscillating motion inside the nanodroplet. That is to say, the Ne atom (for which solvation does not lead to the formation of snowballs) presents an oscillating behaviour inside the HeND that is similar to that of Ba^+, and this also happens for the capture of a Xe atom (with the exception of the highest initial velocity reported, 600 m s^{-1}, which is well above the velocity range of Xe encountered in the experiments).[46] Related to the study developed in ref. 61 is the experimental research on the desorption of an electronically excited Na atom, initially attached to the HeND surface, reported in ref. 62, where the behaviour of several excited states has been analysed. The alkali metal atoms and small alkali clusters, which are classical heliophobic, can be induced to immerse into HeND when a highly polarizable co-solute (C_{60}) is added to the nanodroplet.[63]

Regarding the solvation of the Ne atom in the HeND, it is worth noting that around half of the time the atom is oscillating inside the nanodroplet it is well immersed, with the first and second solvation shells well defined. However, when the atom approaches the surface of the nanodroplet the second solvation layer is partly lost (typically ~1/3 to 1/2 of the second solvation layer is lost, on the side of it which is closer to the surface). Because when the impurity is completely immersed in the HeND its electronic spectrum of excitation moves towards the blue,[64] certain differences are expected to appear in the atomic spectrum, depending on whether the Ne atom is well immersed or not. On the other hand, in the case of neon the formation of the first solvation shell occurs for the first time at ~15 ps, taking as reference the moment the atom hits the nanodroplet surface. In the case of Rb^+, Cs^+ and Ba^+ the snowball structure is formed at about 20, 30 and 10 ps, respectively.[61]

What has been indicated here on the Ne atom oscillating motion inside the HeND and solvation also applies when the angular momentum is different from zero. Furthermore, the formation of vortices in two of the three cationic systems considered above will be taken into account at the end of the next section.

3.4.2. Case 2: angular momentum different from zero

Here we will analyse the influence of angular momentum on the pickup process. The initial velocity of the Ne atom for all the results presented in this sub-section is v_0=500 m

s^{-1} (which corresponds to the most probable value at T=300 K) and the impact parameters examined are b=0, 7, 14, 17, 20, 27 and 34 Å. The results obtained for the other initial velocities are similar.

Snapshots, at representative times, of the movie prepared for v_0=500 m s^{-1} and b=14 Å (Movie 3.2 in section 0) are shown in Figure s3.3, where the helium density in the xy-plane and in the x- and y-axes are presented. The capture mechanism is similar to the case without angular momentum (b=0 Å; cf. Figure 3.1) but in the present situation, of course, the y-axis component also affects the motion of the Ne atom and helium density.

The trajectories of the Ne atom for the studied cases are depicted in Figure 3.8. The dotted lines correspond to the x- and y-axes, which are centred in the HeND, and to the HeND surface circumference (R≈20 Å). From these results it comes out that the Ne atom is captured when it has an impact parameter between zero and a value that is somewhat smaller than the radius of the nanodroplet. For the impact parameters leading to capture, once the Ne atom is inside the nanodroplet, it describes rotating elliptical-like trajectories. In the other situations, the motion of the non-captured Ne atom is affected by the Ne-HeND interaction that is weaker the larger the impact parameter is. The trajectories for v_0=500 m s^{-1} and b=7, 14 and 17 Å show a kink that results from the fact that, a little after the Ne atom enters into the nanodroplet, the atom stops or even moves back due to the helium (the atom experiences the effect of a potential barrier due to the helium density), before the first solvation layer is formed around the Ne atom and then it is able to move inside the nanodroplet.

Qualitatively similar trajectories were found in ref. 48 (using a related but simpler theoretical approach), considering very different systems. The formation of metal dimers ($M + M \rightarrow M_2$; M: Cu, Ag and Au) in HeNDs was studied with the two metal atoms (M) initially placed, randomly distributed, in the nanodroplet, and only small velocities were considered (v_0: 0-56 m s^{-1}, where the largest value corresponds to the experimental Landau's critical velocity). The time values required to form the M_2 dimers obtained in ref. 48 are expected to be reasonably good for "soft" initial reaction conditions, i.e., when the atoms have small velocities and are captured by the HeND. However, under the ordinary conditions of the pickup chambers (T≈300 K), the most probable velocity is substantially larger (281, 215 and 159 m s^{-1} for Cu, Ag and Au, respectively) than the

values indicated before. These higher velocities will probably yield a substantial excitation of the nanodroplet, after the collision with the two atoms, and the helium density waves produced will probably lead to different formation times than in the previous case. Of course, in order to determine in a quantitative way the degree of validity of the interesting model applied in ref. 48, it would be desirable to compare with the M_2 formation times obtained from the TDDFT-CM method, considering initially the capture of both M atoms and following their evolution inside the nanodroplet.

For a captured Ne atom trajectory, the deflection angle has been taken as equal to the angle defined by the initial direction of the Ne atom motion and the direction of the trajectory of this atom during the first approach to the surface of the nanodroplet (once the atom is inside the nanodroplet). For a non-captured Ne atom trajectory, the deflection angle has the usual definition. These deflection angles, α_d, have been found to be 0, -19, -59, -82, -13, 0 and 0º for b=0, 7, 14, 17, 20, 27 and 34 Å, respectively (Figure s3.4). Further short-time calculations, considering some additional impact parameter values, have been performed in order to find the maximum impact parameter for capture (b_{max}) and it has been found to be about 25, 23, 18 and 16 Å for v_0= 90, 210, 500 and 800 m s^{-1}, respectively. The decrease of b_{max} with v_0 suggests that the capture process has no energy theshold[65] (see at the end of this section the comparison with the Xe atom capture).

Velocities evolve over time following similar behaviours as for b=0 Å, the only difference is that the velocity decrease, due to the atom collision against the HeND surface, happens at larger times for larger impact parameters (Figure s3.5), as it takes longer for the atom to reach the HeND surface when b increases. The phase-space like diagrams for Ne (v_0=500 m s^{-1}) are plotted in Figure 3.9, where it can also be seen that the atom with impact parameter a bit smaller than the radius of the nanodroplet is indeed captured (elliptical-like trajectories).

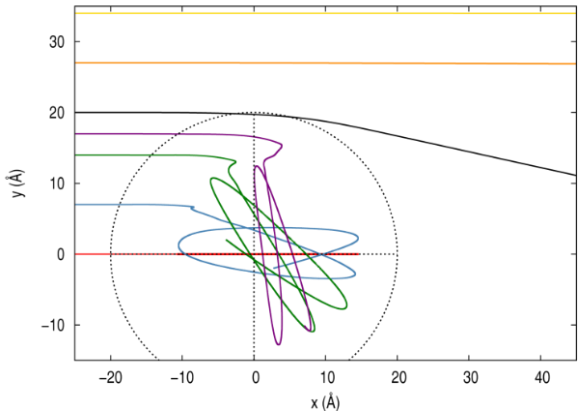

Figure 3.8 Ne atom trajectories for v_0=500 m s^{-1} and impact parameters b=0 (red), 7 (blue), 14 (green), 17 (magenta), 20 (black), 27 (orange) and 34 (yellow) Å.

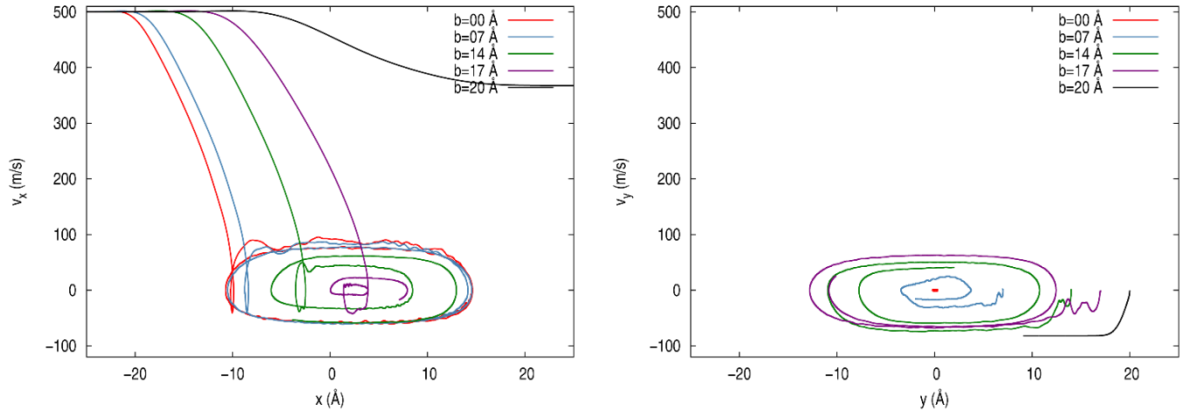

Figure 3.9 Phase-space like diagram of the Ne atom for v_0=500 m s^{-1} at several impact parameters: x component (left); y component (right).

The evolution of the energies and of the time derivatives of the energies *vs.* time is also similar to the b=0 Å case. Higher Ne atom impact parameters (i.e., higher angular momentum values) only introduce smoothness in the whole process, i.e., the pickup process is 'softer' the bigger the impact parameter is (cf. Figure s3.6 and Figure s3.7). Moreover, the kinetic energy transferred by the Ne atom to the HeND is essentially constant (≈300 K) and corresponds to its initial kinetic energy, until the b value is not far from b_{max}, where a strong decrease occurs (Figure s3.8).

The time evolution of the total energy of the system (Ne + HeND), the number of helium atoms of the HeND, and the energy per helium atom of the HeND are given in Figure s3.9 and Figure s3.10, and the required time to evaporate helium atoms is reported in Figure s3.11. These properties also show similar behaviours as those reported for b=0 Å.

The most important difference found between the $b \neq 0$ and $b=0$ results comes from the fact that, in some cases, shortly after the Ne atom has been captured, vortices (vortex lines) are formed in the nanodroplet, as a result of the surface perturbations created by the atom impact. Moreover, the examination of the angular momentum exchange between the Ne atom and the HeND and the distribution of angular momentum in the HeND is also of a large interest. These issues are considered below.

The vortices have been found to travel along with the Ne atom inside the nanodroplet and vortex formation only occurs when the initial angular momentum of neon is high enough (see, e.g., Figure 3.1 and Figure **3.11** and Movie 3.2 to Movie **3.4**). A long-lived vortex (which is close or very close to the HeND surface), i.e., a vortex initially lasting several Ne atom rebounds with the HeND surface and showing subsequent and sequential temporary disappearances and reappearances approximately between the atom rebounds during the whole simulation time, has been found for the $v_0=500$ m s^{-1}, $b=14$ and 17 Å and $v_0=800$ m s^{-1}, $b=14$ Å initial conditions. From this information, we have estimated that the minimum initial angular momentum of neon (L_{Ne}; z-component only) leading to the formation of long-lived vortices is within the interval between -176.3 and -220.3 $\hbar$, where these values correspond to L_{Ne} for $v_0=800$ m s^{-1}, $b=7$ Å and $v_0=500$ m s^{-1}, $b=14$ Å, respectively. The formation of a short-lived vortex, i.e., lasting as long as a Ne atom rebound with the HeND surface has been found in other cases. The different situations observed, including those where no vortex has been formed are collected in Table 3.1, as a function of the initial conditions (v_0, b).

The complexity of the dynamics of vortex formation/disappearance process can be understood better after examination of Movie 3.2 to Movie **3.4**. Thus, for $v_0=500$ m s^{-1}, $b=14$ Å the vortex is formed shortly after the atom enters inside the HeND and exists during the time it takes the Ne atom to make the first three rebounds on the HeND surface. Then, the vortex reappears in the fourth atom rebound, disappears in the fifth and reappears in the sixth one (a bit latter the simulation finishes). In addition, an ephemeral (very short-lived) new vortex is observed in the first rebound of the Ne atom on the HeND surface. The behaviours observed for $v_0=500$ m s^{-1}, $b=17$ Å and $v_0=800$ m s^{-1}, $b=14$ Å are similar to the previous one, particularly for the last condition. Thus, for $v_0=500$ m s^{-1}, $b=17$ Å the initial period of existence of the vortex corresponds to four Ne atom rebounds, the ephemeral vortex occurs before the first rebound and the evolution after the fourth

rebound is somewhat more complex (ephemeral reappearance and reappearance of the vortex at the fifth and sixth rebounds, respectively), while for v_0=800 m s^{-1}, b=14 Å no ephemeral vortex around the first rebound has been found.

Table 3.2 Vortex line formation in the Ne atom capture process.[a,b,c]

v_0 (m/s) \ b(Å)	0.0	7.0	14.0	17.0	20.0
90					
210		1	1	1	1[d]
500		1	6...	6...	
800			4...		

[a] Vortex cases: not formed (red); short-lived (yellow); long-lived (green).

[b] Numbers represent the number of rebounds of the atom against the HeND surface that the vortex survives. "6..." means that six is the maximum number of rebounds the simulation time allows us to find. The vortices indicated in green are expected to last longer.

[c] b_{max} is around 25, 23, 18 and 16 Å for v_0= 90, 210, 500 and 800 m s^{-1}, respectively.

[d] This vortex is formed in the second atom rebound which differs from the other cases indicated in yellow, which are formed in the first rebound.

The helium density in the xy-plane and in the perpendicular planes cutting along the centre of the long-lived vortex found for v_0=500 m s^{-1} and b=17 Å is shown in Figure 3.10. Besides, the helium velocity field, the helium wave function phase, and the volume occupied by the vortex for the situation reported in the previous figure are presented in Figure 3.11. Also, several snapshots of the time evolution of the helium density, velocity field and wave function phase are shown in Figure s3.1; and the time evolution of the helium density and helium wave function phase for v_0=500 m s^{-1} and b=14 and 17 Å and v_0=800 m s^{-1} and b=14 Å can be seen in Movie 3.2 to Movie 3.4, respectively.

The helium density plot shows that the vortex line has a slightly curved tube shape perpendicular to the xy-plane (where the Ne atom is moving), in which there is little or no helium density (Figure s3.10); and the helium velocity field plot indicates that the helium density is moving in circles around the centre of the vortex (Figure s3.11). The bigger helium velocities are found around the vortex, being the velocity in the rest of the points of the nanodroplet small. The helium wave function phase (ϕ) diagram shows that the phase changes in a substantial way (from π to $-\pi$) for the points around the vortex (Figure 3.11). The calculation of the circulation of the velocity of the helium fluid $\left(v = \frac{\hbar}{m}\nabla\phi, \text{where } \phi \text{ is the phase of } \Psi_{\mathrm{He}}(\boldsymbol{R}_{\mathbf{He}}, t)\right)$ in a closed path around the centre of the

vortex $\left(\Gamma = \frac{\hbar}{m}\oint d\boldsymbol{r}\,\nabla\phi\right)$ [66] yields $\Gamma = \frac{\hbar}{m}2\pi = \frac{h}{m}$, which means that the circulation is quantised ($\Gamma = n\frac{h}{m}$, $n \in$ integer) with $n = 1$. All these facts confirm that, in fact, the initial condition v_0=500 m s^{-1} and b=17 Å case shows a quantised vortex line.

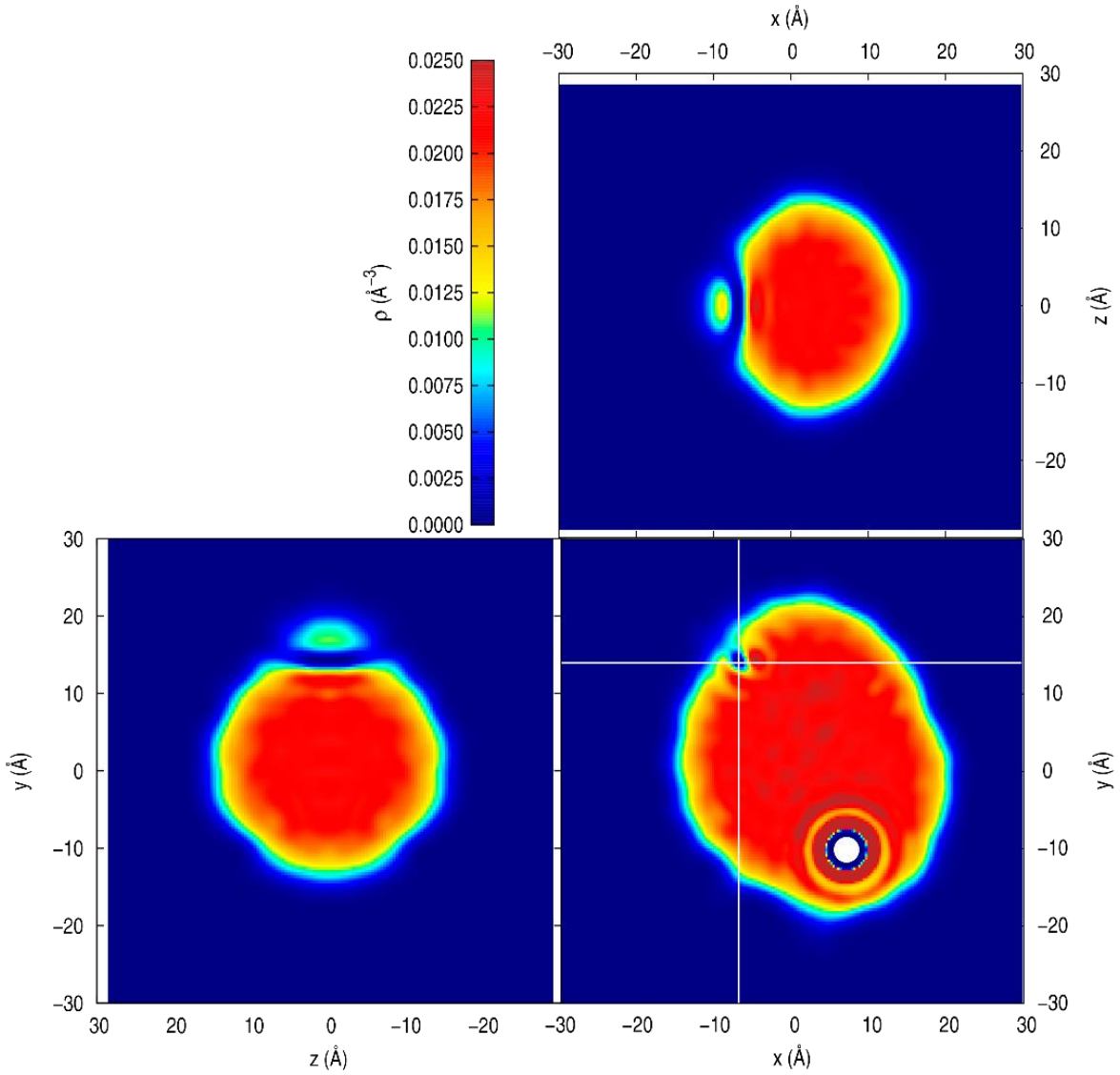

Figure 3.10 Helium density in the xy-plane and in two perpendicular planes cutting along the centre of the vortex line for v0=500 m s-1 and b=17 Å at the final simulation time (171.2 ps). The vortex line displays a bit curved tube perpendicular to the xy-plane.

Regarding the angular momentum (L) and as a representative example, the neon (L_{Ne}), helium nanodroplet (L_{HeND}), and total (L_{tot}) angular momenta, as a function of time, are plotted in Figure 3.12 for v_0=500 m s^{-1} and b=14 Å, where it becomes clear that an important angular momenta exchange process occurs in the system. Initially the HeND has no angular momentum, but once the Ne atom reaches the nanodroplet surface (t≈2.4

ps) it begins to transfer in a fast way its angular momentum to the nanodroplet, which leads to HeND rotational excitation. The maximum angular momentum transfer occurs in about 5 ps after the Ne atom collision, where 92.5% of the initial L_{Ne} ($L_{Ne,0}$) appears as L_{HeND} (≈-203.4 $\hbar$). The correlation between L_{HeND} and $L_{Ne,0}$ for v_0=500 m s^{-1} can be seen in Figure s3.13.

A bit after the collision (≈2.4 ps) the Ne to HeND kinetic energy transfer leads to the evaporation of some He atoms and then the HeND angular momentum is reduced in a substantial way. L_{HeND} evolves from around -203.4 to -109.9 $\hbar$ in about 7.2 ps and reaches a value of ≈-62.3 $\hbar$ in around 32.7 ps. Therefore, a high percentage of $L_{Ne,0}$ is removed by the evaporated He atoms (62.5% of $L_{Ne,0}$ at t≈30 ps and smaller changes at higher times; 70 and 75% of $L_{Ne,0}$ at t=60 and 170 ps, respectively). The angular momentum carried out by each evaporated helium atom is shown in Figure 3.13 for the four initial velocities studied and for b=14 Å. The atoms evaporated at the smaller values of time are produced with a greater amount of angular momentum than those formed later, analogously to what happens for the energy.

In the doped nanodroplet most of the angular momentum is carried out by the helium and some smooth oscillations occur in the Ne atom and HeND angular momenta time evolution (Figure 3.12), due to the collisions of the atom with the nanodroplet surface. These oscillations are in anti-phase, i.e., when the Ne atom angular momentum modulus decreases the HeND angular momentum modulus increases and vice versa.

The velocity of change of angular momenta (dL/dt) *vs.* time is given in Figure 3.14. The major changes are observed in the initial times (the most intense peak occurs at ≈3.2 ps), when the Ne atom reaches the HeND surface and enters into the nanodroplet, as expected. Three main peaks are found, due to similar reasons as the ones driving the variation of the Ne atom kinetic energy (Figure 3.4). At larger times (t above ≈15 ps), variations are small and only happen when the Ne atom rebounds against the surface of HeND, where the corresponding angular momenta are reduced or increased. These variations are more important as the impact parameter value leading to capture increases, due to the larger amount of angular momentum involved.

The angular momentum of the nanodroplet is not evenly stored in all points, as it can be seen for v_0=500 m s^{-1} in Figure 3.15. In this figure the end of simulation radial

distribution of L_{HeND} for all impact parameters leading to capture are presented (the final simulation times are shown in

Table **s3.2**). The angular momentum transferred by the Ne atom to the nanodroplet is mainly placed near the HeND surface, due to the irrotational character of superfluid ^{4}He.[67,68] This corresponds to surface excitations of the helium density (ripplons) and, in some cases, they can collapse into vortices, as we have already detailed (v_0=500 m s^{-1} and b=14 and 17 Å and v_0=800 m s^{-1} and b=14 Å). The wider peak observed for b=17 Å results from the existence of a long-lived vortex, in addition to the surface excitations. As opposed to the surface excitation peaks, which are narrow due to the small value of the surface thickness, the b=17 Å vortex peak is wider as the vortex occupies a wider radial thickness. The angular momentum peaks within the nanodroplet are explained by helium circulations due to the Ne atom motion. For the final simulation time of b=14 Å (177 ps) the long-lived vortex does not exist, in contrast to what happens for b=17 Å (171 ps). In Figure s3.14 the results obtained for the other initial velocities of neon are given.

The angular momentum carried by the HeND (L_{HeND}) can be divided in three components corresponding to the centre of mass (displacement of the entire nanodroplet; L_{cm}), vortex line (L_{vor}) and other excitations (L_{other}). The contribution of each one of these components to the angular momentum of the doped nanodroplet with respect to the origin of coordinates is reported in Table s3.3, including the angular momentum of the vortex with respect to its centre ($L_{vor,centre}$). All angular momenta have been calculated using the quantum operator $\widehat{L_Z}$ except L_{cm} that has been calculated classically using the helium velocity field (both approaches lead to the same results; see the appendix).

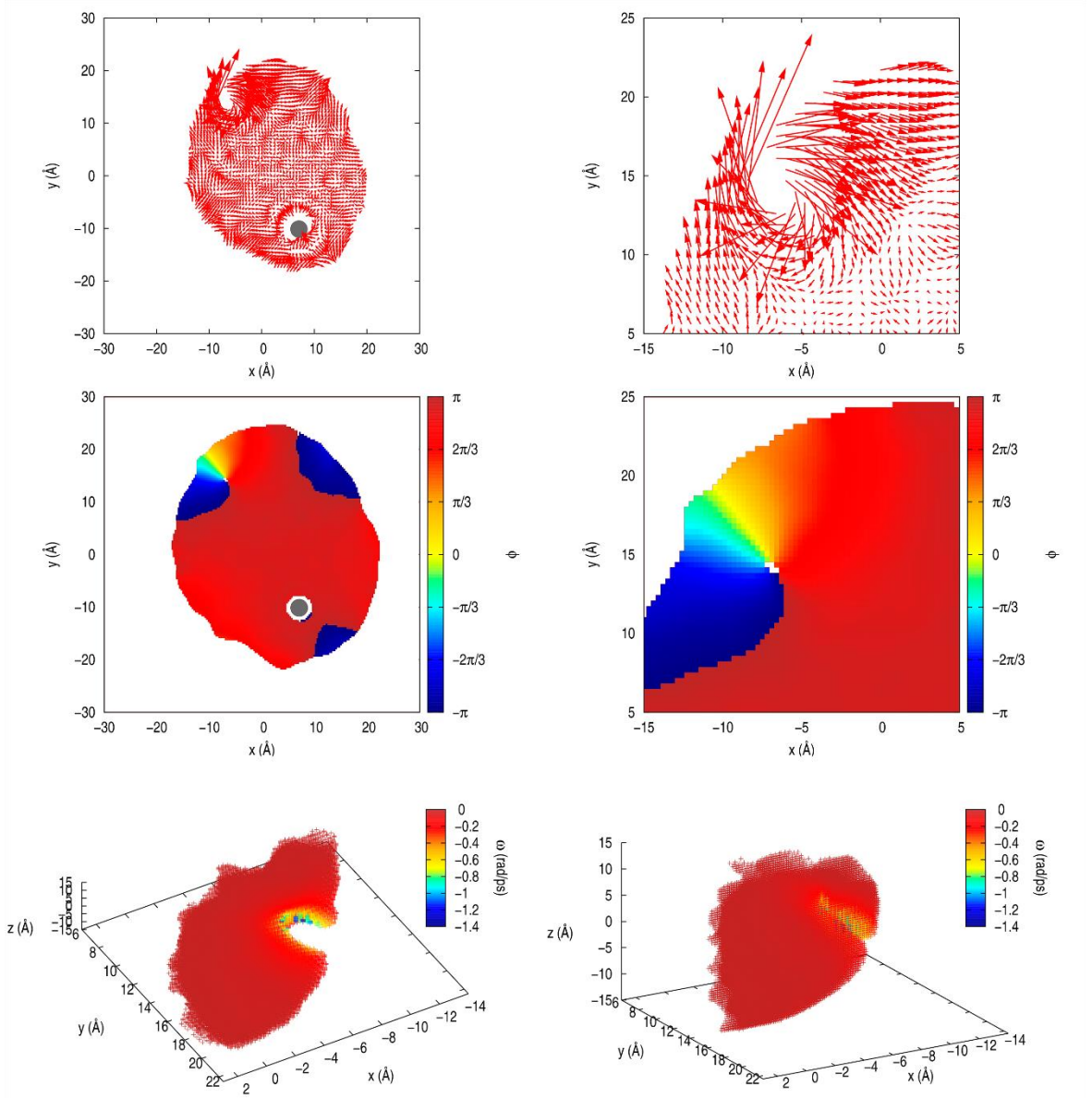

Figure 3.11 The vortex line for v_0=500 m s^{-1} and b=17 Å at the final simulation time (t=171.2 ps) from different viewpoints: velocity field of the HeND and vortex line (top); helium wave function phase diagram of the HeND and vortex line (middle); helium volume associated to the vortex line from two different orientations (bottom).

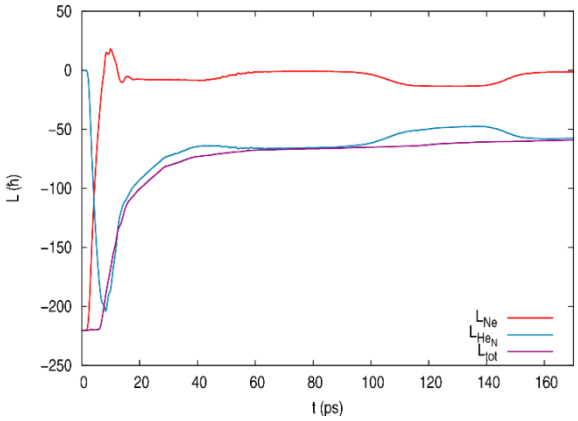

Figure 3.12 Ne atom, HeND and total (without considering the evaporated He atoms) angular momenta *vs.* time for v_0=500 m s^{-1} and b=14 Å.

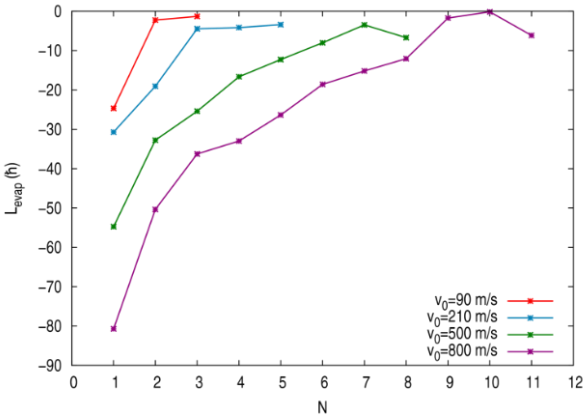

Figure 3.13 Angular momentum released by each evaporated He atom for b=14 Å.

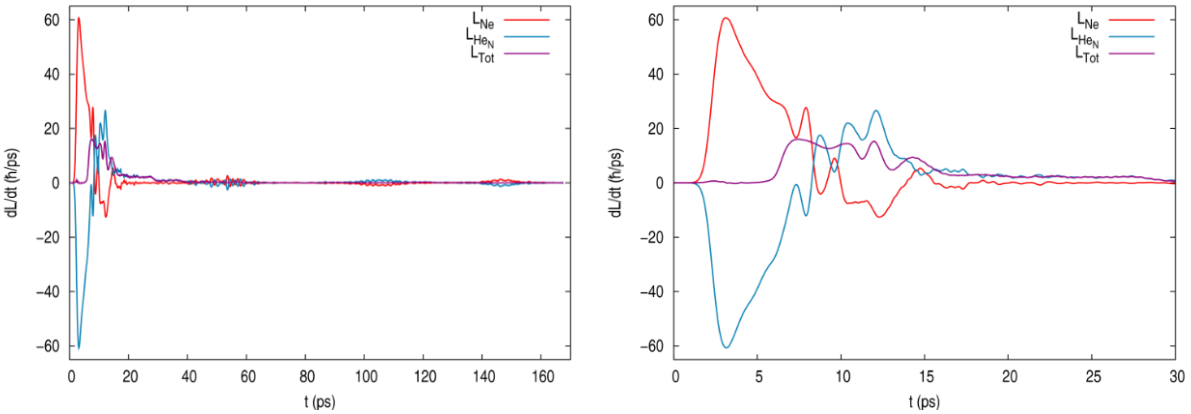

Figure 3.14 Ne atom, HeND and total (without considering the evaporated He atoms) angular momenta *vs.* time for v_0=500 m s^{-1} and b=14 Å. The results for the initial times are shown on the right.

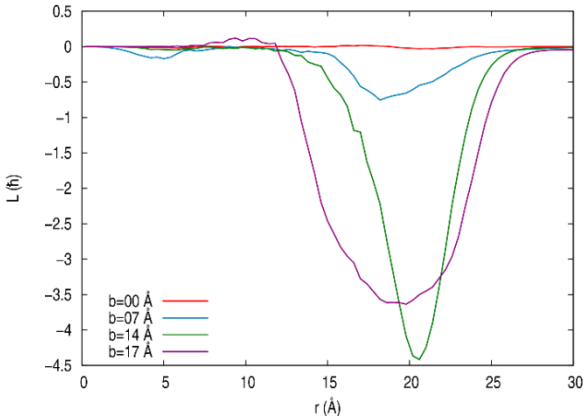

Figure 3.15 Angular momentum radial distribution of the HeND for the final simulation times (cf. Table s2) and as a function of the impact parameter, for v_0=500 m s^{-1}. It should be noted that for the final simulation time of b=14 Å (177 ps) the long-lived vortex did not exist, in contrast to what happens for b=17 Å (171 ps).

L_{cm} and L_{other} shows a non-monotonic complex dependence with the initial conditions (v_0, b) even though, for a given initial velocity, L_{other} increases its modulus with b (Table s3.3). Besides, L_{other} plays a dominant role with the only exception of what happens for v_0=210 m s^{-1}, b=7 and 17 Å. Regarding the case where a long-lived vortex is present at the end of the simulation (v_0=500 m s^{-1} and b=17 Å), the angular momentum of HeND referred to the origin of coordinates (-84.9 $\hbar$) is distributed as follows: centre of mass 9.5% (-8.1 $\hbar$), vortex line 19.2 % (-16.3 $\hbar$) and other excitations 71.3% (-60.5 $\hbar$). 'Other excitations' mostly refer to surface excitations, as there are no relevant peaks in regions near the centre of the HeND.

One would think the fraction of total angular momentum a vortex lines carries should be larger considering the heavy helium circulation it creates (Figure 3.11). The fact is that the angular momentum stored in a vortex line comes from surface excitations that are transformed into vortex rotation. The angular momentum calculated before (L_{vor}) is due to the circulation of the whole vortex as a body around the origin. To better compare the surface angular momentum and the vortex circulation angular momentum, the last one should be calculated with respect to its centre. Doing so, it is seen that the vortex circulation and surface angular momenta are more similar than before (-30.9 $\hbar$ and -60.5 $\hbar$, respectively).

In the context of the capture process when angular momentum is different from zero it is interesting to consider two initial conditions reported for the Xe capture in ref. 47:

v_0=200 m s^{-1} and b=20.3 and 22.2 Å. This velocity was selected in order to simulate the thermal conditions of the pickup chamber and the first b value corresponds to the largest impact parameter value (among the ones calculated in that reference) that leads to capture. It is worth noting that the Ne and Xe atoms at v_0= 500 and 200 m s^{-1}, respectively, have practically the same kinetic energy.

Although b_{max} for Xe capture (20.3 Å) is similar to the geometric HeND radius (22.2 Å), it should be noted that in general, even for the simpler capture process (i.e., those occurring in gas phase),[65] b_{max} depends on the collision energy, the degree of dependence being a function of the interaction potential energy. Consistently with this, we have obtained that b_{max} clearly depends on the initial velocity of the Ne atom (b_{max} ≈ 25, 23, 18 and 16 Å for v_0= 90, 210, 500 and 800 m s^{-1}, respectively). Besides, taking as in ref. 47 the radius of the HeND defined by $R = r_0 N^{1/3}$, where r_0=2.22 Å, we get for $^4He_{500}$ a radius of 17.6 Å; i.e., b_{max} values significantly higher than the nanodroplet radius can be obtained for low initial velocities.

Regarding the collision of Xe with the HeND reported in ref. 47 for which some information is provided on the angular momentum (v_0=200 m s^{-1} and b=22.2 Å), it should be noted that this initial condition does not lead to the Xe atom capture, i.e., corresponds to a situation that differs from the main initial conditions examined here (i.e., the set of conditions leading to atomic capture). Anyway, we have also found that a large amount of the Ne atom initial angular momentum is transferred to the evaporated helium atoms: e.g., 66.0, 74.6, 36.4 and 66.9 % of $L_{Ne,0}$ at v_0=90 m s^{-1} (b=20.0 Å), 210 m s^{-1} (b=20.0 Å), 500 m s^{-1} (b=17.0 Å) and 800 m s^{-1} (b=14.0 Å), respectively; while a transference of 32.7% of $L_{Xe,0}$ was observed for Xe at v_0=200 m s^{-1} (b=22.2 Å).

The final angular momentum of Ne (e.g., 3.9, 15.7, 1.7 and 2.2% of $L_{Ne,0}$ at v_0=90 m s^{-1} (b=20.0 Å), 210 m s^{-1} (b=20.0 Å), 500 m s^{-1} (b=17.0 Å) and 800 m s^{-1} (b=14.0 Å), respectively), however, is small in comparison with the final angular momentum of the non-captured Xe(^{4}He)$_5$ complex reported in ref. 47 for Xe (v_0=200 m s^{-1} and b=22.2 Å), which carries 56.9% of $L_{Xe,0}$. For the final angular momentum of HeND we have, e.g., the following values for the Ne case: 17.0, 12.7, 31.8 and 16.5% of $L_{Ne,0}$ at v_0=90 m s^{-1} (b=20.0 Å), 210 m s^{-1} (b=20.0 Å), 500 m s^{-1} (b=17.0 Å) and 800 m s^{-1} (b=14.0 Å), respectively;

while a percentage of 10.4% of $L_{Xe,0}$ was found for Xe at the initial condition mentioned above.[47]

In what refers to the vortex formation, it is worth noting that for the collision of Xe with the HeND (v_0=200 m s^{-1}; b=20.3 and 22.2 Å) vortex loops appear at the latest stages of the simulation,[47] in contrasts to what happens for the Ne atom case. Concerning the solvation processes mentioned in section 3.4.1 (zero angular momentum initial condition), the large helium density fluctuations involved in the Rb^+ solvation process lead to the nucleation of quantized vortices, that can be either loop or ring vortices; while no vortices are found for the Cs^+ solvation,[61] and the solvation of the Ba^+ cation leads to the nucleation of a ring vortex.[64] This differs from what has been observed for the Ne capture at zero angular momentum, where no vortices have been found.

The diversity of behaviours described here result from the different properties of the dopants (interaction potential energy dopant-helium and dopant mass) and the different initial conditions (v_0, b).

3.5. Summary and conclusions

The capture process of a neon atom by a superfluid helium nanodroplet, $(^4He)_{N=500}$; T=0.37 K), i.e., the Ne + $(^4He)_N \rightarrow$ Ne@$(^4He)_{N'}$ + (N-N') ^4He process, has been investigated in detail using a quantum-classical approach (quantum treatment (TDDFT method) for helium and classical mechanics description of the Ne atom) and taking into account the angular momentum. This work complements and extends a previous quantum dynamics work of our group on this capture process at zero angular momentum and particular attention has been payed to the capture mechanism and to the energy and angular momentum exchange between the Ne atom and the helium nanodroplet.

The atom is captured by the HeND below a certain maximum impact parameter, which decreases with increasing velocities, following elliptical rotating trajectories inside the HeND. Major energy exchanges occur when the atom collides with the nanodroplet and the excitation energy of $(^4He)_{N=500}$ is released by evaporation of helium atoms through the excitation of the surface modes on the HeND. Angular momentum introduces smoothness into the overall process, but the general trends are similar to the zero angular

momentum case (b=0). Energy exchange and variations are softer with increasing impact parameter, while angular momentum exchange and variations are stronger when angular momentum is higher (for b values leading to capture). The neon atom with angular momentum induces a certain amount of angular momentum to the HeND surface so both the atom and the surface tend to rotate solidarily when the atom is captured. Besides, helium density evaporation leads to the decrease of the angular momentum of the doped nanodroplet. The angular momentum of neon can induce vortex nucleation if the initial angular momentum is high enough (in the interval ~176.3-220.3 $\hbar$) and the vortex (vortex line) can be long-lived. Thus, the vortex, which arises from the collapse of surface excitations (ripplons), can exist during three-four initial Ne atom rebounds against the HeND surface and then be successively created and destructed during the following rebounds. Finally, it is worth noting that at zero angular momentum quantum effects are not important under the initial pickup conditions explored in this work.

In spite of the limited information available, it has also been possible to carry out a comparative analysis on the solvation of impurities by superfluid helium. In this analysis the Ne, Ar, Xe, Rb^+, Cs^+ and Ba^+ dopant species have been considered, under different initial conditions, and it has been shown the large diversity of behaviours that can be found in the solvation process.

More theoretical and experimental efforts are desirable in order to obtain a deeper insight into the dynamics of the capture process of atomic/molecular species by superfluid helium nanodroplets, particularly in order to better understand the vortex formation process.

3.6. Appendix 3A: "Quantum" vs. classical angular momentum

The comparison between the angular momentum results calculated using the quantum operator $\widehat{L_z}$ acting on the helium wave function and the classical expression considering the helium "quantum velocity" field is carried out below.

We have that the expected value of the k-component of the angular momentum is given by

$$\langle \mathrm{L_k} \rangle = \langle \Psi | \widehat{\mathrm{L_k}} \Psi \rangle = \int \mathrm{d}\vec{\mathrm{r}}\, \Psi^* \left[-\mathrm{i}\hbar \left(\mathrm{r_i} \frac{\partial}{\partial \mathrm{r_j}} - \mathrm{r_j} \frac{\partial}{\partial \mathrm{r_i}} \right) \right] \Psi$$

$$= -\mathrm{i}\hbar \int \mathrm{d}\vec{\mathrm{r}}\, \Psi^* \mathrm{r_i} \frac{\partial \Psi}{\partial \mathrm{r_j}} + \mathrm{i}\hbar \int \mathrm{d}\vec{\mathrm{r}}\, \Psi^* \mathrm{r_j} \frac{\partial \Psi}{\partial \mathrm{r_i}} \qquad \text{(a3.1)}$$

, where r_i, r_j and r_k correspond to the *x*, *y*, *z* coordinates of helium.

Then, introducing the "quantum velocity" definition from a hydrodynamic analogy (as it was calculated the helium velocity field), we have that the velocity is equal to

$$\mathrm{v_i} \equiv \frac{\vec{\mathrm{j}}(\vec{\mathrm{r}})}{|\Psi|^2} = \frac{1}{|\Psi|^2} \frac{\hbar}{2\mathrm{mi}} \left(\Psi^* \frac{\partial \Psi}{\partial \mathrm{r_i}} - \Psi \frac{\partial \Psi^*}{\partial \mathrm{r_i}} \right) = \frac{\hbar}{2\mathrm{mi}} \left(\frac{1}{\Psi} \frac{\partial \Psi}{\partial \mathrm{r_i}} - \frac{1}{\Psi^*} \frac{\partial \Psi^*}{\partial \mathrm{r_i}} \right)$$

$$\frac{\partial \Psi}{\partial \mathrm{r_i}} = \left(\frac{\mathrm{v_i} 2\mathrm{mi}}{\hbar} + \frac{1}{\Psi^*} \frac{\partial \Psi^*}{\partial \mathrm{r_i}} \right) \Psi \qquad \text{(a3.2)}$$

, where $\vec{j}(\vec{r})$ is the flux and introducing $\frac{\partial \Psi}{\partial r_i}$ into eq (a3.1) we get

$$\langle \mathrm{L_k} \rangle = -\mathrm{i}\hbar \int \mathrm{d}\vec{\mathrm{r}}\, \Psi^* \mathrm{r_i} \left(\frac{\mathrm{i}2\mathrm{mv_j}}{\hbar} + \frac{1}{\Psi^*} \frac{\partial \Psi^*}{\partial \mathrm{r_j}} \right) \Psi + \mathrm{i}\hbar \int \mathrm{d}\vec{\mathrm{r}}\, \Psi^* \mathrm{r_j} \left(\frac{\mathrm{i}2\mathrm{vm_i}}{\hbar} + \frac{1}{\Psi^*} \frac{\partial \Psi^*}{\partial \mathrm{r_i}} \right) \Psi$$

$$= \int \mathrm{d}\vec{\mathrm{r}}\, 2\mathrm{m}\rho(\vec{\mathrm{r}}) \mathrm{r_i} \mathrm{v_j} - \int \mathrm{d}\vec{\mathrm{r}}\, 2\mathrm{m}\rho(\vec{\mathrm{r}}) \mathrm{r_j} \mathrm{v_i} - \mathrm{i}\hbar \int \mathrm{d}\vec{\mathrm{r}}\, \mathrm{r_i} \frac{\partial \Psi^*}{\partial \mathrm{r_j}} \Psi$$

$$+ \mathrm{i}\hbar \int \mathrm{d}\vec{\mathrm{r}}\, \mathrm{r_j} \frac{\partial \Psi^*}{\partial \mathrm{r_i}} \Psi = 2\mathrm{L_{k,"class"}} - \mathrm{i}\hbar \int \mathrm{d}\vec{\mathrm{r}} \left(\mathrm{r_i} \frac{\partial \Psi^*}{\partial \mathrm{r_j}} - \mathrm{r_j} \frac{\partial \Psi^*}{\partial \mathrm{r_i}} \right) \Psi \qquad \text{(a3.3)}$$

And since the angular momentum operator is hermitian:

$$\langle \Psi | \widehat{L_k} \Psi \rangle = \langle \widehat{L_k} \Psi | \Psi \rangle$$

$$-i\hbar \int d\vec{r}\, \Psi^* \left(r_i \frac{\partial \Psi}{\partial r_j} - r_j \frac{\partial \Psi}{\partial r_i} \right) = i\hbar \int d\vec{r} \left(r_i \frac{\partial \Psi^*}{\partial r_j} - r_j \frac{\partial \Psi^*}{\partial r_i} \right) \Psi \tag{a3.4}$$

then expression (a3.3) yields:

$$\langle L_k \rangle = 2\, L_{k,"class"} + i\hbar \int d\vec{r}\, \Psi^* \left(r_i \frac{\partial \Psi}{\partial r_j} - r_j \frac{\partial \Psi}{\partial r_i} \right) = 2L_{class} - \langle L_k \rangle$$

$$\langle L_k \rangle = L_{k,"class"} \tag{a3.5}$$

3.7. Appendix 3B: Supplementary information

Table s3.1 Cartesian grid parameters of helium.[a]

v_0 (m/s)	h_x (Å)	h_y (Å)	h_z (Å)	x_{min} (Å)	x_{max} (Å)	y_{min} (Å)	y_{max} (Å)	z_{min} (Å)	z_{max} (Å)
90	0.40	0.45	0.45	-30.00	29.60	-28.80	28.35	-28.80	28.35
210	0.40	0.45	0.45	-30.00	29.60	-28.80	28.35	-28.80	28.35
500	0.30	0.35	0.40	-30.00	29.70	-31.50	31.35	-28.20	28.40
800	0.20	0.30	0.40	-30.00	29.80	-30.00	29.70	-28.80	28.40

[a] Spatial separation (h_x,..) and minimum (x_{min},..)and maximum (x_{max},..) limits.

Table s3.2 Propagation time steps and final simulation times.[a]

v_0 (m/s)	b (Å)	Δt (ps)	t_{final} (ps)
90	0	$2\cdot10^{-4}$	784.4
	7	$2\cdot10^{-4}$	316.8
	14	$2\cdot10^{-4}$	319.7
	17	$2\cdot10^{-4}$	113.3
	20	$2\cdot10^{-4}$	336.0
	27	$2\cdot10^{-4}$	86.6
	34	$2\cdot10^{-4}$	75.1
210	0	$2\cdot10^{-4}$	385.0
	7	$2\cdot10^{-4}$	433.3
	14	$2\cdot10^{-4}$	433.8
	17	$2\cdot10^{-4}$	408.5
	20	$2\cdot10^{-4}$	430.7
	27	$2\cdot10^{-4}$	35.0
	34	$2\cdot10^{-4}$	55.4
500	0	$1\cdot10^{-4}$	167.5
	7	$1\cdot10^{-4}$	168.5
	14	$1\cdot10^{-4}$	176.9
	17	$1\cdot10^{-4}$	171.2
	20	$1\cdot10^{-4}$	19.4
	27	$1\cdot10^{-4}$	14.2
	34	$1\cdot10^{-4}$	15.4
800	0	$9\cdot10^{-5}$	171.5
	7	$9\cdot10^{-5}$	171.0
	14	$9\cdot10^{-5}$	295.3
	17	$9\cdot10^{-5}$	21.6
	20	$9\cdot10^{-5}$	10.4
	27	$9\cdot10^{-5}$	9.0
	34	$9\cdot10^{-5}$	8.3

[a]In some cases larger simulation times have been considered only in order to follow the evolution of the vortex (cf. movies 2 and 3).

Table s3.3 Angular momentum of the HeND[a] at the final simulation times.[b]

v_0 (m/s)	b (Å)	L_{HeND} ($\hbar$)	L_{cm} ($\hbar$)	L_{vor} ($\hbar$)	$L_{vor,centre}$ ($\hbar$)	L_{other} ($\hbar$)
90	7	-6.59	-0.63	0.00	0.00	-5.96
	14	-7.04	2.17	0.00	0.00	-9.21
	17	-17.83	-3.72	0.00	0.00	-14.11
	20	-9.61	5.86	0.00	0.00	-15.47
210	7	6.96	9.07	0.00	0.00	-2.11
	14	-7.11	4.17	0.00	0.00	-11.28
	17	-1.47	11.13	0.00	0.00	-12.60
	20	-16.77	8.42	0.00	0.00	-25.18
500	7	-13.41	0.32	0.00	0.00	-13.73
	14	-57.34	-4.60	0.00[c]	0.00[c]	-52.73
	17	-84.90	-8.10	-16.32	-30.90	-60.47
800	7	-5.18	3.56	0.00[c]	0.00[c]	-8.74
	14	-58.20	-3.15	0.00	0.00	-55.05

[a] Helium total (L_{HeND}), helium centre of mass (L_{cm}), vortex with respect to the origin (L_{vor}) and with respect to the centre of the vortex ($L_{vor,centre}$) and other excitations angular (L_{other}) momenta. All angular momenta of the HeND have been calculated using the quantum operator $\widehat{L_Z}$ except L_{cm} that has been calculated classically using the velocity field.

[b] See Table s2.

[c] The vortex was not present in the nanodroplet at the final simulation times of these conditions.

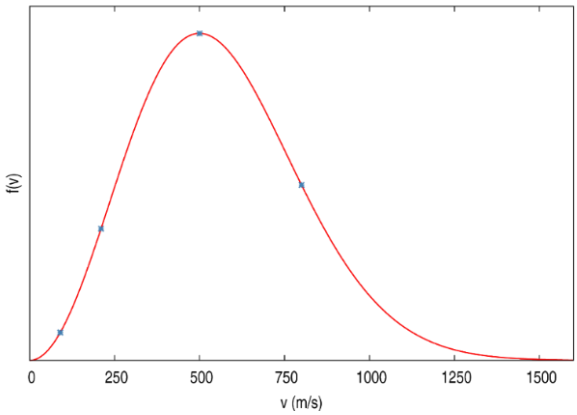

Figure s3.1 Maxwell-Boltzmann velocity distribution of the Ne atom at T=300 K. Blue points are the velocities considered in this work.

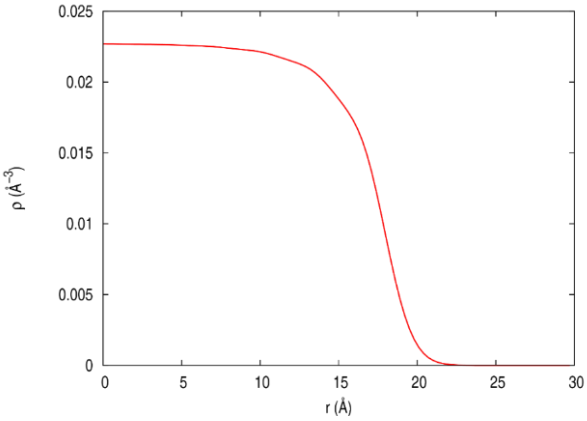

Figure s3.2 Radial density distribution of the $(^4He)_{500}$ nanodroplet.

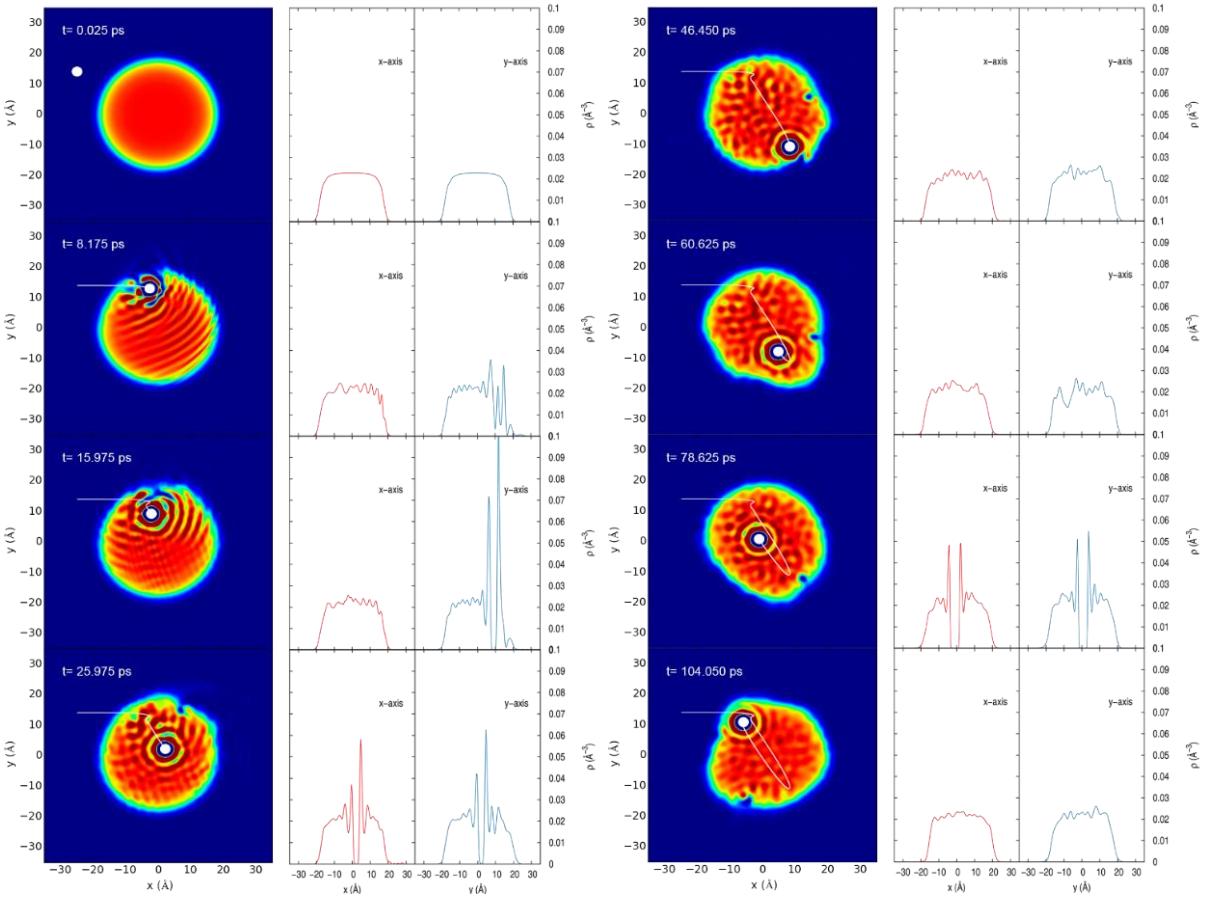

Figure s3.3 Snapshots of the time evolution of the helium density in the xy-plane (left panels) and in the x and y axes (right panels) for v_0=500 m s^{-1} and b=14 Å.

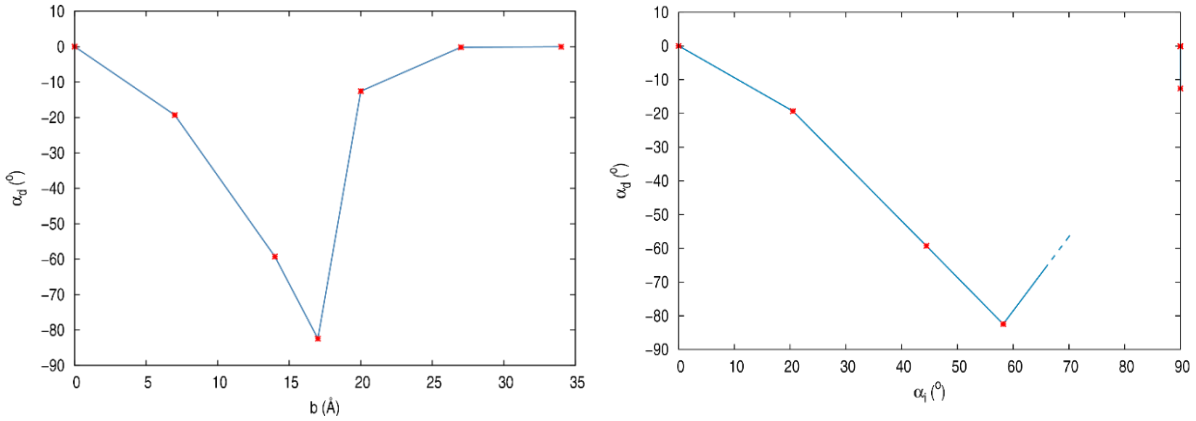

Figure s3.4 Deflection angle *vs*. impact parameter (top) and *vs*. incidence angle (bottom) for v_0=500 m s^{-1}. The Ne atom capture is observed for b=0, 7, 14 and 17 Å only.

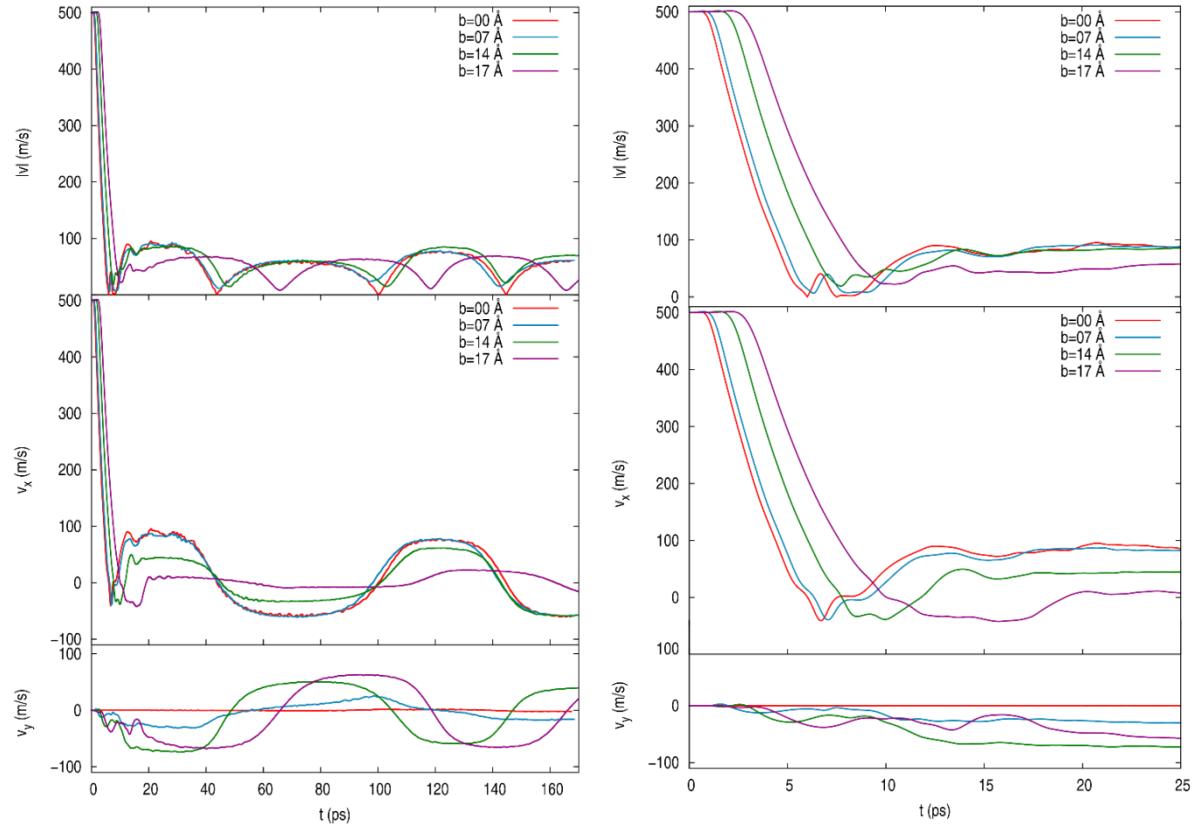

Figure s3.5 Velocity components of the Ne atom *vs*. time for v_0=500 m s^{-1}. Left: modulus (top), x component (middle) and y component (bottom). Right: the same as before but for the initial times.

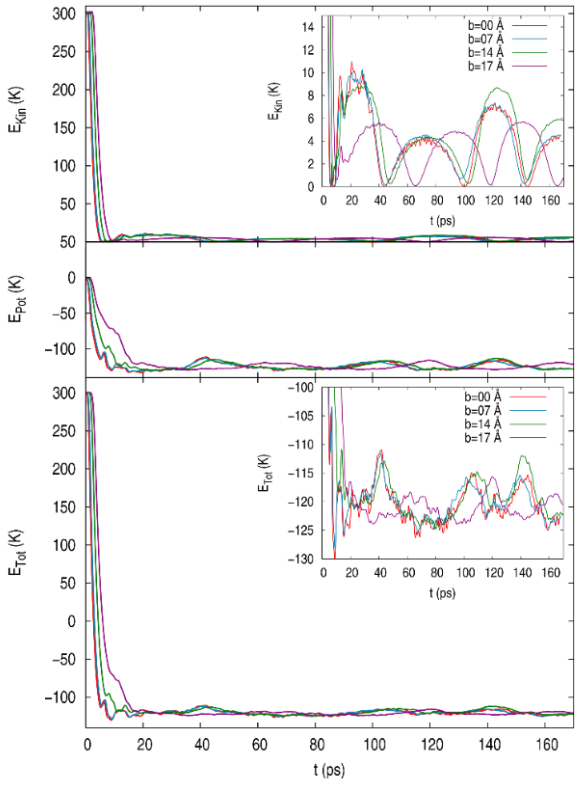

Figure s3.6 Neon atom energies *vs.* time for v_0=500 m s^{-1}: kinetic energy (top), potential energy Ne-helium (middle) and total energy (bottom).

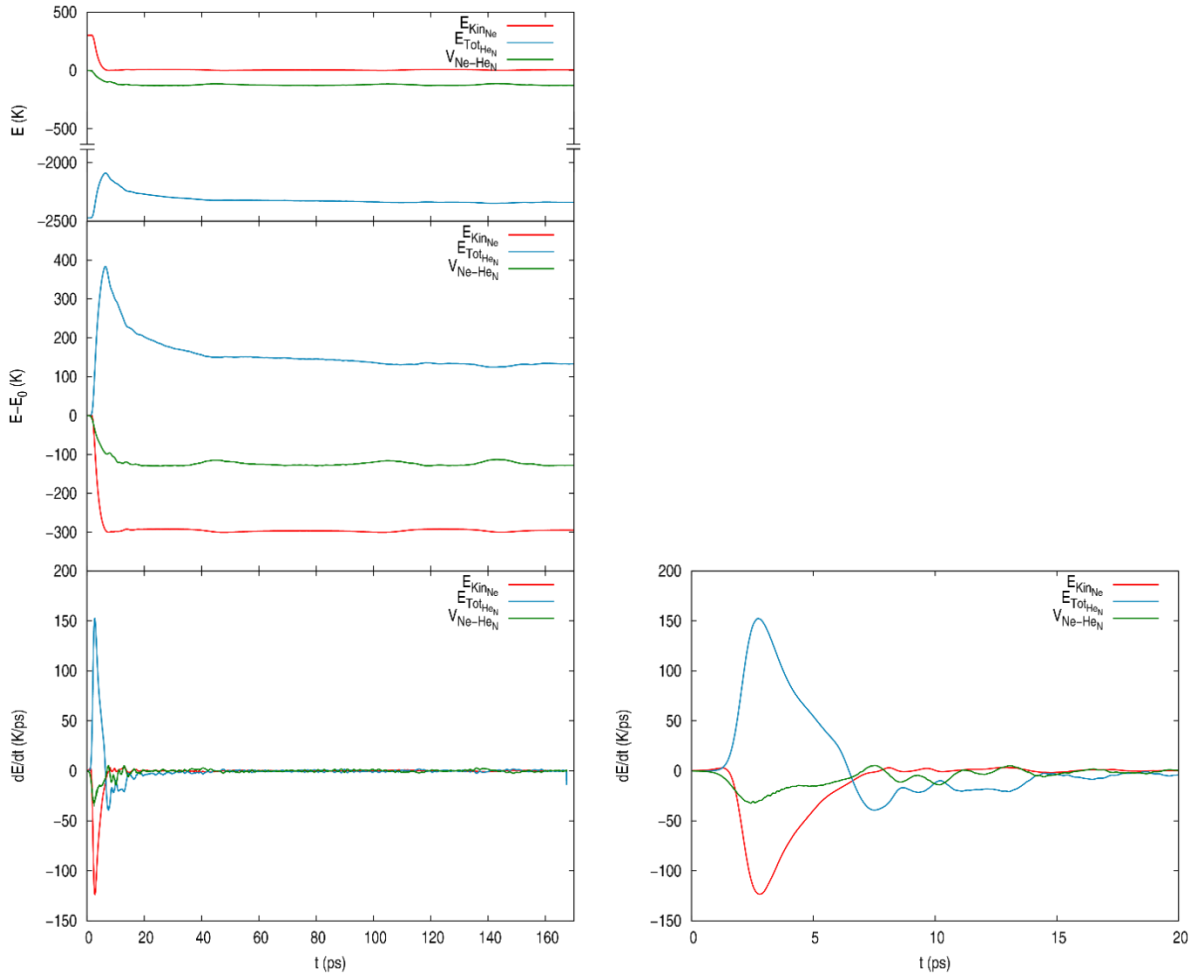

Figure s3.7 Energies and time derivatives of the energies vs. time for v_0=500 m s^{-1}. Left: (top) neon kinetic energy, HeND total energy and interaction energies; (middle) differences between the energies values and their initial values; (bottom) time derivatives of the energies. Right: time derivatives of the energies at initial times.

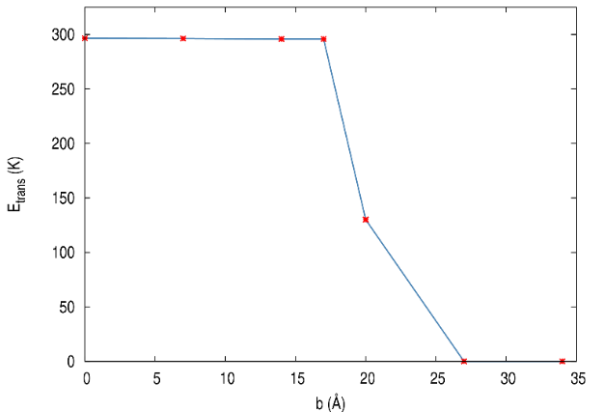

Figure s3.8 Kinetic energy transferred by the Ne atom to the HeND *vs.* impact parameter for v_0=500m s^{-1}. The atom capture is observed for b=0, 7, 14 and 17 Å only.

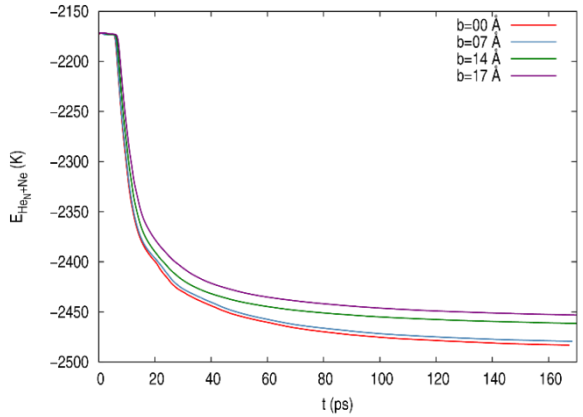

Figure s3.9 Total energy of the system ($E_{\mathrm{HeND}} + E_{\mathrm{Ne}}$) *vs.* time for v_0=500 m s^{-1}.

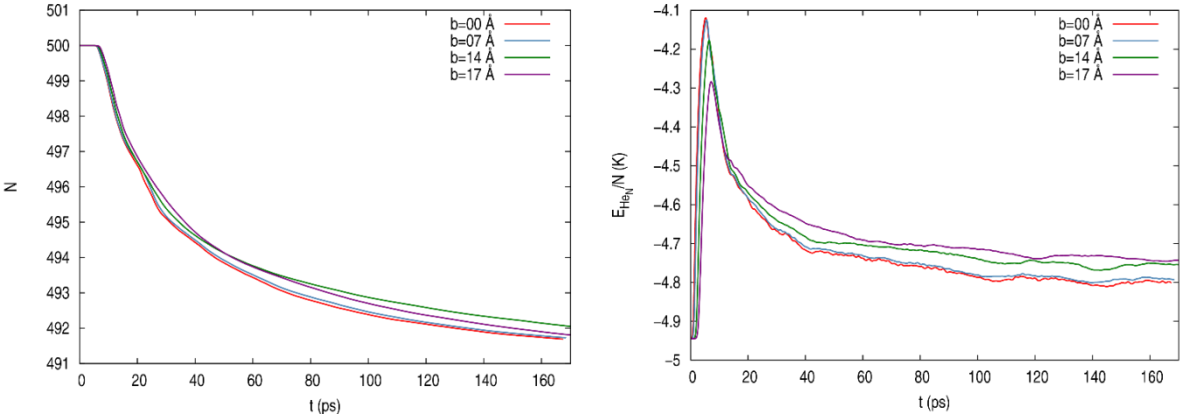

Figure s3.10 Norm (left) and total energy per He atom (right) of the HeND *vs.* time for v_0=500 m s^{-1}.

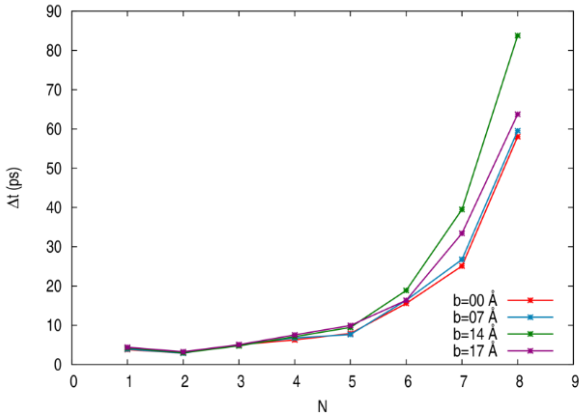

Figure s3.11 Time interval required to evaporate each one of the evaporated He atoms from HeND for v_0=500 m s^{-1}.

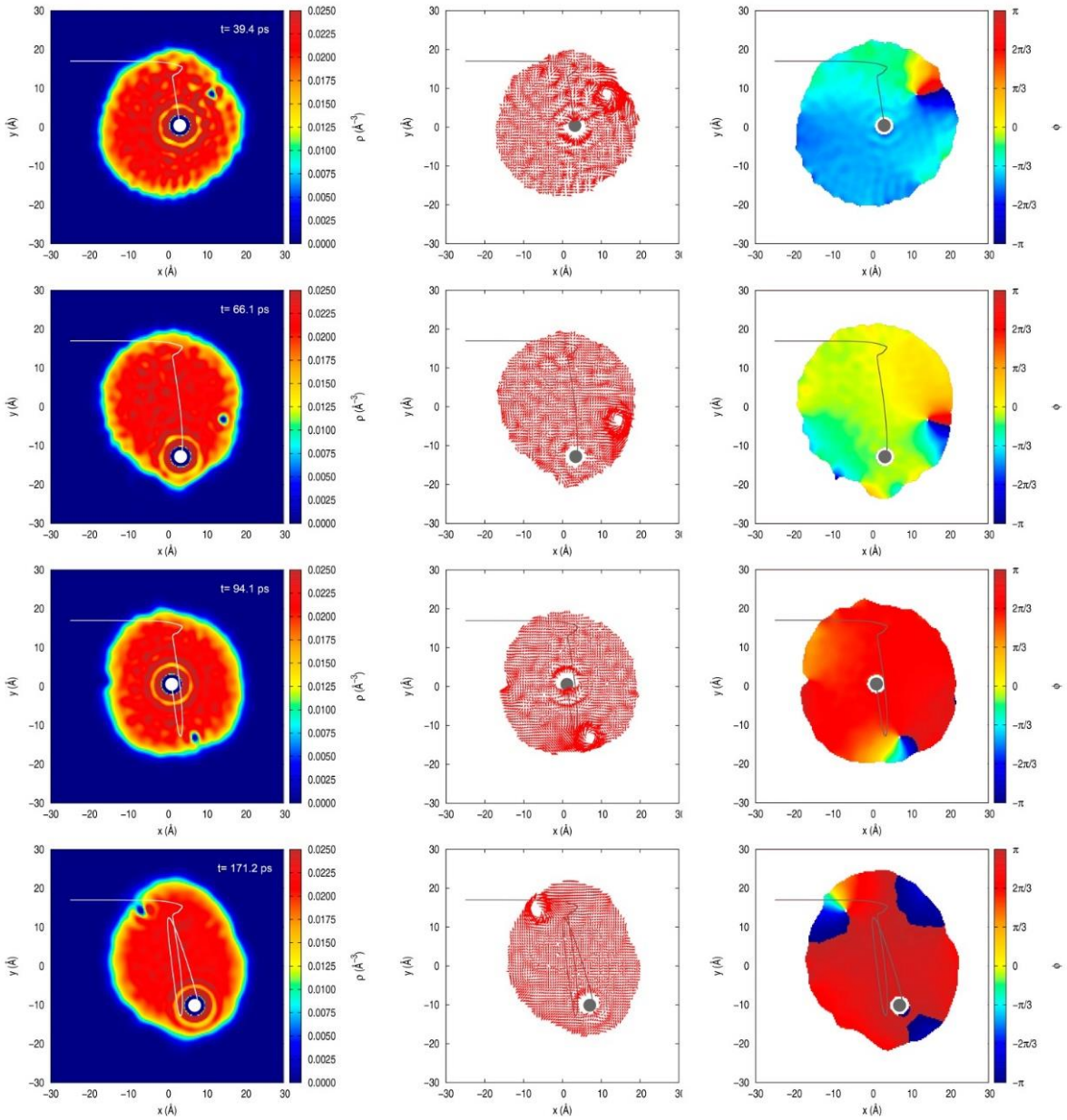

Figure s3.12 Snapshots of the time evolution of the helium density, velocity and wave function phase in the xy-plane for v_0=500 m s^{-1} and b=17 Å, where the vortex is clearly evident.

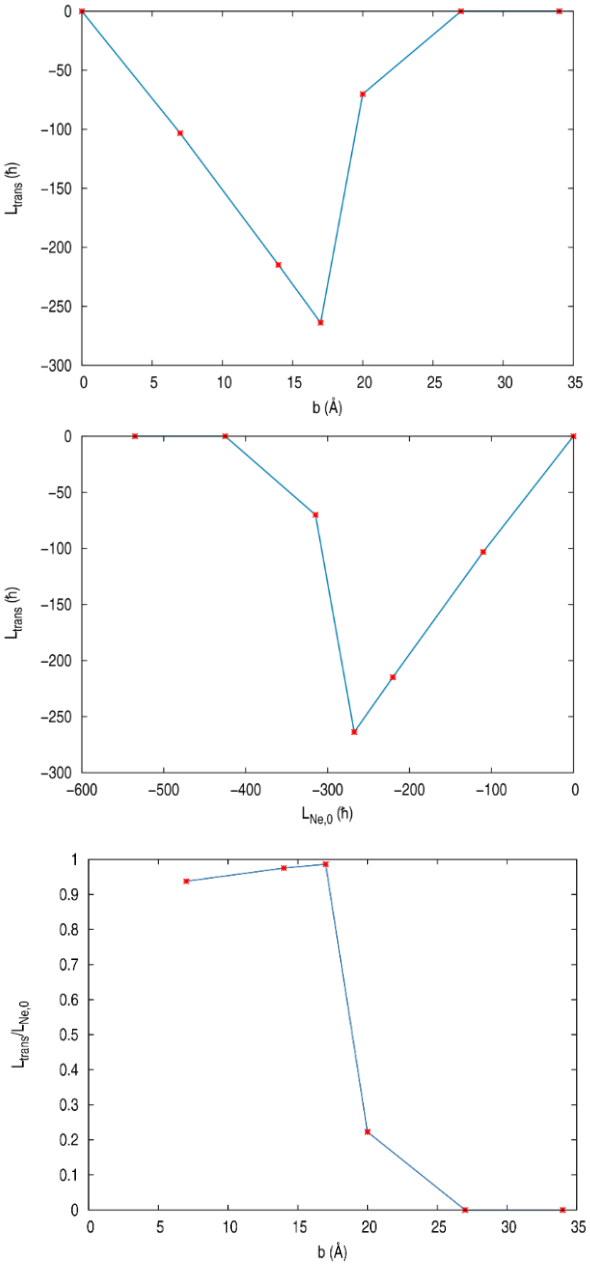

Figure s3.13 Angular momentum transferred to the HeND *vs.* b (top)and *vs.* $L_{Ne,0}$ (middle) and $L_{transf}/L_{Ne,0}$ vs. b (bottom) for v_0=500 m s^{-1}. The Ne atom capture is observed for b=0, 7, 14 and 17 Å only.

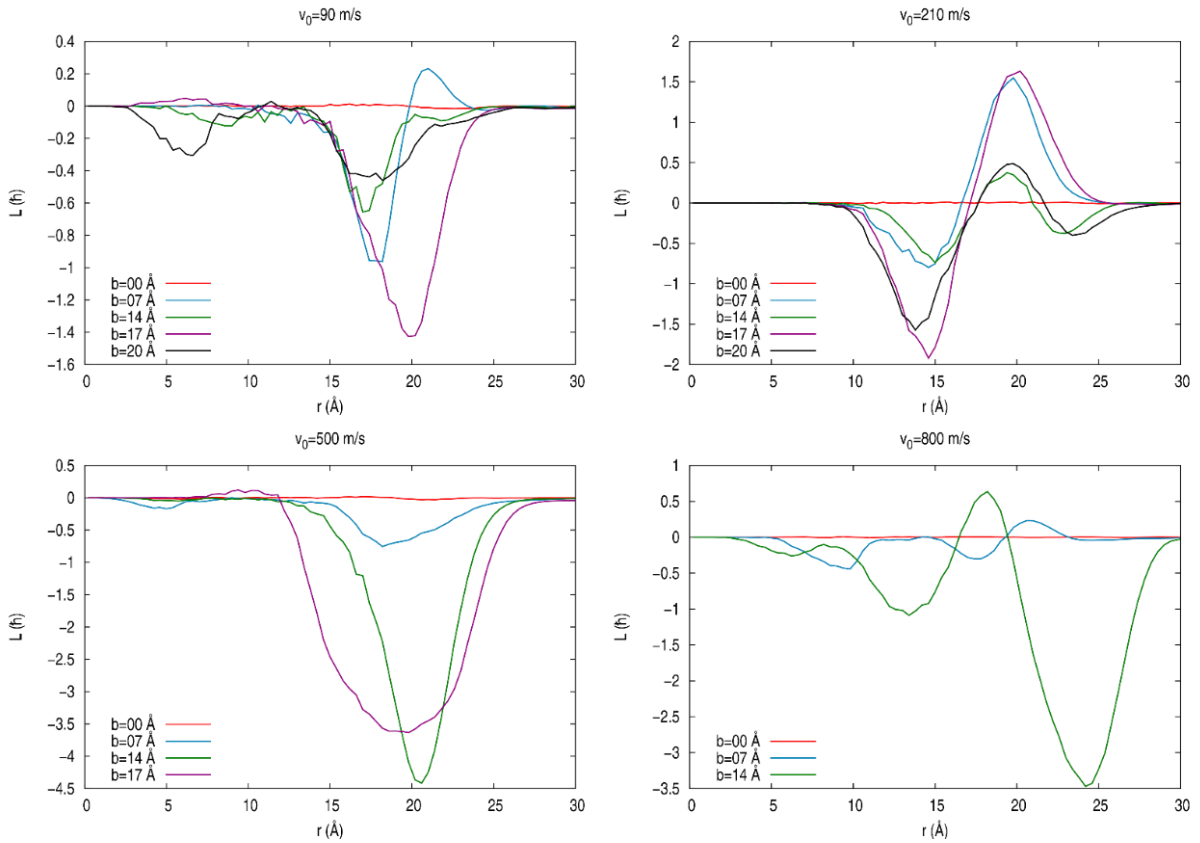

Figure s3.14 Angular momentum radial distribution of the HeND for the final simulation times (cf. Table s2) and as a function of the impact parameter, for v_0=90, 210, 500, and 800 m s^{-1}.

Movie 3.1 Time evolution of the helium density and helium wave function phase in the xy-plane for v_0=500 m s^{-1} and b=0 Å (simulated time≈167 ps). See the mp4 video file "Movie 3.1. v500_b00.mp4" (1.88 MB).

Movie 3.2 Time evolution of the helium density and helium wave function phase in the xy-plane for v_0=500 m s^{-1} and b=14 Å (simulated time≈328 ps; an additional simulated time of 151 ps has been examined here in order to better observe the vortex). See the mp4 video file "Movie 3.2. v500_b14.mp4" (3.86 MB).

Movie 3.3 Time evolution of the helium density and helium wave function phase in the xy-plane for v_0=500 m s^{-1} and b=17 Å (simulated time≈319 ps; an additional simulated time of 148 ps has been examined here in order to better observe the vortex). See the mp4 video file "Movie 3.3. v500_b17.mp4" (3.74 MB).

Movie 3.4 Time evolution of the helium density and helium wave function phase in the xy-plane for v_0=800 m s^{-1} and b=14 Å (simulated time≈295 ps). See the mp4 video file "Movie 3.4. v800_b14.mp4" (3.87 MB).

3.8. Reference

[1] J. P. Toennies and A. F. Vilesov, Superfluid helium droplets: a uniquely cold nanomatrix for molecules and molecular complexes, *Angew. Chem. Int. Ed.*, 2004, **43,** 2622-2648.

[2] M. Barranco, R. Guardiola, S. Hernández, J. Navarro and M. Pi, R. Mayol, Helium nanodroplets: an overview, *J. Low Temp. Phys.,* 2006, **142,** 1-81.

[3] F. Ancilotto, M. Barranco, F. Coppens, J. Eloranta, N.Halberstadt, A. Hernando, D. Mateo and M. Pi, Density functional theory of doped superfluid liquid helium and nanodroplets, *Int. Rev. Phys. Chem.*, 2017, **36**, 621-707.

[4] S. Goyal, D. L. Schutt and G. Scoles, Vibrational spectroscopy of sulfur hexafluoride attached to helium clusters, *Phys. Rev. Lett.,* 1992, **69,** 933-936.

[5] M. Hartmann, R. E. Miller, J. P. Toennies and A. F. Vilesov, High-resolution molecular spectroscopy of van der Waals clusters in liquid helium droplets, *Science,* 1996, **272,** 1631-1634.

[6] A. Vilà, M. González, R. Mayol and M. Paniagua, Theoretical approach to the structure, energy and electronic spectroscopy of O@$(^4He)_N$ doped nanodroplets, *RSC Adv.,* 2014, **4,** 44972-44979.

[7] E. Lugovoj, J. P. Toennies and A. F. Vilesov, Manipulating and enhancing chemical reactions in helium droplets, *J. Chem. Phys.,* 2000, **112,** 8217-8220.

[8] G. E. Douberly and R. E. Miller, The growth of HF polymers in helium nanodroplets: probing the barriers to ring insertion, *J. Phys. Chem. B,* 2003, 107, 4500-4507.

[9] S. A. Krasnokutski and F. Huisken, Low-temperature chemistry in helium droplets: reactions of aluminum atoms with O_2 and H_2O, *J. Phys. Chem. A,* 2011, **115,** 7120-7126.

[10] S. Yang and A. M. Ellis, Helium droplets: a chemistry perspective, *Chem. Soc. Rev.,* 2013, **42,** 472-484.

[11] A. Vilà, M. González and R. Mayol, Photodissociation dynamics of homonuclear diatomic molecules in helium nanodroplets. The case of $Cl_2@(^4He)_N$, *J. Chem. Theory Comput.,* 2015, **11,** 899-906.

[12] A. Vilà, M. González and R. Mayol, Quantum interferences in the photodissociation of $Cl_2(B)$ in superfluid helium nanodroplets $(4He)_N$, *Phys. Chem. Chem. Phys.,* 2015, **17,** 32241-32250.

[13] A. Vilà, M. González and R. Mayol, Quantum dynamics of the pick up process of atoms by superfluid helium nanodroplets: the Ne + $(^4He)_{1000}$ system, *Phys. Chem. Chem. Phys.,* 2016, **18,** 2006-2014.

[14] A. Vilà, M. González and R. Mayol, Relaxation dynamics of helium nanodroplets after photodissociation of a dopant homonuclear diatomic molecule. The case of $Cl_2@(^4He)_N$, *Phys. Chem. Chem. Phys.,* 2016, **18,** 2409-2416.

[15] A. Vilà and M. González, Mass effects in the photodissociation of homonuclear diatomic molecules in helium nanodroplets: inelastic collision and viscous flow energy exchange regimes, *Phys. Chem. Chem. Phys.,* 2016, **18,** 27630-27638.

[16] A. Vilà and M. González, Reaction dynamics inside superfluid helium nanodroplets: the formation of the Ne_2 molecule from Ne + $Ne@(^4He)_N$, *Phys. Chem. Chem. Phys.,* 2016, **18,** 31869-31880.

[17] J. Tiggesbäumker and F. Stienkemeier, Formation and properties of metal clusters isolated in helium droplets, *Phys. Chem. Chem. Phys.,* 2007, **9,** 4748-4770.

[18] T. Döppner, T. Diederich, S. Göde, A. Przystawik, J. Tiggesbäumer and K. H. Meiwes-Broer, Ion induced snowballs as a diagnostic tool to investigate the caging of metal clusters in large helium droplets, *J. Chem. Phys.,* 2007, **126**, 244513.

[19] S. Yang, A. M. Ellis, D. Spence, C. Feng, A. Boatwright, E. Latimer and C. Binnis, Growing metal nanoparticles in superfluid helium, *Nanoscale,* 2013, **5,** 11545-11553.

[20] L. F. Gomez, E. Loginov and A. F. Vilesov, Traces of vortices in superfluid helium droplets, *Phys. Rev. Lett.,* 2012, **108,** 155302.

[21] E. Latimer, D. Spence, C. Feng, A. Boarwright, A. M. Ellis and S. Yang, Preparation of ultrathin nanowires using superfluid helium droplets, *Nano Lett.,* 2014, **14,** 2902-2906.

[22] A. Slenczka and J. P. Toennies, in *Low Temperature and Cold Molecules,* ed. I. W. M. Smith, Imperial College Press, London, 2008, pp. 345-392.

[23] A. Braun and M. Drabbels, Photodissociation of alkyl iodides in helium nanodroplets I: kinetic energy transfer, *J. Chem. Phys.,* 2007, **127,** 114303.

[24] A. Braun and M. Drabbels, Photodissociation of alkyl iodides in helium nanodroplets. II. solvation dynamics, *J. Chem. Phys.,* 2007, **127,** 114304.

[25] A. Braun and M. Drabbels, Photodissociation of alkyl iodides in helium nanodroplets. III. recombination, *J. Chem. Phys.,* 2007, **127,** 114305.

[26] S. A. Krasnokutski and F. Huisken, Ultra-low-temperature reactions of Mg atoms with O_2 molecules in helium droplets , *J. Phys. Chem. A,* 2010, **114,** 7292-7300.

[27] T. Takayanagi and M. Shiga, Photodissociation of Cl_2 in helium clusters: an application of hybrid method of quantum wavepacket dynamics and path integral centroid molecular dynamics, *Chem. Phys. Lett.,* 2003, **372,** 90-96.

[28] A. Vilà, M. Paniagua and M. González, Vibrational energy relaxation dynamics of diatomic molecules inside superfluid helium nanodroplets. The case of the I_2 molecule, *Phys. Chem. Chem. Phys.,* 2018, **20,** 118-130.

[29] A. Scheidemann, J. P. Toennies and J. A. Northby, Capture of neon atoms by ^{4}He clusters, *Phys. Rev. Lett.,* 1990, **64,** 1899-1902.

[30] M. Lewerenz, B. Schilling and J. P. Toennies, Successive capture and coagulation of atoms and molecules to small clusters in large liquid helium clusters, *J. Chem. Phys.,* 1995, **102,** 8191-8207.

[31] F. F. Da Silva, P. Bartl, S. Denifl, O. Echt, T. D. Märk and P. Scheier, Argon clusters embedded in helium nanodroplets, *Phys. Chem. Chem. Phys.,* 2009, **11,** 9791-9797.

[32] H. Schoebel, P. Bartl, C. Leidlmair, S. Denifl, O. Echt, T. D. Maerk and P. Scheier, High-resolution mass spectrometric study of pure helium droplets, and droplets doped with krypton, *Eur. Phys. J. D,* 2011, **63,** 209-214.

[33] M. Ratschek, M. Koch and W. E. Ernst, Doping helium nanodroplets with high temperature metals: formation of chromium clusters, *J. Chem. Phys.,* 2012, **136,** 104201.

[34] F. Lindebner, A. Kautsch, M. Koch and W. E. Ernst, Laser ionization and spectroscopy of Cu in superfluid helium nanodroplets, *Int. J. Mass Spectrom.,* 2014, **365-366,** 255-259.

[35] P. L. Raston, J. Agarwal, J. M. Turney, H. F. Schaefer III and G. E. Douberly, The ethyl radical in superfluid helium nanodroplets: rovibrational spectroscopy and ab initio computations, *J. Chem. Phys.,* 2013, **138,** 194303.

[36] T. Premke, E.-M. Wirths, D. Pentlehner, R. Riechers, R. Lehnig, A. Vdovin, and A. Slenczka, Microsolvation of molecules in superfluid helium nanodroplets revealed by means of electronic spectroscopy, *Front. Chem.,* 2014, **2,** 51.

[37] H. Schöbel, C. Leidlmair, P. Bartl, S. Denifl, T. D. Märk, O. Echt and P. Scheier, Electron ionization of superfluid helium nanodroplets doped with C_{60} and small molecules, *J. Phys.: Conf. Ser.,* 2012, **388,** 012044.

[38] A. Scheidmann, B. Shilling, J. P. Toennies and J. A. Northby, Capture of foreign atoms by helium clusters, *Phys. B,* 1990, **165**, 135-136.

[39] D. Eichenauer, A. Scheidemann and J. P. Toennies, Liquid drop and optical model calculations of elastic, vibrationally inelastic and absorptive scattering of ^{4}He atoms from ^4He_n-clusters, *Z. Phys. D: At., Mol. Clusters,* 1988, **8,** 295-304.

[40] J. P. Toennies and A. F. Vilesov, Novel low-energy vibrational states of foreign particles in fluid ^{4}He clusters, *Chem. Phys. Lett.,* 1995, **235,** 596-603.

[41] K. K. Lehmann, Potential of a neutral impurity in a large ^{4}He cluster, *Mol. Phys.,* 1999, **97,** 645-666.

[42] E. Krotscheck and R. Zillich, Scattering of ^{3}He atoms from ^{4}He surfaces, *Phys. Rev. B: Condens. Matter Mater. Phys.,* 1998, **58,** 5707-5718.

[43] E. Krotscheck and R. Zillich, Dynamics of atom scattering from ^{4}He nanoclusters, *Eur. Phys. J. D,* 2007, **43,** 113-116.

[44] E. Krotscheck and R. Zillich, Hydrogen and ^{3}He atoms on ^{4}He surfaces: bound states and scattering features, *Phys. Rev. B: Condens. Matter Mater. Phys.,* 2008, **77,** 094507.

[45] A. Leal, D. Mateo, A. Hernando, M. Pi and M. Barranco, Capture of heliophobic atoms by ^{4}He nanodroplets: the case of cesium, *Phys. Chem. Chem. Phys.*, 2014, **16,** 23206-23213.

[46] F. Coppens, A. Leal, M. Barranco, N. Halberstadt and M. Pi, Head-on collisions of Xe atoms against superfluid ^{4}He nanodroplets, *J. Low Temp. Phys.*, 2017, **187**, 439-445.

[47] F. Coppens, F. Ancilotto, M. Barranco, N. Halberstadt and M. Pi, Capture of Xe and Ar atoms by quantized vortices in ^{4}He nanodroplets, *Phys. Chem. Chem. Phys.*, 2017, **19**, 24805-24818.

[48] A. W. Hauser, A. Volk, P. Thaler and W. E. Ernst, Atomic collisions in suprafluid helium-nanodroplets: timescales for metal-cluster formation derived from He-density functional theory, *Phys. Chem. Chem. Phys.*, 2015, **17**, 10805-10812.

[49] F. Dalfovo, A. Lastri, L. Pricaupenko, S. Stringari and J. Treiner, Structural and dynamical properties of superfluid helium: A density-functional approach, *Phys. Rev. B: Condens. Matter Mater. Phys.*, 1995, **52**, 1193-1209.

[50] F. Ancilotto, M. Barranco, F. Caupin, R. Mayol and M. Pi, Freezing of ^{4}He and its liquid-solid interface from density functional theory, *Phys. Rev. B*: Condens. Matter Mater. Phys., 2005, **72**, 214522.

[51] N. B. Brauer, S. Smolarek, E. Loginov, D. Mateo, A. Hernando, M. Pi, M. Barranco, W. J. Buma and M. Drabbles, Critical Landau velocity in helium nanodroplets, *Phys. Rev. Lett.*, 2013, **111,** 153002.

[52] D. Mateo, A. Hernando, M. Barranco, E. Loginov, M. Drabbels and M. Pi, Translational dynamics of photoexcited atoms in ^{4}He nanodroplets: the case of silver, *Phys. Chem. Chem. Phys.*, 2013, **15,** 18388-18400.

[53] D. Mateo, F. Gonzalez and J. Eloranta, Rotational superfluidity in small helium droplets, *J. Phys. Chem. A,* 2015, **119,** 2262-2270.

[54] S. M. Cybulski and R. R. Toczylowski, Ground state potential energy curves for He_2, Ne_2, Ar_2, He-Ne, He-Ar, and Ne-Ar: a coupled-cluster study, *J. Chem. Phys.*, 1999, **111,** 10520-10528.

[55] A. Ralston, in *Mathematical methods for digital computers,* ed. A. Ralston and H. S. Wilf, John Wiley & Sons, New York, 1960, vol. 1, pp. 95-109.

[56] R. J. Thompson, Improving round-off in Runge-Kutta computations with Gill's method, *Commun. ACM,* 1970, **13,** 739-740.

[57] M. Frigo and S. G. Johnson, The design and implementation of FFTW3, *IEEE. Proc.*, 2005, **93,** 216-231.

[58] Á. Vibók and G. G. Balint-Kurti, Parametrization of complex absorbing potentials for time-dependent quantum dynamics, *J. Phys. Chem.* 1992, **96**, 8712-8719.

[59] D. R. Tilley and J. Tilley, *Condensates and excitations. Superfluidity and superconductivity*, Institut of Physics Publishing, Bristol, 1990, pp. 41-53.

[60] J. F. Annet, *Superfluid helium-4. Superconductivity, superfluids and condensates*, Oxford University Press, Oxford, 2004, pp. 38-43.

[61] A. Leal, D. Mateo, A. Hernando, M. Pi, M. Barranco, A. Ponti, F. Cargnoni and M. Drabbels, Picosecond solvation dynamics of alkali cations in superfluid ^{4}He nanodroplets, *Phys. Rev. B* 2014, **90**, 224518.

[62] E. Loginov and M. Drabbels, Dynamics of excited sodium atoms attached to helium nanodroplets, *J. Phys. Chem. A* 2014, **118**, 2738-2748.

[63] M. Renzler, M. Daxner, L. Kranabetter, A. Kaiser, A. W. Hauser, W. E. Ernst, A. Lindinger, R. Zillich, P. Scheier and A. M. Ellis, Dopant-induced solvation of alkalis in liquid helium nanodroplets, *J. Chem. Phys.* 2016, **145**, 181101.

[64] D. Mateo, A. Leal, A. Hernando, M. Barranco, M. Pi, F. Cargnoni, M. Mella, X. Zhang and M. Drabbels, Nucleation of quantized vortex rings in ^{4}He nanodroplets, *J. Chem. Phys.* 2014, **140**, 131101.

[65] R. D. Levine, *Molecular reaction dynamics*, Cambridge University Press, Cambridge, 2005, pp. 91-94.

[66] R. J. Donnelly, *Quantized vortices in helium II*, Cambridge University Press, Cambridge, 1991.

[67] Aage Bohr and Ben R. Mottelson, *Nuclear structure,* W. A. Benjamin, INC., Advanced Book Program, Reading, Massachussets, USA, 1975, pp. 674-676.

[68] G. M. Seidel and H. J. Maris, Morphology of superfluid drops with angular momentum, *Physica B Condens Matter*, 1994, **194-196,** 577-578.

4. Quantum-classical approach to the reaction dynamics in a superfluid helium nanodroplet. The Ne_2 dimer and Ne-Ne adduct formation reaction $Ne + Ne@(^4He)_N$

4.1. Abstract

The dynamics of the Ne_2 dimer and Ne-Ne adduct formation in a superfluid helium nanodroplet [$(^4He)_N$; T=0.37 K], $Ne + Ne@(^4He)_N \rightarrow Ne_2@(^4He)_{N'}/Ne\text{-}Ne@(^4He)_{N'} + (N\text{-}N')^4He$ with N=500, has been investigated using a hybrid approach (quantum and classical mechanics (QM-CM) descriptions for helium and the Ne atoms, respectively) and taking into account the angular momentum of the attacking Ne atom, $Ne_{(1)}$. Comparison with zero angular momentum QM results shows that the present results are similar to the quantum ones for the initial $Ne_{(1)}$ velocities (v_0) of 500 and 800 m s^{-1} (the former one being the most probable velocity of Ne at 300 K), in all cases leading to the Ne_2 dimer (r_e=3.09 Å). However, significant differences appear at v_0=210 m s^{-1}, because in the QM-CM dynamics instead of the dimer a Ne-Ne adduct is formed (r_e=5.45 Å). Angular momentum adds further difficulties to produce the dimer, since it makes more difficult to remove the helium density found between both Ne atoms to lead, subsequently, to the Ne_2 molecule. Hence, the formation of the neon-neon adduct, $Ne\text{-}Ne@(^4He)_{N'}$, clearly dominates the reactivity of the system, which results in the formation of a "quantum gel"/"quantum foam", because the two Ne atoms essentially maintain their identities inside the nanodroplet. Large enough $Ne_{(1)}$ initial angular momentum values can induce the formation of vortex lines by the collapse of superficial excitations (ripplons), but they occur with greater difficulty than in the case of the capture of the Ne atom by a non doped helium nanodroplet, due to the wave interferences induced by the Ne atom originally

placed inside the nanodroplet. We hope that this work will encourage other researchers to investigate the reaction dynamics in helium nanodroplets, an interesting topic about which there are few studies available.

4.2. Introduction

The study of the structure, energetics and dynamics of superfluid helium nanodroplets, [(^{4}He)$_N$, T=0.37 K], is a well-established research field in physics.[1,2,3] These systems have a large interest as, among other things, they allow to determine the evolution of the properties of quantum fluids when the size of the system is modified. These nanodroplets can also be used, e.g., as low T matrices in high resolution spectroscopy, thanks to the chemically inert character and superfluidity of helium below T=2.17 K.[4,5,6]

These systems can also be considered as nanoreactors, as a single reactive collision event can take place inside a nanodroplet which, of course, is of large interest from a chemical point of view.[7,8] The excess of energy of the nanodroplet, which arises from the reactants kinetic energy and the chemical bonds breaking and formation energy changes, is easily released through evaporation of some helium atoms.[9] Moreover, the liquid helium solvation shells formed around the atomic or molecular dopants, are able to stabilize metastable chemical species.

After the first study of a chemical reaction in (^{4}He)$_N$,[10] there has been a significant number of contributions reported on this subject (see, e.g., refs. 7, 8, 11, 12, 13, 14, 15, 16, 17, 18, 19, 20, 21, 22, 23, 24, 25). Even though, the activity developed in the chemical context has been lower than that in the physical one. However, in recent times the interest of the chemical researchers on this quantum fluid has augmented considerably. This has been probably due, at least in part, to the new synthetic opportunities offered by superfluid liquid helium (chemical systems not stable in gas phase, e.g., some metallic nanoclusters[26,27,28] and nanowires,[29,30] can be synthetized using this solvent).

The reaction dynamics[1,7] has also been the subject of some attention from an experimental view. Thus, we can mention studies on photodissociation of alkyl iodides,[31,32,33] fs photoexcitation dynamics (In),[24] fs solvation dynamics (In_2),[25] reactions

involving metals, Mg + O_2,[13] Al + O_2, H_2O,[14] Ba + N_2O,[10] etc. From the theoretical side, in this context the photodissociation of $Cl_2(B)$ in superfluid[34,35,36] and non-superfluid[37] helium nanodroplets and the Ne_2 dimer formation reaction (Ne + Ne@($^4He)_N$ ⟶ Ne_2@($^4He)_N$)[38] have been investigated. In addition, it should be noted that the reaction products can also be viewed as probes to achieve a deeper understanding on the properties of nanodroplets, thanks to the different types of motions involved (i.e., translational, vibrational and rotational motions) and intensities of the atom/molecule-helium interactions.

We have recently proposed a hybrid quantum dynamics method to investigate the photodissociation of diatomic molecules, X_2, inside superfluid helium nanodroplets.[34] As far as we know, this was the first theoretical attempt to study the dynamics of a reactive process in ($^4He)_N$. Although we are mainly interested in the chemical reaction dynamics involving ($^4He)_N$, we have also studied different types of physico-chemical processes, using that hybrid method (or a related one) and in most cases for the first time: photodissociation of diatomic molecules,[34,35,36] dimerization of atoms,[38] capture of atoms[39,40] (and formation of quantum vortices),[40] vibrational[41] and rotational[42] relaxation of diatomic molecules and relaxation of nanodroplets (after a X_2 photodissociation process).[43]

The main goal of the present work has been to investigate the dynamics of the Ne_2 dimer and Ne-Ne adduct formation in a superfluid helium nanodroplet, Ne + Ne@($^4He)_N$ → Ne_2@($^4He)_{N'}$/Ne-Ne@($^4He)_{N'}$ + (N-N')^{4}He, considering a nanodroplet of 500 He atoms and outer Ne atom velocities that are typical in a pick-up experimental chamber. To do this we have used a hybrid approach involving quantum (helium) and classical (Ne atoms) mechanics (QM-CM method) and taking into account the angular momentum of the outer Ne atom (i.e., different impact parameters) for the first time. This contribution complements and extends a previous investigation carried out by us on the same reaction,[38] where the relative motion of the Ne atoms was treated quantum mechanically (QM) and at zero angular momentum (head-on collisions). Angular momentum effects have been studied using a classical description of the neon atoms for computational reasons. However, in our view CM provides a quite good description of them.

The comparison of the results obtained here at zero angular momentum with the corresponding results of the QM study[38] will allow us to determine the importance of quantum effects. Likewise, the inclusion of the angular momentum will allow us to investigate its effect on dynamics and, in particular, the possible formation of quantum vortices. These results can also be compared with those obtained by us, also at the QM-CM level, for the simpler case of the Ne atom capture by a helium nanodroplet,[40] which corresponds to a stage prior to the present study.

As an initial step for studying the possible formation of quantum gels by doping liquid helium with many atoms,[44,45] the formation of the Ne_2 dimer was also studied previously using density functional theory (DFT).[44] An effective adiabatic potential energy surface (PES) for Ne_2 was constructed, assuming an instantaneous relaxation of superfluid helium (bulk) for each value of the neon atoms relative distance. Here our theoretical approach to this van der Waals reaction is completely different, since we have performed a real-time dynamics study on this reaction.

This chapter has the following structure: the theoretical methods are explained in Section 4.3; the description and analysis of the most important results are presented in Section 4.4; and the summary and conclusions are reported in Section 4.5. Supplementary information with useful material, including tables, figures and movies, has also been provided in Section4.6.

4.3. Theoretical methods

The Ne + Ne@$(^4He)_N$ → Ne_2@$(^4He)_{N'}$/Ne-Ne@$(^4He)_{N'}$ + (N-N')^{4}He dynamics has been performed employing a quantum-classical hybrid approach ("divide and conquer strategy"). The helium nanodroplet has been modelled employing one of the main approaches used to describe large systems of bosonic liquid ^{4}He, i.e., the time dependent DFT (TDDFT) method, and the Ne atoms have been treated as classical particles as, e.g., in our recent study of the capture process of a Ne atom by a helium nanodroplet.[40]

The Orsay-Trento (OT) phenomenological density functional[46] has been employed to describe the superfluid liquid helium and the back-flow term and the non-local contributions to the helium correlation energy have been neglected for numerical and

computational reasons. The investigation of the dynamics of chemical and physical processes involving superfluid helium nanodroplets has only been possible recently and in all cases the approach indicated above has been used.[34,35,36,38,39,40,41,42,43,47,48,49,50] Moreover, when it has been possible to compare with experimental results, a satisfactory agreement has been obtained by using such simplification in the OT functional,[47,48,51] and some satisfactory tests have been reported in the context of the helium nanodroplet relaxation.[43]

Here we only show a brief description of the main expressions used to model the time evolution of the system. The quantum-classical action, in terms of the effective complex wave function of (^{4}He)$_N$, $|\Psi_{He}(\boldsymbol{R_{He}}, t)|^2 \equiv \rho_{He}(\boldsymbol{R_{He}}, t)$, reads:

$$\mathcal{A}\left[\Psi_{He}(\boldsymbol{R_{He}}),\ \boldsymbol{R_{Ne_{(1)}}}, \boldsymbol{R_{Ne_{(2)}}}\right] = \int dt \left\{ E[\Psi_{He}(\boldsymbol{R_{He}}), \boldsymbol{R_{Ne}}] - i\hbar \int d\boldsymbol{R_{He}} \Psi^*_{He}(\boldsymbol{R_{He}}) \frac{\partial}{\partial t} \Psi_{He}(\boldsymbol{R_{He}}) - \frac{1}{2} m_{Ne} \left(\frac{d\boldsymbol{R_{Ne_{(1)}}}}{dt}\right)^2 - \frac{1}{2} m_{Ne} \left(\frac{d\boldsymbol{R_{Ne_{(2)}}}}{dt}\right)^2 \right\} \quad (4.1)$$

where E is the total energy of the system which given by:

$$E\left[\Psi_{He}(\boldsymbol{R_{He}}),\ \boldsymbol{R_{Ne_{(1)}}}, \boldsymbol{R_{Ne_{(2)}}}\right] = \frac{\hbar^2}{2m_{He}} \int d\boldsymbol{R_{He}} |\boldsymbol{\nabla}\Psi_{He}|^2 + \int d\boldsymbol{R_{He}} \varepsilon_c[\rho_{He}] + \int d\boldsymbol{R_{He}} \rho_{He} V_{He-Ne}\left(\left|\boldsymbol{R_{He}} - \boldsymbol{R_{Ne_{(1)}}}\right|\right) + \int d\boldsymbol{R_{He}} \rho_{He} V_{He-Ne}\left(\left|\boldsymbol{R_{He}} - \boldsymbol{R_{Ne_{()}}}\right|\right) + \frac{1}{2} m_{Ne} \left(\frac{d\boldsymbol{R_{Ne_{(1)}}}}{dt}\right)^2 + \frac{1}{2} m_{Ne} \left(\frac{d\boldsymbol{R_{Ne_{(2)}}}}{dt}\right)^2 \quad (4.2)$$

where $\varepsilon_c[\rho_{He}]$ is the density functional for the liquid helium. The He-Ne diatomic potential energy, $V_{\text{He-Ne}}$, has been taken from ref. [52] (results from *ab initio* coupled-cluster

calculations with a large basis set) and the nanodroplet-Ne interaction has been calculated using the pairwise approach.

To determine the equations of motion the quantum action must be minimized by making variations in Ψ_{He}, $\boldsymbol{R}_{\mathrm{Ne}(1)}$ and $\boldsymbol{R}_{\mathrm{Ne}(2)}$, obtaining a non-linear Schrödinger-like equation for helium and the classical laws of motion for the Ne atoms (motion in the xy-plane):

$$i\hbar\frac{\partial}{\partial t}\Psi_{He}(\boldsymbol{R_{He}}) = \left[-\frac{\hbar^2}{2m_{He}}\nabla^2 + \frac{\delta\varepsilon_c[\rho_{He}]}{\delta\rho_{He}} + V_{He-Ne}\left(\left|\boldsymbol{R_{He}} - \boldsymbol{R_{Ne_{(1)}}}\right|\right) + V_{He-Ne}\left(\left|\boldsymbol{R_{He}} - \boldsymbol{R_{Ne_{(2)}}}\right|\right)\right]\Psi_{He}(\boldsymbol{R_{He}}) \tag{4.3}$$

$$m_{Ne_{(1)}}\ddot{\boldsymbol{R}}_{\boldsymbol{Ne}_{(1)}} = -\nabla_{Ne_{(1)}}\left[\int d\boldsymbol{R_{He}}\rho_{He}V_{He-Ne}\left(\left|\boldsymbol{R_{He}} - \boldsymbol{R_{Ne_{(1)}}}\right|\right) + V_{Ne-Ne}\left(\left|\boldsymbol{R_{Ne_{(1)}}} - \boldsymbol{R_{Ne_{(2)}}}\right|\right)\right]$$

$$m_{Ne_{(2)}}\ddot{\boldsymbol{R}}_{\boldsymbol{Ne}_{(2)}} = -\nabla_{Ne_{(2)}}\left[\int d\boldsymbol{R_{He}}\rho_{He}V_{He-Ne}\left(\left|\boldsymbol{R_{He}} - \boldsymbol{R_{Ne_{(2)}}}\right|\right) + V_{Ne-Ne}\left(\left|\boldsymbol{R_{Ne_{(1)}}} - \boldsymbol{R_{Ne_{(2)}}}\right|\right)\right] \tag{4.4}$$

The equation of helium has been solved using a discretization method (Cartesian grid), while no grid has been used to solve the equations of the Ne atoms. The helium grid depends on the initial velocity of the attacking Ne atom, the grid being denser the higher the velocity is (Table s4.1). The numerical integration (temporal propagation) of eqn (4.3) has been carried out by means of the Adams predictor-corrector-modifier method,[53] initialised by a fourth order Runge-Kutta method.[54] The time step used in the numerical integration also is a function of the initial velocity of Ne considered (Table s4.2). The derivatives involved in the calculations have been calculated in momentum space using a fast Fourier transform as implemented in the FFTW package.[55] A quartic negative imaginary potential (NIP) has been placed at the edges of the grids (1.0 Å before the minimum and maximum limits of the x, y, z axes), so as to avoid possible unphysical reflections of the helium effective wave function,[56]using the same absorption strength and length as in ref. 40.

4.4. Results and discussion

The reaction leading to the formation of a neon dimer inside a superfluid helium nanodroplet [Ne + Ne@(^{4}He)$_N$ → Ne_2@(^{4}He)$_{N'}$ + (N-N')^{4}He] has been investigated considering a nanodroplet of 500 helium atoms doped with a neon atom ($Ne_{(2)}$) which is placed in its centre [Ne@(^{4}He)$_{N=500}$; T=0.37 K] (Figure 4.1). The attacking outer neon atom ($Ne_{(1)}$) is projected towards the nanodroplet at three selected initial velocities (v_0=210, 500 and 800 m s^{-1} along the x-axis) and five impact parameters, ranging from b=0 Å to b=b_{max} or a close value; where b_{max} is the maximum impact parameter at which the Ne atom is captured by the HeND (b_{max}=20, 18 and 16 Å for v_0=210, 500 and 800 m s^{-1}, respectively). This has been done in order to account for the influence of angular momentum on the reaction dynamics. The intermediate velocity chosen (500 m s^{-1}) is the most probable velocity of Ne at T=300 K (Figure s4.1). Besides, the initial value of the $Ne_{(1)}$ x-coordinate has been taken as equal to -30 Å; this leads to distances from the HeND which are large enough so that we can consider that this initial situation essentially corresponds to the reactants asymptote.

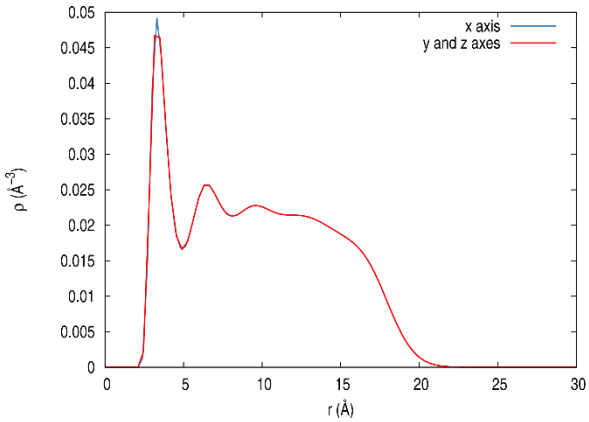

Figure 4.1 Radial density distribution of helium for the Ne@(^{4}He)$_{500}$ doped nanodroplet.

The radial density distribution of helium in the Ne@(^{4}He)$_{500}$ nanodroplet that has been used as initial condition (Figure 4.1) has been obtained after a suitable optimization (static calculations) carried out prior to the dynamics. The helium nanodroplet density strongly decreases near its surface, which is placed at about 20 Å, the centre of the nanodroplet is occupied by the $Ne_{(2)}$ inner atom, and three peaks of decreasing intensity as the distance to the center (r) increases are evident [at r=3.3 Å (0.0493 Å^{-3}), 6.6 Å (0.0257 Å^{-3}) and 9.6 Å (0.0228 Å^{-3})], which reflect the three solvation layers surrounding $Ne_{(2)}$. Besides, the surface thickness, which is defined as the distance at which the helium

density varies from 90% to 10% of the saturation value (0.0224 $Å^{-3}$, while the experimental result is 0.02185 $Å^{-3}$), is equal to 5.2 Å. The initial energies involved in the reaction under consideration are shown in Table 4.1.

Table 4.1 Initial values of the helium and neon atoms energies (in K).[a]

N	E_{kin} helium	$E_{pot+corr}$ helium	E_{tot} helium	E_{pot} $Ne_{(2)}$-helium
500	119.08	-2543.3	-2424.2	-127.50

[a] E_{kin} of $Ne_{(1)}$=53.02, 300.6 and 769.4 K for v_0 (m s^{-1})=210, 500 and 800 m s^{-1}, respectively.

4.4.1. Reaction dynamics at zero angular momentum

The results from the calculations with impact parameter b=0 Å and initial attacking neon atom velocities v_0=210, 500 and 800 m s^{-1} are presented in this section. Additional useful material can be found in the supplementary information (Section 4.6) document where, in particular, the time evolution of the helium density and helium wave function phase in the xy-plane are shown in Movie 4.1, Movie **4.2** and Movie **4.3**, for the three initial conditions indicated above, respectively.

Snapshots of the time evolution (x-axis) of the helium density and neon atoms positions for v_0=500 m s^{-1} (the most probable velocity of neon atoms at $T = 300\ K$) and b=0 Å are shown in Figure 4.2. Besides, the time evolution of the helium density in the xy-plane can be seen in the Movie 1 (supplementary information), together with the helium wave function phase. The temporal evolution of the position and velocity of the neon atoms and of the velocity as a function of position for the selected velocities is presented in Figure 4.3.

The microscopic mechanism of the neon dimer formation inside the nanodroplet can be understood quite well with the help of Figure 4.2 and Figure 4.3 and Movie 4.1-Movie 4.3 (supplementary information). The pick-up process of the $Ne_{(1)}$ atom is similar to that described by us in ref. 38 although a significant difference appears for the lowest velocity examined (see below). Therefore, when the attacking neon atom approaches to the doped nanodroplet its velocity rapidly (~5 ps) decreases and, in some cases, it reaches negative values; i.e., the atom bounces back at some extent, as it can be observed in the time evolution of the position.

The velocity of the attacking neon atom is slightly increased before reaching the nanodroplet, due to the attractive interaction it feels from the nanodroplet (for v_0=800 m s^{-1} the increase is particularly small). The collision with the nanodroplet surface, which occurs at about 3.7, 1.5 and 1.0 ps for v_0=210, 500 and 800 m s^{-1}, respectively, induces compression in the helium density that is translated into waves, compression increasing with v_0. After the collision, the helium density surrounds the attacking neon atom at the surface, as the interaction is attractive, and drags it inside the nanodroplet. Then, the $Ne_{(1)}$ atom, with its solvation layers being progressively formed, travels inside the nanodroplet and approaches the $Ne_{(2)}$ atom pushing it towards the impact direction. Later, a particularly strong compression of the superfluid liquid helium placed between the two neon atoms is produced, as it is evident from the high peak found in the helium density (at about 34 ps for v_0=500 m s^{-1}; cf. Figure 4.2 and Movie 4.2).

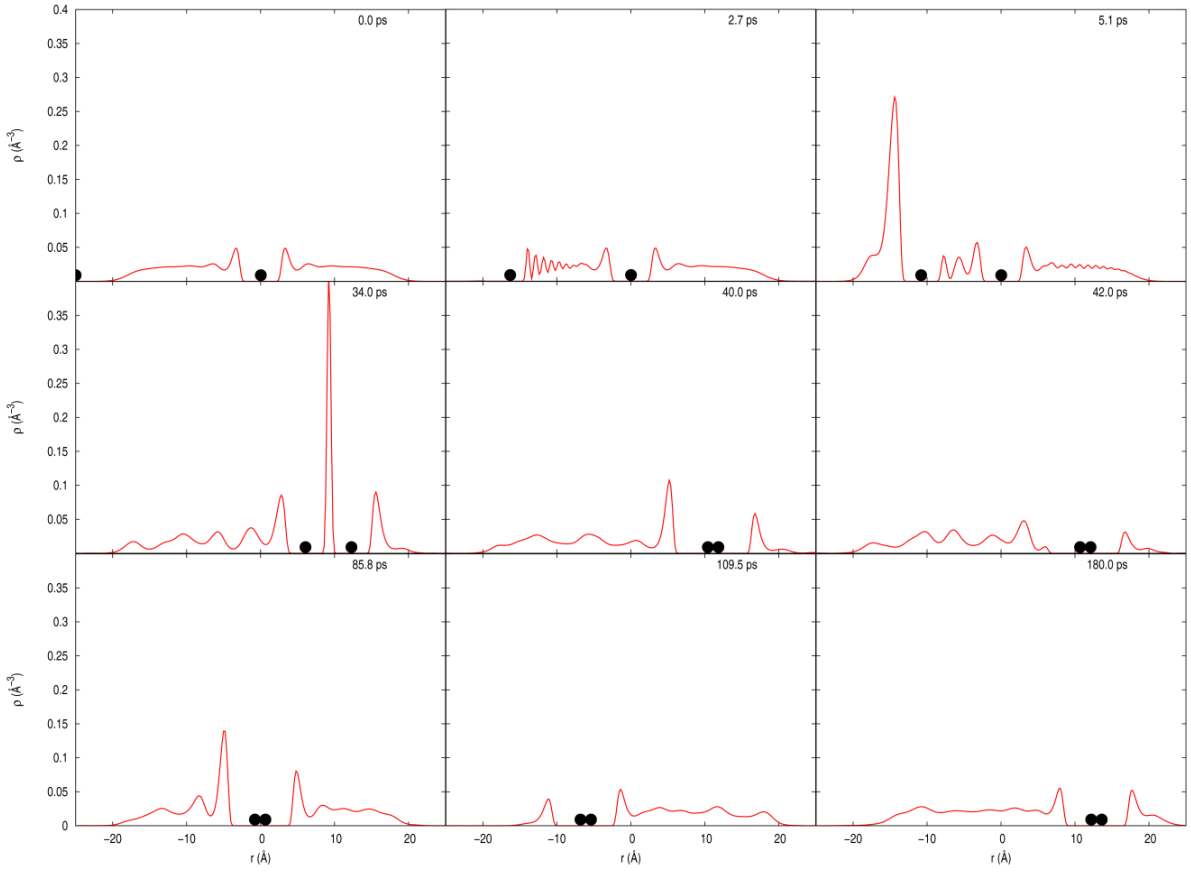

Figure 4.2 Snapshots showing the time evolution of the helium density in the x-axis for v_0=500 m s^{-1} and b=0 Å at representative times. The position of the Ne atoms is indicated by the black balls.

Nevertheless, this helium density barrier can be removed and the solvation layers of both Ne atoms merge into the solvation layers of the Ne-Ne system, with the Ne_2 dimer

being formed at around 45 ps for v_0=500 m s^{-1}. For the lower initial velocity investigated (v_0=210 m s^{-1}), however, the helium density between the neon atoms is not fully removed and the resulting Ne-Ne system is formed with a large equilibrium internuclear distance. This structure does not really correspond to the true Ne_2 dimer (Figure s4.2) but to a Ne-Ne adduct or pseudo-dimer. Additionally, it should be noted that, just before that the dimer formation has taken place, sharp oscillations of progressively decreasing amplitude (so as to dissipate the vibrational energy) occur in the velocities of both neon atoms for v_0=500 and 800 m s^{-1} (Figure 4.3).

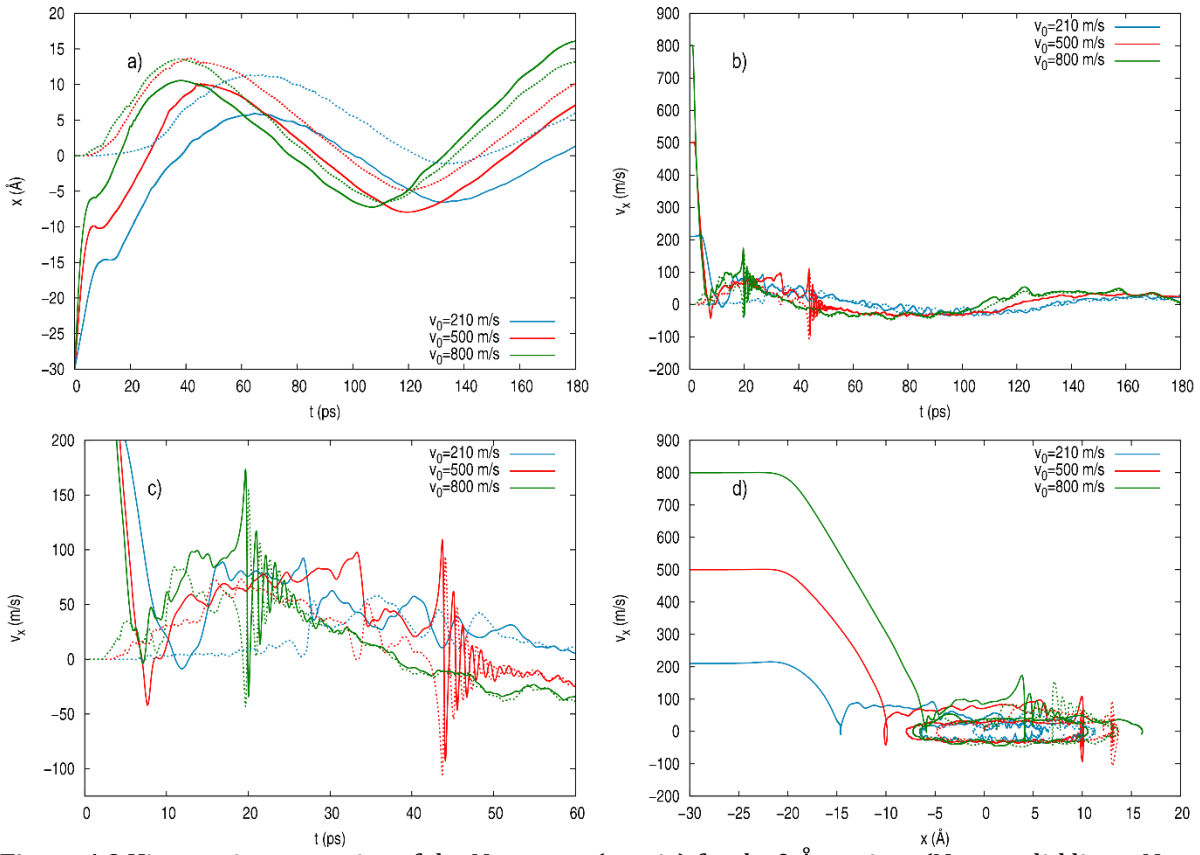

Figure 4.3 Kinematic properties of the Ne atoms (x-axis) for b=0 Å *vs.* time ($Ne_{(1)}$: solid lines, $Ne_{(2)}$: dashed lines): (a) position; (b) velocity; (c) velocity at short-intermediate times; (d) phase-space like diagram.

It is worth noting here that according to our previous quantum study at total angular momentum equal to zero (J=0)[38] the Ne_2 dimer formation happens for all the expected values of the initial velocity, $<v_0>$, selected in the 120-1000 m s^{-1} velocity range. This is in contrast with the present quantum-classical results for v_0=210 m s^{-1}, showing that quantum effects are relevant at this initial condition and, probably, also at smaller velocities.

Once the Ne_2 dimer or the Ne-Ne pseudo-dimer has been finally produced, it travels inside the nanodroplet at the Landau critical velocity. This velocity remains constant unless the product molecule approaches the nanodroplet surface (Figure 4.3 and Movie 4.1-Movie 4.3 (supplementary information)). Thus, the asymmetric distribution of helium density with respect to the molecule pushes it back and forward inside the nanodroplet.

The evolution of the Ne-Ne internuclear distance with time is presented in Figure 4.4. At the initial times it decreases more rapidly as the initial attacking neon velocity increases and then it reaches an almost constant value (plateau) before the final value is obtained (oscillating values for v_0=210 m s^{-1}). This plateau results from the fact that the attacking atom spends some time near the nanodroplet surface before being solvated by the liquid helium, as mentioned above. Then, sometime after entering the nanodroplet, the dimer (Ne_2) or the pseudo-dimer (Ne-Ne adduct) is formed with two different internuclear distances, 3.09 and 5.45 Å, respectively. The former is seen for the higher velocities (500 and 800 m s^{-1}) and the latter for the smaller velocity (210 m s^{-1}). That is to say, only for a high enough kinetic energy of $Ne_{(1)}$ (around 500 m s^{-1}) is possible for the system to remove the helium density between $Ne_{(1)}$ and $Ne_{(2)}$ and produce the Ne_2 dimer.

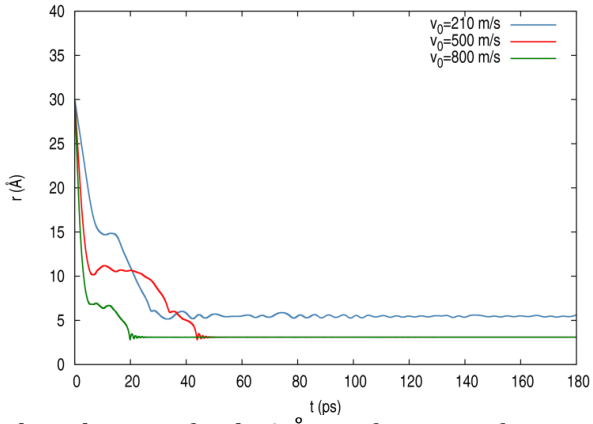

Figure 4.4 Ne-Ne internuclear distance for b=0 Å as a function of time.

The energies of the neon atoms and the neon-helium interaction energy for the v_0=500 m s^{-1} and b=0 Å case are shown in Figure 4.5. Both neon atoms are stabilised by capture and dimer formation, the biggest energy stabilisation arising during the capture of the attacking atom (~5 ps), where both the $Ne_{(1)}$ kinetic and $Ne_{(1)}$-HeND interaction energies substantially decrease. At the initial times the energies of the neon atom in the centre of the nanodroplet, $Ne_{(2)}$, are slightly modified because its surroundings are not

changed so much. When the dimer is formed some sharp oscillations are seen in the kinetic energy (oscillations were previously reported for the neon atoms velocities; Figure 4.3). Once the minimum energy Ne-Ne structure is formed (Ne_2 dimer) the kinetic and Ne-HeND interaction energies are very similar for both neon atoms. The formation of the dimer induces the final energy stabilization due to the decrease of the Ne-Ne interaction potential energy.

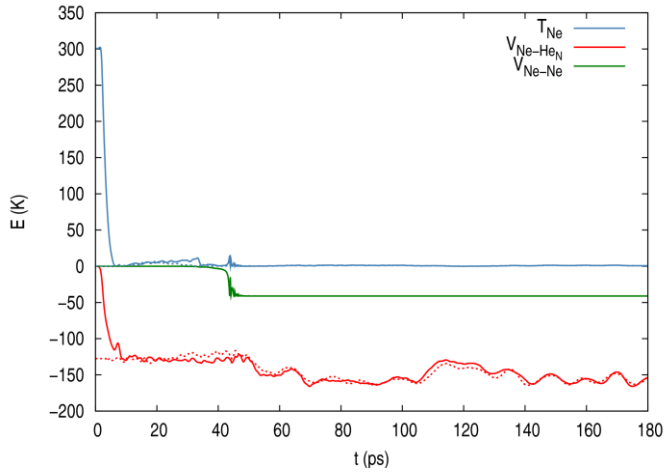

Figure 4.5 Kinetic energy of the Ne atoms, Ne-nanodroplet and Ne-Ne interaction energies for v_0=500 m s^{-1} and b=0 Å, as a function of time ($Ne_{(1)}$: solid lines, $Ne_{(2)}$: dashed lines).

Apart from looking at the behaviour of the $Ne_{(1)}$ and $Ne_{(2)}$ atoms energies, it is also of interest to pay attention to the energies of the $Ne_{(1)}$-$Ne_{(2)}$ system as a single entity, which finally leads to the Ne_2 dimer or to the Ne-Ne pseudo-dimer, as a single entity. Figure 4.6 shows the $Ne_{(1)}$-$Ne_{(2)}$ kinetic energy ($E_{\mathrm{kin,Ne_{(1)}}} + E_{\mathrm{kin,Ne_{(2)}}}$), potential energy ($V_{\mathrm{Ne_{(1)}-Ne_{(2)}}}$) and effective potential energy ($V_{\mathrm{Ne_{(1)}-He_N}} + V_{\mathrm{Ne_{(2)}-He_N}} + V_{\mathrm{Ne_{(1)}-Ne_{(2)}}}$) for the three initial velocities and b=0 Å. There is an important energy decrease in the Ne atoms + HeND system when the dimer is formed (v_0= 500 and 800 m s^{-1}), which is smaller in the case of the pseudo-dimer formation (v_0=210 m s^{-1}). The kinetic energy decreases during the attacking neon atom capture and a sharp oscillations are evident, prior to dimer formation, at about 20 ps and 45 ps for v_0= 500 and 800 m s^{-1}, respectively. Besides, the effective potential energy decreases up to around 200 K and then its values present irregular oscillations with amplitudes of the order of 50 K. The values are bigger for v_0=210 m s^{-1} because the Ne-Ne interaction energy is weaker in the Ne_2 pseudo-dimer (-2.1 K; Ne-Ne distance oscillating around 5.45 Å) than in the dimer (-41.1 K; Ne-Ne distance=3.09 Å).

Another important aspect of the dynamics corresponds to the energy exchanges that take place during the process. This can be seen in Figure 4.7 for v_0=500 m s^{-1} and b=0 Å, where the total energy of the Ne-Ne system, the total energy of the helium nanodroplet, the Ne-HeND interaction energy, and the total energy of the system (Ne atoms and HeND) are shown. An energy transfer occurs from Ne-Ne to the HeND that is efficiently released by evaporation of helium density (nanodroplet relaxation), with the amount of energy transferred increasing substantially with the initial velocity/kinetic energy of $Ne_{(1)}$ (Figure 4.8 and Figure 4.9). This last figure also shows that the number of helium atoms evaporated increases with the initial velocity of the attacking atom. Moreover, evaporation also causes an increase in the total energy of the system because some helium mass is lost.

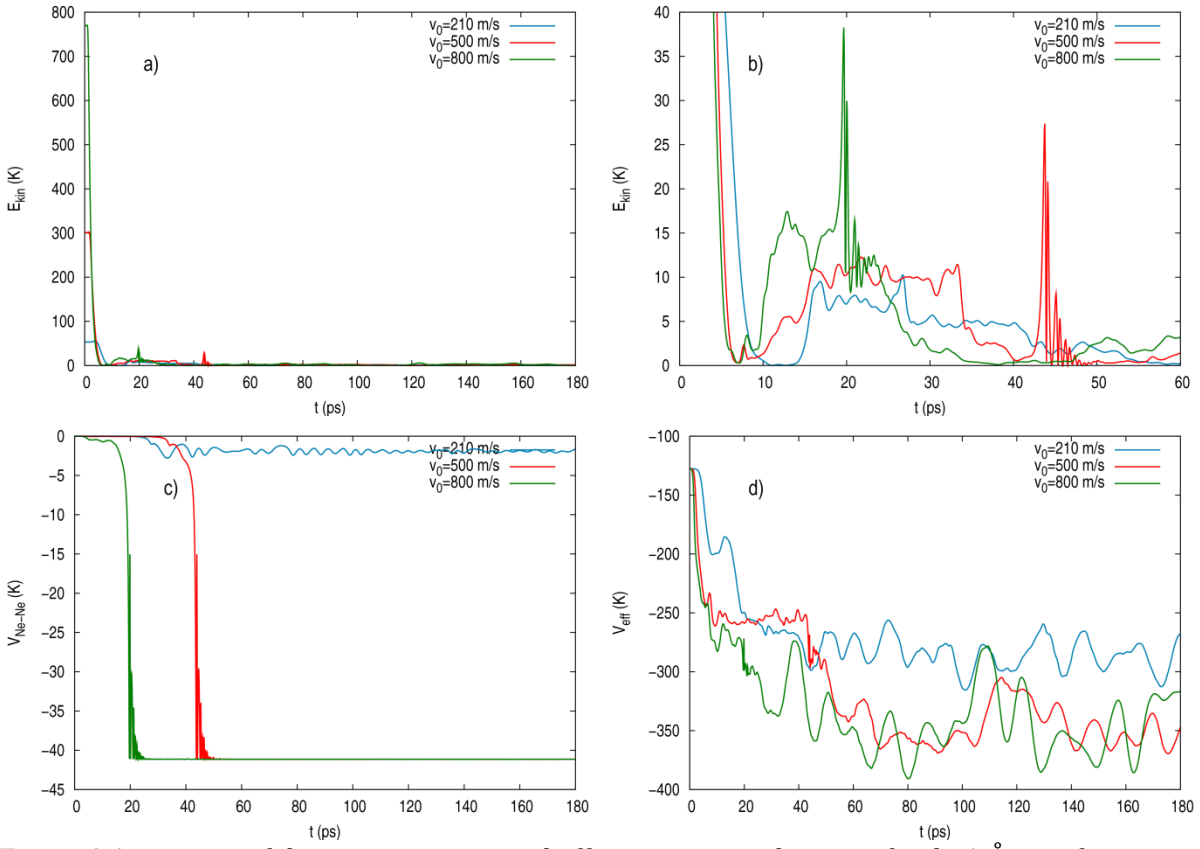

Figure 4.6 Energies of the Ne-Ne system and effective potential energy for b=0 Å, as a function of time: a) kinetic energy ($E_{\mathrm{kin,Ne(1)}}+E_{\mathrm{kin,Ne(2)}}$); b) kinetic energy at short-intermediate times; c) Ne-Ne interaction energy; d) effective potential energy ($V_{\mathrm{Ne_{(1)}-He_N}}+V_{\mathrm{Ne_{(2)}-He_N}}+V_{\mathrm{Ne-Ne}}$).

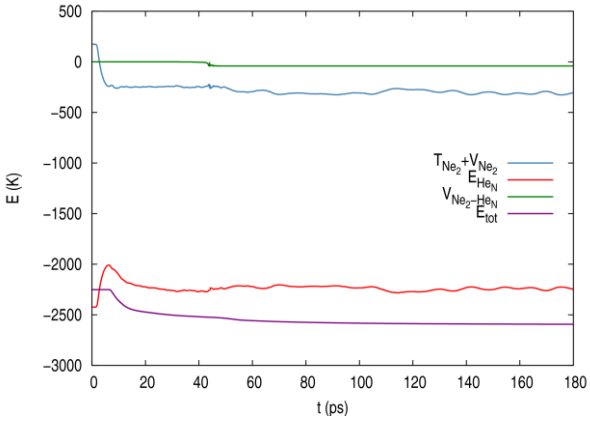

Figure 4.7 Total energy of Ne-Ne ($T_{\mathrm{Ne_2}} + V_{\mathrm{Ne_2}}$), total energy of the HeND ($E_{\mathrm{He_N}}$), Ne atoms-HeND interaction energy ($V_{\mathrm{Ne_2-He_N}}$), and total energy of the system (Ne atoms and HeND; E_{tot}), for v_0=500 m s^{-1} and b=0 Å as a function of time.

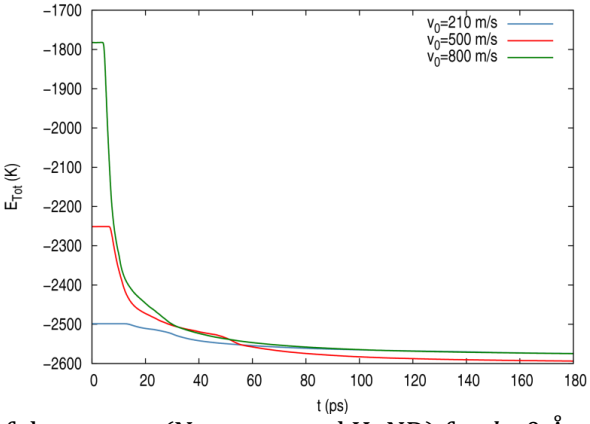

Figure 4.8 Total energy of the system (Ne atoms and HeND) for b=0 Å, as a function of time.

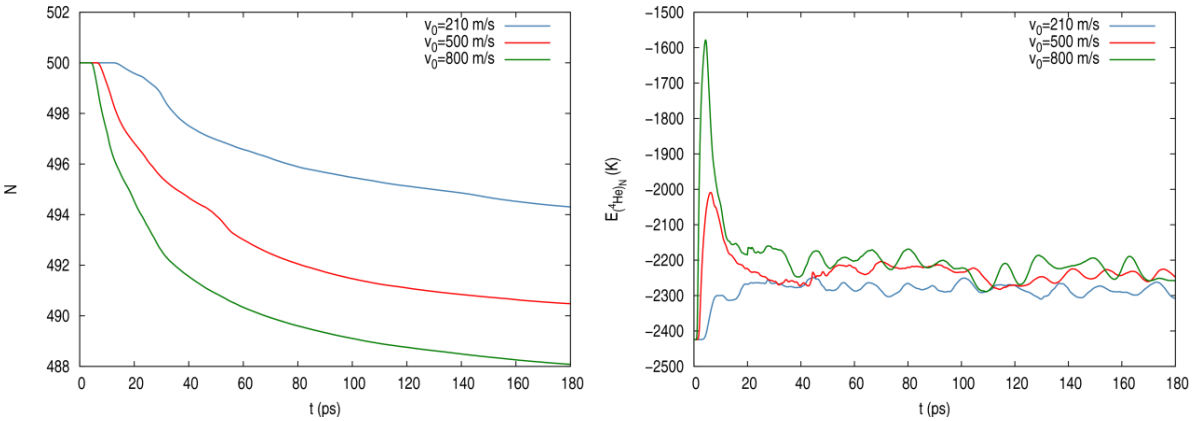

Figure 4.9 Number of He atoms of the HeND (left) and total energy of the He atoms of the HeND (right) for b=0 Å, as a function of time.

4.4.2. Reaction dynamics at angular momentum different from zero

The influence of the initial angular momentum of the attacking neon atom ($L_{\mathrm{Ne(1),0}}$) on the reaction leading to the dimer or adduct formation for v_0=210, 500 and 800 m s^{-1} is

considered in this section (modulus of $L_{Ne(1),0}=m_{Ne}v_0b$). Thus, selected values of the impact parameter ($b\neq0$ Å) in the 0-20, 0-18 and 0-16 Å intervals have been examined, respectively. With the largest b value for each initial velocity corresponding to or being similar to b_{max}.

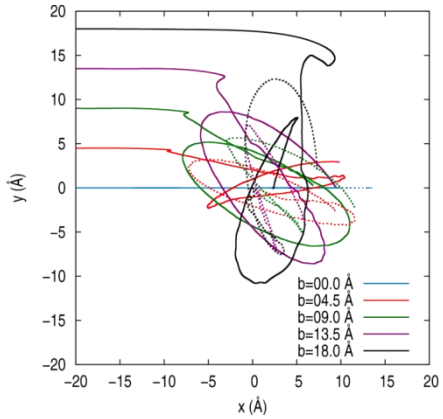

Figure 4.10 Trajectories of the Ne atoms for v_0=500 m s^{-1} and several impact parameters ($Ne_{(1)}$: solid lines, $Ne_{(2)}$: dashed lines).

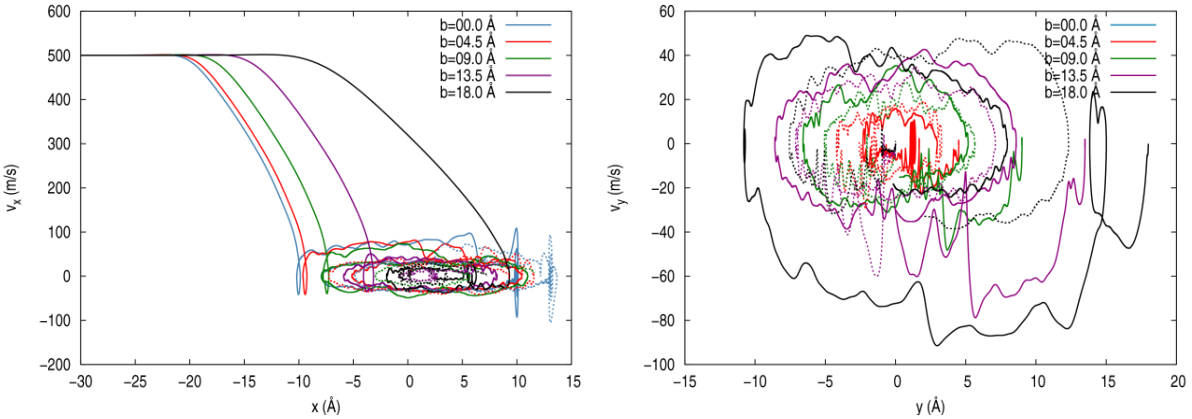

Figure 4.11 Phase-space like diagram of the Ne atoms trajectories: velocity as a function of position for the x-axis (left) and y-axis (right), ($Ne_{(1)}$: solid lines, $Ne_{(2)}$: dashed lines).

The observed behaviours are in general similar to those of the b=0 Å case with softer energy exchanges found for $b\neq0$ Å, but there are two main differences that should be remarked. Thus, for $b\neq0$ Å the $Ne_{(1)}$ capture process only leads to the formation of Ne-Ne adducts and for high enough b values the formation of vortex lines takes place. This will be discussed in detail in this section. Besides, to understand better the way the reaction proceeds (microscopic reaction mechanism) Movie 4.4-Movie 4.9 are included in the supplementary information, where the temporal evolution of helium (density and

wave function phase; xy-plane) are shown for v_0=210 m s^{-1} (b=5.0 and 20.0 Å), 500 m s^{-1} (b=4.5 and 18.0 Å) and 800 m s^{-1} (b=4.0 and 16.0 Å).

Figure 4.10 shows the trajectories of both neon atoms during the simulations for v_0=500 m s^{-1} and several impact parameters and Figure 4.11 shows the x and y velocities of the Ne atoms as a function of the position for both the x and y directions (the modulus of both atoms velocities is shown in Figure s4.11.

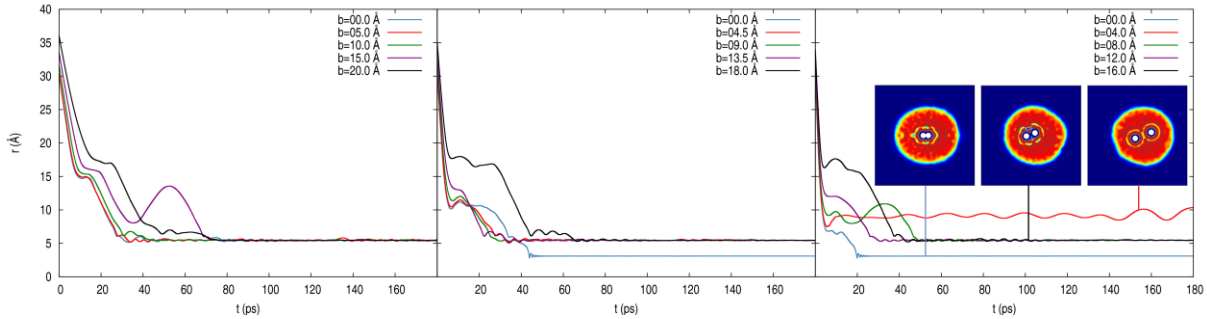

Figure 4.12 Ne-Ne internuclear distance as a function of time for v_0=210, 500 and v_0=800 m s^{-1} from left to right, at the impact parameters selected. The last subfigure shows the helium density (xy plane) and Ne atoms positions for the three representative cases.

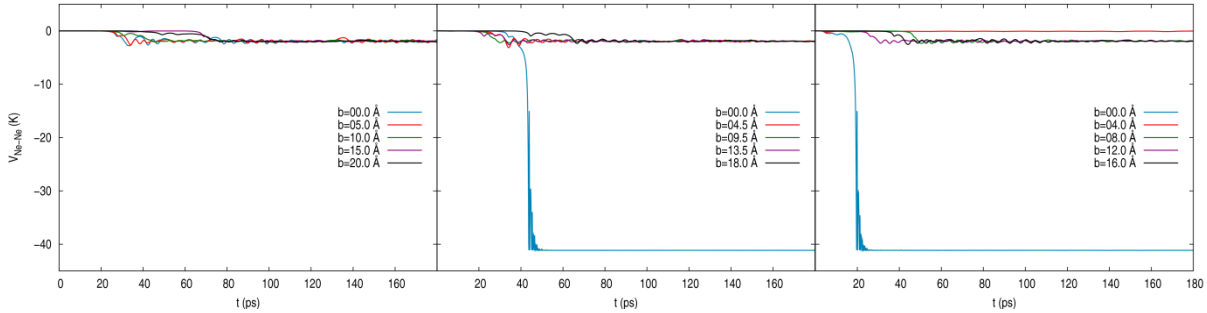

Figure 4.13 Ne-Ne interaction energy as a function of time for v_0=210, 500 and v_0=800 m s^{-1} from left to right, at the impact parameters selected.

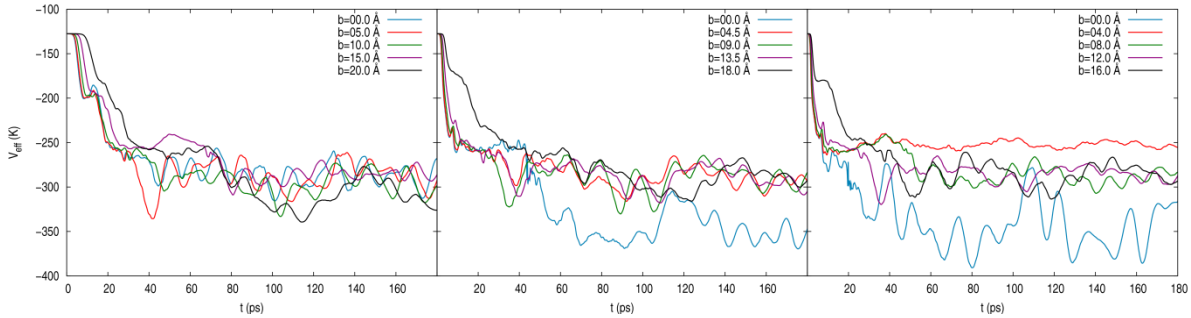

Figure 4.14 Effective potential energy ($V_{Ne_{(1)}-He_N}+V_{Ne_{(2)}-He_N}+V_{Ne-Ne}$) as a function of time for v_0=210, 500 and v_0=800 m s^{-1} from left to right, at the impact parameters selected.

The evolution of the Ne-Ne internuclear distance *vs*. time does not only depend on the initial velocity of the attacking neon atom, $Ne_{(1)}$, but also on its impact parameter, as it can be seen in Figure 4.12 for the three initial velocities and impact parameters selected for $Ne_{(1)}$. In order to understand better the dynamics, additional useful information is provided in Figure 4.13 and Figure 4.14, where the Ne-Ne interaction potential energy ($V_{\text{Ne-Ne}}$) and the effective potential energy ($V_{\text{eff}}=V_{\text{Ne}_{(1)}-\text{He}_N}+V_{\text{Ne}_{(2)}-\text{He}_N}+V_{\text{Ne}-\text{Ne}}$) *vs*. time are plotted for the selected initial conditions (v_0, b), respectively.

At the lower initial velocity (210 m s^{-1}) and for all the initial angular momentum values explored in this work, the neon-neon structure that is finally formed never corresponds to that of the Ne_2 dimer, but to a Ne-Ne adduct that shows an equilibrium internuclear distance r_e of 5.45 Å, which is substantially larger than that of the dimer (r_e=3.09 Å). This happens in this way because the attacking neon atom, $Ne_{(1)}$, does not approach to the inner neon atom, $Ne_{(2)}$, with enough energy along the Ne-Ne internuclear axis line so as to be able to remove the helium density placed between them.

For the middle initial velocity of $Ne_{(1)}$ (500 m s^{-1}) the Ne_2 dimer is only formed for the lower impact parameter (b=0 Å) and for the initial angular momentum different from zero cases only the previously mentioned Ne-Ne adduct is formed. Furthermore, a particularly rich situation from the dynamics point of view is observed for the biggest initial velocity of $Ne_{(1)}$ (800 m s^{-1}). In fact, we can see that the dimer is only formed for b=0 Å, as in the case of v_0=500 m s^{-1}, but in addition to the formation of the Ne-Ne adduct with r_e=5.45 Å a very weakly bounded Ne-Ne adduct with r_e =9.14 Å is also observed.

At v_0=800 m s^{-1} we can also see that there is a non-monotonic behaviour of the system with respect to the angular momentum, as the very weakly bound adduct is not formed at the highest value of b explored but at a relatively small one (4.0 Å). This means that the system does not behave monotonically and this behaviour can be interpreted on the basis of complex dynamic effects mainly involving the helium density, the waves produced as a result of the collision with the attacking neon atom, and the reflections of these waves inside the nanodroplet. A non-monotonic behaviour has also been reported in the quantum study of this system at zero angular momentum.[38]

The first important difference found between results for b=0 and b≠0 corresponds to the non-production of the dimer for the second case. That angular momentum does not

favour the dimer reaction is easy to understand. Although here we cannot refer to the neon-neon centrifugal barrier originated by the angular momentum, as it happens in the gas phase reaction dynamics, it is clear that the increase of angular momentum leads to a diminution of the relative velocity along the imaginary line that links the centre of both atoms. This is expected to hinder the reaction since it makes more difficult the elimination of the helium density that is placed between both atoms to lead, subsequently, to the transformation of the helium solvation shells of each atom into that of the dimer.

From these results it comes out that for the Ne + Ne@(^{4}He)$_N$ system the formation of the neon-neon adduct, Ne-Ne@(^{4}He)$_{N'}$ (and mainly that one with r_e=5.45 Å), clearly dominates the reactivity of the system, and the neon dimer formation, Ne$_2$@(^{4}He)$_{N'}$, plays a minor role. This situation corresponds to what is commonly referred as "quantum gel" or "quantum foam", because instead of forming the dimer molecule the two atomic species basically maintain their identity inside the helium nanodroplet.

This behaviour has been previously reported in a few cases. It has been observed in spectroscopic studies on superfluid helium nanodroplets doped with Mg atoms,[57,58] where the results have been interpreted on the basis of static calculations (structure and energy) using a DFT approach for helium (OT density functional) and the HeNe and Ne$_2$ potential energy curves.[57,59] Moreover, the quantum gel formation has been also considered theoretically in analogous static studies performed on Ne atoms[44] and F atoms[45] in superfluid helium (bulk), the former case being the first investigation on this issue.

The helium solvation layers modify the gas phase X$_2$ dimer potential energy curve and several shallow minima and energy barriers appear in the X$_2$ dimer effective potential energy curve. For the X=Ne case, in addition to the minimum corresponding to the Ne$_2$ dimer, two additional minima are found at around 5.7 and 9.3 Å, which have shallow character (particularly the last one), and there is an energy barrier of about 1.5 K for the evolution from the adduct at 5.7 Å to the dimer (r_e=3.09 Å).[44] This structural information clearly correlates with what we have found in the present dynamics study, where the dimer, a Ne-Ne adduct with r_e=5.45 Å and a very weakly bounded Ne-Ne adduct with r_e =9.14 Å have been observed.

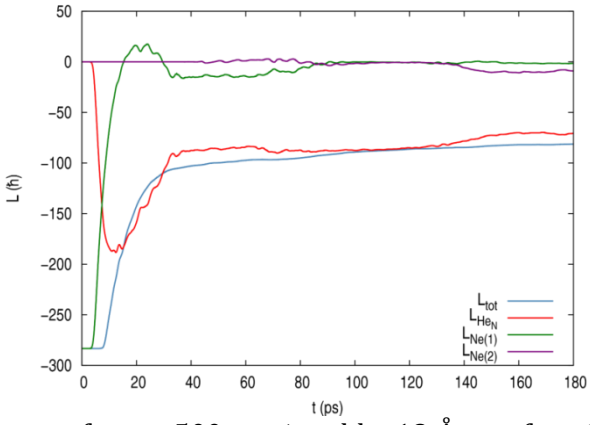

Figure 4.15 Angular momenta for v_0=500 m s^{-1} and b=18 Å as a function of time: total angular momentum, HeND angular momentum, $Ne_{(1)}$ angular momentum and $Ne_{(2)}$ angular momentum.

Energies behave in the same fashion as in the case with angular momentum equal to zero. Angular momentum only introduces some delay and smoothness to the energies evolution. The energies of the neon atoms change later when the impact parameter is higher (Figure 4.5 and Figure s4.12). The comparison can also be seen, e.g., for the kinetic energy of the Ne--Ne system (Figure s4.13), the total energy of the system (Figure s4.15) and the number of helium atoms and helium energy of the nanodroplet (Figure s4.16). Besides, it can also be seen that the energy exchanges are smoother when angular momentum increases (Figure 4.7 and Figure s4.14).

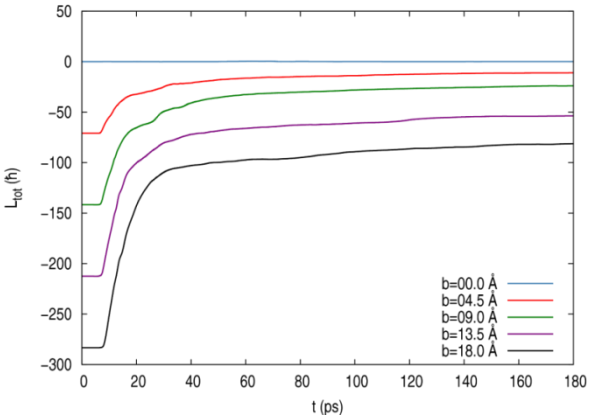

Figure 4.16 Total angular momentum for v_0=500 m s^{-1} and the selected impact parameters, as a function of time.

The second main difference between the b=0 and b≠0 results comes from the fact that, shortly after the neon atom has been captured, quantized vortex lines are formed in the nanodroplet, as a result of the collapse of surface excitations (ripplons) created by the

atom impact. Moreover, the exchange of angular momentum between the attacking Ne atom and the nanodroplet is also of interest. These issues are considered below.

The time evolution of the total angular momentum (L_{tot}), angular momentum of the nanodroplet ($L_{\mathrm{He_N}}$) and angular momentum of both neon atoms ($L_{\mathrm{Ne(1)}}$ and $L_{\mathrm{Ne(2)}}$) for v_0=500 m s^{-1} and b=18 Å is given in Figure 4.15; where $L_{\mathrm{tot}} = L_{\mathrm{Ne(1)}} + L_{\mathrm{Ne(2)}} + L_{\mathrm{He_N}}$, i.e., without including the angular momentum of the evaporated helium atoms. Initially, the HeND has no angular momentum, but when the $\mathrm{Ne_{(1)}}$ atom reaches the surface it begins to transfer in a fast way its angular momentum to the HeND, which becomes rotationally excited. Shortly after, the nanodroplet angular momentum is effectively decreased by helium density evaporation. Finally, once the Ne-Ne adduct is formed, the HeND carries most of the total angular momentum and some smooth oscillations are evident in the nanodroplet and neon atoms angular momenta, due to the collisions of the adduct against the nanodroplet surface. Angular momenta exchanges are stronger for higher impact parameters and the transfer of angular momentum from Ne(1) to the HeND is especially intense at the initial collision times with the HeND surface (Figure 4.16).

Although it is not the main topic of this study, we also paid some attention to the formation of vortices as a result of the interaction of the attacking neon atom with the nanodroplet, determining the initial conditions that lead to their formation.

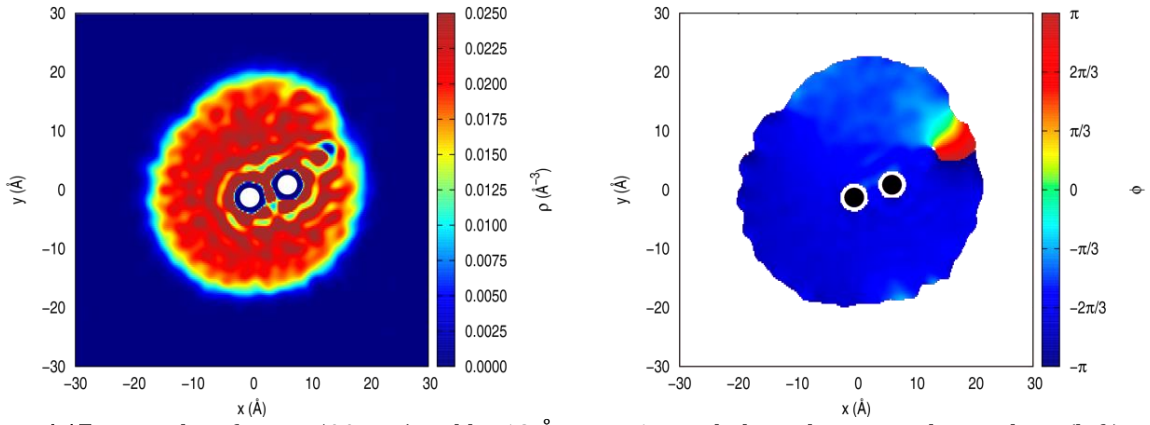

Figure 4.17 Vortex line for v_0=500 ms^{-1} and b=18 Å at t=46.7 ps: helium density in the xy plane (left) and helium wave function phase (right). The time evolution can be seen in Movie 8 (ESI).

The capture of $\mathrm{Ne_{(1)}}$ induces the creation of brief vortex rings created by the collapse of superficial excitations (ripplons). For low angular momentum these vortexes are destroyed by the helium density waves created by the capture and the strong interference

generated by the solvation layers of $Ne_{(2)}$ (they allow a more direct reflection of the waves generated during the collision and entrance of $Ne_{(1)}$). Otherwise, if the angular momentum is high enough, these vortex rings evolve into vortex lines which last longer. These vortex lines are more difficult to form and are observed for somewhat higher initial angular momenta than in the case of the Ne atom capture by a HeND.[40]

These vortices are seen as holes in the helium density and the phase of the helium effective wave function changes from $-\pi$ to π around them (Figure 4.17). This variation means that the fluid circulation around the vortex is closed, which means that this vortex is quantized. The duration of these vortex lines depend on the angular momentum induced by the attacking Ne atom. For higher angular momenta the vortex lines are seen to last during the whole simulation time (long-lived vortex lines) and for lower angular momenta vortexes are destroyed by the helium density waves (short-lived vortex lines). Short-lived vortices are observed for v_0=500 ms^{-1} (b=13.5 Å) and v_0=800 ms^{-1} (b=12.0 Å) and long-lived ones are found for v_0=500 ms^{-1} (b=18.0 Å) and v_0=800 ms^{-1} (b=16.0 Å). Movie 4.2 shows the formation of a long-lived vortex using a xy-plane representation of the helium density and wave function phase.

4.5. Summary and conclusions

The reaction dynamics involving the Ne_2 dimer/Ne-Ne adduct formation inside a superfluid helium nanodroplet [(^{4}He)$_{N=500}$; T=0.37 K], Ne + Ne@(^{4}He)$_N$ → Ne_2@(^{4}He)$_{N'}$/Ne-Ne@(^{4}He)$_{N'}$ + (N-N')^{4}He, has been studied. This has been done employing a hybrid method: quantum (time dependent DFT; Orsay-Trento functional) and classical mechanics approaches (QM-CM method) for helium and the neon atoms, respectively. As far as we know, this study corresponds to the second theoretical investigation available about the bimolecular reaction dynamics in (^{4}He)$_N$.

To investigate the influence of the initial velocity and angular momentum of the attacking neon atom, $Ne_{(1)}$, on the dynamics several initial conditions have been examined (v_0=210, 500 and 800 m s^{-1} and b in the 0-20, 0-18 and 0-16 Å intervals, respectively), where v_0=500 m s^{-1} corresponds to the most probable velocity of neon at T=300 K.

When the present results are compared with zero angular momentum quantum results it comes out that they are similar to the quantum ones for v_0=500 and 800 m s^{-1} and the formation of the Ne_2 dimer (r_e=3.09 Å) takes place in all cases. In contrast to this, a strong difference is evident for v_0=210 m s^{-1}, because in the QM-CM dynamics instead of the Ne_2 dimer a Ne-Ne adduct (r_e=5.45 Å) is produced. There are energy exchanges during the incoming atom capture and dimer/adduct formation. The helium nanodroplet is excited by both processes and relaxes by evaporation of some He atoms. Once the dimer/adduct is formed both neon atoms travel together, and their velocities reach the Landau's critical velocity.

Energy exchanges become softer with increasing impact parameter/angular momentum. The main angular momenta exchange occurs during the capture process. The attacking Ne atom transfers most of the angular momentum to the nanodroplet and to the evaporated helium atoms. Moreover, angular momentum does not help the dimer formation reaction to occur, since it makes more difficult the removal of the helium density located in the middle of the neon atoms, which is needed so as to form the Ne_2 molecule. Therefore, the formation of a neon-neon adduct, Ne-Ne@(^{4}He)$_{N'}$, with an equilibrium distance of 5.45 Å, clearly governs the reactivity of the system. This leads to the formation of a "quantum gel"/"quantum foam", as in the adduct the two Ne atoms essentially maintain their identity. Furthermore, a particularly complex dynamics is observed at v_0=800 m s^{-1}, where, in addition of the previously reported dimer and adduct, a very weakly bound Ne-Ne adduct (r_e=9.14 Å) is observed for b=4 Å.

Large enough values of the initial angular momentum can create short-lived vortex lines. They arise from the collapse of superficial excitations of the nanodroplet (ripplons) and occur with more difficulty than in case of the Ne atom capture by a pure (non-doped) helium nanodroplet, owing to the wave interferences induced by the solvation layers of the Ne atom initially placed inside the nanodroplet.

We hope that this work will encourage other theoreticians and experimentalists to investigate the reaction dynamics in superfluid helium nanodroplets, an interesting subject about which there are only a few studies available.

4.6. Appendix 4: Supplementary information

Table s4.1 Cartesian grid parameters of the helium density.[a]

v_0 (m/s)	n_x	n_y	n_z	h_x (Å)	h_y (Å)	h_z (Å)	x_{min} (Å)	x_{max} (Å)	y_{min} (Å)	y_{max} (Å)	z_{min} (Å)	y_{max} (Å)
210	200	180	180	0.30	0.35	0.35	-30.00	29.70	-31.50	31.15	-31.50	31.15
500	300	200	200	0.20	0.30	0.30	-30.00	29.80	-30.00	29.70	-30.00	29.70
800	300	200	200	0.20	0.30	0.30	-30.00	29.80	-30.00	29.70	-30.00	29.70

[a] Number of points (n_x,..), spatial separation (h_x,..) and minimum (x_{min},..)and maximum (x_{max},..) limits.

Table s4.2 Propagation time steps and final simulation times.

v_0 (m/s)	b (Å)	Δt (ps)	t_{final} (ps)
210	0	$1\cdot10^{-4}$	221.3
	7	$1\cdot10^{-4}$	180.0
	14	$1\cdot10^{-4}$	221.6
	17	$1\cdot10^{-4}$	220.8
	20	$1\cdot10^{-4}$	214.8
	27	$1\cdot10^{-4}$	183.8
	34	$1\cdot10^{-4}$	190.5
500	0	$1\cdot10^{-4}$	189.7
	7	$1\cdot10^{-4}$	188.6
	14	$1\cdot10^{-4}$	187.9
	17	$1\cdot10^{-4}$	184.0
	20	$1\cdot10^{-4}$	184.2
	27	$1\cdot10^{-4}$	183.4
	34	$1\cdot10^{-4}$	181.2
800	0	$9\cdot10^{-5}$	203.8
	7	$9\cdot10^{-5}$	221.3
	14	$9\cdot10^{-5}$	180.0
	17	$9\cdot10^{-5}$	221.6
	20	$9\cdot10^{-5}$	220.8
	27	$9\cdot10^{-5}$	214.8
	34	$9\cdot10^{-5}$	183.8

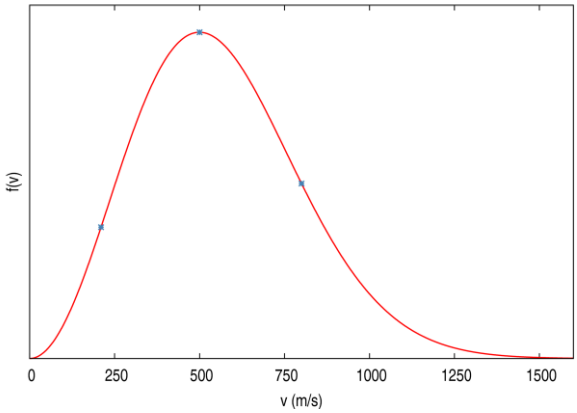

Figure s4.1 Maxwell velocity distribution of the Ne atoms at T=300K. The blue points correspond to the three initial velocities considered in this study.

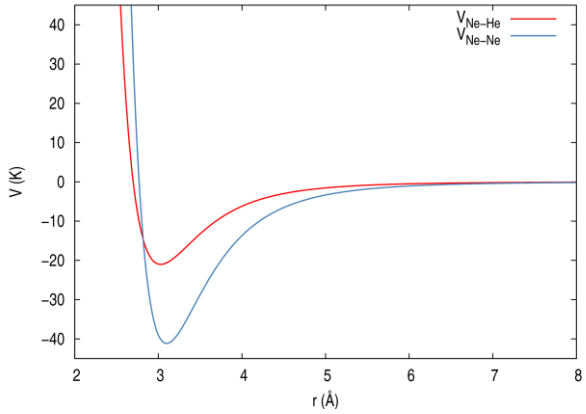

Figure s4.2 Potential energy curves of the He-Ne and Ne-Ne molecules (ref. 52).

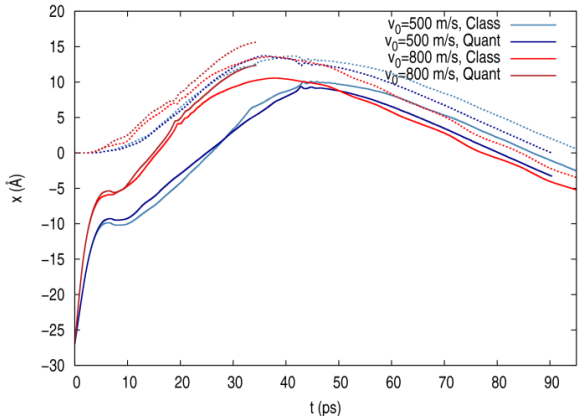

Figure s4.3 Quantum-classical *vs.* quantum results (ref. 38) for angular momentum equal to zero: position of the Ne atoms as a function of time ($Ne_{(1)}$: solid lines, $Ne_{(2)}$: dashed lines).

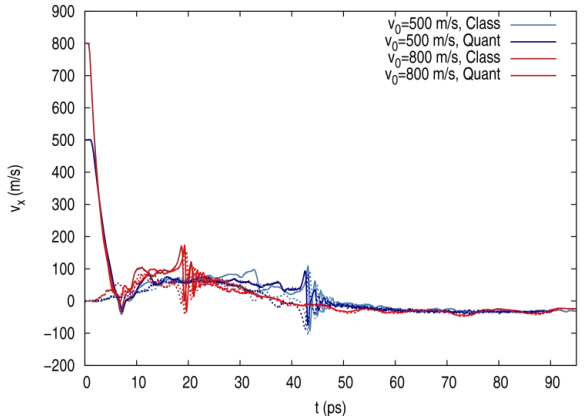

Figure s4.4 Quantum-classical *vs.* quantum results (ref. 38) for angular momentum equal to zero: velocity of the Ne atoms as a function of time ($Ne_{(1)}$: solid lines, $Ne_{(2)}$: dashed lines).

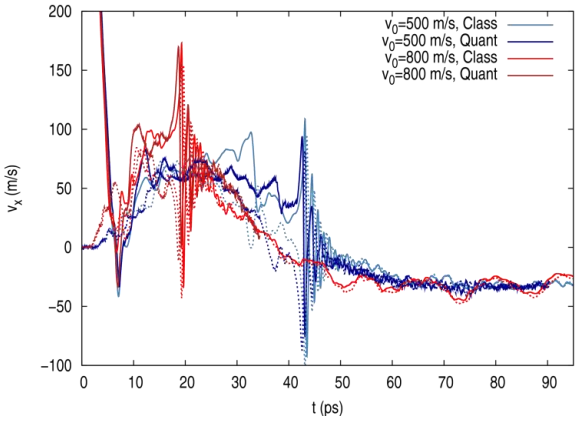

Figure s4.5 Quantum-classical *vs.* quantum results (ref. 38) for angular momentum equal to zero: velocity of the Ne atoms as a function of time; zoom 1 ($Ne_{(1)}$: solid lines, $Ne_{(2)}$: dashed lines).

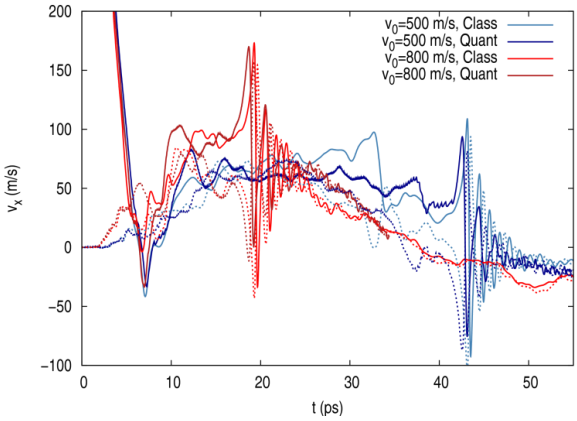

Figure s4.6 Quantum-classical *vs.* quantum results (ref. 38) for angular momentum equal to zero: velocity of the Ne atoms as a function of time; zoom 2 ($Ne_{(1)}$: solid lines, $Ne_{(2)}$: dashed lines).

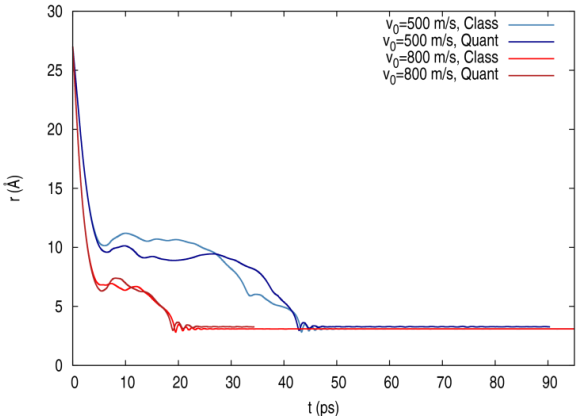

Figure s4.7 Quantum-classical *vs.* quantum results (ref. 38) for angular momentum equal to zero: Ne-Ne internuclear distance as a function of time.

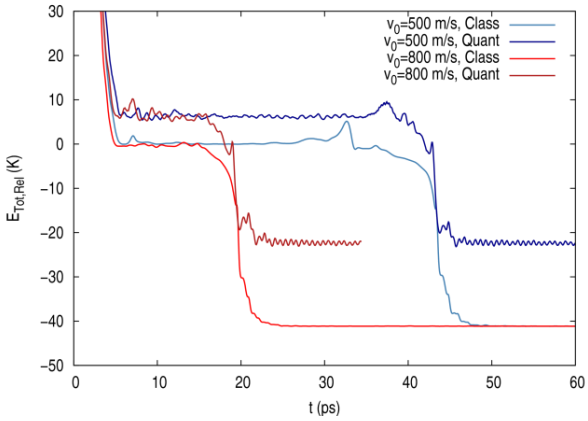

Figure s4.8 Comparison between the quantum-classical and quantum results (ref. 38) for angular momentum equal to zero: total relative energy (kinetic energy of the Ne atoms + Ne-Ne potential energy) as a function of time.

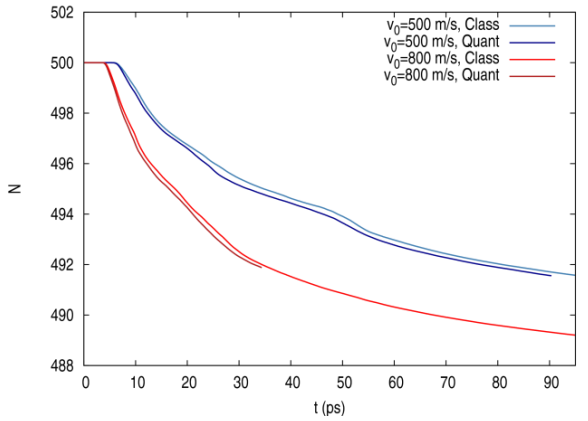

Figure s4.9 Comparison between the quantum-classical and quantum results (ref. 38) for angular momentum equal to zero: number of helium atoms of the nanodroplet as a function of time.

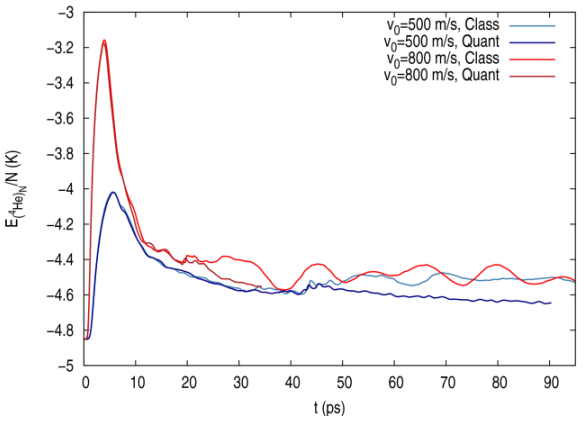

Figure s4.10 Comparison between the quantum-classical and quantum results (ref. 38 **¡Error! Marcador no definido.**) for angular momentum equal to zero: energy per helium atom of the nanodroplet as a function of time.

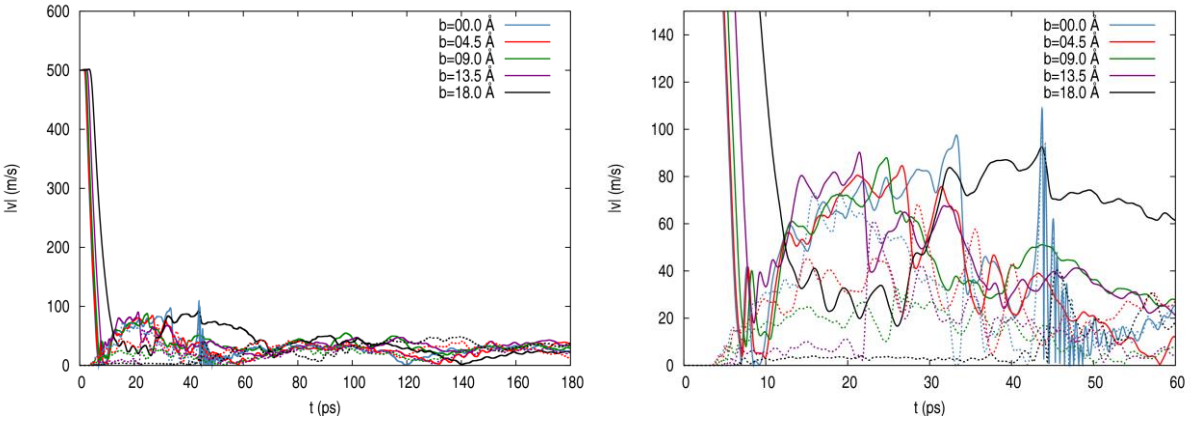

Figure s4.11 Module of the velocity of the Ne atoms for v_0=500 m s^{-1} as a function of time (Ne$_{(1)}$: solid lines, Ne$_{(2)}$: dashed lines): full simulation (left) and short-intermediate times (right).

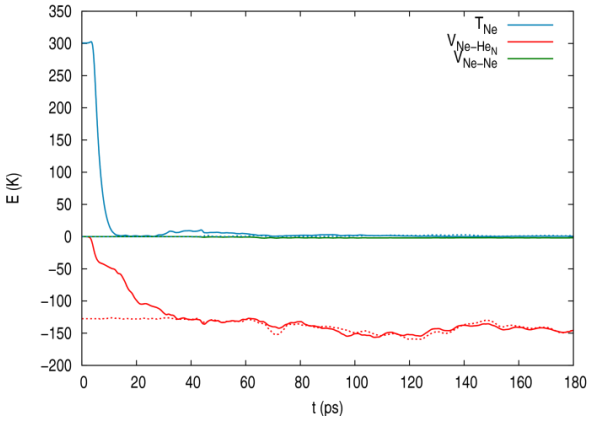

Figure s4.12 Kinetic energy of the Ne atoms, Ne-nanodroplet and Ne-Ne interaction energies for v_0=500 m s^{-1} and b=18 Å, as a function of time (Ne$_{(1)}$: solid lines, Ne$_{(2)}$: dashed lines).

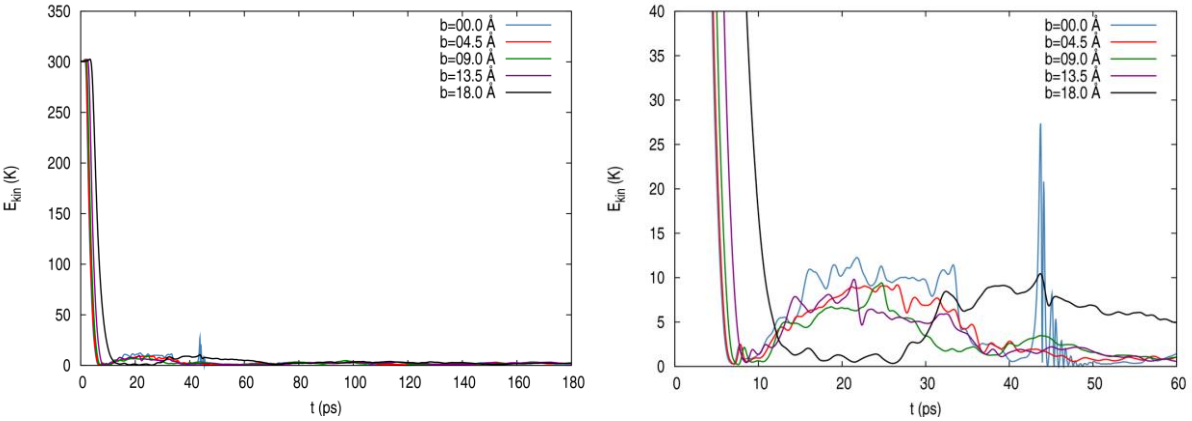

Figure s4.13 Kinetic energy of the Ne-Ne system ($E_{\mathrm{kin,Ne(1)}}$+$E_{\mathrm{kin,Ne(2)}}$) for v_0=500 m s^{-1}, as a function of time: full simulation (left) and short-intermediate times (right).

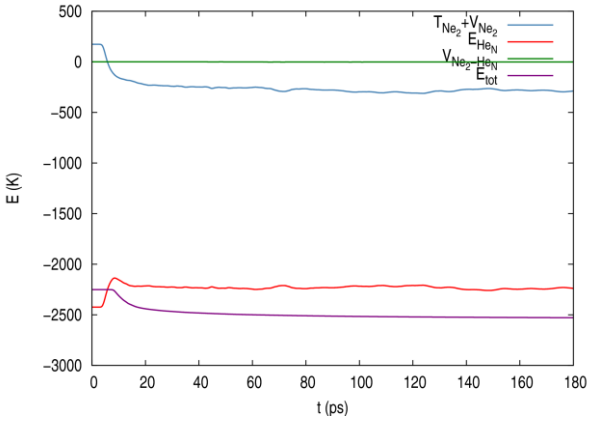

Figure s4.14 Total energy of Ne-Ne ($T_{\mathrm{Ne}_2} + V_{\mathrm{Ne}_2}$), total energy of the HeND (E_{He_N}), Ne atoms-HeND interaction energy ($V_{\mathrm{Ne}_2-\mathrm{He}_N}$), and total energy of the system (Ne atoms and HeND; E_{tot}), for v_0=500 m s^{-1} and b=18 Å as a function of time.

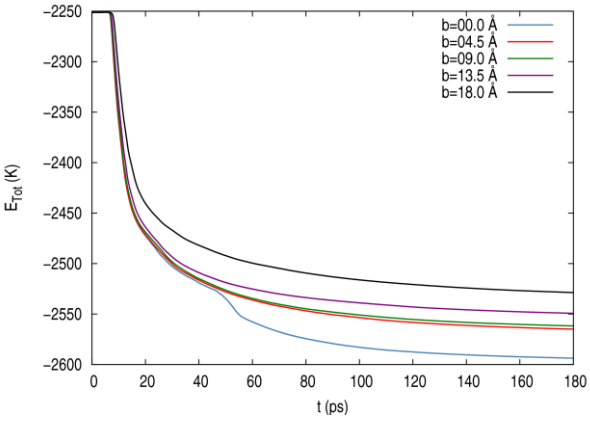

Figure s4.15 Total energy of the system (Ne atoms and HeND) for v_0=500 m s^{-1}, as a function of time.

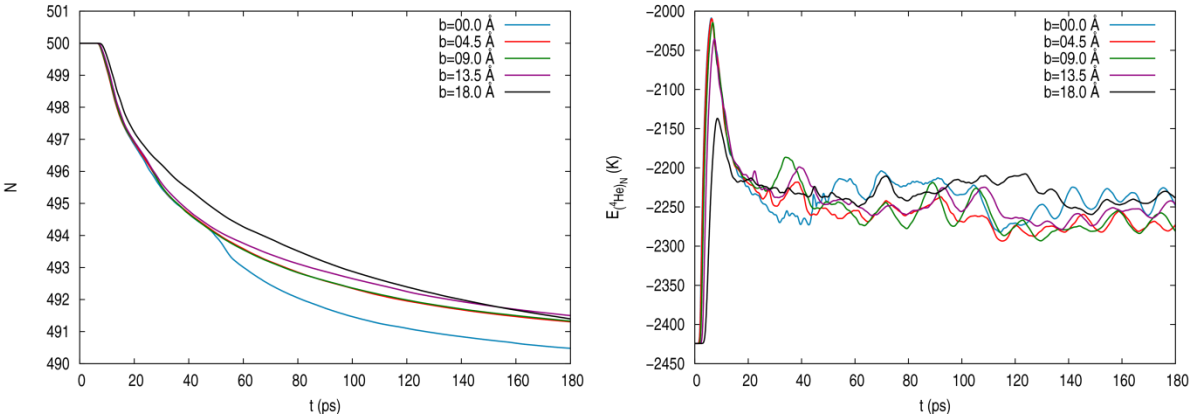

Figure s4.16 Number of helium atoms of the HeND (left) and total energy of the helium atoms of the HeND (right) for v_0=500 m s^{-1}, as a function of time.

Movie 4.1 Time evolution of the helium density and helium wave function phase in the xy-plane for v_0=210 m s^{-1} and b=0 Å (simulated time≈131 ps). See the mp4 video file "Movie 4.1. v210_b00.mp4" (1.51 MB).

Movie 4.2 The same as movie 1 but for v_0=500 m s^{-1} and b=0 Å (simulated time≈175 ps). See the mp4 video file "Movie 4.2. v500_b00.mp4" (1.98 MB).

Movie 4.3 The same as movie 1 but for v_0=800 m s^{-1} and b=0 Å (simulated time≈157 ps). See the mp4 video file "Movie 4.3. v800_b00.mp4" (1.98 MB).

Movie 4.4 The same as movie 1 but for v_0=210 m s^{-1} and b=5.0 Å (simulated time≈85 ps). See the mp4 video file "Movie 4.4. v210_b05.mp4" (0.97 MB).

Movie 4.5 The same as movie 1 but for v_0=500 m s^{-1} and b=4.5 Å (simulated time≈190 ps). See the mp4 video file "Movie 4.5. v500_b04.5.mp4" (2.18 MB).

Movie 4.6 The same as movie 1 but for v_0=800 m s^{-1} and b=4.0 Å (simulated time≈184 ps). See the mp4 video file "Movie 4.6. v800_b04.mp4" (2.36 MB).

Movie 4.7 The same as movie 1 but for v_0=210 m s^{-1} and b=20.0 Å (simulated time≈84 ps). See the mp4 video file "Movie 4.7. v210_b20.mp4" (1.00 MB).

Movie 4.8 The same as movie 1 but for v_0=500 m s^{-1} and b=18.0 Å (simulated time≈188 ps). See the mp4 video file "Movie 4.8. v500_b18.mp4" (2.16 MB).

Movie 4.9 The same as movie 1 but for v_0=800 m s^{-1} and b=16.0 Å (simulated time≈204 ps). See the mp4 video file "Movie 4.9. v800_b16.mp4" (2.64 MB).

4.7. Reference

[1] J. P. Toennies and A. F. Vilesov, Superfluid helium droplets: a uniquely cold nanomatrix for molecules and molecular complexes, *Angew. Chem. Int. Ed.*, 2004, **43,** 2622-2648.

[2] M. Barranco, R. Guardiola, S. Hernández, R. Mayol, J. Navarro and M. Pi, Helium nanodroplets: an overview, *J. Low Temp. Phys.,* 2006, **142,** 1-81.

[3] F. Ancilotto, M. Barranco, F. Coppens, J. Eloranta, N.Halberstadt, A. Hernando, D. Mateo and M. Pi, Density functional theory of doped superfluid liquid helium and nanodroplets, *Int. Rev. Phys. Chem.*, 2017, **36**, 621-707.

[4] S. Goyal, D. L. Schutt and G. Scoles, Vibrational spectroscopy of sulfur hexafluoride attached to helium clusters, *Phys. Rev. Lett.,* 1992, **69,** 933-936.

[5] M. Hartmann, R. E. Miller, J. P. Toennies and A. F. Vilesov, High-resolution molecular spectroscopy of van der Waals clusters in liquid helium droplets, *Science,* 1996, **272,** 1631-1634.

[6] A. Vilà, M. González, R. Mayol and M. Paniagua, Theoretical approach to the structure, energy and electronic spectroscopy of O@$(^4He)_N$ doped nanodroplets, *RSC Adv.,* 2014, **4,** 44972-44979.

[7] A. Slenczka, and J. P. Toennies, in *Low Temperature and Cold Molecules*, ed. I. W. M. Smith, Imperial College Press, London, 2008, pp. 345-392 and references cited therein.

[8] S. Yang and A. M. Ellis, Helium droplets: a chemistry perspective, *Chem. Soc. Rev.,* 2013, **42,** 472-484.

[9] M. Lewerenz, B. Schilling and J. P. Toennies, Successive capture and coagulation of atoms and molecules to small clusters in large liquid helium clusters, *J. Chem. Phys.*, 1995, **102**, 8191-8207.

[10] E. Lugovoj, J. P. Toennies and A. F. Vilesov, Manipulating and enhancing reactions in helium droplets, *J. Chem. Phys.,* 2000, **112,** 8217-8220.

[11] G. E. Douberly and R. E. Miller, The growth of HF polymers in helium nanodroplets: probing the barriers to ring insertion, *J. Phys. Chem. B,* 2003, **107**, 4500-4507.

[12] S. Denifl, F. Zappa, I. Mähr, F. F. da Silva, A. Aleem, A. Mauracher, M. Probst, J. Urban, P. Mach, A. Bacher, O. Echt, T. D. Märk and P. Scheier, Ion–molecule reactions in helium nanodroplets doped with C_{60} and water clusters, *Angew. Chem. Int.,* 2009, **48,** 8940-8943.

[13] S. A. Krasnokutski and F. Huisken, Ultra-low-temperature reactions of Mg atoms with O_2 molecules in helium droplets, *J. Phys. Chem. A,* 2010, **114,** 7292-7300.

[14] S. A. Krasnokutski and F. Huisken, Low-temperature chemistry in helium droplets: reactions of aluminium atoms with O_2 and H_2O, *J. Phys. Chem. A,* 2011, **115,** 7120-7126.

[15]. M. Ratschek, M. Koch and W. E. Ernst, Doping helium nanodroplets with high temperature metals: Formation of chromium clusters, *J. Chem. Phys.,* 2012, **136,** 104201.

[16] C. P. Moradi, A. M. Morrison, S. J. Klippenstein, C. F. Goldsmith and G. E. Douberly, Propargyl + O2 reaction in helium droplets: entrance channel barrier or not?, *J. Phys. Chem. A,* 2013, **117,** 13626.

[17] S. A. Krasnokutski and F. Huisken, Reactivity of iron atoms at low temperature, *J. Phys. Chem. A,* 2014, **118,** 2612-2617.

[18] S. A. Krasnokutski and F. Huisken, Ultra-low-temperature reactions of C($^3P_0$) atoms with benzene molecules in helium droplets, *J. Chem. Phys.,* 2014, **141,** 214306.

[19] G. Haberfehlner, P. Thaler, D. Knez, A. Volk, F. Hofer, W. E. Ernst and G. Kothleitner, Formation of bimetallic clusters in superfluid helium nanodroplets analysed by atomic resolution electron tomography, *Nat. Commun.*, 2015, **6**, 8779.

[20] A. Kautsch, M. Koch and W. E. Ernst, Photoinduced molecular dissociation and photoinduced recombination mediated by superfluid helium nanodroplets, *Phys. Chem. Chem. Phys.,* 2015, **17,** 12310.

[21] S. A. Krasnokutski, M. Kuhn, M. Renzler, C. Jäger, Th. Henning, and P. Scheier, Ultra-low-temperature reactions of carbon atoms with hydrogen molecules, *Astrophys. J. Lett.,* 2016, **818,** L31.

[22] S. A. Krasnokutski, M. Kuhn, A. Kaiser, A. Mauracher, M. Renzler, D. K. Bohme and P. Scheier, Building Carbon bridges on and between fullerenes in helium nanodroplets, *J. Phys. Chem. Lett.,* 2016, **7,** 1440-1445.

[23] S. A. Krasnokutski, M. Goulart, E. B. Gordon, A. Ritsch, C. Jäger, M. Rastogi, W. Salvenmoser, Low-temperature condensation of carbon, *Astrophys. J.,* 2017, **847,** 89.

24 B. Thaler, S. Ranftl, P. Heim, S. Cesnik, L. Treiber, R. Meyer, A. W. Hauser, W. E. Ernst and M. Koch, Femtosecond photoexcitation dynamics inside a quantum solvent, *Nat. Commun.,* 2018, **9,** 4006.

[25] B. Thaler, M. Meyer, P. Heim and M. Koch, Long-lived nuclear coherences inside helium nanodroplets, *arXiv*: 1907.04157 v1 [physics. chem-ph].

[26] J. Tiggesbäumker and F. Stienkemeier, *Phys. Chem. Chem. Phys.*, 2007, **9**, 4748-4770.

[27] T. Döppner, T. Diederich, S. Göde, A. Przystawik, J. Tiggesbäumker and K.-H. Meiwes-Broer, *J. Chem. Phys.*, 2007, **126**, 244513.

[28] S. Yang, A. M. Ellis, D. Spence, C. Feng, A. Boatwright, E. Latimer and C. Binns, *Nanoscale*. 2013, **5**, 11545-11553.

[29] L. F. Gomez, E. Loginov and A. F. Vilesov, *Phys. Rev. Lett.*, 2012, **108**, 155302.

[30] E. Latimer, D. Spence, C. Feng, A. Boatwright, A. M. Ellis and S. Yang, *Nano Lett.*, 2014, **14**, 2902-2906.

[31] A. Braun and M. Drabbels, Photodissociation of alkyl iodides in helium nandroplets. I. kinetic energy transfer, *J. Chem. Phys.,* 2007, **127,** 114303.

[32] A. Braun and M. Drabbels, Photodissociation of alkyl iodides in helium nanodroplets II: solvation dynamics, *J. Chem. Phys.,* 2007, **127,** 114304

[33] A. Braun and M. Drabbels, Photodissociation of alkyl iodides in helium nanodroplets III: recombination, *J. Chem. Phys.,* 2007, **127,** 114305.

[34] A. Vilà, M. González and R. Mayol, Photodissociation dynamics of homonuclear diatomic molecules in helium nanodroplets. The case of Cl_2@(^4He)$_N$, *J. Chem. Theory Comput.,* 2015, **11,** 899-906.

[35] A. Vilà, M. González and R. Mayol, Quantum interferences in the photodissociation of Cl_2(B) in superfluid helium nanodroplets (^4He)$_N$, *Phys. Chem. Chem. Phys.,* 2015, **17,** 32241-32250.

[36] A. Vilà and M. González, Mass effects in the photodissociation of homonuclear diatomic molecules in helium nanodroplets: inelastic collision and viscous flow energy exchange regimes, *Phys. Chem. Chem. Phys.,* 2016, **18,** 27630-27638.

[37] T. Takayanagi and M. Shiga, *Chem. Phys. Lett.,* 2003, **372**, 90-96.

[38] A. Vilà and M. González, Reaction dynamics inside superfluid helium nanodroplets: the formation of the Ne_2 molecule from Ne + Ne@(^4He)$_N$, *Phys. Chem. Chem. Phys.,* 2016, **18,** 31869-31880.

[39] A. Vilà, M. González and R. Mayol, Quantum dynamics of the pick up process of atoms by superfluid helium nanodroplets: The Ne + (^4He)$_{1000}$ system, *Phys. Chem. Chem. Phys.,* 2016, **18,** 2006-2014.

[40] M. Blancafort-Jorquera, A. Vilà and M. González, Quantum-classical dynamics of the capture of neon atoms by superfluid helium nanodroplets, *Phys. Chem. Chem. Phys.*, 2018, **20,** 29737-29753.

[41] A. Vilà, M. Paniagua and M. González, Vibrational energy relaxation dynamics of diatomic molecules inside superfluid helium nanodroplets. The case of the I_2 molecule, Phys. *Chem. Chem. Phys.,* 2018, **20,** 118-130.

[42] M. Blancafort-Jorquera, A. Vilà and M. González, Rotational energy relaxation quantum dynamics of a diatomic molecule in a superfluid helium nanodroplet and study of the hydrogen isotopes case, *Phys. Chem. Chem. Phys.*, revised version submitted**.**

[43] A. Vilà, M. González and R. Mayol, Relaxation dynamics of helium nanodroplets after photodissociation of a dopant homonuclear diatomic molecule. The case of Cl_2@(^4He)$_N$, *Phys. Chem. Chem. Phys.,* 2016, **18,** 2409-2416.

[44] J. Eloranta, Self-assembly of neon into a quantum gel with crystalline structure in superfluid ^4He: prediction from density functional theory, *Phys. Rev. B*: *Condens. Matter Mater. Phys.*, 2008, **77**, 134301.

[45] J. Eloranta, Solvation of atomic fluorine in bulk superfluid ^4He, *Low Temp. Phys.*, 2011, **37**, 384-386.

[46] F. Dalfovo, A. Lastri, L. Pricaupenko, S. Stringari and J. Treiner, Structural and dynamical properties of superfluid helium: A density-functional approach, *Phys. Rev. B: Condens. Matter Mater. Phys.*, 1995, **52**, 1193-1209.

[47] N. B. Brauer, S. Smolarek, E. Loginov, D. Mateo, A. Hernando, M. Pi, M. Barranco, W. J. Buma and M. Drabbles, Critical Landau velocity in helium nanodroplets, *Phys. Rev. Lett.*, 2013, **111,** 153002.

[48] D. Mateo, A. Hernando, M. Barranco, E. Loginov, M. Drabbles and M. Pi, Translational dynamics of photoexcited atoms in ^4He nanodroplets: the case of silver, *Phys. Chem. Chem. Phys.*, 2013, **15,** 18388-18400.

[49] A. Leal, D. Mateo, A. Hernando, M. Pi and M. Barranco, Capture of heliophobic atoms by ^4He nanodroplets: the case of cesium, *Phys. Chem. Chem. Phys.*, 2014, **16,** 23206-23213.

[50] F. Coppens, A. Leal, M. Barranco, N. Halberstadt and M. Pi, Head-on collisions of Xe atoms against superfluid ^4He nanodroplets, *J. Low Temp. Phys.*, 2017, **187**, 439-445.

[51] D. Mateo, F. Gonzalez and J. Eloranta, Rotational superfluidity in small helium droplets, *J. Phys. Chem. A,* 2015, **119,** 2262-2270.

[52] S. M. Cybulski and R. R. Toczylowski, Ground state potential energy curves for He_2, Ne_2, Ar_2, He-Ne, He-Ar and Ne-Ar: a coupled-cluster study. *J. Chem. Phys.*, 1999, **111,** 10520-10528.

[53] A. Ralston, in *Mathematical methods for digital computers,* ed. A. Ralston and H. S. Wilf, John Wiley and Sons, New York, 1960, vol. 1, pp. 95-109.

[54] R. J. Thompson, Improving round-off in Runge-Kutta computations with Gill's method, *Commun. ACM,* 1970, **13,** 739-740.

[55] M. Frigo and S. G. Johnson, The design and implementations of FFTW3, *IEEE. Proc.*, 2005, **93,** 216-231.

[56] A. Vibók and G. G. Balint-Kurti, Parametrisation of complex absorbing potentials for time-dependent quantum dynamics, *J. Phys. Chem.* 1992, **96,** 8712-8719.

[57] A. Przystawik, S. Göde, T. Döppner, J. Tiggesbäumker and K.-H. Meiwes-Broer, Light-induced collapse of metastable magnesium complexes formed in helium nanodroplets, *Phys. Rev. A: Atomic, Molecular, and Optical Physics*, 2008, **78**, 021202(R).

[58] S. Göde, R. Irsig, J. Tiggesbäumker and K.-H. Meiwes-Broer, Time-resolved studies on the collapse of magnesium atom foam in helium nanodroplets, *New J. Phys.*, 2013, **15**, 015026.

[59] A. Hernando, M. Barranco, R. Mayol and Martí Pi, Density functional theory of the structure of magnesium-doped helium nanodroplets, *Phys. Rev. B*: *Condens. Matter Mater. Phys.*, 2008, **78**, 184515.

5. Rotational energy relaxation quantum dynamics of a diatomic molecule in a superfluid helium nanodroplet and study of the hydrogen isotopes case

5.1. Abstract

The rotational energy relaxation (RER) of a molecule $X_2(j, m_j)$ in a ^{4}He superfluid nanodroplet [HeND or $(^4He)_N$; T=0.37 K] has been investigated using a hybrid quantum dynamics approach recently proposed by us. As far as we know, this is the first theoretical study about rotational relaxation inside HeNDs, and here several (real and hypothetical) isotopes of H_2 have been examined, in order to analyse the influence of the rotational constant B_e of these fast rotors on the dynamics. The structure of the nanodroplet practically does not change during the RER process, which approximately takes place according to a cascade mechanism $j \rightarrow j$-2; j-2 $\rightarrow j$-4; ... ; 2 $\rightarrow$ 0, and the m_j is conserved. The results are consistent with the very scarce estimated experimental data available. The lifetime of an excited rotational state (≈1.0-7.6 ns) increases when: (a) B_e increases; (b) j increases; (c) N decreases (above N=100 there is a small influence of N on the lifetime). This also applies to the global relaxation time and transition time. The analysis of the influence of the coupling between the j - j-2 rotational states (due to the X_2-helium interaction) and the X_2 angular velocity on the lifetime and related properties has been helpful to better understand the dynamics. In contrast to the RER results, for the vibrational energy relaxation (VER) in HeND when the quantum number v increases a decrease is observed in the lifetime of the excited vibrational state. This difference can be interpreted taking into account that RER and VER are associated to very different types of motion. Besides, in VER the intermediate excited states show metastability,

differing from the RER case. We hope that the present study will encourage more studies to be developed on the RER dynamics in HeND, a basic, interesting and difficult to study physical phenomenon about which we still know very little.

5.2. Introduction

The singular properties of superfluid helium nanodroplets [HeND or $(^4He)_N$; T=0.37 K] have stimulated a wide range of applications in Chemical Physics/Physical Chemistry.[1,2,3,4,5,6] Thus, they play an important role in different situations, such as, e.g., high-resolution spectroscopy, the stabilization of metastable species, and the synthesis of metal nanoparticles and nanowires. The superfluidity and the inert chemical character of helium are probably the most relevant characteristics of this quantum solvent in the present context.

Infrared (IR) spectroscopy has been widely applied to determine the influence of HeNDs in the properties of a large and varied number of species (see, e.g., refs. 7, 8, 9, 10, 11, 12, 13, 14, 15, 16, 17, 18, 19, 20, 21, 22, 23, 24, 25, 26, 27, 28, 29, 30, 31, 32, 33, 34 and 35). The quantum solvent induces small vibrational and rotational line shifts and band broadening. The interaction of the solute with the liquid helium is not strong enough to induce vibrational splitting and, therefore, for molecules in HeND the vibrational symmetry is not modified with respect to the gas phase (more details on the molecular vibrational dynamics in HeNDs can be found in ref. 36 and in the refs. cited therein). All the experiments indicated above have been performed in the frequency domain, i.e., they are not resolved in time.

Regarding the molecular rotation dynamics in HeNDs, which constitutes the main issue of the present contribution, effective moment of inertia, centrifugal distortion constant and estimates of the rotational relaxation time have been reported,[4,7,8,9,10,11,12,13,14,15,16,17,18,19,20,21,22,23,24,25,26,27,28,29,30,31,32,33,34,35] with nearly all of these contributions being of experimental type (IR spectroscopy and a few of them considering the pure rotational spectrum[14,24] and both the vibrational and pure rotational spectra[30]). These properties depend significantly on the rotational constant of the molecules and two limit dynamical behaviours have been identified: adiabatic

following (heavy rotors) and non-following (light rotors) regimes; where in the last case the movement of the rotor is too fast for the helium to be able to follow it.

The relaxation times of excited rotational states have only been experimentally estimated, based on the comparative analysis of the line widths corresponding to a small number of transitions and assuming the validity of applying the energy-time uncertainty relation ($\Delta E\,\Delta t \geq \hbar/2$), as if it were a strict identity. Besides, in the rotational dynamics context mention should also be made of the research carried out on molecular alignment through the use of intense/moderately intense non-resonant lasers.[37,38,39] In what respects to ordinary (non-quantum) liquids, the experimental information available on the molecular rotational dynamics is also very limited, even though in this case there are a few direct measurements available (cf. Section 5.4.1).

The theoretical efforts addressed to investigate effective moments of inertia and, in some cases, centrifugal distortion constants have been based on the correlated basis functions-diffusion Monte Carlo (CBF/DMC) method[10,15,24] and on the diffusion and path integral Monte Carlo method.[40] Besides, for the rotational alignment analysis the path integral Monte Carlo (PIMC) and the angulon theory methods have been employed.[38]

Here, we report the first theoretical study of the rotational energy relaxation (RER) of a molecule embedded in a superfluid ^{4}He nanodroplet, to the best of our knowledge. To carry out this work, we have used a hybrid quantum dynamics approach recently proposed by us[36,41] and, as initial application, we have examined the RER of several isotopes of the H_2 molecule. These real-time quantum dynamics simulations have been feasible only recently, thanks to the use of the time dependent density functional theory (TDDFT) for the description of superfluid liquid helium (the X_2 molecule has been described using an ordinary quantum wave function). An analogous/related strategy has been recently employed by our group to investigate the dynamics of other relevant physico-chemical processes involving HeNDs (photodissociation of diatomics,[41,42,43,] atom capture,[44,45] dimerization reaction,[46] nanodroplet relaxation,[47] and vibrational energy relaxation of diatomics[36]).

The paper is organized as follows. The hybrid theoretical quantum dynamics approach employed is described in Section 5.3. The most important results obtained for several isotopes of H_2 and initial rotational excitations are reported and discussed in

Section 5.4, and the summary and conclusions are given in Section 5.5. Finally, some additional information can be found in Section 0 and 5.7.

5.3. Theoretical methods

Before describing in detail, the theoretical method used for the study of rotational relaxation, it is convenient to make some considerations of fundamental character. Given the complexity of the problem under analysis, a mean field approach has been applied. So, we have the wave function of helium and the wave function of the molecule, and the quantum evolutions of both are coupled through the expected value of the X_2-helium interaction potential energy. That is, in this framework we are not taking into account the quantum correlation between the liquid and the rotor. A related approach to the one we apply here was employed to study the solvation of an electron in superfluid helium,[48] which is a more favourable situation due to the large mass difference between the electron and the He atom (besides, some correlation was included in the electron-helium pseudopotential used).

To describe the quantum correlation, the wave function of the system should be expressed simultaneously in terms of the helium and molecule coordinates, rather than as the product of two functions, one that depends on helium and the other on the molecule. However, the problem posed in this rigorous way is very difficult to solve. An additional difficulty arises from the use of a DFT description (operators are non-linear) for a part of the system (helium) and an ordinary quantum mechanics treatment for the other part (molecule), which makes generally not possible to account for quantum correlation (and DFT is the only currently available description for superfluid helium in dynamics studies).

Notwithstanding the previous remarks, there are two important aspects to keep in mind that are specific of the selected systems: (a) the H_2 molecule and isotopic variants are the fastest molecular rotors and due to this they will move at much higher velocities than liquid helium (except, of course, when the molecules are close to finish the relaxation to the ground rotational state); (b) the H_2-helium interaction is particularly weak compared to the interaction of other molecules with helium. Based on these facts, we believe that, although the quantum correlation is not described, the theoretical

approach proposed here is reasonable. At least as starting point for the study of the complex problem of the rotational relaxation dynamics in superfluid helium nanodroplets.

The rotational relaxation of a homonuclear diatomic molecule, X_2, in a HeND has been investigated using a hybrid theoretical approach proposed by our group[36,41] (see below). In this first study the selected molecules are several, real or hypothetical, isotopes of hydrogen in the electronic ground state: D_2, T_2, Qa_2, Qi_2 or Sx_2; where the last three molecules are hypothetical species with rotational constant (B_e) equal to 1/4, 1/5 and 1/6 of $B_e(H_2)$, respectively. We have proceeded in this way in order to analyse the effect of the rotational constant (i.e., the effect of the mass) on the relaxation dynamics. Although some results have been provided on the H_2 rotational relaxation, the practical difficulties to simulate this relaxation (which is even slower than that of D_2) has made it impossible for us to carry out its study.

The initial conditions of the dynamics are represented by the helium density of the $X_2(j=0,\ m_j=0)@(^4He)_N$ ground state doped nanodroplet, but with a sudden change of the rotational wave function of X_2 to a particular (j, m_j) excited rotational state, obtained using, e.g., Raman techniques. The rotational excitation and global relaxation processes, that happens through the evaporation of some helium atoms of the nanodroplet, can be represented as

$$X_2\left(j=0,m_j=0\right)@(^4He)_N\ +\ h\nu\ \rightarrow\ \left[X_2\left(j,m_j=0\right)@(^4He)_N\right]^*+h\nu' \tag{5.1}$$

$$\left[X_2\left(j,m_j=0\right)@(^4He)_N\right]^*\rightarrow\ \left[X_2\left(j=0,m_j=0\right)@(^4He)_{N'}\right]^*\ +\ (N-N')^4He \tag{5.2}$$

$$\left[X_2\left(j=0,m_j=0\right)@(^4He)_{N'}\right]^*\rightarrow\left[X_2\left(j=0,m_j=0\right)@(^4He)_{N''}\right]+(N'-N'')^4He \tag{5.3}$$

, where the * symbol indicates that we are considering an excited system, and eqns (5.2) and (5.3) show that the time required for the X_2 rotational relaxation does not necessarily have to match with the liquid helium relaxation time (even though for the systems and initial conditions selected the liquid helium is essentially relaxed shortly after the X_2 rotational relaxation has taken place). According to the selection rules for pure rotational excitations (rotational Raman), due to the nuclear symmetry

(homonuclear diatomic molecules) the resulting state will have $\Delta j = \pm 2$ ($+2$ in the present case) and $\Delta m_j = 0$ with respect to the initial state.

Owing to the low temperature of the nanodroplets ($T = 0.37$ K), only the rotational ground state of these molecules is populated. This is in contrast to what happens for other molecules such as, e.g., F_2, Cl_2, Br_2 or I_2, which have very small rotational constants and stronger interaction with helium; and due to this their rotational ground states in HeND have contributions of higher (j, m_j) rotational states of the free diatomic molecule (See Section 0). Hence, these cases are significantly more difficult to describe theoretically than the systems selected here to carry out the first investigation on RER in HeNDs.

In this initial study, in order to avoid additional difficulties, we have described the X_2 molecule as a rigid rotor, i.e., the vibrational degree of freedom has not been taken into account, and the X_2 centre of mass (CM) has been fixed in the origin of coordinates (centre of the doped nanodroplet). Due to the strength of the molecule-helium interaction in comparison to the helium-helium interaction, the optimization of the $X_2(j = 0, m_j = 0)@(^4He)_N$ nanodroplet leads the diatomics to the center of the nanodroplet in the equilibrium configuration.

The description of the X_2 CM motion would involve the inclusion of additional and very significant computational difficulties, as three more coordinates should be taken into account. However, here we have considered a reasonable approximation to assume that the X_2 CM is fixed, due to the following reasons: (a) the liquid helium structure around the X_2 molecule shows spherical symmetry in the equilibrium configuration (cf. Section 5.4); (b) the liquid helium structure during the I_2 vibrational relaxation practically does not change after the initial excitations and subsequent relaxations;[36] which suggests that in the "softer" conditions associated to the rotational relaxations to be studied an analogous situation would probably occur (in addition, the H_2-$(^4He)_{100}$ interaction energy is about seven times less intense than the I_2-$(^4He)_{100}$ one). The structure of the nanodroplet in fact remains essentially unchanged during the rotational relaxation, as it will be confirmed in Section 5.4.

The RER dynamics has been studied using a 'divide and conquer' hybrid approach. The real-time quantum dynamics simulations have been performed combining a

commonly used method to describe rather large bosonic systems as superfluid ^{4}He (time dependent density functional theory)[36,41,42,43,44,45,46,47,49,50,51,52] and a usual quantum method to account for atoms/molecules in gas phase (time dependent wave function) has been applied to describe the X_2 molecule,[36,41,42,43,44,46] including only the rotational degrees of freedom.

The Orsay Trento (OT) phenomenological density functional[53] has been used in the TDDFT calculations, and the non-local contribution to the helium correlation energy and back-flow terms have been neglected for computational reasons, as usual.[36,41,42,43,44,45,46,47,49,50,51,52] This strategy allows us dealing with relatively large nanodroplets if needed, so that comparison with experimental results is possible, while keeping a reasonable computational time.

Nowadays, the dynamics study of physico-chemical processes involving HeNDs is only attainable if the superfluid liquid helium is treated by means of the DFT approach; and the OT density functional is the best available one and has been employed in almost all dynamics studies involving superfluid liquid helium. Moreover, when necessary, a modification can be added to the OT density functional to avoid unphysical helium densities that may occur when the interaction between the dopant molecule and helium is strong (e.g., in the case of the interaction of an halogen molecule with helium),[36,41] a situation that does not correspond to the present case.[54]

The equations of motion for the different degrees of freedom are found by minimising the quantum action ($\mathcal{A}$):

$$\mathcal{A}\left[\Psi_{He}, \varphi_{X_2}\right] = \int dt \left\{ E\left[\Psi_{He}, \varphi_{X_2}\right] - i\hbar \int d\boldsymbol{R}_{He} \Psi^*_{He}(\boldsymbol{R}_{He}) \frac{\partial}{\partial t} \Psi_{He}(\boldsymbol{R}_{He}) \right.$$
$$\left. - i\hbar \int sin\theta \; d\theta \; d\phi \; \varphi^*_{X_2}(\theta, \phi) \frac{\partial}{\partial t} \varphi_{X_2}(\theta, \phi) \right\} \tag{5.4}$$

, where $\Psi_{He}(\boldsymbol{R}_{He}, t)$ is the complex effective wave function describing the liquid helium [$\Psi_{He}(\boldsymbol{R}_{He}, t) = \rho^{\frac{1}{2}}_{He}(\boldsymbol{R}_{He}, t) \exp(-i\,\Theta(\boldsymbol{R}_{He}, t)\; t)$, i. e., $|\Psi_{He}(\boldsymbol{R}_{He}, t)|^2 = \rho_{He}(\boldsymbol{R}_{He}, t)$], which satisfies the normalization condition $\int d\boldsymbol{R}_{He} |\Psi_{He}(\boldsymbol{R}_{He}, t)|^2 = N$, $\varphi_{X_2}(\theta, \phi)$ is the rotational wave function of the molecule, and E is the total energy of the system, which is given by

$$E[\Psi_{He},\varphi_{X_2}] = \frac{\hbar^2}{2m_{He}}\int d\boldsymbol{R}_{He}|\boldsymbol{\nabla}\Psi_{He}(\boldsymbol{R}_{He})|^2 + \int d\boldsymbol{R}_{He}\varepsilon_c[\rho_{He}]$$
$$+ \int d\boldsymbol{R}_{He}\int sin\theta\, d\theta\, d\phi\, V_{He-X_2}(\theta,\phi,\boldsymbol{R}_{He})\,\rho_{He}(\boldsymbol{R}_{He})\,|\varphi_{X_2}(\theta,\phi)|^2$$
$$-\frac{\hbar^2}{2\mu_{X_2}r_{eq,X_2}^2}\int sin\theta\, d\theta\, d\phi\, \varphi_{X_2}^*(\theta,\phi)[\frac{1}{sin\theta}\frac{\partial}{\partial\theta}(sin\theta\frac{\partial}{\partial\theta})$$
$$+\frac{1}{sin^2\theta}\frac{\partial^2}{\partial\phi^2}]\varphi_{X_2}(\theta,\phi) \qquad (5.5)$$

, where μ_{X_2} and $r_{eq,X2}$ are the reduced mass and equilibrium distance of the molecule, respectively, and $\varepsilon_c[\rho_{He}]$ corresponds to the potential energy and correlation energy densities of superfluid liquid helium. $V_{He-X_2}(\theta,\phi,\boldsymbol{R}_{He})$ stands for the interaction potential energy between helium and the diatomic molecule, which has been taken from ref. [55] and is based on high level *ab initio* calculations.

The quantum action described above is minimised by taking variations with respect to each one of the wave functions. This leads to two coupled time dependent Schrödinger-like nonlinear equations governing the evolution of helium and the molecule, respectively:

$$i\hbar\frac{\partial}{\partial t}\Psi_{He}(\boldsymbol{R_{He}}) = \left[-\frac{\hbar^2}{2m_{He}}\boldsymbol{\nabla}^2 + \int \sin\theta\, d\theta\, d\phi\, V_{He-X_2}(\theta,\phi,\boldsymbol{R_{He}})\,\left|\varphi_{X_2}(\theta,\phi)\right|^2\right.$$
$$\left. + \frac{\delta\varepsilon_c[\rho_{He}]}{\delta\rho_{He}}\right]\Psi_{He}(\boldsymbol{R}_{He}) \qquad (5.6)$$

$$i\hbar\frac{\partial}{\partial t}\varphi_{X_2}(\theta,\phi) = \left[-\frac{\hbar^2}{2\mu_{X_2}r_{eq,X_2}^2}\left[\frac{1}{sin\theta}\frac{\partial}{\partial\theta}\left(sin\theta\frac{\partial}{\partial\theta}\right)+\frac{1}{sin^2\theta}\frac{\partial^2}{\partial\phi^2}\right]\right.$$
$$\left. + \int d\boldsymbol{R}_{He}V_{He-X_2}(\theta,\phi,\boldsymbol{R}_{He})\rho(\boldsymbol{R_{He}})\right]\varphi_{X_2}(\theta,\phi) \qquad (5.7)$$

These equations are analogous to those reported in the photodissociation of Cl_2(B←X) in HeND,[41,42,43] but in the present case they involve the two angular degrees of freedom instead of the X-X relative distance. In addition, equations (5.6) and (5.7) have been transformed following an analogous strategy as in ref. 36 (vibrational relaxation of I_2), which is more efficient to account for the dynamics when only energy transfer

processes are involved. Thus, the rotational wave function has been expressed in terms of the rotational eigenfunctions basis set $\left\{\varphi_{j,m_j}(\theta,\phi)\right\}$ of the rotational Hamiltonian operator corresponding to the isolated molecule (i.e., without including the interaction of X_2 with the helium environment). These eigenfunctions are the spherical harmonics, $\left\{Y_{j,m_j}(\theta,\phi)\right\}$, and hence we have expressed $\varphi_{X_2}(\theta,\phi)$ as

$$\varphi_{X_2}(\theta,\phi)=\sum_{j,m_j} c_{j,m_j} Y_{j,m_j}(\theta,\phi) \tag{5.8}$$

Equation (5.7) can now be transformed into the differential equation (5.9), which can be solved more efficiently in terms of numerical accuracy and computational time. According to this, the equations of motion that have been used are the following:

$$i\hbar\frac{\partial}{\partial t}\Psi_{He}(\boldsymbol{R}_{He})=\left[-\frac{\hbar^2}{2m_{He}}\boldsymbol{\nabla}^2+\sum_{i,m_i,j,m_j} c^*_{i,m_i}(t)c_{j,m_j}(t)V_{i,m_i,j,m_j}(\boldsymbol{R}_{He})\right.$$
$$\left.+\frac{\delta\varepsilon_c[\rho_{He}]}{\delta\rho_{He}}\right]\Psi_{He}(\boldsymbol{R}_{He}) \tag{5.9}$$

$$i\hbar\frac{dc_{i,m_i}(t)}{dt}=E_{rot,i,m_i}c_{i,m_i}(t)+\sum_{j,m_j} c_{j,m_j}(t)V_{i,m_i,j,m_j}$$

$$i=0,1,2,\dots n \qquad m_i=-i,\dots,0,\dots,i \tag{5.10}$$

, where $\left\{E_{rot,i,m_i}\right\}$ are the associated rotational eigenvalues of the free molecule, and the helium coordinate-dependent, $V_{i,m_i,j,m_j}(\boldsymbol{R}_{He})$, and the ordinary, V_{i,m_i,j,m_j}, potential energy matrix elements are given by

$$V_{i,m_i,j,m_j}(\boldsymbol{R}_{He})\equiv\int sin\theta\ d\theta\ d\phi\ \ V_{He-X_2}(\theta,\phi,\boldsymbol{R}_{He})\ \ Y^*_{i,m_i}(\theta,\phi)\,Y_{j,m_j}(\theta,\phi) \tag{5.11}$$

$$V_{i,m_i,j,m_j}\equiv\int sin\theta\ d\theta\ d\phi\ d\boldsymbol{R}_{He}V_{He-X_2}(\theta,\phi,\boldsymbol{R}_{He})\rho_{He}(\boldsymbol{R}_{He})\ \ Y^*_{i,m_i}(\theta,\phi)\,Y_{j,m_j}(\theta,\phi) \tag{5.12}$$

Several static and dynamic calculations have been performed in order to select the number of functions included in the basis set. For the selected systems, it has been found

that for an initial excited rotational state ($j_0, m_{j,0} = 0$), produced from the excitation of the ($j = 0, m_j = 0$) ground state, only states with even Δj and $m_j = 0$ are needed. For a given initial excited state ($j_0, m_{j,0} = 0$), in order to converge the time propagation of equations (5.9) and (5.10) it is enough to include in the calculations the rotational states with even Δj and $m_j = 0$ from ($j_0, m_j = 0$) to ($j = j_0 + 6\,, m_j = 0$). That is, only up to three basis functions above the initial rotational exited state have been needed, as it was also observed in ref. 36 for the vibrational relaxation of I_2.

The initial time ground state of the doped nanodroplet has been obtained (static calculation) by finding the lowest energy solution of equations (5.9) and (5.10). To do this, we have followed an analogous strategy as for the time evolution (dynamic calculations; see below), but employing the imaginary time step propagation method, varying simultaneously the helium density and the molecular wave function, while keeping the number of the He atoms of the nanodroplet constant (see, e.g., ref. 41). The resulting rotational wave function is constituted by the (j, m_j) state (0,0), with negligible contributions of the (2,0), (4,0), (6,0), … rotational states (populations below/much below 10^{-6}). This result probably mainly arises from both the large energy separation between the rotational states and the rather small molecule-helium interaction potential energy.

The time evolution of the helium effective wave function (Eq. (5.9)) has been calculated numerically by discretising the space in a grid of points and the kinetic energy terms have been determined using the fast Fourier transform (FFTW package).[56] A fourth order predictor-corrector method,[57] initiated by a fourth order Runge-Kutta method,[58] has been used for the numerical propagation and the time step is equal to 1.5 10^{-3} ps.

The Cartesian grid has a spacing of 0.40 Å for all axis and each one of them has a total length of 38.0 Å. Besides, in order to avoid artificial reflections, a quartic negative imaginary potential (NIP)[59] has been placed at the edges of the Cartesian grid, so as to absorb the helium wave function fragments located outside the nanodroplet arising from evaporation of some helium atoms. The NIP is given by the following expression:

$$V_{\mathrm{NIP}} = -iA\frac{5}{2}\left(\frac{d - d_{\mathrm{NIP}}}{L}\right)^4 \tag{5.13}$$

The absorption strength (A) is equal to 331.0 K Å^{-4}, the length (L) has a value of 1.0 Å, and this potential has been placed at a distance (d_{NIP}) of 1.0 Å before the limit of the grid.

For the numerical time propagation of equation (5.10) the basis set functions have been discretised, using an angular grid of 50 points between 0 to π for the angle θ and of 100 points between 0 to 2π for the angle ϕ. Then, to propagate in time, the following steps, which are analogous to those of ref. 36, have been followed:

1) At a given time t, the matrix representation of the full effective rotational Hamiltonian of X_2 (equation (5.7)), H_{Rot}, that is expressed in terms of $\{|i, m_i\rangle\}$, is diagonalized, obtaining H_α.
2) In the new rotational basis set $\{|\alpha\rangle\}$ just determined the time evolution ($t \rightarrow t + \delta t$) of the coefficients $\{c_\alpha\}$ of the X_2 rotational vector state is easy to obtain, as we are considering stationary states: $c_\alpha(t + \delta t) = c_\alpha(t)e^{-E_\alpha \delta t/\hbar}$.
3) The $c_{i,m_i}(t + \delta t)$ coefficients are now calculated from the $c_\alpha(t + \delta t)$ ones coming back to the reference basis set $\{|i, m_i\rangle\}$.
4) Steps (1)-(2)-(3) are repeated for the time evolution $t + \delta t \rightarrow t + 2\delta t$ and so on for the following times, until the propagation is completed.

The Hamiltonian matrix has been diagonalized using the Jacobi method as it is a real and symmetric matrix. This procedure is faster and much more numerically stable than the usual method applied to solve equation (5.10)[41,42,43] (the error only comes from the diagonalization and round-off numerical computer errors). This computational strategy has been essential to make the present study possible, as the rotational relaxation processes can be particularly slow in superfluid liquid helium nanodroplets.

5.4. Results and discussion

The rotational energy relaxation of several isotopes of hydrogen (D_2, T_2, Qa_2, Qi_2 and Sx_2) embedded in a superfluid helium nanodroplet of one hundred ^{4}He atoms has

been investigated, considering a sudden excitation of the molecule from the rotational ground state (j=0, m_j=0) up to a given rotational excited state (even j, m_j=0).

The selection of a small helium nanodroplet, $(^4He)_{100}$, is based on computational reasons, as in the case of the theoretical study of the vibrational relaxation.[36] Rotational relaxation processes imply long time scales, so a large number of propagation steps is needed to solve the equations of motion and complete the simulations. Moreover, as this relaxation process is expected to involve mainly the interaction between the molecule and the first and second helium solvation shells, the selected size of the nanodroplet seems reasonable (this will be confirmed in Section 5.4.3). The radial helium density of the $H_2(j=0, m_j=0)@(^4He)_{100}$ ground state doped nanodroplet is shown in Figure 5.1 and is identical for all the isotopes.

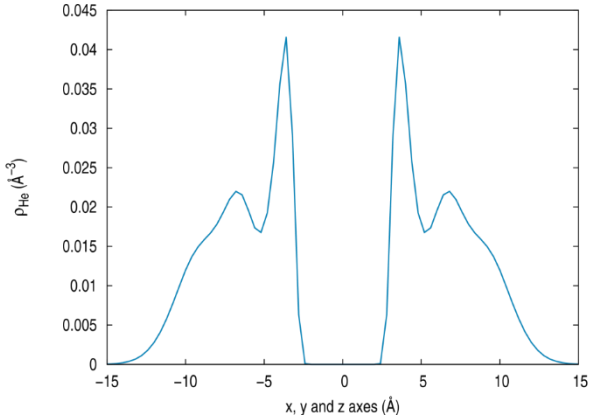

Figure 5.1 Helium radial density of the $H_2(j=0, m_j=0)@(^4He)_{100}$ ground state nanodroplet along the x, y and z-axes.

5.4.1. Rotational relaxation of $X_2(j=2, m_j=0)$ *vs.* rotational constant

The time evolution of the (j=2, m_j=0) and (j=0, m_j=0) state populations for the five selected molecules is shown in Figure 5.2. Besides, the essentially negligible (j=0, mj=0) H_2 population is also given for illustrative purposes, showing that relaxation from (j=2, m_j=0) is particularly slow for this isotope (only a population of the order of 10^{-7} has been obtained for the rotational ground state, after 7 ns of simulation). This fact has made us to focus in this work on the D_2, T_2, Qa_2, Qi_2 and Sx_2 species. From these results it comes out that the (j=2, m_j=0) state is metastable in these systems, because relaxation takes quite a lot of time.

The state populations can be successfully modelled using the sigmoid function. Thus, the (j=0, m_j=0) population *vs*. time has been taken as equal to $1/\{1+\exp[-k(t-t_0)]\}$, where k and t_0 are constants that depend on the system [k is related to the coupling between the two involved states and t_0 is the time for which the (j=0, m_j=0) population is 0.5] (Figure s5.5). This equation was recently obtained by us modeling the vibrational relaxation in HeNDs using a Hermitian non-linear two-state Hamiltonian operator.[36]

The values of the global relaxation times, lifetimes and transition times of the (j=2, m_j=0) excited state are gathered in Table 5.1 and plotted in Figure 5.3. The global relaxation time has been taken from $t = 0$ to the time corresponding to a population of this state equal to 0.01. The lifetime is defined from $t = 0$ to the time corresponding to a population of 0.5 of the same state. The transition time is defined as the time it takes for the population of this state to decay from 0.99 to 0.01.

These three properties are of the order of the nanosecond and they increase in a significant way with the rotational constant B_e (i.e., when the mass decreases), which leads to an increase of the energy gap between the rotational states (Table 5.1). Thus, for (j=2, mj=0) the global relaxation times, lifetimes and transition times are in the 1.32-5.33 ns, 1.01-4.17 ns and 0.64-2.36 ns intervals, respectively. Moreover, if we take as a reference, e.g., the values of the Sx_2 properties, for each isotopic variant the three properties, expressed in relative terms, take quite similar values (around 1.0, 1.2, 1.7 and 3.9 for Qi_2, Qa_2, T_2, and D_2, respectively).

Figure 5.3 shows the global relaxation times, lifetimes and transition times for (j=2, m_j=0) and the fitting curves (quadratic polynomials) to which the results have been satisfactory described. By extrapolation according to these curves, for H_2(j=2, m_j=0) in HeND these properties are estimated to be ≈26.3, ≈20.8, and ≈ 10.1 ns, respectively (Table 5.1). The interpretation of these results will be given at the end of this section, after consideration of other properties of the system.

Unfortunately, there is no previous information available on the rotational lifetimes of the molecules studied here to compare with, but there are some estimated experimental data on HF(j=1)[7] and HCl(j=1)[8] in HeNDs (lifetimes ≥12 and ≥5.3 ps, respectively). Because of this, we have carried out a model calculation on the relaxation

of T_2(j=2, m_j=0) considering the H_2-He interaction potential energy multiplied by a factor equal to 3.597, in order to make it more similar to the HF-He one [V_{min}(HF-He)[60]/V_{min}(H_2-He)[55]=3.597].[61,62] The T_2 molecule was selected as it has a rotational constant (20.3350 cm^{-1}) that is similar to that for HF (20.9557 cm^{-1}).[63] The calculated lifetime of T_2(j=2, m_j=0) obtained using this model (3.597 V(H_2-He)) led to a lifetime estimate of ~120 ps (while the value obtained using the real V(H_2-He) potential energy was 1785 ps). Moreover, if we had also taken into account that the anisotropy of V(HF-He) is larger than that for V(H_2-He) an even lower lifetime value would be expected for HF in a HeND. Thus, this model calculation suggests that the theoretical approach employed here is reasonable, at least as initial step, to describe the rotational energy relaxation of molecules in HeNDs.

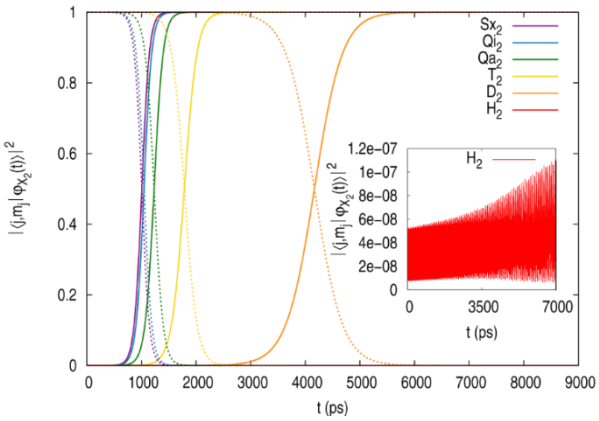

Figure 5.2 Populations of the (j=0, m_j=0) (solid lines) and (j=2, m_j=0) (dashed lines) rotational states of the molecules, as a function of time.

Table 5.1 Global relaxation times, lifetimes, and transition times of the (j=2, m_j=0) rotational state for all molecules.

	B_e[a] (cm^{-1})	Global relax. time (ps)	Lifetime (ps)	Transition time (ps)
Sx_2	10.1422	1321	1008	636
Qi_2	12.1706	1371	1047	656
Qa_2	15.2133	1606	1233	757
T_2	20.3350	2311	1785	1063
D_2	30.4436	5329	4167	2357
H_2	60.8530	26335[b]	20755[b]	10138[b]

[a] The experimental values from ref. [63] have been used.
[b] Extrapolated values from a quadratic polynomial fitting.

The experimental data on molecular rotational dynamics is also very limited in the case of ordinary liquids, although a few direct measurements have been reported in this

context,[64,65,66,67,68,69] with some of these studies including molecular dynamics (MD) simulations. Theoretical information has been reported on the rotational relaxation of H_2 and D_2 in supercritical liquid Ar[70,71] and in near critical liquid CO_2,[66] and also on the relaxation of other systems (e.g., CN in liquid Ar[72]). In the former case ($Ar_{(l)}$ at 299.5 K) the lifetime of the j=2 state in the relaxation to j=0 is about 3.6 and 2.0 ps for H_2 and D_2,[70] respectively (perturbation theory results evaluated by MD simulations). In the second case ($CO_{2(l)}$ at 308 K) a substantially larger lifetime (somewhat above 34 ps) can be estimated from the MD simulation results for D_2.[66] This last result is about 17 times larger than when D_2 is in supercritical liquid Ar, which probably arises from the diverse nature of the solvents [the D_2-Ar and D_2-CO_2 interactions have different strength and anisotropy; see also refs. [73] and [74] (V_{min} = -56.5 and -211.932 cm^{-1}, respectively)] and their different number densities (40.0 M vs. 8.5 M for $Ar_{(l)}$ and $CO_{2(l)}$, respectively; in both cases very far from an infinite dilution solution).

These situations are, of course, very different from the D_2 molecule embedded in a HeND, where the interaction of the molecule with the solvent is much weaker than in the case of the ordinary liquids which, in addition, are at much higher temperature (additionally, the D_2 molecule in the nanodroplet cannot interact with other species of the same type). Hence, it is reasonable to obtain much larger rotational lifetimes using as solvent superfluid helium than when using ordinary liquids, as we have obtained here.

Regarding the molecular state after relaxation, it is essentially identical to $|j = 0, m_j = 0\rangle$, as the populations of the other states are clearly below 10^{-6}. This means that the helium environment does not significantly affect the rotational structure of the X_2 molecule, as we have already observed in the calculation of the ground state of the doped nanodroplet. This is probably due to the important rotational energy differences and the weak $H_2 - (^4He)_{100}$ vdW interaction potential energy (≈-100 K).

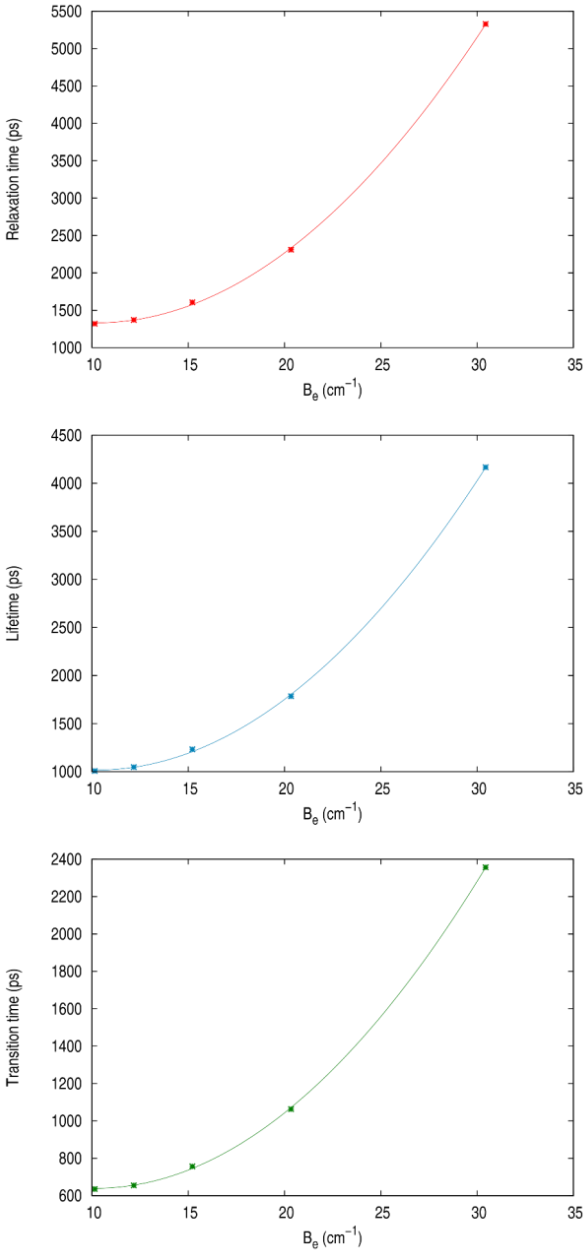

Figure 5.3 Global relaxation times (top), lifetimes (middle) and transition times (bottom) of the (j=2, m_j=0) state, as a function of the rotational constant of the molecules, from the lower (Sx_2) to the higher (D_2) B_e values.

The expected value of $\cos^2\theta$ *vs.* time varies with the composition of the wave function, as it is shown in Figure 5.4. At the initial times of the simulations $\langle\cos^2\theta\rangle$ remains essentially constant (0.522) and oscillates with a significant amplitude during the transition (between ≈0.10 and ≈0.75). Once the transition to the ($j = 0$, $m_j = 0$) state has been completed, $\langle\cos^2\theta\rangle$ finally reaches a value of 0.333. Moreover, the expected value of $\cos^2\phi$ is constant and equal to ½ for all rotational states, and the expected value of the $\hat{j}^2$ operator vs. time varies in a smooth way from $6\hbar^2$ to $0\hbar^2$,

values that correspond to the ($j = 2$, $m_j = 0$) and ($j = 0$, $m_j = 0$) states, respectively (Figure s5.6).

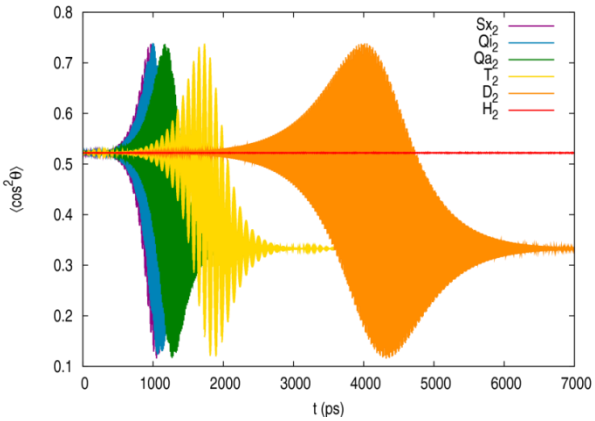

Figure 5.4 Expected value of $\cos^2\theta$ for the (j=0, m_j=0)←(j=2, m_j=0) relaxation of the molecules *vs.* time.

The total energy of the system (X_2@HeND) decreases when relaxation is taking place, and this decrease is larger when the B_e value increases (i.e., for the lighter isotopes), finally obtaining the same total energy for all the molecules (Figure 5.5). This means that the bigger rotational constant B_e the more energy the single evaporated ^{4}He atom carries with it (the important amount of energy released by the atom will be analysed in more detail later). Unlike the other cases, for the H_2 molecule the excited doped nanodroplet has positive energy, due to the large value of the j=2-j=0 energy separation.

The relaxation of the liquid helium (which takes place thanks to the evaporation of some He atoms) needs a time that is basically coincident with that of the rotational relaxation. Thus, comparison of the X_2@HeND energy at the global relaxation time with the corresponding ground state (i.e., fully relaxed) value reveals differences of 0.03, 0.01, 0.08, 0.19 and 0.45% for Sx_2, Qi_2, Qa_2, T_2 and D_2, respectively. Since the main priority of this study has been to investigate the rotational relaxation and for computational reasons, we have stopped the calculations some time after verifying that the rotational relaxation has been completed.

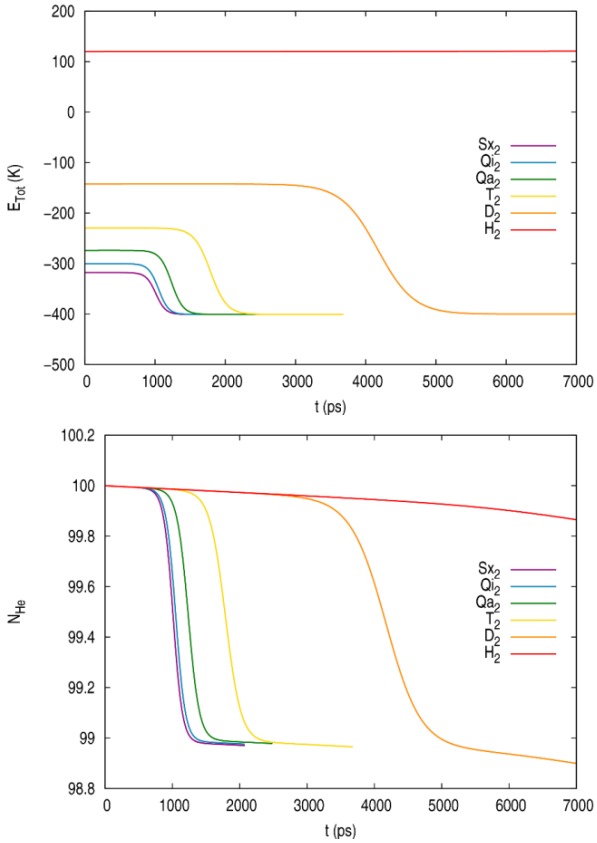

Figure 5.5 X_2@HeND total energy (top) and number of ^{4}He atoms of the HeND (bottom) for the (j=2, m_j=0) rotational relaxation of the molecules *vs*. time.

Rotational relaxation mainly arises from the interaction of the molecule with the He atoms of the first and second solvation layers (cf. Section 5.4.3) and other properties of interest during the molecular relaxation are the next ones: (a) the rotational energies of the molecules evolve in an analogous way and according to the (j=2, m_j=0)-(j=0, m_j=0) energy gap (87.55-262.81 K range from Sx_2 to D_2, respectively), following the evolution of the populations; (b) the energy of helium in the nanodroplet increases ≈4.7 K [this value is similar to the increase of helium energy observed in the vibrational relaxation of I_2 in HeND[36] (≈4.4 K for each ^{4}He atom evaporation; ΔE_{vib}=308.621 K, i.e., of the same order of magnitude as the present rotational energy differences)]; (c) the X_2-HeND interaction potential energy depends very little on the molecule, as it is essentially constant (global change of ΔE_{int}≈-0.07 K); (d) the structure of the nanodroplet does not change appreciably.

The nanodroplet structure has been characterized in terms of the helium density, which remains practically constant and preserves the initial spherical symmetry; cf.

Figures s3 and s4, where the T_2(j=2, m_j=0) relaxation is presented as an illustrative example. Since for all the excited rotational states m_j is equal to zero, there is a higher probability of finding the molecular axis located in the vicinity of the z axis. Then, one would expect a certain ellipsoidal deformation of the nanodroplet before the relaxation to the ground rotational state, but this is not the case as indicated above. This is probably consequence of the superfluid helium nature and the weakness of the molecule-helium interaction.

It should be noted that in all cases, as a result of the model used to describe the superfluid helium (continuous character of the density functional approach), a very small amount of helium is evaporated before the molecular relaxation takes place (Figure 5.5). This arises from very small changes suffered by the liquid due to the initial sudden excitation of the molecule. As an example, in the case of the excited H_2, during the 7000 ps time interval investigated, a total of 0.13 He atoms are evaporated.

Furthermore, from the calculations it comes out that superfluid liquid helium efficiently releases its excess of energy resulting from the rotational relaxation process, as it is expected for a superfluid. However, the number of evaporated He atoms (a single atom in all cases) is smaller than the ratio between the energy to be released (ΔE_{Tot}) and the binding energy of a He atom in the nanodroplet (7.2 K).[75] Thus, ratio values of 12.2, 14.6, 18.2, 24.4, 36.5 have been obtained for Sx_2, Qi_2, Qa_2, T_2 and D_2, respectively; taking into account that, according to the experiments, [75] the evaporated atoms carry a negligible amount of translational kinetic energy (as it is close to the thermal value at T=0.37 K). The excitation energy essentially serves to break the vdW bonds between the He atoms that will be evaporated and the nanodroplet, and this will lead to the stabilization of the system.

This discrepancy has already been reported for other physico-chemical problems, such as, e.g., the vibrational energy relaxation of I_2 (ref. 36) and the formation of Ne_2 (ref. 46) inside a HeND, employing an analogous theoretical approach. This probably results from the continuous character of the DFT method used to account for the superfluid liquid helium, as it can allow liquid helium departing from the nanodroplet with excess of energy. Then, the transformation of the amount of liquid helium evaporated into discrete He atoms would yield a smaller number of evaporated atoms.

In spite of this difference, it should be highlighted that in the present study the interaction between the molecule and the liquid helium has been described using the best H_2-He intermolecular potential energy available, the superfluid character of helium has been taken into account employing the best density functional available and, as we will see in Section 5.4.3, the two first helium solvation shells are clearly the main ones involved in the relaxation process. Based on these facts and the comparisons previously reported, we believe that the results obtained here are reasonable.

To interpret the relaxation times results, the coupling term between the (j=2, m_j=0) and (j=0, m_j=0) states (cf. equations (5.11) and (5.12)) has been analysed, since it is expected to influence the transition probability in an important way (more exactly, we have examined the coupling squared terms, V_{ij}^2, where V_{ij} take real values). The initial, average, maximum and minimum V_{ij}^2 values for the transition time interval are shown in Table s5.3. For all isotopes coincident values have been obtained for the initial V_{ij}^2 (1.4 10^{-3} K^2) and quite similar results have been found for the average V_{ij}^2 (3.2 10^{-3}-3.5 10^{-3} K^2). The maximum values are less similar (1.0 10^{-2}-1.6 10^{-2} K^2) and the minimum ones in general differ (2.4 10^{-8}-4.7 10^{-4} K^2) and are lower or substantially lower than the other V_{ij}^2 values.

Given the similarity of the initial and average couplings, it does not seem feasible to interpret the results based on the coupling terms. It is reasonable to think that the different relaxation times are probably due to a property that is different enough for the five isotopic species, i.e., the velocity at which they move. From the angular velocity (ω) associated to a given rotational state, the corresponding linear velocity (v) can be found, and it comes out that the v values are at least one order of magnitude greater than the velocity of the He atoms of the nanodroplet (v=699, 839, 1049, 1402 and 2099 m s^{-1} for Sx_2, Qi_2, Qa_2, T_2 y D_2, respectively, while $<v_{He}^2>^{1/2}$ is only 50 ms^{-1}). The progressively more difficult relaxation observed from Sx_2 to D_2 correlates with the fact that the molecular velocity is increasingly higher than that of the He atoms.

The dependence of the molecular relaxation times with the rotational constant (a_0 + a_1 Be + a_2 Be^2; Figure 5.3) has its origin in the quadratic polynomial dependence of these time properties on the angular velocity (ω=4πB_e [j (j+1)]$^{1/2}$ for a rigid rotator; B_e in frequency units). Some additional plots to show in a more clear way the behaviours

found are presented in Figure s5.9, where the inverse of the relaxation time properties vs. 1/Be and these inverse values relative to those of Sx_2 vs. *B*e are given. Quadratic (with the linear term being the most important one) and linear dependences are found, respectively. The complexity of these systems, due to the presence of a superfluid quantum liquid, makes it very difficult to go beyond qualitative considerations.

In this context it is helpful to represent in a single plot the temporal evolution of the different components of the helium energy, according to the OT functional, the X_2-helium interaction energy and the V_{ij} term, so as to have a somewhat more complete perspective of the dynamics (Figure s5.10). The T_2(j=2, m_j=0) relaxation has been shown as a representative example, and it is worth noting that, during the transition time, the T_2-helium interaction energy and the (j=2, m_j=0)-(j=0, m_j=0) V_{ij} coupling term show oscillations of significant amplitude. Besides, the kinetic energy of helium initially increases a little bit, reaches a maximum and then decreases slightly below its initial value. Then, the transition approximately begins when the helium is finally able to accept a very small amount of kinetic energy from the molecule (the helium kinetic energy seems to play the role of "switch" of the relaxation process).

5.4.2. Rotational relaxation of Sx_2(j, mj=0) vs. j

The rotational relaxation of an Sx_2 molecule embedded in a superfluid helium nanodroplet of 100 ^{4}He atoms, considering a sudden excitation from the rotational ground state (j=0, m_j=0) to three different excited states (j, m_j), (2, 0), (4, 0) and (6, 0), is analyzed in this section.

The temporal evolution of the rotational states populations for the three relaxations of Sx_2 investigated are shown in Figure 5.6. The global relaxation times for $(j_0 = 2, m_{j,0} = 0)$, $(j_0 = 4\, m_{j,0} = 0)$ and $(j_0 = 6\, m_{j,0} = 0)$ are equal to 1.32, 4.27 and 12.30 ns, respectively. Therefore, rotational relaxation becomes more difficult as rotational excitation increases, in sharp contrast to what happens for vibrational relaxation.[36] Vibrational relaxation is faster for higher vibrational energies as in this case the molecule vibrates with larger amplitudes, interacting in a stronger way with the neighbouring liquid helium; and due to this it is easier for helium to oscillate in phase with the diatomics.[36] See Section 5.4.4 for more details.

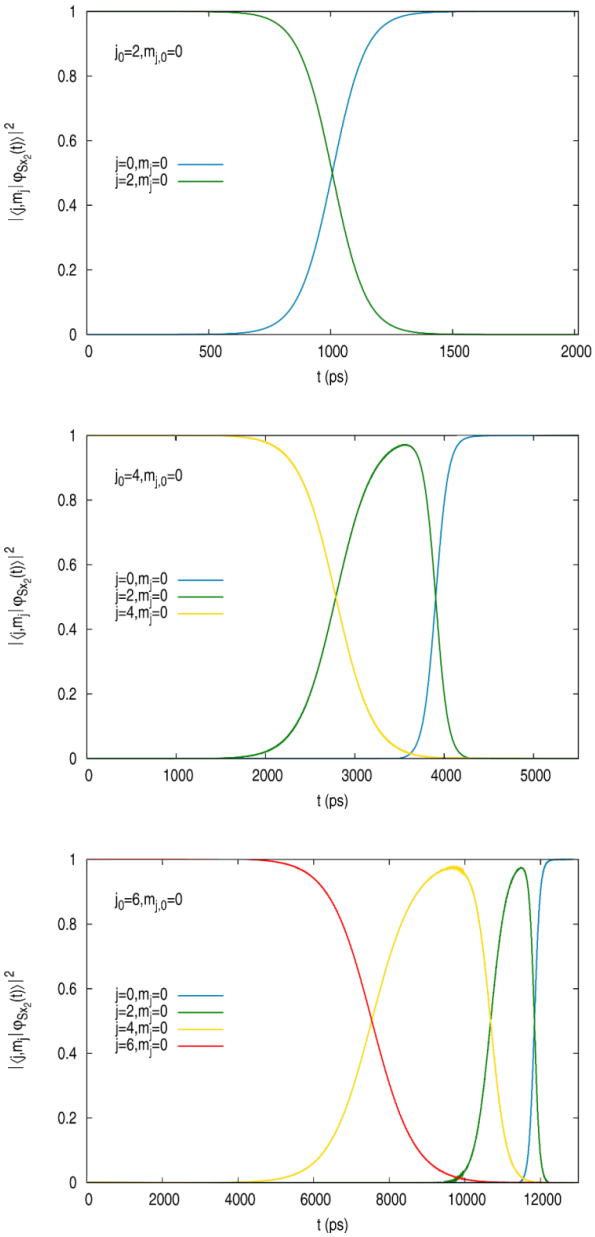

Figure 5.6 Populations of the $Sx_2(j, m_j{=}0)$ states for three different initial excitations, (j_o, $m_{jo}{=}0$), as a function of time: (2, 0), (4, 0) and (6, 0), from the top to the bottom, respectively.

The lifetime of the initial rotational states, 1.00, 2.80 and 7.58 ns for $(2, 0)$, $(4, 0)$ and $(6, 0)$, respectively, increases in an important way with the energy gap with respect to the immediately lower allowed state, which increases with j (Figure 5.7); $\Delta E_{\mathrm{Rot},2\to0} = 87.55$ K, $\Delta E_{\mathrm{Rot},4\to2} = 204.29$ K, and $\Delta E_{\mathrm{Rot},6\to4} = 321.03$ K. Besides, transitions to lower rotational states are faster when j decreases. The lifetime of each rotational state and the duration of the transitions are given in Table 5.2 and Table 5.3, respectively. The increase of the lifetime with increasing j has also been reported in theoretical

calculations on H_2 and D_2 in ordinary liquids.[66,70] The interpretation of the relaxation time properties will be presented at the end of this section.

From Figure 5.6 it can also be seen that rotational relaxation takes place approximately according to a cascade mechanism: the de-excitation process takes place in several steps implying each one of them mainly two rotational levels. Besides, for a given j state, the $j-4$ state starts being populated before the $j-2$ state is completely populated and the j state is completely unpopulated, which implies that there is no metastability for the intermediate rotational states.

The expected values of $\cos^2\theta$ for the initial rotational levels j_0=2, 4, and 6 are equal to 0.522, 0.503 and 0.499, respectively, and they decrease up to a value of 0.333 (Figure 5.8). Oscillations in $<\cos^2\theta>$ are particularly intense when the transitions are taking place. In addition, $<\widehat{J^2}>$ evolves in a smooth manner from 6, 20 and 42 $\hbar^2$, corresponding to j_0=2, 4, and 6, respectively, up to 0 $\hbar^2$, with intermediate quasi-steps for each de-excitation (at $\approx 6\ \hbar^2$ for $j_0 = 4$ and $\approx 20\ \hbar^2$ and $\approx 6\ \hbar^2$ for $j_0 = 6$; cf. Figure s5.11).

In the molecular relaxation process the energy of the doped nanodroplet decreases progressively, presenting quasi-steps that correspond to the intermediate rotational states involved, and a single helium atom is evaporated in each j → j -2 transition (Figure 5.9). Comparison of the Sx_2@HeND energy at the global relaxation time with the ground state value shows differences of about 0.03, 0.22 and 0.83% for the initial excitations to (j=2, m_j=0), (j=4, m_j=0) and (j=6, m_j=0), respectively. Besides, analogous comments as those given in Section 5.4.1 on the rotational energy of the molecules, energy of helium in the nanodroplet, X_2-HeND interaction potential energy and structure of the nanodroplet apply here.

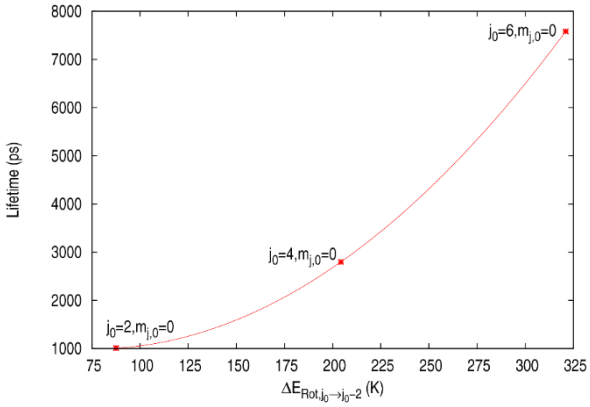

Figure 5.7 Initial rotational states lifetimes of Sx_2 as a function of the $j_0 \to j_0$-2 rotational energy gap for (j_0, m_{j0}=0): (2, 0), (4, 0) and (6, 0) from left to right, respectively (the red line serves only as a guide).

Table 5.2 Lifetimes (in ps) of each Sx_2 rotational state for three initial excitations.

j	2	4	6
2	1008		
4	1112	2798	
6	1145	3126	7583

Table 5.3 Duration of the transitions (in ps) between Sx_2 rotational states for three initial excitations.

j	$2 \to 0$	$4 \to 2$	$6 \to 4$
2	636		
4	689	1725[a]	
6	765	1772[b]	4770[c]

[a] $\max\left(\left|\langle j=2, m_j=0|\varphi(t)\rangle\right|^2\right) = 0.9680$

[b] $\max\left(\left|\langle j=2, m_j=0|\varphi(t)\rangle\right|^2\right) = 0.9669$

[c] $\max\left(\left|\langle j=4, m_j=0|\varphi(t)\rangle\right|^2\right) = 0.9686$

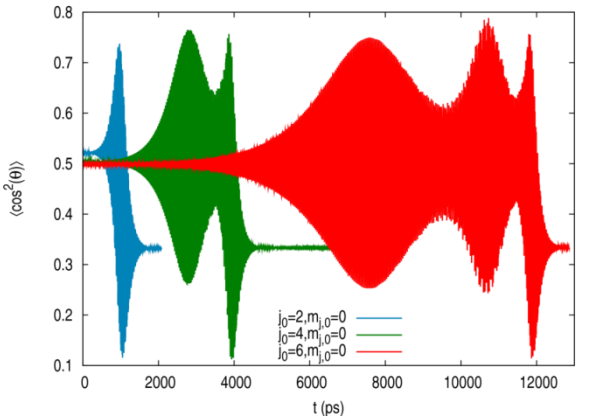

Figure 5.8 Expected value of $\cos^2\theta$ for Sx_2 at three different initial excitations, (j_o, m_{jo}=0): (2, 0), (4, 0) and (6, 0), *vs.* time.

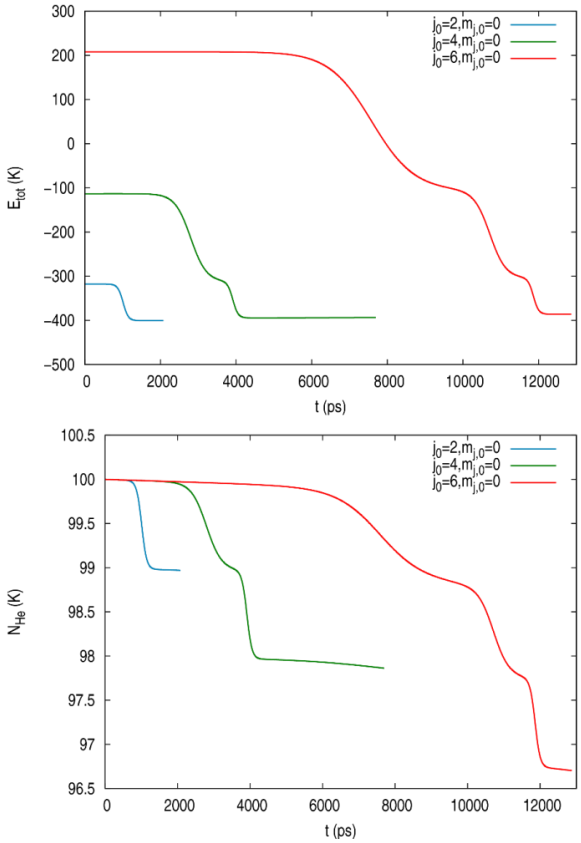

Figure 5.9 X_2@HeND total energy (top) and number of ^{4}He atoms of the HeND (bottom) for three initial excitations of $Sx_2(j_o, m_{jo}=0)$ *vs.* time.

Concerning the relaxation times, since in this case for each $j \longrightarrow j$-2 transition there are different coupling term (Table s5.3) and angular velocity values, even for the sequence of relaxations for which there is more information available ($j_0=6 \longrightarrow j=4$; $j=4 \longrightarrow j=2$; $j=2 \longrightarrow j=0$), it is not possible to characterize the type of dependence that the lifetime and transition time have on V_{ij}^2 and ω. Besides, regarding the $j \longrightarrow j$-2 couplings it is worth mentioning that the associated V_{ij}^2 average term increases in a substantial manner with the degree of excitation (Table s5.3), and shows an almost linear dependence with $j(j+1)$, i.e., with the rotational energy, as Be is constant here. Thus, for instance if we pay attention to the V_{ij}^2 average value for the sequence of relaxations $j_0=6 \longrightarrow j=4$, $j=4 \longrightarrow j=2$ and $j=2 \longrightarrow j=0$ and take as a reference the value of $j=2 \longrightarrow j=0$, the following average values are obtained: 34.2, 11.2 and 1.0, respectively.

As the couplings strongly favours the relaxations involving higher j levels and we observe that the relaxation times are larger for these levels, we can conclude that the angular velocity of the molecule is playing a dominant role, leading to more difficult

relaxations when higher j levels are considered. In what respects to the temporal evolution of the different components of the helium energy, Sx_2-helium interaction energy and V_{ij}, analogous results as those reported in the previous section apply in the present situation.

5.4.3. Rotational relaxation *vs.* nanodroplet size

The rotational relaxation of $T_2(j=2, m_j=0)$ inside a superfluid helium nanodroplet has been studied considering several nanodroplet sizes (N=25, 50, 75, 100 and 125), in order to investigate the effect of the size on the relaxation process.

The helium radial density of the ground state doped nanodroplets $T_2(j=0, m_j=0)@(^4He)_N$ along the three axis is plotted in Figure 5.10, where the evolution of the first and second solvation shells with N can be seen. The number of He atoms in the first solvation layer is moderately modified by N ($N_{solv,1}$=14.6, 14.5, 14,2, 13.6 and 12.0 for N=125, 100, 75, 50 and 25, respectively). However, significant changes are evident in the second solvation layer, whose size is reduced in an important way when the number of He atoms of the nanodroplet decreases. As the interaction between the molecule and the liquid helium probably mainly involves the first solvation layer with some contribution of the second one,[36] the effect of the nanodroplet size on the rotational relaxation is expected to be noticeable, with similar results for the two nanodroplets of larger size.

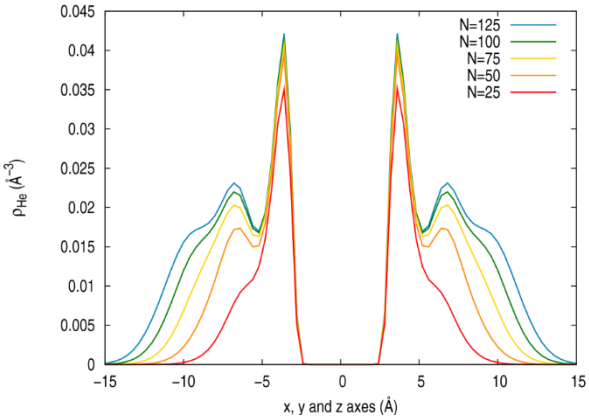

Figure 5.10 Helium radial density of the $T_2(j=0, m_j=0)@(^4He)_N$ ground state nanodroplet, with N=25, 50, 75, 100 and 125, along the x, y and z-axes.

The time evolution of the ($j=2$, $m_j=0$) and ($j=0$, $m_j=0$) populations for the five nanodroplet sizes is presented in Figure 11, where it can be seen that the results

obtained for the nanodroplets with N=100 and N=125 are quite similar (see also Table 5.4). The global relaxation times, lifetimes and transition times are in the 2.28-2.93 ns, 1.76-2.27 ns and 1.05-1.32 ns time intervals, respectively, and they decrease with increasing the nanodroplet size (Table 5.4). A situation not far from a saturation value is expected to occur for the higher N values, which corresponds to the situation in which the first and second solvation layers are essentially completely defined. The addition of more atoms in the HeND does not change the structure of the two first layers but only increases the volume of the nanodroplet.

The observed decrease in the global relaxation times, lifetimes and transition times with increasing the nanodroplet size results from the increase of interaction between the molecule and the liquid helium of the HeND as N increases. For bigger nanodroplets the helium environment surrounding the impurity is denser and the interaction becomes stronger (the interaction energy varies from $E_{\mathrm{Int}}(N=25)$ = -81.248 K to $E_{\mathrm{Int}}(N=125)$ = -105.160 K).

This coupling increase happens when increasing the size of the nanodroplet as the helium occupation of the main solvation layers (i.e., the first and second layers) increases. Once these layers are completed, increasing the nanodroplet size does not change in a substantial way the molecule-helium interaction energy, so the time scales of the rotational relaxation are stable and correspond to defined saturation values of the global relaxation times, lifetimes and transition times.

Furthermore, it is possible to analyze the dependence of the temporal properties with the coupling (V_{ij}^2 average), which depends on the nanodroplet size (Table s5.3). The inverse of the relaxation time properties show a linear dependence with the coupling between the two rotational states involved (Figure s5.12). Also, as the coupling depends linearly on the T_2-helium interaction energy, this implies that the inverse of the relaxation time properties also depend in a linear way on the interaction energy (which presents a smooth but not linear dependence on N).

The set of results obtained for all the initial conditions analyzed in this work suggests that, in the rotational relaxation of diatomic molecules in superfluid helium nanodroplets, the transition time frequency increases linearly with the coupling (V_{ij}^2 average), while its dependence with the angular velocity, whose increase makes the

transition more difficult, is more complex (quadratic dependence on $(1/\omega)$, although the most important term of the corresponding polynomial function is linear). The same trends are also evident for the other relaxation time properties.

For a transition between two specific states, the use of the Fermi golden rule (first order perturbation theory context),[76] which is often employed in spectroscopy and scattering, leads to a dependence on the transition time frequency that would simply be proportional to the associated V_{ij}^2 term. More complex situations could lead, e.g., to a dependence proportional to V_{ij}^2 and inversely proportional to B_e, which is not the present case.

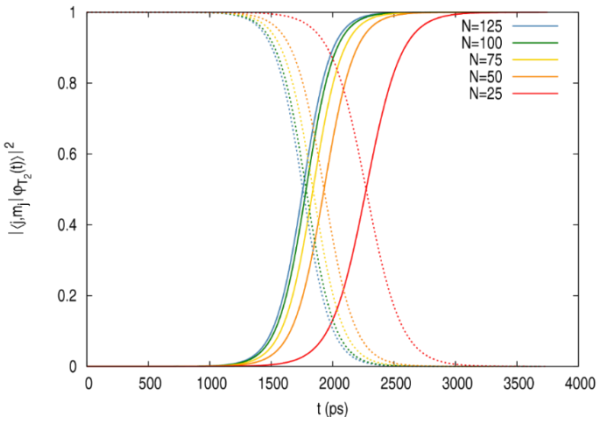

Figure 5.11 Populations of the $T_2(j=0, m_j=0)$ (solid lines) and $(j=2, m_j=0)$ (dashed lines) rotational states for the five nanodroplet sizes *vs.* time.

Table 5.4 Global relaxation times, lifetimes and transition times of $T_2(j=2, m_j=0)$ and T_2-HeND interaction potential energies for the five nanodroplet sizes.

N	Global relax. time (ps)	Lifetime (ps)	Transition time (ps)	T_2-HeND interaction energy (K)
25	2928	2274	1319	-81.248
50	2496	1930	1140	-94.860
75	2382	1842	1091	-100.306
100	2311	1785	1063	-103.222
125	2277	1759	1049	-105.160

5.4.4. Rotational relaxation *vs.* vibrational relaxation

To achieve a better understanding of the rotational energy relaxation dynamics inside HeNDs, it is useful to compare the results obtained here with recently reported vibrational energy relaxation data (I_2 in HeNDs; analogous theoretical approach).[36] VER also occurs following sequential transitions, above N=100 there is also small influence

of N on the lifetime, and heavier isotopes lead to smaller vibrational lifetimes.[77] Besides, the structure of the HeND does not change significantly during the VER.

However, in contrast to the RER results, for the VER when the initial excitation increases a decrease is observed in the lifetime of the excited vibrational state.[36] This difference can be interpreted in a rather simple way taking into account that RER and VER are associated to very dissimilar types of motion/degrees of freedom. Thus, when vibrational excitation increases: (a) the motion frequency is approximately constant and equal to ν_e (for low-moderate excitations); (b) the energy separation $v \leftrightarrow v\text{-}1$ is around constant ($h\nu_e$); and (c) the interaction with helium is stronger as the vibrational amplitude increases. It should also be noted that in the case of VER metastability has been observed for intermediate excited states,[36] in contrast to what happens for RER.

The results obtained in this work on the rotational relaxation seem reasonable and the numerical methods employed to solve the Schrödinger-like equations for long time simulations are efficient. We expect that this initial theoretical study will be useful to motivate further analysis on this interesting and not easy to investigate relaxation process.

5.5. Summary and conclusions

The rotational energy relaxation of a homonuclear diatomic molecule inside a superfluid helium nanodroplet has been investigated using a hybrid theoretical approach analogous to that proposed recently by us for the study of the vibrational energy relaxation in a HeND. The helium and molecule dynamics have been described using a hybrid approach (TDDFT and standard quantum dynamics methods, respectively). To the best of our knowledge this is the first theoretical study about rotational relaxation of molecules inside liquid helium nanodroplets.

Several real (D_2 and T_2) and hypothetical (Qa_2, Qi_2 and Sx_2) isotopes of H_2 have been examined in order to make the investigation easier (taking advantage of the large rotational constants of the selected systems) and allowing us to explore the influence of the rotational constant B_e of these fast rotors on the relaxation dynamics. The rotational relaxation from the $(j = 2, m_j = 0)$ state has been considered in all cases and additional

simulations have been considered for Sx_2 and T_2, so as to determine the influence of the initial excited rotational state and nanodroplet size on the relaxation dynamics, respectively.

The structure of the HeND essentially does not change during the RER process and the superfluid liquid helium efficiently removes from the nanodroplet the energy released by the molecule during the relaxation (although the number of evaporated helium atoms is small compared with the expected values). Besides, the RER approximately occurs following sequential transitions between two "consecutive" rotational levels (cascade mechanism): $j \rightarrow j$-2; j-2 $\rightarrow j$-4; ... 4 $\rightarrow$ 2; 2 $\rightarrow$ 0 (m_j is conserved) in this case, due to the nuclear symmetry. In addition, the $(j = 0, m_j = 0) \leftarrow (j = 2, m_j = 0)$ global relaxation time is of the order of the nanosecond (from 1.3 to 5.3 ns for Sx_2 and D_2, respectively).

Regarding the lifetime of an excited rotational state, it increases when: (a) the rotational constant increases; (b) the quantum number j increases; (c) the nanodroplet size decreases (above N=100 there is a small influence of N on the lifetime). The analysis of the dependence of the relaxation time properties on the coupling (V_{ij}^2 average) and X_2 angular velocity has provided some additional insight on the dynamics. Besides, the study suggests that the transition time frequency increases linearly with the coupling, while its dependence with respect to the angular velocity (which makes transition more difficult as it increases) is not so simple. A similar behavior is also found for the other time properties.

Furthermore, it has been interesting to compare the rotational relaxation with the vibrational one. Even though both relaxation processes take place following sequential transitions, the lifetime of the excited vibrational states decreases as excitation increases, differing from what happens for the rotational case. This discrepancy has been interpreted on the basis of the very different types of motion involved. Moreover, it is worth noting that the metastability was found for intermediate excites vibrational states, unlike what happens for RER.

In future investigations it would be interesting to include the zero-point motion of the centre of mass of the molecule, which nowadays is very difficult to consider due to the very large computational resources needed. Another interesting question for future

work would be to analyse the influence of the vibration-rotation coupling on the relaxation dynamics and to try to include the quantum correlation. We hope that this initial contribution will encourage more researchers to study this interesting issue about which our knowledge is still very limited.

5.6. Appendix 5A: The difficulty of treating heavy diatomic molecules of in helium nanodroplets

In a first attempt to study the rotational relaxation of homonuclear diatomic molecules we tried to consider the I_2 system, as we treated the vibrational relaxation of this system in a previous work[36]. However, in the ground state the I_2 molecule is found to be described by a superposition of rotational states. This makes excitations more complicated, in the sense that it is not clear which excited state excitation would lead. Considering (in test calculations) a basis set containing all rotational wave functions until the rotational level $j_{max} = 4$ (i.e., considering all j and m_j quantum numbers), the rotational state of the I_2 molecule holds contributions from the following (j, m_j) states: (0,0), (2,-2), (2,0), (2,2), (4,-4), (4,-2), (4,0), (4,2) and (4,4). That is to say, only states with even j and m_j quantum numbers are populated.

The rather strong interaction with the helium nanodroplet and the small energy gap between the rotational states ($B_e = 0.037372\ \mathrm{cm}^{-1}$) can explain that I_2 in HeND is described by a superposition of rotational states. In order to try to simplify things in this initial investigation and obtain a pure rotational ground state, optimisations with a similar diatomic molecule with a higher rotational constant (B_e) and a softer interaction with helium were performed. The chosen molecule was F_2 ($B_e = 0.89019\ \mathrm{cm}^{-1}$) and a basis set up to $j_{max} = 6$ was considered. In this case the states (6,-6), (6,-4), (6,-2), (6,0), (6,2), (6,4) an (6,6) were also populated. Optimisations delivered similar results with respect to those corresponding to I_2. The evolution of the energies, total j populations and (j, m_j) populations and the resulting helium nanodroplet densities are shown for I_2 and F_2 in Figure s5.1, Figure **s5.2**, Figure **s5.3** and Figure **s5.4** . Table s5.1 and Table s **5.2** show the contributions of the (j, m_j) states to the rotational state of the diatomic molecules.

The evolution of the total energies and populations show that the optimisation (static calculation) leads to a metastable state before the system reaches the true ground state. Before finding the minimum energy state, this metastable state was initially thought to be the ground state and using it as the input for the relaxation dynamics program produced an unphysical evolution of the state. It was not until an exhaustive revision of the rotational relaxation code confirmed that no errors were made, that this

metastable state was questioned to be the real ground state. After that, even longer optimisations were carried out and the true ground states of the doped nanodroplet were found.

These complex rotational states make it difficult to have well-defined excitations and rotational relaxations. For these reasons, isotopes of H_2 were used as diatomic molecules inside the nanodroplets in order to perform the first theoretical rotational relaxation studies in HeND. These molecules have much larger rotational constants and softer interactions with helium. Because of this the ground state of the corresponding droplet nanodroplet only involves the $j = 0, m_j = 0$ state.

Table s5.1 Contributions of the main populated j,m_j states to the X_2 rotational state for the optimisations of $X_2@(^4He)_{100}$ with $X_2 = F_2$ and I_2, considering $j_{max} = 4$ and $j_{max} = 6$ for the rotational basis set of the molecule.

(j, m_j)	(0,0)	(2,-2)	(2,0)	(2,2)	(4,-4)	(4,-2)	(4,0)	(4,2)	(4,4)	(6,-6)	(6,-4)	(6,-2)	(6,0)	(6,2)	(6,4)	(6,6)
I_2, j_{max}=4	0.183	0.211	0.141	0.211	0.069	0.040	0.035	0.040	0.069	---	---	---	---	---	---	---
F_2, j_{max}=4	0.299	0.219	0.146	0.219	0.032	0.018	0.016	0.018	0.032	---	---	---	---	---	---	---
F_2, j_{max}=6	0.252	0.212	0.141	0.212	0.046	0.026	0.023	0.026	0.046	0.003	0.002	0.001	0.001	0.001	0.002	0.003

Table s 5.2 Contributions of the main populated j states to the X_2 rotational state for the optimisations of $X_2@(^4He)_{100}$ with $X_2 = F_2$ and I_2 considering $j_{max} = 4$ and $j_{max} = 6$ for the rotational basis set of the molecule.

j	0	2	4	6
I_2, j_{max}=4	0.183	0.564	0.253	---
F_2, j_{max}=4	0.299	0.583	0.117	---
F_2, j_{max}=6	0.252	0.565	0.166	0.015

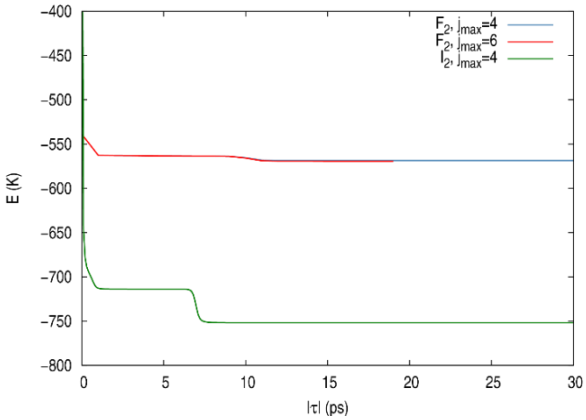

Figure s5.1 Evolution of the total energy of the system as a function of $|\tau|$ (modulus of the imaginary time) for the optimisations of $X_2@(^4He)_{100}$ with $X_2 = F_2$ and I_2, considerin$j_{max} = 4$g and $j_{max} = 6$ for the rotational basis sets.

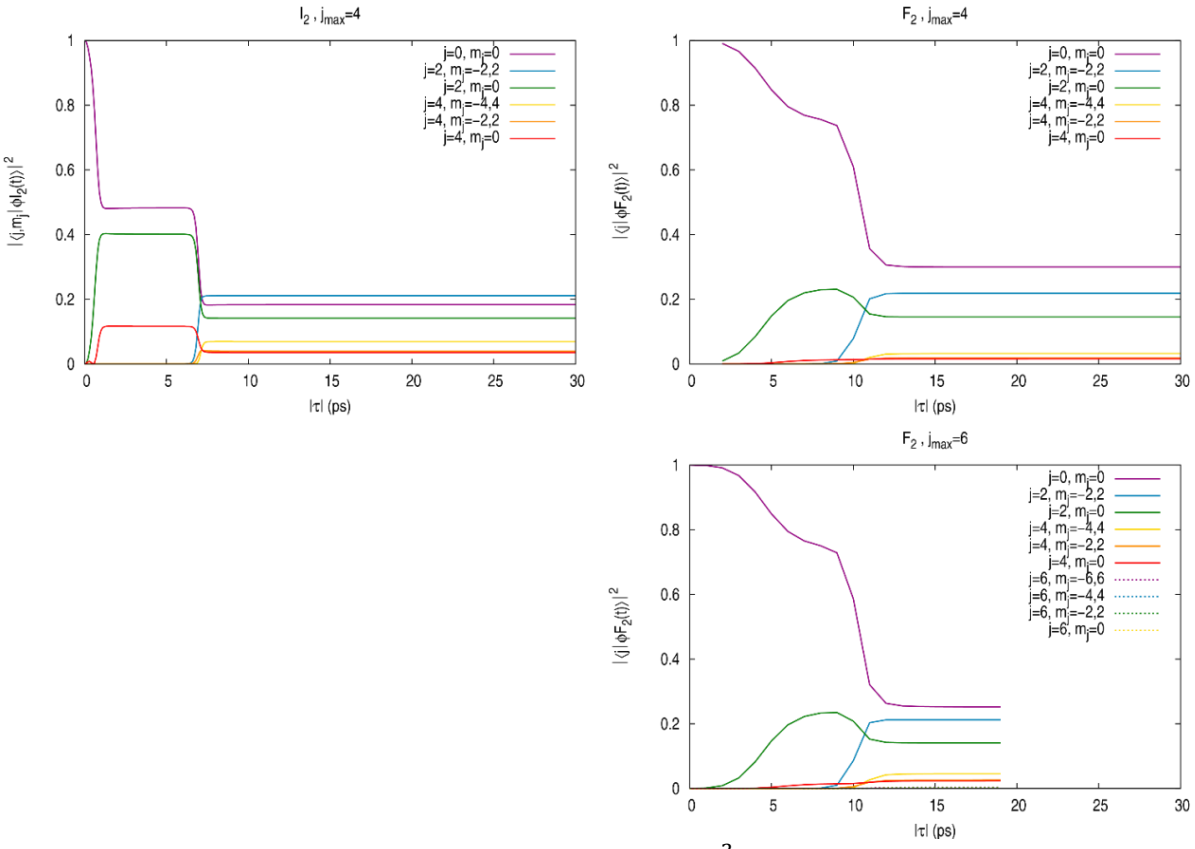

Figure s5.2 Evolution of the populations ($\left|\langle j, m_j|\varphi X_2(t)\rangle\right|^2$) of the main rotational states for the optimisations of $X_2@(^4He)_{100}$ with $X_2 = F_2$ and I_2, considering $j_{max} = 4$ and $j_{max} = 6$ for the rotational basis sets.

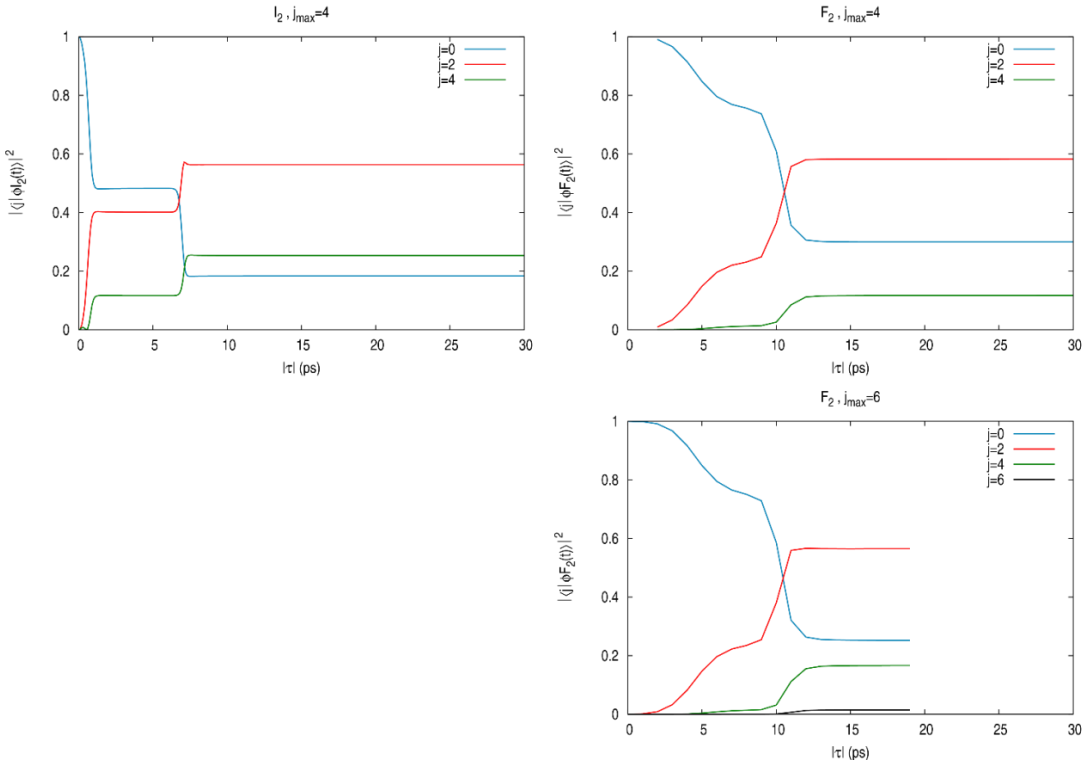

Figure s5.3 Evolution of the populations ($|\langle j|\varphi X_2(t)\rangle|^2$) of the main rotational states for the optimisations of $X_2@(^4He)_{100}$ with $X_2 = F_2$ and I_2, considering $j_{max} = 4$ and $j_{max} = 6$ for the rotational basis sets.

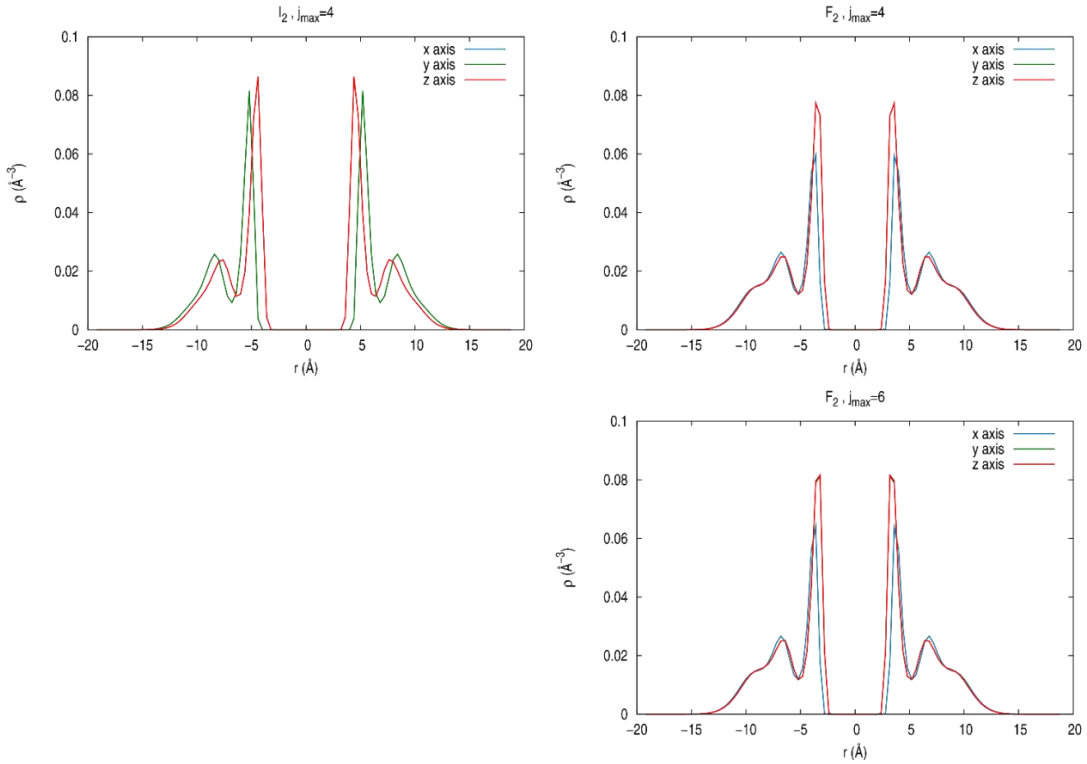

Figure s5.4 Helium densities from the optimisations of $X_2@(^4He)_{100}$ with $X_2 = F_2$ and I_2, considering $j_{max} = 4$ and $j_{max} = 6$ for the rotational basis sets.

5.7. Appendix 5B: Supplementary information

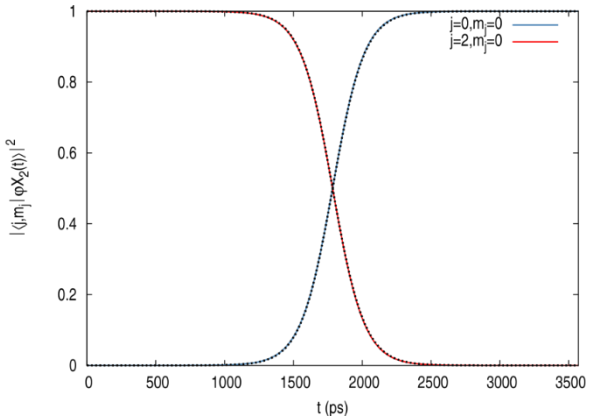

Figure s5.5 Comparison between the time evolution of the (j=0, m_j=0) and (j=2, m_j=0) populations for the T_2@(^{4}He)$_{100}$ nanodroplet obtained from the relaxation dynamics (blue and red lines, respectively) and the results derived from a sigmoid function fitting of the (j=0, m_j=0) populations.

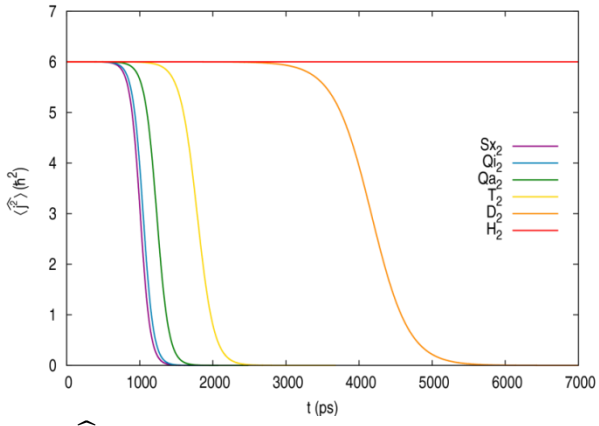

Figure s5.6 Expected value of $\hat{j}^2$ for the (j=0, m_j=0)←(j=2, m_j=0) relaxation of the molecules in (^{4}He)$_{100}$, as a function of time.

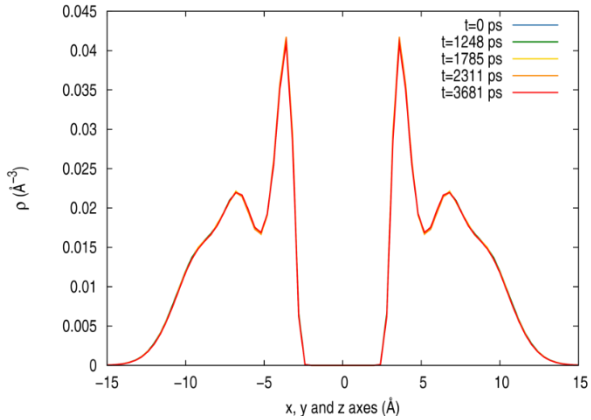

Figure s5.7 Helium radial density of the T_2(j=2, m_j=0)@(^{4}He)$_{100}$ nanodroplet along the x, y and z-axes, as a function of time. The time values of 0, 1785 and 2311 ps correspond to the initial excitation, lifetime and global relaxation time of the molecule, respectively (cf. Table 1).

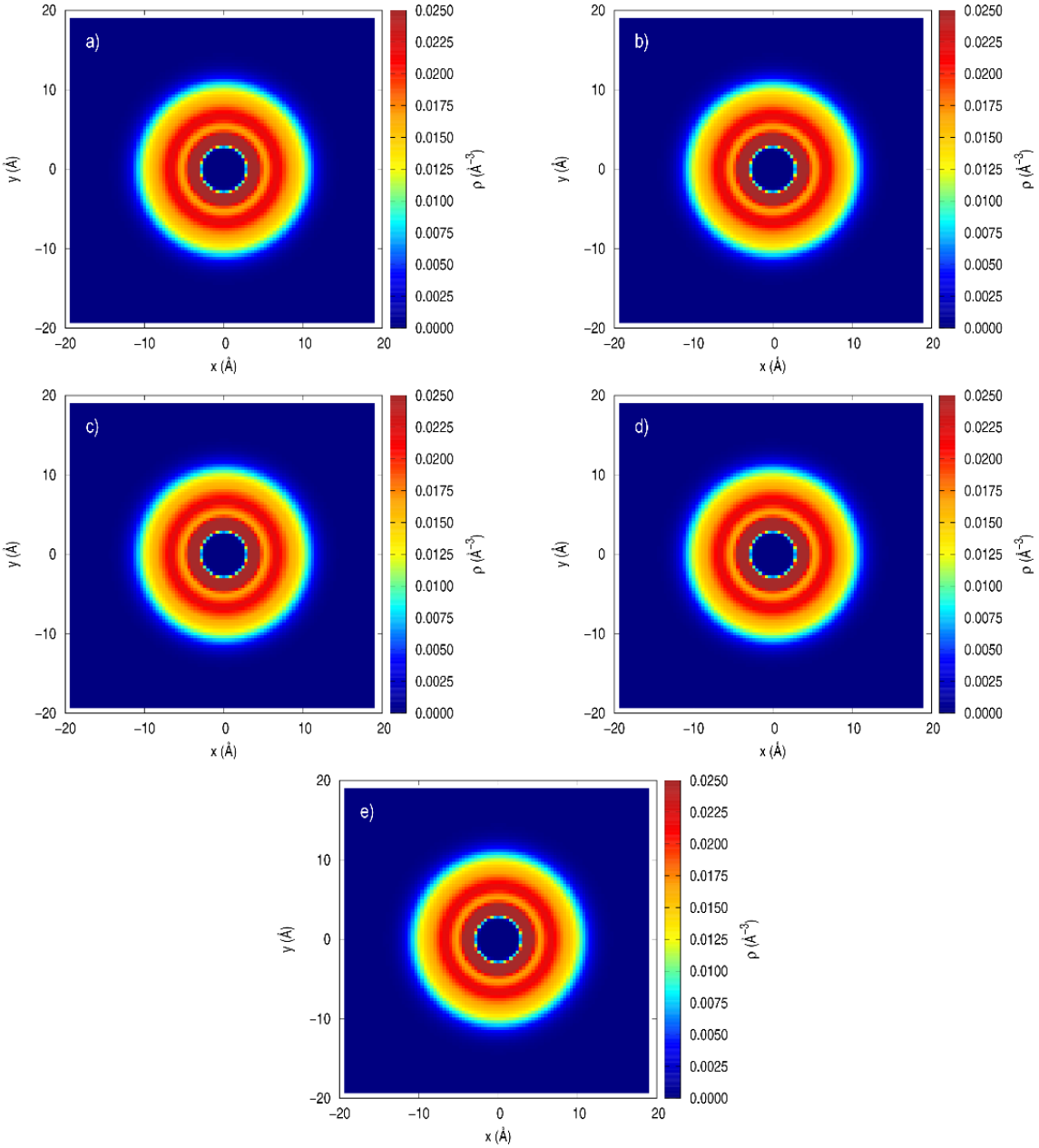

Figure s5.8 Snapshots of the helium density in the xy-plane for the $T_2(j=2, m_j=0)@(^4He)_{100}$ nanodroplet, as a function of time. The same time values as in Figure s3 are considered (t=0, 1248, 1785, 2311 and 3681 ps for (a), (b), (c), (d) and (e), respectively).

Table s5.3 Coupling terms squared values (in K^2) between the rotational states.[a]

Relaxation from j=2,m_j=0 to j=0,m_j=0

	V_{ij}^2 initial	V_{ij}^2 average	V_{ij}^2 max	V_{ij}^2 min	t(p=0.99)	t(p=0.01)	N points
D_2	1.43 E-03	3.23E-03	9.98E-03	4.73E-04	2972	5334	1576
T_2	1.43E-03	3.42E-03	1.01E-02	2.99E-04	1248	2310	709
Qa_2	1.43E-03	3.37E-03	1.23E-02	4.45E-05	849	1606	506
Qi_2	1.43E-03	3.45E-03	1.45E-02	1.34E-07	715,5	1369	437
Sx_2	1.42E-03	3.29E-03	1.58E-02	2.38E-08	685,5	1320	424

Several relaxations of Sx_2 ($j0,m_j0$=0)

		V_{ij}^2 initial	V_{ij}^2 average	V_{ij}^2 max	V_{ij}^2 min	t(p=0.99)	t(p=0.01)	N points
j_0=2	0←2	1.42E-03	3.29E-03	1.58E-02	2.38E-08	685.5	1320	424
j_0=4	0←2	1.73E-03	3.35E-03	1.69E-02	1.01E-08	3564	4253	459
	2←4	4.24E-02	4.18E-02	5.20E-02	3.24E-02	1839	3564	1150
j_0=6	0←2	1.80E-03	3.65E-03	2.43E-02	5.34E-09	11532	12297	510
	2←4	4.26E-02	4.10E-02	6.35E-02	2.51E-02	9760	11532	1184
	4←6	1.25E-01	1.25E-01	1.53E-01	1.01E-01	4990	9760	3188

Relaxation from j=2,m_j=0 to j=0,m_j=0 for T_2

N	V_{ij}^2 initial	V_{ij}^2 average	V_{ij}^2 max	V_{ij}^2 min	t(p=0.99)	t(p=0.01)	N points
25	7.01E-04	1.95E-03	5.99E-03	1.43E-04	1609	2927	879
50	1.11E-03	2.81E-03	8.26E-03	2.59E-04	1356	2495	760
75	1.32E-03	3.11E-03	9.18E-03	3.24E-04	1290	2380	728
100	1.43E-03	3.42E-03	1.01E-02	2.99E-04	1248	2310	709
125	1.50E-03	3.54E-03	1.02E-02	3.76E-04	1228	2278	701

[a] The Vij coupling terms are real numbers. The reported initial values correspond to the value at t=0, that is after the sudden rotational excitation. They essentially coincide with the values at the propagation time where the population of the excited state is equal to 0.99. In this table are also indicated the time values at which the population of the excited state is equal to 0.99, t(p=0.99), and 0.01, (t(p=0.01)), where the time is given in ps. N points indicates the number of propagation times considered when analyzing the data in the corresponding time interval.

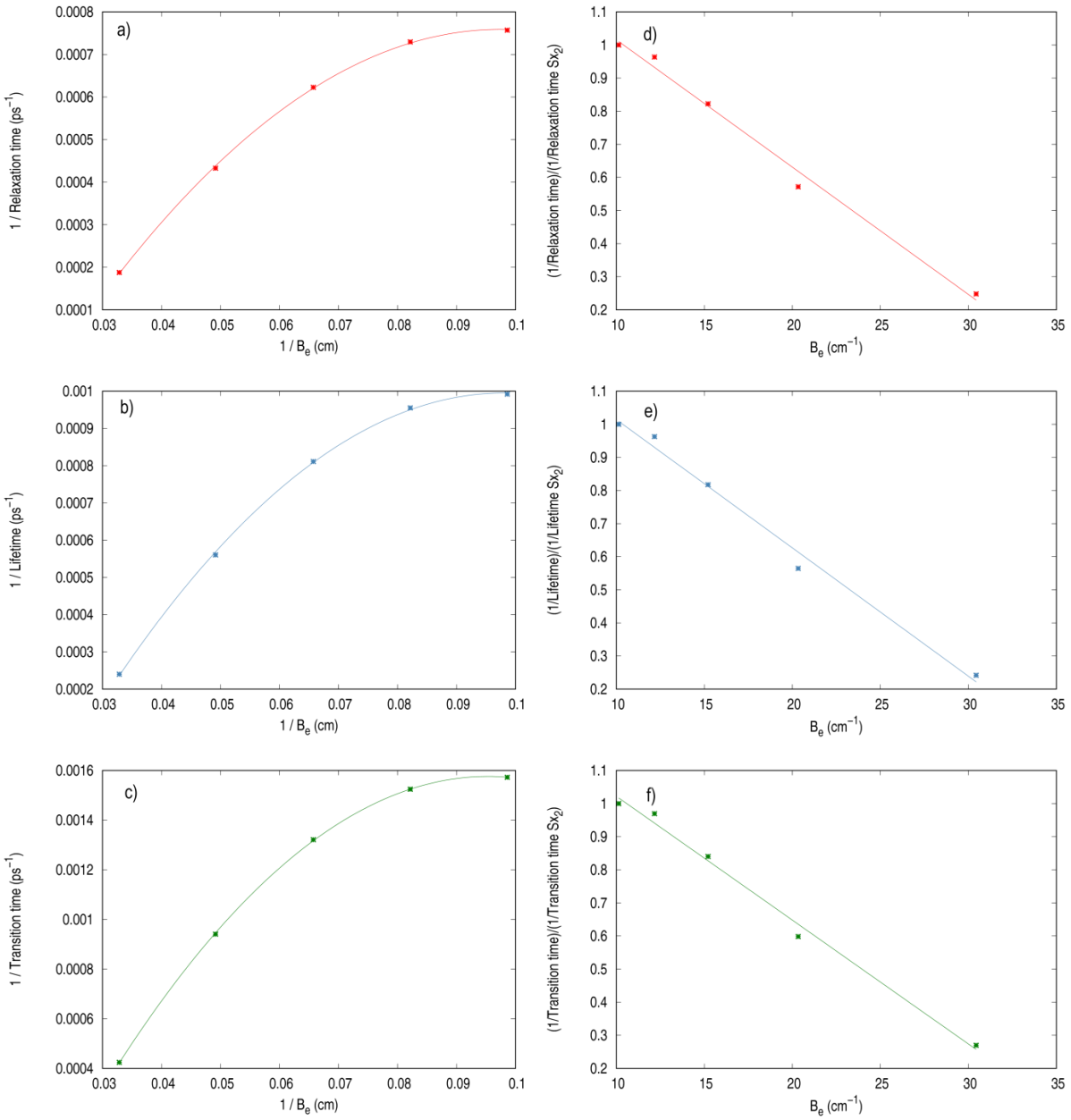

Figure s5.9 Relaxation of the (j=2, m_j=0) state of the molecules in $(^4He)_{100}$. Inverse of the relaxation time properties (global relaxation time (a), lifetime (b) and transition time (c)) *vs.* $1/B_e$. Moreover, the previous inverse values, taken with respect to the corresponding inverse values of Sx_2, *vs.* B_e (d-f, respectively) are also given.

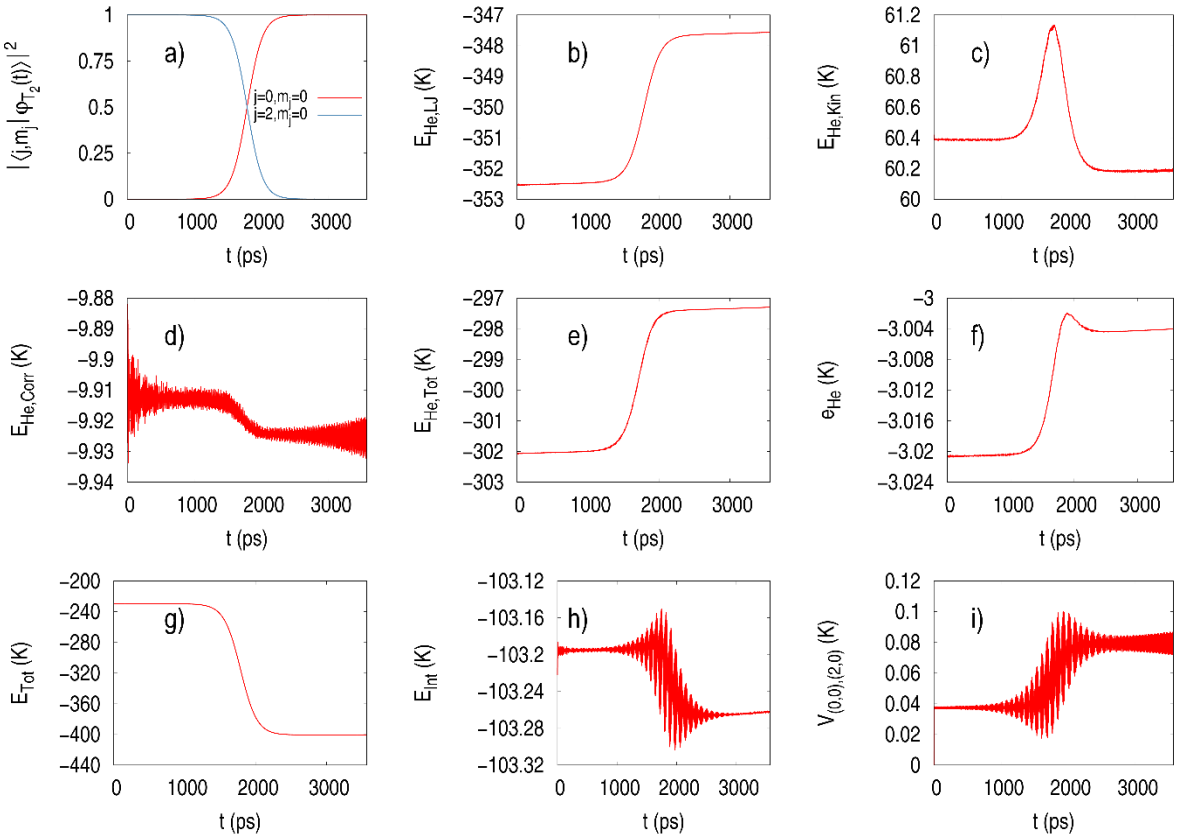

Figure s5.10 Relaxation of $T_2(j=2, m_j=0)$ in $(^4He)_{100}$: (a) populations of $(j=2, m_j=0)$ and $(j=0, m_j=0)$; (b) potential energy of helium; (c) kinetic energy of helium; (d) correlation energy of helium; (e) energy of helium (sum of the previous three energy terms); (f) energy per helium atom of the HeND; (g) energy of the doped HeND; (h) interaction potential energy T_2-helium; (i) V_{ij} coupling term between $(j=2, m_j=0)$ and $(j=0, m_j=0)$. Please, note the different energy scales.

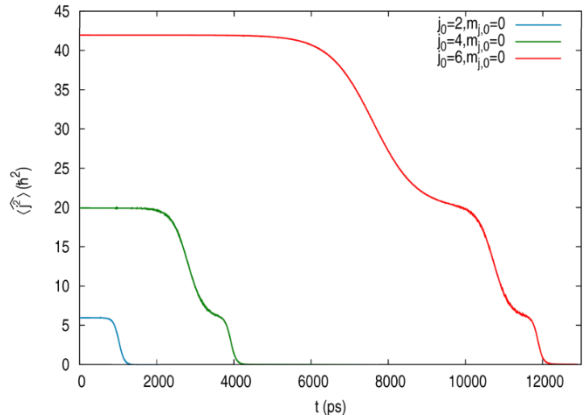

Figure s5.11 Expected value of $\hat{j}^2$ for Sx_2 in $(^4He)_{100}$ at three different initial excitations, $(j_o, m_{jo}=0)$: (2, 0), (4, 0) and (6, 0), as a function of time.

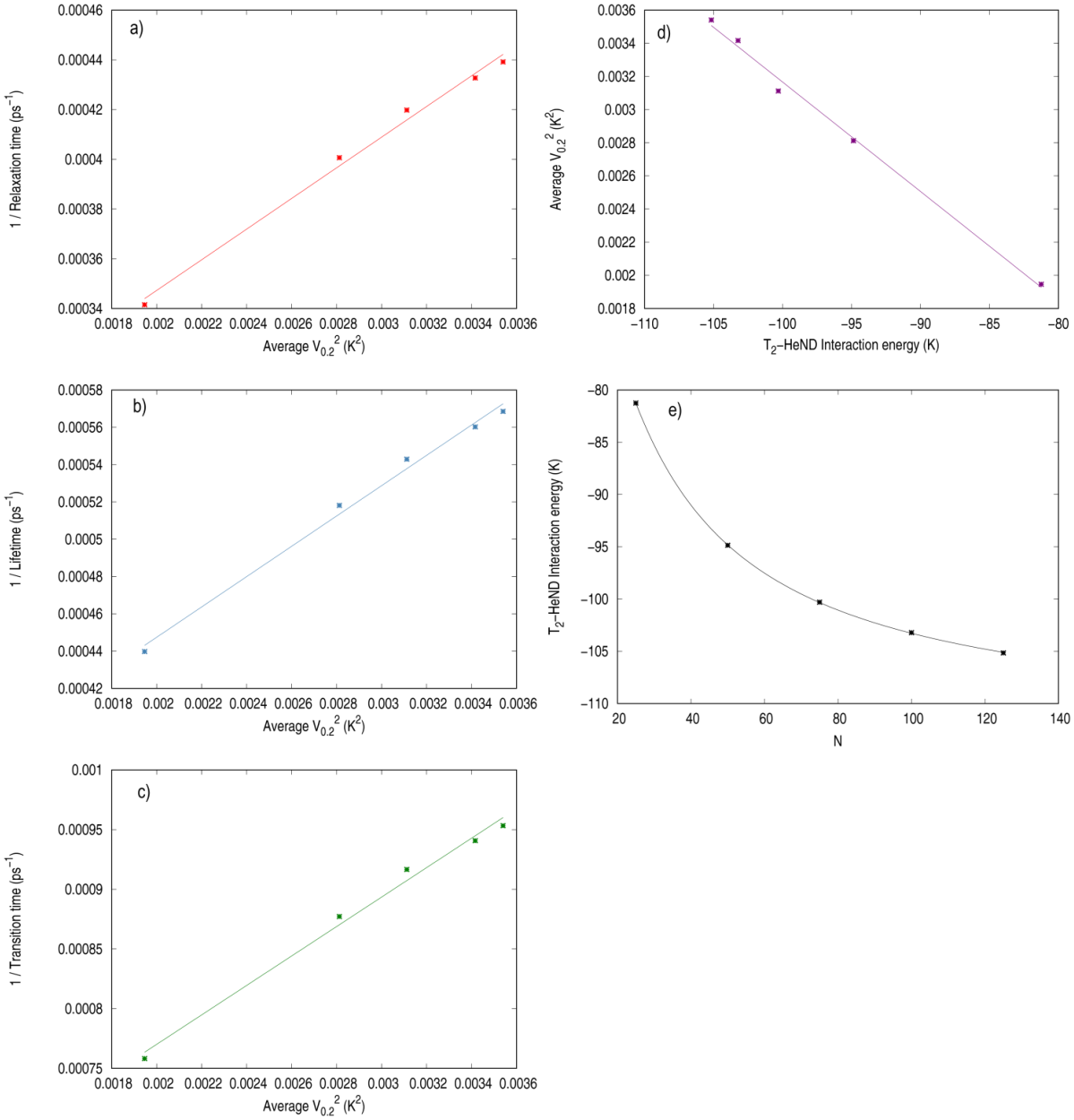

Figure s5.12 Relaxation of $T_2(j=2, m_j=0)$ in HeNDs of different sizes. Inverse of the relaxation time properties (global relaxation time (a), lifetime (b) and transition time (c)) *vs.* the average V_{ij}^2. Moreover, the average V_{ij}^2 *vs.* the T_2-helium interaction energy (d) and the T_2-helium interaction energy *vs.* N (e) are also given.

5.8. References

[1] C. Callegari, K. K. Lehmann, R. Schmied and G. Scoles, Helium nanodroplet isolation rovibrational spectroscopy: methods and recent results, *J. Chem. Phys.*, 2001, **115**, 10090-10110.

[2] J. P. Toennies and A. F. Vilesov, Superfluid helium droplets: a uniquely cold nanomatrix for molecules and molecular complexes, *Angew. Chem. Int. Ed.*, 2004, **43**, 2622-2648.

[3] F. Stienkemeier and K K. Lehmann, Spectroscopy and dynamics in helium nanodroplets, *J. Phys. B.*, 2006, **39**, R127-R166.

[4] M. Y. Choi, G. E. Douberly, T. M. Falconer, W. K. Lewis, C. M. Lindslay, J. M. Merritt, P. L. Stiles and R. E. Miller, Infrared spectroscopy of helium nanodroplets: novel methods for physics and chemistry, *Int. Rev. Phys. Chem.*, 2006, **25**, 15-75.

[5] A. Slenczka and J. P. Toennies, in *Low temperature and cold molecules*, ed. I. W. M. Smith, Imperial College Press, London, 2008, pp. 345-392.

[6] S. Yang and A. M. Ellis, Helium droplets: a chemistry perspective, *Chem. Soc. Rev.*, 2013, **42**, 472-484.

[7] K. Nauta and R. E. Miller, Metastable vibrationally excited HF(v=1) in helium nanodroplets, *J. Chem. Phys.*, 2000, **113**, 9466-9469.

[8] M. Ortlieb, Ö. Birer, M. Letzner, G. W. Schwaab and M. Havenith, Observation of rovibrational transitions of HCl, $(HCl)_2$, and H_2O-HCl in liquid helium nanodroplets, *J. Phys. Chem. A.*, 2007, **111**, 12192-12199.

[9] S. D. Flynn, D. Skvortsov, A. M. Morrison, T. Liang, M. Y. Choi, G. E. Douberly and A. F. Vilesov, Infrared Spectra of HCl−H_2O clusters in helium nanodroplets, *J. Phys. Chem. Lett.*, 2010, **1**, pp 2233–2238.

[10] K. von Haeften, S. Rudolph, I. Simanovski, M. Havenith, R. E. Zillich and K. B. Whaley, Probing phonon-rotation coupling in helium nanodroplets: infrared spectroscopy of CO and its isotopomers, *Phys. Rev. B*, 2006, **73**, 054502.

[11] C. M. Lindsay, G. E. Douberly and R. E. Miller, Rotational and vibrational dynamics of H_2O and HDO in helium nanodroplets, *J. Mol. Struct.*, 2006, **786**, 96-104.

[12] R. Schwan, M. Kaufmann, D. Leicht, G. Schwaab, M. Havenith, Infrared spectroscopy of the ν_2 band of the water monomer and small water clusters $(H_2O)_{n=2,3,4}$ in helium droplets, *Phys. Chem. Chem. Phys.*, 2016, **18**, 24063-24069.

[13] K. Nauta and R. E. Miller, Stark spectroscopy of polar molecules solvated in liquid helium droplets, *Phys. Rev. Lett.*, 1999, **82**, 4480-4483.

[14] A. Conjusteau, C. Callegari, I. Reinhard, K. K. Lehmann and G. Scoles, Microwave spectra of HCN and DCN in ^{4}He nanodroplets: a test of adiabatic following, *J. Chem. Phys.*, 2000, **113**, 4840-4843.

[15] R. E. Zillich and K. B. Whaley, Quantum rotation of HCN and DCN in ^{4}He, *Phys. Rev. B*, 2004, **69**, 104517.

[16] P. L. Raston, D. D. Kelloway and W. Jäger, Infrared spectroscopy of HOCl embedded in superfluid helium nanodroplets: probing the dynamical response of the solvent, *J. Chem. Phys.*, 2012, **137**, 014302.

[17] B. A. Harruff-Miller, C. E. Bunker and W. K. Lewis, Infrared spectroscopy of the ν_3 band of C_3 in helium droplets, *AIP Adv.*, 2018, **8**, 025308.

[18] T. Faulkner, I. Miller and P. L. Raston, Quantum cascade laser spectroscopy of OCS isotopologues in ^{4}He nanodroplets: a test of adiabatic following for a heavy rotor, *J. Chem. Phys.*, 2018, **148**, 044308.

[19] A. M. Morrison, P. L. Raston and G. E. Douberly, Rotational dynamics of the methyl radical in superfluid ^{4}He nanodroplets, *J. Phys. Chem. A.*, 2013, **117**,11640-11647.

[20] M. Behrens, U. Buck, R. Fröchtenicht, M. Hartmann, F. Huisken and F. Rohmund, Rotationally resolved IR spectroscopy of ammonia trapped in cold helium clusters, *J. Chem. Phys.*, 1998, **109**, 5914-5920.

[21] P. L. Raston, C. J. Knapp and W. Jäger, Rotovibrational spectroscopy of hydrogen peroxide embedded in superfluid helium nanodroplets, *Phys. Chem. Chem. Phys.*, 2011, **13**, 18789-18798.

[22] P. L. Raston and G. E. Douberly, Rovibrational spectroscopy of formaldehyde in helium nanodroplets, *J. Mol. Spectrosc.*, 2013, **292**, 15-19.

[23] K. Nauta and R. E. Miller, The vibrational and rotational dynamics of acetylene solvated in superfluid helium nanodroplets, *J. Chem. Phys.*, 2001, **115**, 8384-8392.

[24] R. E. Zillich, Y. Kwon and K. B. Whaley, Roton-rotation coupling of acetylene in ^{4}He, *Phys. Rev. Lett.*, 2004, **93**, 250401.

[25] M. Briant, E. Mengesha, M. A. Gaveau, B. Soep, J. M. Mestdagh, and L. Poisson, Dynamics of acetylene dimers hosted in helium droplets, *Phys. Chem. Chem. Phys.*, 2018, **20**, 2597-2605.

[26] D. A. Thomas, E. Mucha, S. Gewinner, W. Schöllkopf, G. Meijer and G. von Helden, Vibrational spectroscopy of fluoroformate, FCO_2^-, trapped in helium nanodroplets, *J. Phys. Chem. Lett.*, 2018, **9**, 2305-2310.

[27] B. J. Thomas, B. A. Harruff-Miller, C. E. Bunker and W. K. Lewis, Infrared spectroscopy of Mg–CO_2 and Al–CO_2 complexes in helium nanodroplets, *J. Chem. Phys.*, 2015, **142**, 174310.

[28] K. Nauta and R. E. Miller, Rotational and vibrational dynamics of methane in helium nanodroplets, *Chem. Phys. Lett.*, 2001, **350**, 225-232.

[29] H. Hoshina, D. Skvortsov, B. G. Sartakov and A. F. Vilesov, Rotation of methane and silane molecules in He droplets, *J. Chem. Phys.*, 2010, **132**, 074302.

[30] C. Callegari, I. Reinhard, K. K. Lehmann and G. Scoles, Finite size effects and rotational relaxation in superfluid helium nanodroplets: microwave-infrared double-resonance spectroscopy of cyanoacetylene, *J. Chem. Phys.*, 2000, **113**, 4636-4646.

[31] M. I. Sulaiman, S. Yang and A. M. Ellis, Infrared spectroscopy of methanol and methanol/water clusters in helium nanodroplets: the OH stretching region, *J. Phys. Chem. A*, 2017, **121**, 771–776.

[32] C. M. Lindsay and R. E. Miller, Rotational and vibrational dynamics of ethylene in helium nanodroplets, *J. Chem. Phys.*, 2005, **122**, 104306.

[33] I. Scheele, A. Conjusteau, C. Callegari, R. Schmied, K. K. Lehmann and G. Scoles, Near-infrared spectroscopy of ethylene and ethylene dimer in superfluid helium droplets, *J. Chem. Phys.*, 2005, **122**,104307.

[34] P. L. Raston, E. I. Obi and G. E. Douberly, Infrared spectroscopy of the entrance channel complex formed between the hydroxyl radical and methane in helium nanodroplets, *J. Phys. Chem. A*, 2017, **121**, 7597–7602.

[35] M. Kaufmann, D. Leicht, R. Schwan, D. Mani, G. Schwaab and M. Havenith, Helium droplet infrared spectroscopy of glycine and glycine–water aggregates, *Phys. Chem. Chem. Phys.*, 2016, **18**, 28082-28090.

[36] A. Vilà, M. Paniagua and M. González, Vibrational energy relaxation dynamics of diatomic molecules inside superfluid helium nanodroplets. The case of the I_2 molecule, *Phys. Chem. Chem. Phys.,* 2018, **20,** 118-130.

[37] D. Pentlehner, J. H. Nielsen, A. Slenczka, K. Mølmer and H. Stapelfeldt, Impulsive laser induced alignment of molecules dissolved in helium nanodroplets, *Phys. Rev. Lett.*, 2013, **110**, 093002.

[38] B. Shepperson, A. A. Søndergaard, L. Christiansen, J. Kaczmarczyk, R. E. Zillich, M. Lemeshko and H. Stapelfeldt, Laser-induced rotation of iodine molecules in helium nanodroplets: revivals and breaking free, *Phys. Rev. Lett.*, 2017, **118**, 203203.

[39] A. S. Chatterley, B. Shepperson and H. Stapelfeldt, Three-dimensional molecular alignment inside helium nanodroplets, *Phys. Rev. Lett.*, 2017, **119**, 073202.

[40] Y. Kwon, P. Huang, M. V. Patel, D. Blume and K. B. Whaley, Quantum solvation and molecular rotations in superfluid helium clusters, *J. Chem. Phys.*, 2000, **113**, 6469-6501.

[41] A. Vilà, M. González and R. Mayol, Photodissociation dynamics of homonuclear diatomic molecules in helium nanodroplets. The case of $Cl_2@(^4He)_N$, *J. Chem. Theory.* Comput., 2015, **11**, 899-906.

[42] A. Vilà, M. González and R. Mayol, Quantum interferences in the photodissociation of $Cl_2(B)$ in superfluid helium nanodroplets $(^4He)_N$, *Phys. Chem. Chem. Phys.*, 2015, **17**, 32241-32250.

[43] A. Vilà and M. González, Mass effects in the photodissociation of homonuclear diatomic molecules in helium nanodroplets: inelastic collision and viscous flow energy exchange regimes, *Phys. Chem. Chem. Phys.*, 2016, **18,** 27630-27638.

[44] A. Vilà, M. González and R. Mayol, Quantum dynamics of the pick up process of atoms by superfluid helium nanodroplets: the Ne + $(^4He)_{1000}$ system, *Phys. Chem. Chem. Phys.*, 2016, **18,** 2006-2014.

[45] M. Blancafort-Jorquera, A. Vilà and M. González, Quantum-classical dynamics of the capture of neon atoms by superfluid helium nanodroplets, *Phys. Chem. Chem. Phys.*, 2018, **20,** 29737-29753.

[46] A. Vilà and M. González, Reaction dynamics inside superfluid helium nanodroplets: the formation of the Ne_2 molecule from Ne + $He@(^4He)_N$, *Phys. Chem. Chem. Phys.,* 2016, **18,** 31869-31880.

[47] A. Vilà, M. González and R. Mayol, Relaxation dynamics of helium nanodroplets after photodissociation of a dopant homonuclear diatomic molecule. The case of $Cl_2@(^4He)_N$, *Phys. Chem. Chem. Phys.,* 2016, 18, 2409-2416.

[48] F. Aitken, N. Bonifaci, K. von Haeften, J. Eloranta, Theoretical modeling of electron mobility in superfluid ^4He, J. Chem. Phys., 2016, 145, 044105.

[49] D. Mateo, A. Hernando, M. Barranco, E. Loginov, M. Drabbels and M. Pi, Translational dynamics of photoexcited atoms in ^4He nanodroplets: the case of silver, *Phys. Chem. Chem. Phys.,* 2013, **15,** 18388-18400.

[50] N. B. Brauer, S. Smolarek, E. Loginov, D. Mateo, A. Hernando, M. Pi, M. Barranco, W. J. Bruma and M. Drabbels, Critical Landau velocity in helium nanodroplets, *Phys. Rev. Lett.,* 2013, **111,** 153002.

[51] A. Leal, D. Mateo, A. Hernando, M. Pi and M. Barranco, Capture of heliophobic atoms by ^4He nanodroplets: the case of cesium, *Phys. Chem. Chem. Phys.,* 2014, **16,** 23206-23213.

[52] D. Mateo, F. Gonzalez and J. Eloranta, Rotational superfluidity in small helium droplets, *J. Phys. Chem. A,* 2015, **119,** 2262-2270.

[53] F. Dalfovo, A. Lastri, L. Pricaupenko, S. Stringari and J. Treiner, Structural and dynamical properties of superfluid helium: a density-functional approach, *Phys. Rev. B: Condens. Matter Mater. Phys.,* 1995, **52,** 1193-1209.

[54] F. Ancilotto, M. Barranco, F. Caupin, R. Mayol and M. Pi, Freezing of ^{4}He and its liquid-solid interface from density functional theory, *Phys. Rev. B: Condens. Matter Mater. Phys.,* 2005, **72,** 214522.

[55] F. Thibault, K. Patkowski, P. S. Żuchowski, H. Jóźwiak, Roman Ciuryło, Piotr Wcisło, Rovibrational line-shape parameters for H_2 in He and new H_2-He potential energy surface, *Journal of Quantitative Spectroscopy & Radiative Transfer,* 2017, **202,** 308-320.

[56] M. Frigo and S. G. Johnson, The design and implementation of FFTW3, *Proc. IEE,* 2005, **93,** 216-231.

[57] A. Ralston, in *Mathematical methods for digital computers,* ed. A. Ralston and H. S. Wilf, John Wiley & Sons, New York, 1960, vol. 1, pp. 95-109.

[58] R. J. Thompson, Improving round-off in Runge-Kutta computations with Gill's method, *Commun. ACM,* 1970, **13,** 739-740.

[59] Á. Vibók and G. G. Balint-Kurti, Parametrization of complex absorbing potentials for time-dependent quantum dynamics, *J. Phys. Chem.,* 1992, **96,** 8712-8719.

[60] R. Moszynski, P. E. S. Wormer, B. Jeziorski and A. van der Avoird, Symmetry-adapted perturbation theory calculation of the He–HF intermolecular potential energy surface, *J. Chem. Phys.*, 1994, **101**, 2811-2824.

[61] Taking into account the V_{min}(HF-He) value from a more recent work (see the next ref.) it comes out that the V_{min}(HF-He)/V_{min}(H_2-He) ratio is a bit larger (3.975).

[62] J. L. Cagide Fajin, B. Fernandez, A. Mikosz and D. Farrelly, Accurate computations of the rovibrational spectrum of the He–HF van der Waals complex, *Mol. Phys.*, 2006, **104**, 1413-1420.

[63] K. P. Huber and G. Herzberg, *Constants of diatomic molecules*, Van Nostrand Reinhold, New York, 1979.

[64] A. C. Moskun and S. E. Bradforth, Photodissociation of ICN in polar solvents: evidence for long lived rotational excitation in room temperature liquids, *J. Chem. Phys.*, 2003, **119**, 4500-4515.

[65] A. C. Moskun, A. E. Jailaubekov, S. E. Bradforth, G. Tao and R. M. Stratt, Rotational coherence and a sudden breakdown in linear response seen in room-temperature liquids, *Science*, 2006, **311**, 1907-1911.

[66] J. Peng, T. C. Castonguay, D. F. Coker and L. D. Ziegler, Ultrafast H_2 and D_2 rotational Raman responses in near critical CO_2: an experimental and theoretical study of anisotropic solvation dynamics, *J. Chem. Phys.*, 2009, **131**, 054501.

[67] C. A. Rivera, N. Winter, R. V. Harper, I. Benjamin and S. E. Bradforth, The dynamical role of solvent on the ICN photodissociation reaction: connecting experimental observables directly with molecular dynamics simulations, *Phys. Chem. Chem. Phys.*, 2011, **13**, 8269-8283.

[68] A. S. Case, E. M. Miller, J. P. Martin, Y.-J. Lu, L. Sheps, A. B. McCoy and W. C. Lineberger, Dynamic mapping of CN rotation following photoexcitation of ICN^-, *Angew. Chem. Int. Ed.*, 2012, **51**, 2651-2653.

[69] M. P. Grubb, P. M. Coulter, H. J. B. Marroux, B. Hornung, R. S. McMullen, A. J. Orr-Ewing and M. N. R. Ashfold, Translational, rotational and vibrational relaxation dynamics of a solute molecule in a non-interacting solvent, *Nat. Chem.*, 2016, **8**, 1042-1046.

[70] J. Jang and R. M. Stratt, Rotational energy relaxation of individual rotational states in liquids, *J. Chem. Phys.*, 2000, **113**, 5901-5916.

[71] J. Jang and R. M. Stratt, Dephasing of individual rotational states in liquids, *J. Chem. Phys.*, 2000, **113**, 11212-11221.

[72] G. Tao and R. M. Stratt, The molecular origins of nonlinear response in solute energy relaxation: the example of high-energy rotational relaxation, *J. Chem. Phys.*, 2006, **125**, 114501.

[73] C. Bissonnette, C. E. Chuaqui, K. G. Crowell, R. J. Le Roy, R. J. Wheatley and W. J. Meath, A reliable new potential energy surface for H_2–Ar, *J. Chem. Phys.*, 1996, **105**, 2639-2653.

[74] L. Wang, M. Yang, A. R. W. McKellar and D. H. Zhang, Spectroscopy and potential energy surface of the H_2–CO_2 van der Waals complex: experimental and theoretical studies, *Phys. Chem. Chem. Phys.*, 2007, **9**, 131–137.

[75] M. Lewerenz, B. Schilling and J. P. Toennies, Successive capture and coagulation of atoms and molecules to small clusters in large liquid helium clusters, *J. Chem. Phys.*, 1995, **102**, 8191-8207.

[76] G. C. Schatz and M. A. Ratner, Quantum mechanics in chemistry, Dover, Mineola, 2002, pp. 70-74.

[77] Miquel Blancafort-Jorquera (University of Barcelona). Personal communication.

6. Vibrational energy relaxation quantum dynamics of a diatomic molecule in a superfluid liquid helium nanodroplet. Influence of the nanodroplet size, interaction energy and energy gap

6.1. Abstract

The influence of the nanodroplet size, molecule-helium interaction potential energy and $v = 1 - v = 0$ vibrational energy gap on the vibrational energy relaxation (VER) of a diatomic molecule (X_2) in a superfluid helium nanodroplet [HeND or $(^4He)_N$; T=0.37 K] was studied using a hybrid quantum approach recently proposed by us and taking as a reference the VER results on the $I_2@(^4He)_{100}$ doped nanodroplet (Vilà et al., *Phys. Chem. Chem. Phys.,* 2018, **20,** 118, which corresponds to the first theoretical study on the VER of molecules embedded a HeND). This allowed us to obtain a deep insight into the vibrational relaxation dynamics. The nanodroplet size has a very small effect on the VER as the interaction between the molecule and the nanodroplet mainly arises from the first solvation shell. Regarding the interaction potential energy and the energy gap, both factors play an important role on the VER time properties (global relaxation time, lifetime and transition time). As the former becomes stronger the relaxation time properties decrease in a significant way and this is also the case when the energy gap diminishes, both playing a comparable role on the VER. An interpretation based on the coupling terms, $\langle V_{01}^2 \rangle$, between the two vibrational levels involved and the vibrational frequency has been attempted. We expect that this work will motivate further theoretical and experimental work on this interesting relaxation process about which our knowledge is still rather limited.

6.2. Introduction

Vibrational energy relaxation (VER) is one of the most important molecular relaxations, apart from electronic relaxation, in chemical reactivity[1]. VER can take place through two different ways: by energy exchange with other atoms/molecules and by exchanging energy with other degrees of freedom of the same molecule (intramolecular vibrational relaxation).

The mechanism of VER depends on the phase in which the molecules are located. In gas phase, vibrational relaxation happens in a not very efficient manner by means of binary molecular collisions. In contrast to this, in condensed phases the number of molecules surrounding the vibrationally excited molecule is bigger, so that the exchange of energy becomes much easier[2,3]. Besides, the study of the VER processes in condensed phase also allows to obtain information on the liquid phase structure, intermolecular dynamics and solute-solvent interactions[4].

Ultrafast time-resolved spectroscopic techniques have extensively contributed to the knowledge of the VER mechanism in the condensed phase.[5,6] Pump (excite) – probe (detect) techniques are the most used spectroscopic techniques (a first ultrashort laser pulse excites the molecules and a delayed second pulse probes the vibrational populations).[2,3,7] Depending on the system under consideration, the ways to pump and probe may be different[8]: in general, excitation involves stimulated Raman scattering or infrared (IR) absorption, and the probe depends on the type of experiment. In phase coherence experiments, sub-picosecond IR pump-probe spectroscopy as well as coherent anti-Stokes Raman spectroscopy and photon echo are used to study VER.[9]

Several theoretical approaches have been developed to investigate VER in condensed phase. Using classical mechanics the friction exerted by the liquid on the vibrational motion of the solvated molecule damps its amplitude while heating the bath.[10] Langevin equation for a damped oscillator subject to a fluctuation force is applied here and relaxation takes place efficiently when the excited oscillator and solvent fluctuation frequencies coincide. This classical approach is suitable for low frequencies or high temperatures.

The first order time dependent perturbation theory is the simplest quantum approach to calculate the rate constant for the transition between two vibrational levels

(through the Fourier transform of the time correlation function of the interaction energy). The quantum time correlation function in general is not available due to the large number of solvent molecules, so approximate treatments are needed. One way to proceed is finding the classical analogous for the rate constant equation considering the detailed balance principle and the equivalence between the classical and real parts of the quantum correlation functions.[2] Then, the classical correlation function is derived from molecular dynamics (MD) simulations. Another way to treat this is by modelling the liquid as a bath of independent harmonic oscillators and then calculate the corresponding quantum correlation function.[11]

Finally, another theoretical approach is based on the real-time simulations of the VER dynamics, which has only been possible for a classical non-equilibrium MD coupled to quantum oscillators.[5,6,10] This strategy is highly demanding due to the large number of solvent molecules and the different time scales involved.

Here in the context of superfluid ^{4}He nanodroplets (HeND; T=0.37 K),[12,13,14,15] we consider real-time simulations of the VER employing a full quantum treatment of the system, which is formed by a homonuclear diatomic molecule (X_2) embedded in a HeND. This has been achieved using a hybrid approach proposed by our group,[16] which is based in a previous work of our own.[17] with significant modifications in the numerical procedure used in the time-propagation of the wave functions. These modifications are very relevant as the VER in HeND is a very slow process. In the first study of VER in HeND the (I_2(X)) molecule was investigated and the main goal of the present study is to obtain a deeper insight into the VER dynamics using the same diatomic as a reference. These quantum simulations have been feasible thanks to the use of the time dependent density functional theory (TDDFT) for the description of the superfluid helium. This has also allowed us to study the dynamics of different physico-chemical processes involving HeND (photodissociation of diatomics,[17,18,19] capture of atoms,[20,21] dimerization reactions,[22] vibrational energy relaxation[16] and HeND relaxation[23]).

The interest in HeNDs resides in their special properties such as superfluidity, chemical inert character and finite size, that have inspired important applications in the field of chemical physics/physical chemistry,[12,13,14,15] such as high resolution

spectroscopy of atoms and molecules, stabilisation of metastable species, and the synthesis of metal nanoparticles[24,25] and nanowires.[26,27]

With respect to the I_2 molecule in the electronic ground state (benchmark system), its high-resolution rovibrational spectroscopy has been widely investigated in several contexts.[28,29,30,31,32,33,34,35,36] The energy separation between two consecutive vibrational levels of $I_2(X)$ is quite small, $\nu_e = 214.502\ \mathrm{cm}^{-1}$ (308.621 K),[37] which provides a high density of vibrational states. This leads to relatively fast VER rates in comparison to other molecules, making this system particularly attractive to be studied. Thus, e.g., the VER of $I_2(X)$ has been examined in the gas phase (He-$I_2(X)$ mainly[38,39,40]) and condensed media such as mesitylene[41] and liquid Xe.[42,43,44,45,46,47,48,49,50,51,52,53]

Rovibrational spectroscopy has been well studied in HeNDs[12,13,14] and this solvent induces small band broadening and vibrational line shifts (typically less than 2 cm^{-1}). As the interaction with the helium solvent is weak the vibrational symmetry of the molecule is not modified in liquid helium. Moreover, only a few studies have been reported on the VER of molecules in helium nanodroplets and they consider, e.g., IR spectroscopy and bolometric detection of some molecules and binary complexes[54,55,56,57].

The VER of HF($\nu = 1$) in HeND is very slow ($t \geq 0.5$ ms)[56] due to its large vibrational energy gap ($\nu_e = 4138.32\ \mathrm{cm}^{-1}$ (5954.12 K)),[37] which leads to an important metastability. The nanodroplet size dependent line shifts and broadening indicate that the coupling of the HF vibration with the HeND surface excitations (ripplons) is the main relaxation mechanism.[56] For binary complexes of HF such as Ne, Ar, Kr-HF(ν), the relaxation takes place in similar time scales to the HF case and the relaxation rate is also size dependent.[57]

Furthermore, the vibrational relaxation and dephasing of some alkali dimers (Rb_2, Na_2 and K_2) placed in a dimple on the surface of a HeND[58,59,60] and the photoinduced non-adiabatic dynamics of Na_3 and K_3 in quartet states (also formed on the HeND surface) have been also studied,[61] providing information on the $Na_3(2^4E')$ VER. Besides, the de-alignment of the $I_2(X)$ rotation in HeNDs has been also reported.[62]

This chapter is organised as follows. The hybrid quantum method employed in the simulation of the real-time VER dynamics is described in Section 6.3. The main results

obtained for the several initial conditions explored are presented and discussed in Section 6.4. The summary and conclusions are presented in Section 6.5. Finally, some additional information is given in Section 6.6

6.3. Theoretical methods

As the same methodology used in ref. 16 has been employed here, only a brief description of the main aspects is given. At the low temperature of the HeND ($T = 0.37\ K$) only the vibrational ground state ($v = 0$) of the molecule is populated in the thermal equilibrium. The zero time condition of the dynamics is then represented by the helium density corresponding to the $I_2(X,v{=}0)@^4He_N$ ground state doped nanodroplet, but with a sudden change of the I_2 vibrational wave function from $v{=}0$ to the first excited vibrational level ($v{=}1$). The global vibrational relaxation process can be represented as:

$$I_2(X, v{=}0)@^4He_N + h\nu \rightarrow [I_2(X, v{=}1)@^4He_N]^* + h\nu'$$

$$[I_2(X, v{=}1)@^4He_N]^* \rightarrow [I_2(X, v{=}0)@^4He_{N'}]^* + (N\text{-}N')^4He \qquad (6.1)$$

, where the vibrational relaxation time does not necessarily coincide with the liquid helium relaxation time.

The impurity is placed in the centre of the nanodroplet in the ground state. This fact, and the symmetry of the system allows us keeping frozen the I_2 centre of mass (CM) during the VER dynamics.[16,17] Furthermore, as the mass of the I_2 CM is much bigger than that of and He atom the classical description of this degree of freedom is justified (i.e., the zero-point motion of the I_2 CM is not considered). In this study the rotational degrees of freedom of the molecule have not been taken into account.

The real-time quantum simulations of VER have been performed following the "divide and conquer" strategy, combining a commonly used method to study rather large systems of the bosonic superfluid liquid ^{4}He (TDDFT)[16,17,18,19,20,21,22,23,63,64,65,66] and a usual method to study atoms and molecules in gas phase (time dependent wave function)[16,17,18,19, 20 ,22].

In the TDDFT calculations the Orsay Trento (OT) phenomenological density functional[67] has been used, and the non-local contributions to the helium correlation energy and the back-flow terms have been neglected for computational reasons, as usual.[16,17,18,19,20,21,22,23,63,64,65,66] A modification has been added to the OT functional in order to avoid unphysical helium densities when the interaction between the dopant molecule and helium is strong[68]. The X_2 vibrational degree of freedom has been described using standard quantum mechanics, employing suitable time dependent wave functions.

Using this hybrid approach the equations of motion are found by minimising the quantum action ($\mathcal{A}$):

$$\mathcal{A}[\Psi_{He}, \varphi_{X_2}] = \int dt \left\{ E[\Psi_{He}, \varphi_{X_2}] - i\hbar \int d\boldsymbol{R_{He}} \Psi^*_{He}(\boldsymbol{R_{He}}) \frac{\partial}{\partial t} \Psi_{He}(\boldsymbol{R_{He}}) \right.$$
$$\left. - i\hbar \int dr \varphi^*_{X_2}(r) \frac{\partial}{\partial t} \varphi_{X_2}(r) \right\} \tag{6.2}$$

, where $\Psi_{He}(\boldsymbol{R_{He}}, t)$ is the complex effective wave function describing the liquid helium ($|\Psi_{He}(\boldsymbol{R_{He}}, t)|^2 \equiv \rho_{He}(\boldsymbol{R_{He}}, t)$), $\varphi_{X_2}(r)$ is the vibrational wave function and E is the total energy of the system.

The quantum action must be minimised by taking variations with respect to each one of the wave functions to obtain two coupled time dependent Schrödinger-like nonlinear equations that rule the evolution of helium and the diatomic molecule respectively:

$$i\hbar \frac{\partial}{\partial t} \Psi_{He}(\boldsymbol{R_{He}}) = \left[-\frac{\hbar^2}{2m_{He}} \boldsymbol{\nabla}^2 + \int dr V_{He-X_2}(r, \boldsymbol{R_{He}}) \left|\varphi_{X_2}(r)\right|^2 + \frac{\delta \varepsilon_c[\rho_{He}]}{\delta \rho_{He}} \right] \Psi_{He}(\boldsymbol{R_{He}}) \tag{6.3}$$

$$i\hbar \frac{\partial}{\partial t} \varphi_{X_2}(r) = \left[-\frac{\hbar^2}{2\mu_{X_2}} \frac{\partial^2}{\partial r^2} + \int d\boldsymbol{R_{He}} V_{He-X_2}(r, \boldsymbol{R_{He}}) \rho(\boldsymbol{R_{He}}) + V_{X_2}(r) \right] \varphi_{X_2}(r) \tag{6.4}$$

, where μ_{X_2} is the reduced mass of X_2. The $\varepsilon_c[\rho_{He}]$ term corresponds to the potential energy and correlation energy densities of superfluid liquid helium. The term $V_{He-X_2}(r, \boldsymbol{R_{He}})$ stands for the interaction potential energy between helium and the X_2 molecule, which has been taken from ref. 69. The $V_{I_2}(r)$ potential energy curve describing the interaction between the two atoms of the molecule has been described by a Morse

function (eq. (4)), using the experimental parameters from ref. 37 ($r_e = 2.6663$ Å, $D_e = 18052.42\ K$ and $a = 1.857608$ Å^{-1}), where

$$V(r) = D_e\left(1 - e^{-a(r-r_e)}\right)^2 \tag{6.5}$$

Equations (6.3) and (6.4) are identical to those employed in the photodissociation of Cl_2(B←X) in HeNDs.[17] However, this process is very different from the VER process, where the relative coordinate wave function always is placed around the equilibrium distance, r_e, of the X_2 potential energy curve. In this case, we have applied in our group a much more efficient strategy to calculate the time evolution of the system.[16] Thus, the $\varphi_{X_2}(r)$ vibrational wave function has been expressed as a linear combination of the vibrational eigenfunctions basis set $\{\varphi_i(r)\}$ of the vibrational Hamiltonian operator of the isolated molecule:

$$\varphi_{X_2}(r) = \sum_i c_i \varphi_i(r) \tag{6.6}$$

Equation (6.4) can now be transformed into equation (6.8), which can be solved in a more efficient way in terms of the numerical accuracy and computational time. Then, to describe the VER dynamics the following equations have been propagated in time:

$$i\hbar \frac{\partial}{\partial t}\Psi_{He}(\boldsymbol{R_{He}}) = \left[-\frac{\hbar^2}{2m_{He}}\boldsymbol{\nabla}^2 + \sum_{i,j} c_i^*(t)c_j(t)V_{ij}(\boldsymbol{R_{He}}) + \frac{\delta\varepsilon_c[\rho_{He}]}{\delta\rho_{He}}\right]\Psi_{He}(\boldsymbol{R_{He}}) \tag{6.7}$$

$$i\hbar \frac{dc_i(t)}{dt} = E_{vib,i}c_i(t) + \sum_j c_j(t)\langle i|\int d\boldsymbol{R_{He}} V_{He-X_2}(r, \boldsymbol{R_{He}})\rho_{He}(\boldsymbol{R_{He}})\,|j\rangle$$

$$i = 0, 1, 2, \ldots n \tag{6.8}$$

, where $\{E_{vib,i}\}$ are the corresponding vibrational energy eigenvalues, and the helium coordinate-dependent potential energy matrix elements, $V_{ij}(\boldsymbol{R_{He}})$, are equal to

$$V_{ij}(\boldsymbol{R_{He}}) = \langle i|V_{He-X_2}|j\rangle = \int dr dr' \langle i|r\rangle\langle r|V_{He-X_2}|r'\rangle\langle r'|j\rangle$$

$$= \int dr V_{He-X_2}(r, \boldsymbol{R_{He}})\varphi_i^*(r)\varphi_j(r) \tag{6.9}$$

To converge the calculations for the initial excited vibrational level $v = 1$ it has been enough to include in the calculations all vibrational levels from $v = 0$ up to $v_{max} = v + 3$ ($v_{max} = 4$ in this case). This strategy is highly computational efficient for the numerical description of φ_{X_2}.

The determination of the initial time ground state $I_2(X, v = 0)@^4He_N$ configuration has been obtained by finding the stationary solution of eq. (6.7) but keeping fixed the vibrational wave function to the $v = 0$ one ($c_0 = 1, c_i = 0, i \neq 0$). This approximation is acceptable because of the large differences between the involved energies (I_2 chemical bond versus van der Waals (vdW) I_2-He interaction), and has been validated in the dynamical calculations (the asymptotic $\varphi_{X_2}(r)$ that corresponds to the global relaxation time is just equal to $\varphi_0(r)$).

Equation (6.7) has been solved numerically discretising the space in a grid of points in which the spatial derivatives of the kinetic energy terms have been calculated using the fast Fourier transform (FFT)[70]. The numerical time integration has been performed employing a fourth order predictor-corrector method[71], initiated by a fourth order Runge-Kutta method[72] (time step=1.0×10^{-3} ps).

The Cartesian grid has a spacing of 0.40 Å for the x and y axes and of 0.30 Å for the z axis (where the molecule is placed) and each axis has a total length of 38 Å. A quartic negative imaginary potential (NIP)[73] has been defined in the edges of the grid, so as to absorb possible fragments of the helium wave function off the droplet that come from the evaporation of helium (avoiding in this way artificial reflections). The NIP has the following expression:

$$V_{NIP} = -iA\frac{5}{2}\left(\frac{d - d_{NIP}}{L}\right)^4 \tag{6.10}$$

where the absorption strength (A) is equal to 331.0 K, the length (L) has a value of 1.0 Å, and the NIP has been placed (d_{NIP}) at a distance of 1.0 Å before the limit of the grid.

The numerical time integration of eq. (6.8) takes benefit from the basis set expansion of $\varphi_{X_2}(r)$. For the evaluation of the required integrals the basis set functions have been discretised into a grid of 1000 points between r=2.3 Å and 3.5 Å. To integrate in time, for each time step $t \rightarrow t + \delta t$ the full Hamiltonian of the diatomic molecule (Eq.

(6.8)) is diagonalized, and the time evolution from t to $t + \delta t$ is determined in terms of the stationary states $\{|\alpha\rangle\}$. Then we come back to the original basis set $\{|i\rangle\}$, and the procedure is repeated for the new time, $t + \delta t$, to determine the evolution to $t + 2\delta t$, and so on.[16] The analogous procedure used for the propagation of the rotational wave function can be seen in the previous chapter. The parameters of the grids, NIP and time steps have been taken from ref. 16.

6.4. Results and discussion

To analyse the influence of the nanodroplet size, molecule-helium interaction potential and vibrational energy separation of the molecule on the VER, a number of simulations have been performed. In this study, these variables have been modified taking as a reference the VER of a I_2(X) molecule, embedded in a nanodroplet of 100 ^{4}He atoms, from $v = 1$ to $v = 0$, which was studied in ref. 16.

For the nanodroplet size the number of ^{4}He atoms has been taken as equal to N=50, 100, 150 and 200; for the effect of the molecule-nanodroplet interaction energy the I_2-HeND interaction potential has been multiplied by several scalar factors ($V = xV_{I_2-He}$ with x=1.50, 1.25, 1.00, 0.75 and 0.50); and the vibrational energy separation has been modified changing the equilibrium frequency of the oscillator, ν_e: $E_{vib}(v) = h\nu_e\left(v + \frac{1}{2}\right) - h\nu_e x_e\left(v + \frac{1}{2}\right)^2$, where $\nu_e = x\nu_{e,I_2}$ with x=1.50, 1.25, 1.00 and 0.75.

6.4.1. Vibrational relaxation vs. nanodroplet size

The helium density of the I_2(X,v=0)@^{4}He$_N$ in the ground state is shown in Figure 6.1. The nanodroplet size has a very small effect on the vibrational energy relaxation (Figure 6.2). This happens in this way because the interaction energy of the molecule with the nanodroplet essentially arises from the first solvation layer, which is very large in comparison to the other ones and is completely defined for all the nanodroplet sizes (Figure 6.1), due to the relatively strong I_2-He interaction potential energy.

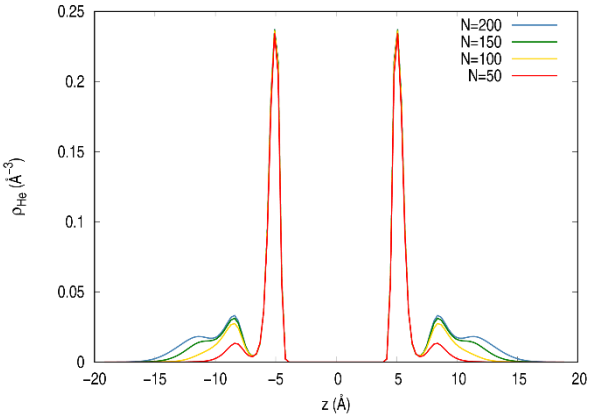

Figure 6.1 Helium density of the $I_2(X,v=0)@^4He_N$ nanodroplet in the ground state along the molecular axis (z axis), with N=50, 100, 150 and 200.

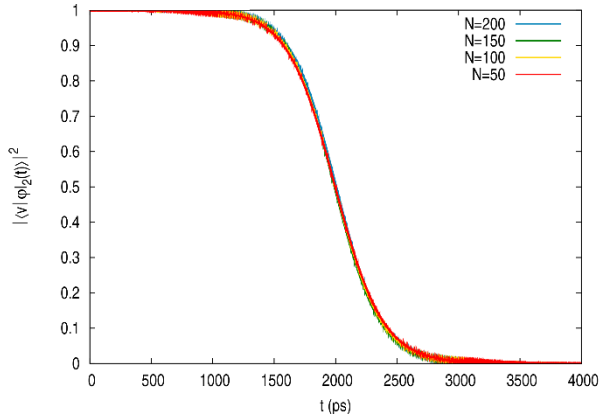

Figure 6.2 Populations of the v=1 excited vibrational state as a function of time for N=50, 100, 150 and 200.

6.4.2. Vibrational energy relaxation vs. I_2-He interaction potential

The shape of the nanodroplet helium density is quite affected by the "I_2-He" interaction potential energies selected (Figure 6.3). For the stronger interaction potential energies the first and second solvation shells are denser. The nanodroplet radius (~15 Å) is essentially not affected by the interaction potential, which means that the interaction potential energies mainly affect the density of the solvation shells.

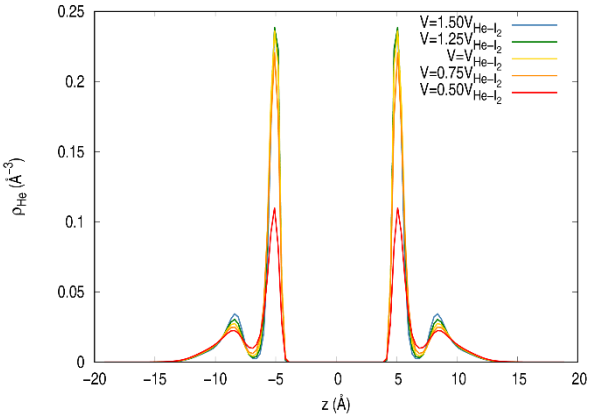

Figure 6.3 Helium density of the $I_2(X,v=0)@^4He_{100}$ nanodroplet in the ground state along the molecular axis (z axis) for $V=xV_{I_2\text{-}He}$ with x=1.50, 1.25, 1.00, 0.75 and 0.50.

Vibrational relaxation is clearly faster for increasing "I_2-He" interaction potentials energies (Figure 6.4). The time scales involved in the vibrational relaxation from $v = 1$ to $v = 0$ for the five selected "I_2-He" interaction potential energies are shown in Table 6.1 and Figure 6.5. The global relaxation time is defined as the time it takes for the whole relaxation to occur, this is from $t = 0$ to the time at which the population of the excited vibrational state is equal to 1%; the lifetime is taken from $t = 0$ to the time at which the population of this state is 50%; and the transition time is the time needed for the population of the excited state to decrease from 99 to 1%. All three relaxation time properties decrease in a substantial way with increasing interaction potential energies and tend towards an asymptotic behaviour. More concretely, taking as a reference the results for x=1.00 the lifetime is equal to 4.87, 1.84, 1.00. 0.40 and 0.22 for x=0.50, 0.75, 1.00, 1.25 and 1.50 respectively, and similar values are obtained for the other time properties (with the exception of the transition time for x=0.50 (3.88)). This results will be interpreted at the end of this section.

The time evolution of the energies and number of helium atoms of the HeND and the increments with respect to t=0 are shown in Figure 6.6 and Figure **6.7**, respectively. The temporal evolution of the vibrational energy implied in the VER process follows the same pattern as the populations with respect to the changes in the "I_2-He" interaction potential and changes from 460 to 154 K. The helium nanodroplet energy increases ~4 K during the relaxation, as a result of the evaporation of a single ^{4}He atom. The interaction energy between the diatomic molecule and the helium nanodroplet changes very little as a result of the relaxation process (of the order of 0.1 K), as the helium nanodroplet structure is

not affected. And only small oscillations can be seen during the transitions which vary from ≈ -3 to 4 K and ≈ -0.5 to 0.5 K from stronger to weaker interaction potential energies. As a result of the single ^{4}He atom evaporated from the nanodroplet, the total energy of the doped nanodroplet decreases ≈300 K for all cases.

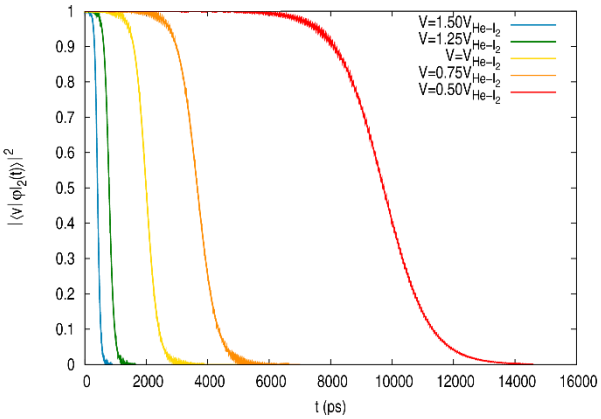

Figure 6.4 Populations of the ν=1 excited vibrational state as a function of time for V=$xV_{I_2\text{-}He}$, with x=1.50, 1.25, 1.00, 0.75 and 0.50.

The expected value of the V_{01}^2 coupling term, $\langle V_{01}^2 \rangle$, as a function of the interaction potential energy is presented in Table s6.1. It can be seen that $\langle V_{01}^2 \rangle$ increases with the potential energy. From the analysis of the inverse of the relaxation time properties as a function of $\langle V_{01}^2 \rangle$ it comes out that there is an approximate linear relation between these properties and $\langle V_{01}^2 \rangle$ (Figure s6.1). This dependence is close to that given by the Fermi golden rule for the transition probability between two states.[74]

Table 6.1 Global relaxation times, lifetimes and transition times of the $\nu = 1$ excited vibrational state for the five "I_2-He" potential energies considered (V=$xV_{I_2\text{-}He}$).

x	Global Relax. time (ps)	Lifetime (ps)	Transition time (ps)
0.50	13060	9721	6705
0.75	5094	3661	2856
1.00	2873	1995	1726
1.25	1176	789	748
1.50	640	413	432

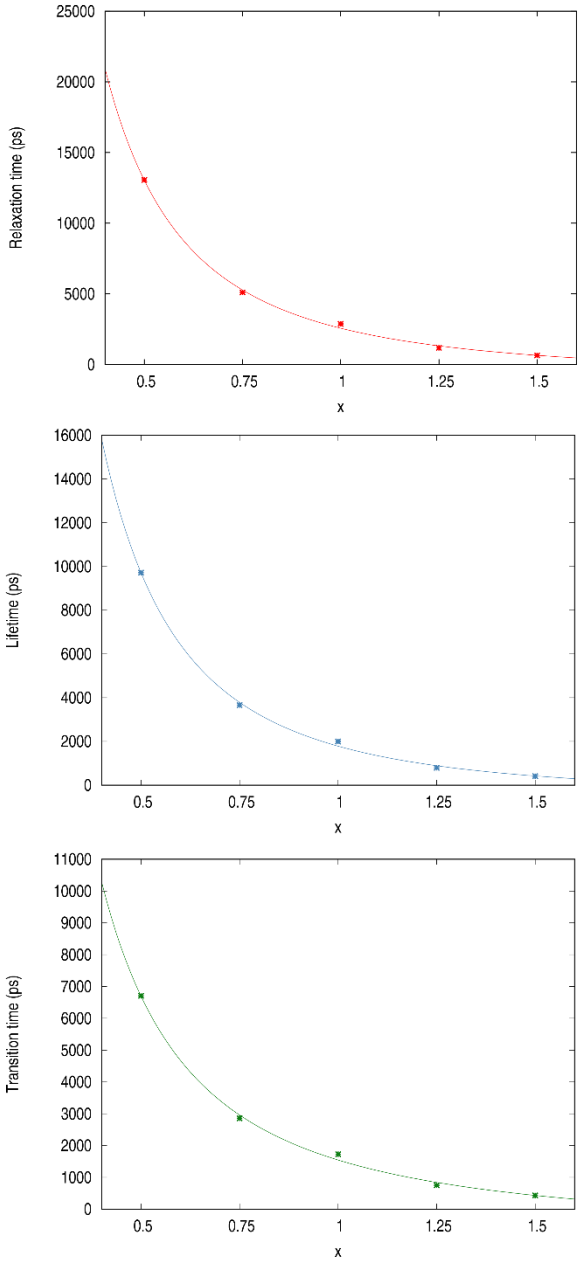

Figure 6.5 Global relaxation times (top), lifetimes (middle) and transition times (bottom) of the v=1 excited vibrational state, as a function of x (V=$xV_{I_2\text{-}He}$), and fitting curve (quadratic polynomial).

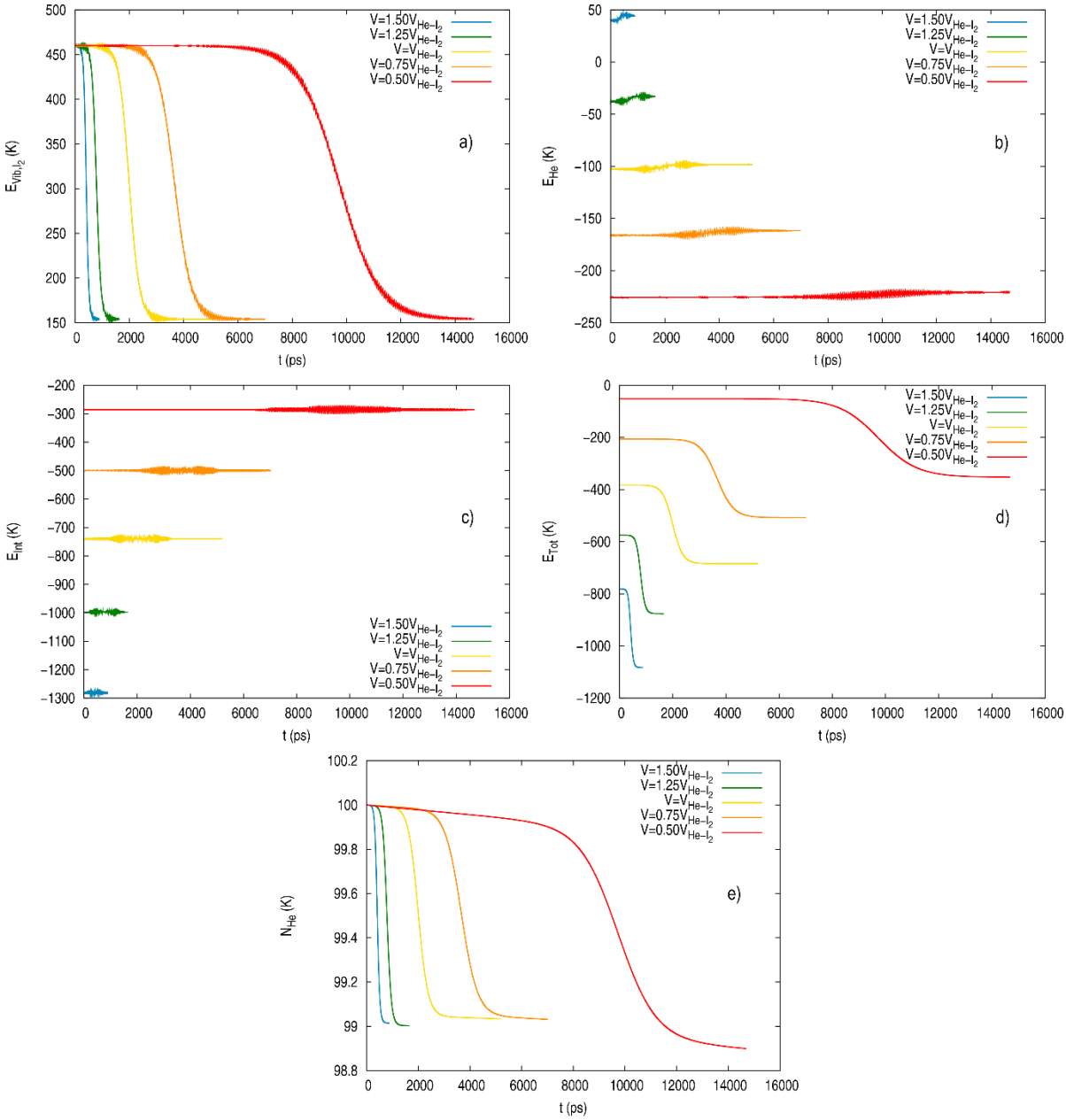

Figure 6.6 Energies involved in the vibrational relaxation from the $v = 1$ state at the five selected "I_2-HeND" interaction potential energies and the number of ^{4}He atoms of the nanodroplet, as a function of time: a) vibrational energy of the molecule; b) energy of the helium nanodroplet; c) molecule-nanodroplet interaction energy; d) total energy of the system (I_2@HeND); e) number of ^{4}He atoms of the HeND.

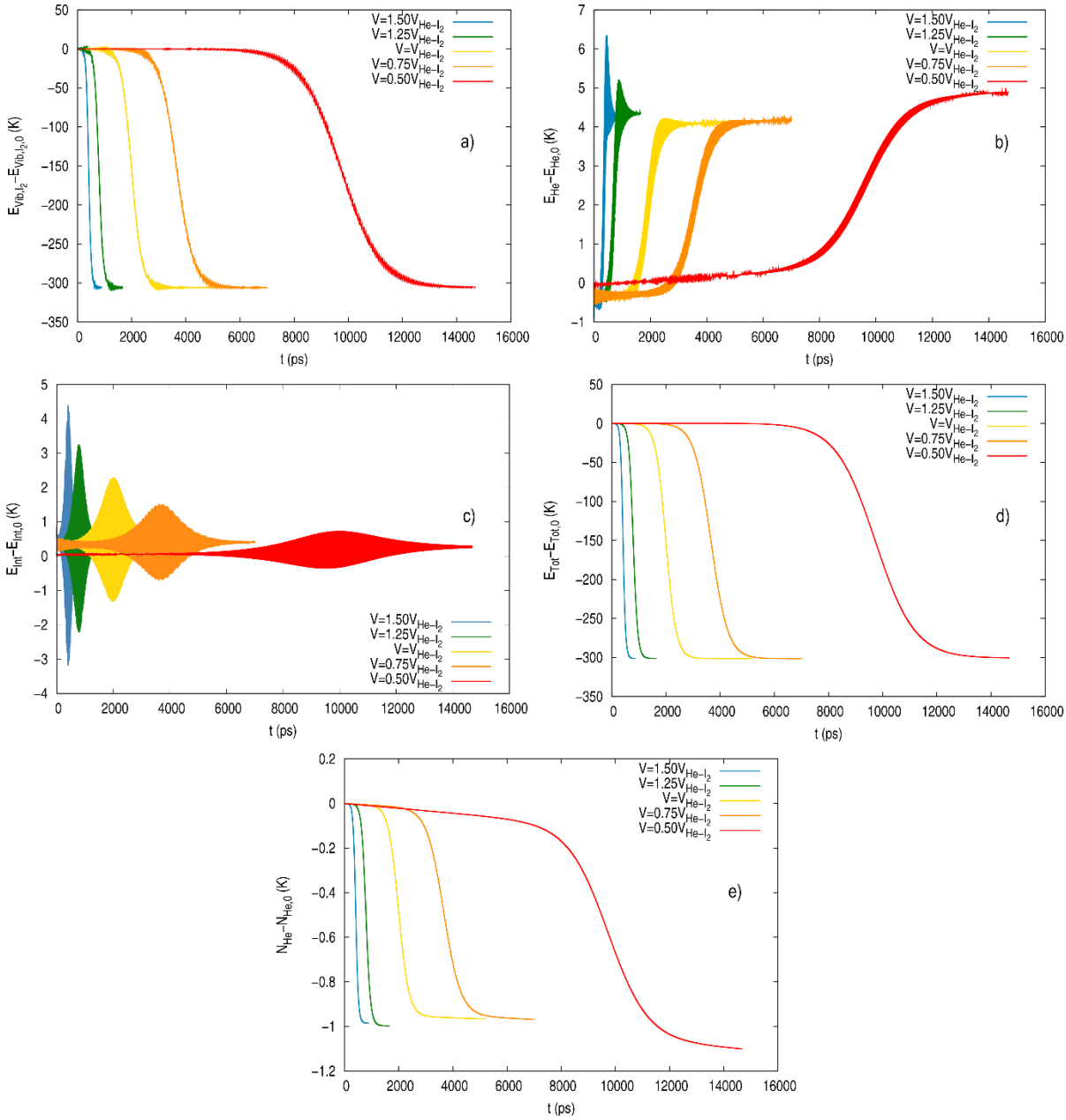

Figure 6.7 Energy increments involved in the vibrational relaxation from the $v = 1$ state at the five selected "I_2-HeND" interaction potential energies and the number of ^{4}He atoms of the nanodroplet, as a function of time: a) vibrational energy of the molecule; b) energy of the helium nanodroplet; c) molecule-nanodroplet interaction energy; d) total energy of the system (I_2@HeND); e) number of ^{4}He atoms of the HeND.

6.4.3. Vibrational relaxation vs. energy gap

Changes in the oscillator frequency affects the energies of the vibrational levels and the gaps between them, and the energy gaps between the $|v = 1\rangle$ and $|v = 0\rangle$ vibrational states of the diatomic molecule take the following values: $\Delta E_{vib,1-0} =$ 230, 306, 382 and 457 K for the $\nu_e = 0.75\nu_{e,I_2}, 1.00\nu_{e,I_2}, 1.25\nu_{e,I_2}$ and $1.50\nu_{e,I_2}$ frequencies

analysed, respectively. So as the energy separation increases relaxation is expected to be more difficult (this will be confirmed below).

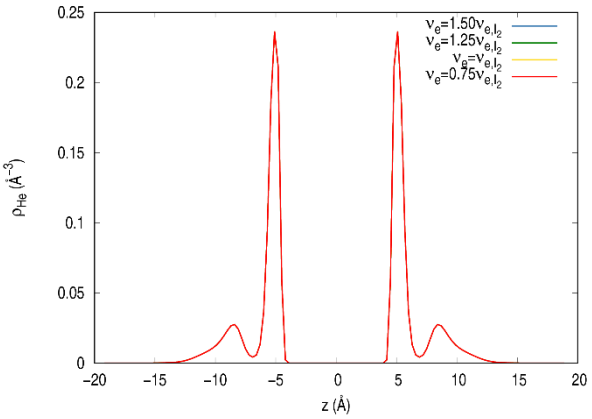

Figure 6.8 Helium density of the I_2(X,v=0)@$^4He_{100}$ nanodroplet in the ground state along the molecular axis (z axis) for $\nu_e = x\nu_{e,I_2}$ with x=1.50, 1.25, 1.00 and 0.75.

The structure of the vibrational wave function is very little affected by the equilibrium frequencies of the I_2(X) Morse oscillator, and for this reason the initial helium density is identical for all cases studied in this section (Figure 6.8). Moreover, Figure 6.9 shows that the changes in the frequency of the Morse oscillator lead to important changes in the VER time properties. The global relaxation times, lifetimes and transition times of the four cases considered are shown in Table 6.2 and Figure 6.10. It can be seen that the bigger the frequency of the oscillator the slower relaxation is (approximately linear dependence for the interval of frequencies investigated). If we take as a reference the time properties obtained when x=1.00, the lifetime values are 0.35, 1.00, 1.90 and 3.05 for x=0.75, 1.00, 1.25 and 1.50, respectively, the other properties taking similar values (with the exception of the global relaxation and transition times for x=1.50 (2.73 and 2.60, respectively)). These results will be interpreted at the end of this section.

During the VER analogous patterns are seen in the evolutions of the energies and number of ^{4}He atoms of the nanodroplet, with the transition from v=1 to v=0 happening faster for smaller oscillator frequencies (i.e., for lower vibrational energy gaps); Figure 6.11. The vibrational energy of the molecule decreases according to the energy gap and the helium energy of the nanodroplet increases ≈4 K. Small changes in the interaction energy from -0.5 to 0.5 K with oscillations of about 3-3.5 K during transitions denote that the structure of the liquid helium does not change significantly during the VER. Changes in the total energy of the doped nanodroplet are similar to the vibrational energy released,

which means that, for bigger vibrational energy gaps, the single evaporated ^{4}He atom carries with it larger kinetic energy, and the final helium energy of the nanodroplet is similar for all cases.

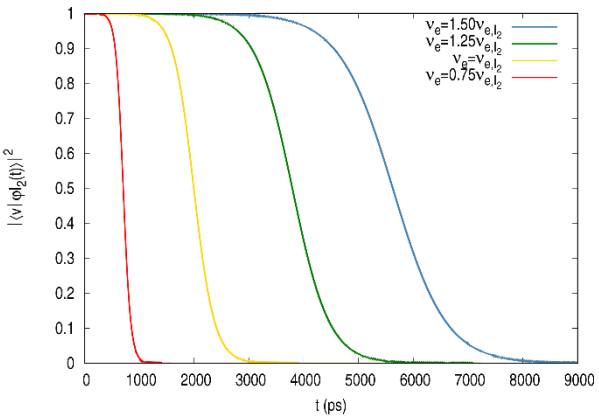

Figure 6.9 Populations of the v=1 excited vibrational state as a function of time for $\nu_e = x\nu_{e,I_2}$ with x=1.50, 1.25, 1.00 and 0.75.

The dependence of $\langle V_{01}^2 \rangle$ with respect to the energy gap is presented in Table s6.2, which shows that this term increases moderately with the energy gap. According to this the relaxation time properties values should decrease as the energy gap increases. However, from the dynamics results the opposite trend is found. This means that there is another factor that is playing a dominant role here. The results obtained for the rotational relaxation suggest, by analogy, that the velocity of the oscillator ($\langle v_{oscillator}^2 \rangle^{1/2} \propto \nu_e^{1/2}$) could be involved making the VER process more difficult as it increases. Unfortunately, the information available does not allow us to characterise the dependence of the time relaxation properties with respect to $\langle V_{01}^2 \rangle$ and $\nu_e^{1/2}$.

Table 6.2 Global relaxation times, lifetimes and transition times of the $v = 1$ excited vibrational state for the four vibrational frequencies ν_e considered ($\nu_e = x\nu_{e,I_2}$).

x	Global Relax. time (ps)	Lifetime (ps)	Transition time (ps)
0.75	1027	707	628
1.00	2873	1995	1726
1.25	5334	3793	3101
1.50	7842	6079	4493

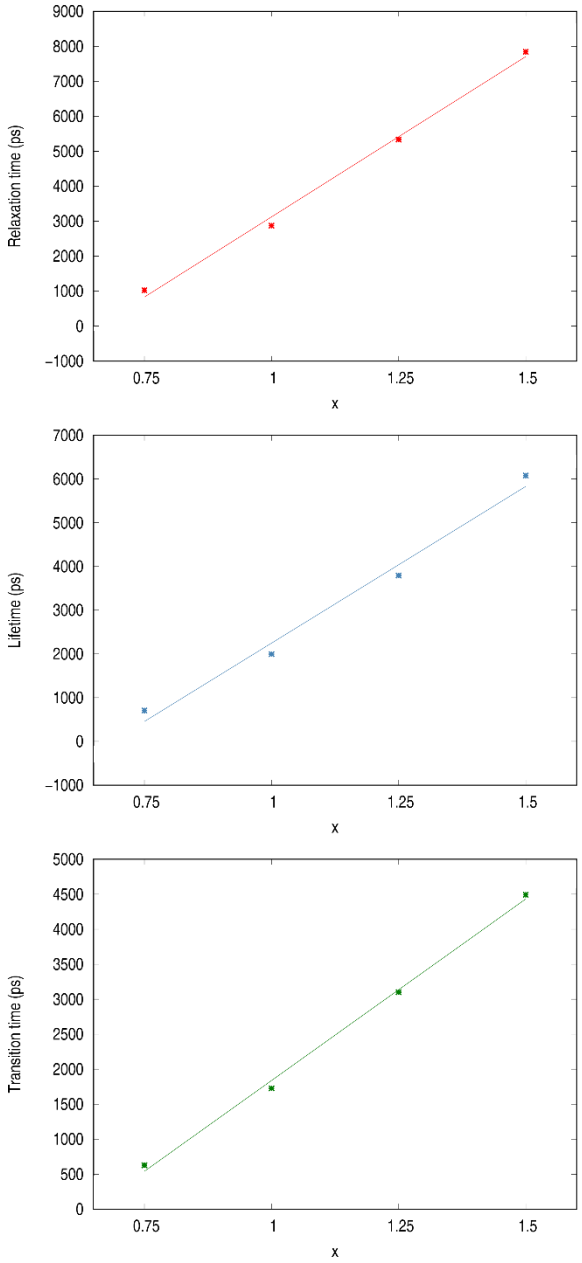

Figure 6.10 Global relaxation times (top), lifetimes (middle) and transition times (bottom) of the v=1 excited vibrational state, as a function of $x(\nu_e = x\nu_{e,I_2})$.

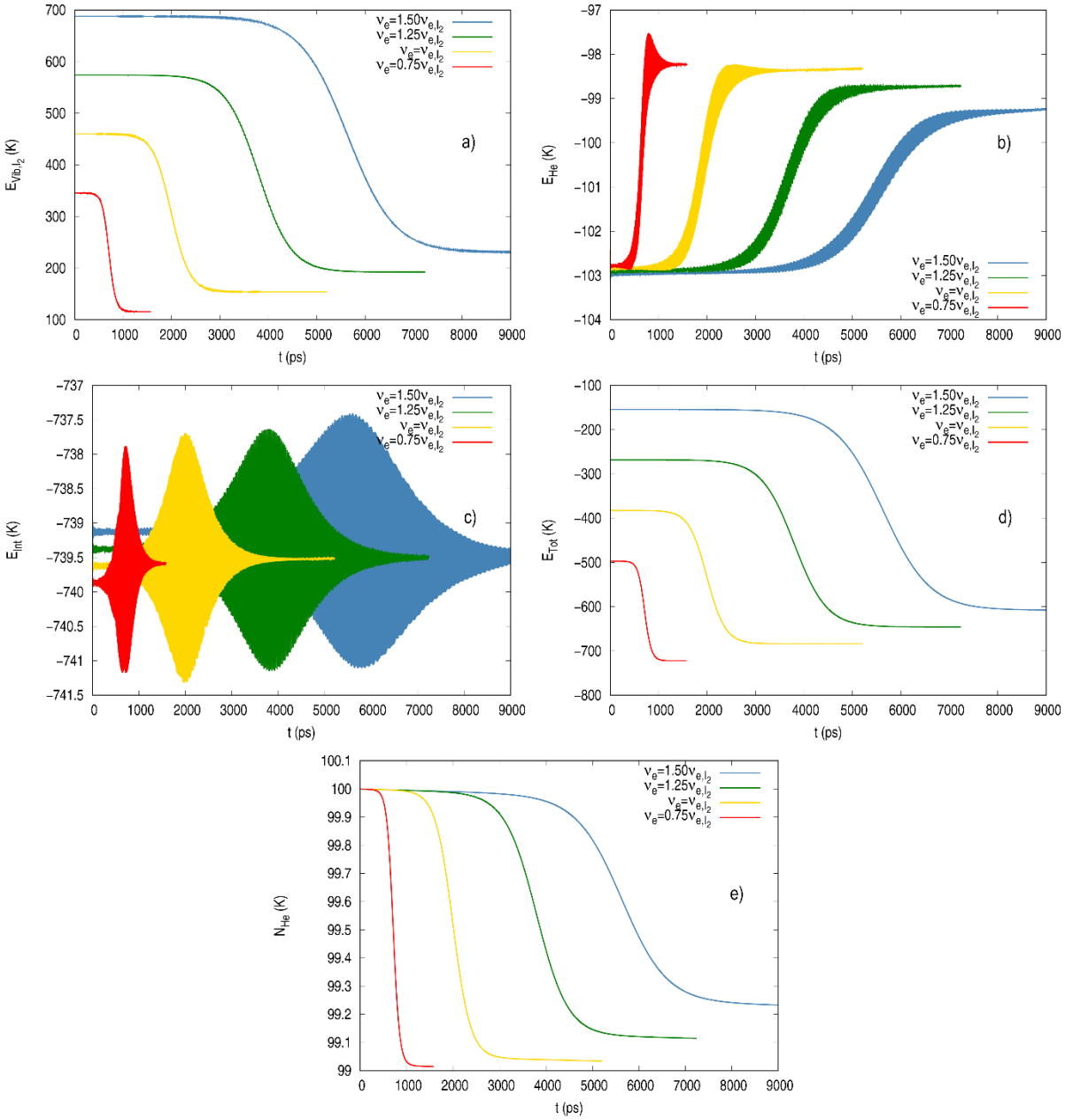

Figure 6.11 Energies involved in the vibrational relaxation from the $v = 1$ state at the four ν_e vibrational frequencies selected and the number of ^{4}He atoms of the nanodroplet, as a function of time: a) vibrational energy of the molecule; b) energy of the helium nanodroplet; c) molecule-nanodroplet interaction energy; d) total energy of the system (I_2@HeND); e) number of ^{4}He atoms of the HeND.

6.5. Summary and conclusions

The VER of a homonuclear diatomic molecule (X_2) inside a HeND has been investigated using a hybrid quantum approach. The helium and X_2 molecule have been described using TDDFT and standard quantum dynamics methods, respectively, as in ref. 16.

This works complements and extends a very recent study carried out by our group, where the VER in HeNDs was studied for the first time.[16] Thus, taking as a reference the $I_2(X)@(^4He)_{100}$ system, we have obtained a deeper insight into the vibrational relaxation dynamics through the analysis of the influence of the nanodroplet size (N=50, 100, 150 and 200), molecule-helium interaction potential energy ($V = xV_{I_2-He}$ with x = 0.50, 0.75, 1.00, 1.25 and 1.50) and v=1-v=0 vibrational energy gap ($\nu_e = x\nu_{e,I_2}$ with x=0.75, 1.00, 1.25 and 1.50) on this process.

The results show that the nanodroplet size has a little effect on the VER dynamics, as the interaction between the molecule and the liquid helium is mainly due to the first solvation shell (due to the relatively large I_2-He interaction it is fully formed for all the nanodroplet sizes studied). The interaction potential energy and the energy gap have an important influence on the VER time properties, which decrease in a significant way as the interaction potential energy is stronger and the vibrational energy gap decreases. Furthermore, the molecule-helium interaction energy is hardly modified during the relaxation process, but it shows oscillations during the transition, which means that the nanodroplet structure is essentially unchanged. An interpretation based on the coupling terms, $\langle V_{01}^2 \rangle$, between the two vibrational levels involved and the oscillator velocity (that is proportional to $\nu_e^{1/2}$) has been attempted.

We encourage further theoretical and experimental research on this important relaxation process in HeNDs about which our knowledge is still very scarce.

6.6. Appendix 6: Supplementary information

Table s6.1 Inverse of the global relaxation times, lifetimes and transition times of the $v = 1$ excited state and $\langle V_{01}^2 \rangle$ coupling terms for the five interaction potential energies considered ($V=xV_{I_2\text{-}He}$).

x	$\langle V_{01}^2 \rangle$ (K²)	1/Global Relax. time (ps⁻¹)	1/Lifetime (ps⁻¹)	1/Transition time (ps⁻¹)
1.50	5.98	$1.56 \cdot 10^{-3}$	$2.31 \cdot 10^{-3}$	$2.42 \cdot 10^{-3}$
1.25	3.09	$8.50 \cdot 10^{-4}$	$1.34 \cdot 10^{-3}$	$1.27 \cdot 10^{-3}$
1.00	1.56	$3.48 \cdot 10^{-4}$	$5.79 \cdot 10^{-4}$	$5.01 \cdot 10^{-4}$
0.75	0.61	$1.96 \cdot 10^{-4}$	$3.50 \cdot 10^{-4}$	$2.73 \cdot 10^{-4}$
0.50	0.15	$7.66 \cdot 10^{-5}$	$1.49 \cdot 10^{-4}$	$1.03 \cdot 10^{-4}$

Table s6.2 Inverse of the global relaxation times, lifetimes and transition times of the $v = 1$ excited state, $\langle V_{01}^2 \rangle$ coupling terms and $\sqrt{x}$ for the four vibrational frequencies ν_e considered ($\nu_e = x\nu_{e,I_2}$).

x	$\sqrt{x}$	$\langle V_{01}^2 \rangle$ (K²)	1/Global Relax. time (ps⁻¹)	1/Lifetime (ps⁻¹)	1/Transition time (ps⁻¹)
0.75	0.87	1.16	$9.74 \cdot 10^{-4}$	$1.59 \cdot 10^{-3}$	$1.41 \cdot 10^{-3}$
1.00	1.00	1.56	$3.48 \cdot 10^{-4}$	$5.79 \cdot 10^{-4}$	$5.01 \cdot 10^{-4}$
1.25	1.12	1.93	$1.87 \cdot 10^{-4}$	$3.22 \cdot 10^{-4}$	$2.64 \cdot 10^{-4}$
1.50	1.22	2.30	$1.28 \cdot 10^{-4}$	$2.23 \cdot 10^{-4}$	$1.65 \cdot 10^{-4}$

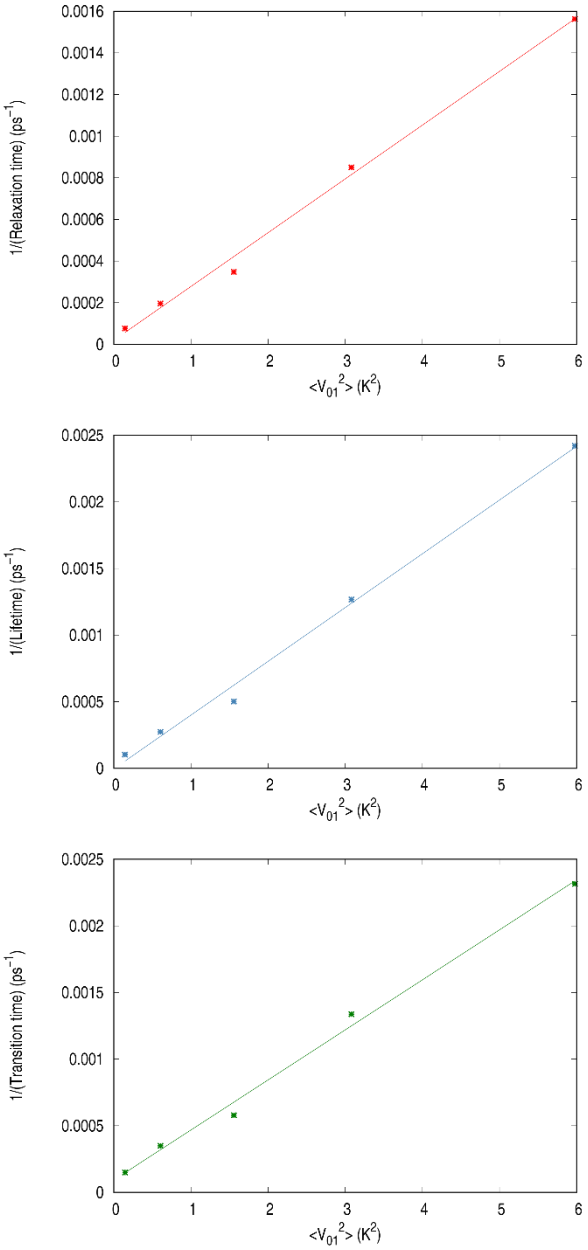

Figure s6.1 Inverse of the global relaxation times (top), lifetimes (middle) and transition times (bottom) of the ν=1 excited state, as a function of the $\langle V_{01}^2 \rangle$ coupling term for the different interaction potential energies.

6.7. References

[1] R. D. Levine, *Molecular reaction dynamics,* Cambridge University Press, Cambridge, 2005.

[2] D. W. Oxtoby, Vibrational population relaxation in liquids, *Adv. Chem. Phys.,* 1981, **47,** 487-519.

[3] D. W. Oxtoby, Vibrational relaxation in liquids: quantum states in a classical bath, *J. Phys. Chem.,* 1983, **87,** 3028-3033.

[4] Q. Shi and E. Geva, Semiclassical theory of vibrational energy relaxation in the condensed phase, *J. Phys. Chem. A,* 2003, **207,** 9059-9069.

[5] A. Nitzan, *Chemical dynamics in condensed phases,* Oxford University Press, Oxford, 2006.

[6] B. Bagchi, *Molecular relaxation in liquids,* Oxford University Press, Oxford, 2012.

[7] J. C. Owrutsky, D. Raftery and R. M. Hochtrasser, Vibrational relaxation dynamics in solutions, *Annu. Rev. Phys. Chem.,* 1994, **45,** 519-555.

[8] *Ultrashort laser pulses. Generation and applications,* ed. W. Kaiser, Springer, Berlin, 1993.

[9] S. Mukamel, *Principles of nonlinear optical spectroscopy,* Oxford University Press, New York, 1999.

[10] A. Tokmakoff, Time-dependent quantum mechanics and spectroscopy, https://tdqms.uchicago.edu/page/tdqms-notes accessed January 2019.

[11] J. S. Bader and B. J. Berne, Quantum and classical relaxation rates from classical simulations, *J. Chem. Phys.,* 1994, **100,** 8359-8366.

[12] J. P. Toennies and A. F. Vilesov, Superfluid helium droplets: a uniquely cold nanomatrix for molecules and molecular complexes, *Angew. Chem., Int. Ed.,* 2004, **43,** 2622-2648.

[13] M. Y. Choi, G. E. Douberly, T. M. Falconer, W. K. Lewis, C. M. Lindsay, J. M. Merritt, P. L. Stiles and R. E. Miller, Infrared spectroscopy of helium nanodroplets: novel methods for physics and chemistry, *Int. Rev. Phys. Chem.,* 2006, **25,** 15-75.

[14] A. Slenczka and J. P. Toennies, in *Low Temperature and Cold Molecules,* ed. I. W. M. Smith, Imperial College Press, London, 2008, pp. 345-392 and references therein.

[15] S. Yang and A. M. Ellis, Helium droplets: a chemistry perspective, *Chem. Soc. Rev.,* 2013, **42,** 472-484.

[16] A. Vilà, M. Paniagua and M. González, Vibrational energy relaxation dynamics of diatomic molecules inside superfluid helium nanodroplets. The case of the I_2 molecule, *Phys. Chem. Chem. Phys.,* 2018, **20,** 118-130.

[17] A. Vilà, M. González and R. Mayol, Photodissociation dynamics of homonuclear diatomic molecules in helium nanodroplets. The case of $Cl_2@(4He)_N$, *J. Chem. Theory Comput.,* 2015, **11,** 899-906.

[18] A. Vilà, M. González and R. Mayol, Quantum interferences in the photodissociation of $Cl_2(B)$ in superfluid helium nanodroplets $(^4He)_N$, *Phys. Chem. Chem. Phys.,* 2015, **17,** 32241-32250.

[19] A. Vilà and M. González, Mass effects in the photodissociation of homonuclear diatomic molecules in helium nanodroplets: inelastic collision and viscous flow energy exchange regimes, *Phys. Chem. Chem. Phys.,* 2016, **18,** 27630-27638.

[20] A.Vilà, M. González and R. Mayol, Quantum dynamics of the pick up process of atoms by superfluid helium nanodroplets: the $Ne+(^4He)_{1000}$ system, *Phys. Chem. Chem. Phys.,* 2016, **18,** 2006-2014.

[21] M. Blancafort-Jorquera, A. Vilà and M. González, Quantum-classical dynamics of the capture of neon atoms by superfluid helium nanodroplets, *Phys. Chem. Chem. Phys.,* 2018, **20,** 29737-29753.

[22] A. Vilà and M. González, Reaction dynamics inside superfluid helium nanodroplets: the formation of Ne_2 molecule from Ne+Ne@(^{4}He)$_N$, *Phys. Chem. Chem. Phys.,* 2016, **18,** 31869-31880.

[23] A. Vilà and M. González and R. Mayol, Relaxation dynamics of helium nanodroplets after photodissociation of a dopant homonuclear diatomic molecule. The case of Cl_2@(^{4}He)$_N$, *Phys. Chem. Chem. Phys.,* 2016, **18,** 2409-2416.

[24] J. Tiggesbäumker and F. Stienkemeier, Formation and properties of metal clusters isolated in helium nanodroplets, *Phys. Chem. Chem. Phys.,* 2007, **9,** 4748-4770.

[25] S. Yang, A. M. Ellis, D. Spence, C. Feng, A. Boatwright, E. Latimer and C. Binns, Growing metal nanoparticles in superfluid helium, *Nanoscale,* 2013, **5,** 11545-11553.

[26] L. F. Gomez, E. Loginov and A. F. Vilesov, Traces of vortices in superfluid helium droplets, *Phys. Rev. Lett.,* 2012, **108,** 155302.

[27] E. Latimer, D. Spence, C. Feng, A. Boatwright, A. M. Ellis and S. Yang, Preparation of ultrathin nanowires using superfluid helium droplets, *Nano Lett.,* 2014, **14,** 2902-2906.

[28] R. Zadoyan, J. Almy and V. A. Apkarian, Lattice dynamics from the 'eyes' of the chromophore. Real-time studies of I_2 isolated in rare gas matrices, *Faraday Discuss.,* 1997, **108,** 255-269.

[29] J. Almy, K. Kizer, R. Zadoyan and V. A. Apkarian, Resonant Raman, hot, and cold luminiscence of iodine in rare gas matrices, *J. Phys. Chem. A,* 2000, **104,** 3508-3520.

[30] M. Karavitis, R. Zadoyan and V. A. Apkarian, Time resolved coherent anti-Stokes Raman scattering of I_2 isolated in matrix argon: vibrational dynamics on the electronic ground state, *J. Chem. Phys.,* 2001, **114,** 4131-4140.

[31] Z. Bihary, M. Karavitis and V. A. Apkarian, Onset of decoherence: six-wave mixing measurements of vibrational decoherence on the excited electronic state of I_2 in solid argon, *J. Chem. Phys.,* 2004, **120,** 8144-8156.

[32] M. Karavitis, T. Kumada, I. U. Goldschleger and V. A. Apkarian, Vibrational dissipation and dephasing of $I_2(v = 1\text{-}19)$ in solid Kr, *Phys. Chem. Chem. Phys.,* 2005, **7,** 791-796.

[33] T. Kiviniemi, J. Aumanen, P. Myllyperkiö, V. A. Apkarian and M. Petterson, Time-resolved coherent anti-Stokes Raman scattering measurements of I2 in solid Kr: vibrational dephasing on the ground electronic state at 2.6-32 K, *J. Chem. Phys.,* 2005, **123,** 064509.

[34] M. Gruebele and A. H. Zewail, Femtosecond wave packet spectroscopy: coherences, the potential, and structural determination, *J. Chem. Phys.,* 1993, **98,** 883-902.

[35] Q. Liu, C. Wan and A. H. Zewail, Solvation ultrafast dynamics of reactions 13. Theoretical and experimental studies of wave packet reaction coherence and its density dependence, *J. Phys. Chem. A,* 1996, **100,** 18666-18682.

[36] J.-K. Wang, Q. Liu and A. H. Zewail, Solvation ultrafast dynamics of reactions 9. Femtosecond studies of dissociation and recombination of iodine in argon clusters, *J. Chem. Phys.,* 1995, **99,** 11309-11320.

[37] K. P. Huber and G. Herzberg, *Molecular spectra and molecular structure IV. Constants of diatomic molecules,* Van Nostrand Reinhold Co., New York, 1979.

[38] D. W. Schwenke and D. G. Truhlar, The effect of Wigner singularities on low-temperature vibrational relaxation rates, *J. Chem. Phys.,* 1985, **83,** 3454-3461.

[39] Z. Ma, S. D. Jons, C. F. Giese and W. R. Gentry, Crossed beam studies of state-to-state vibrational energy transfer from the $v = 5$ excited state of $I_2(X^1\Sigma_g^+)$ prepared by stimulated emission pumping, *J. Chem. Phys.,* 1991, **94,** 8608-8610.

[40] M. L. Nowlin and M. C. Heaven, Energy transfer rate constants for highly excited rovibrational levels of $I_2(X)$, *J. Chem. Phys.,* 1993, **99,** 5654-5660.

[41] H. J. Liu, S. H. Pullen, L. A. Walker II and R. J. Sension, The vibrational relaxation of $I_2(X^1\Sigma_g^+)$ in mesitylene, *J. Chem. Phys.,* 1998, **108,** 4992-5001.

[42] S. Li, and W. H. Thomson, Simulations of the vibrational relaxation of I_2 in Xe, *J. Phys. Chem. A,* 2003, **107,** 8696-8704.

[43] S. Li and W. H. Thomson, Molecular dynamics simulations of the vibrational relaxation of I_2 in Xe on an ab initio-based potential function, *Chem. Phys. Lett.,* 2004, **383,** 326-331.

[44] S. A. Egorov and J. L. Skinner, A theory of vibrational relaxation in liquids, *J. Chem. Phys.,* 1996, **105,** 7047-7058.

[45] D. W. Miller and S. A. Adelman, Time correlation function approach to liquid phase vibrational energy relaxation: dihalogen solutes in rare gas solvents, *J. Chem. Phys.,* 2002, **117,** 2672-2687.

[46] S. A. Adelman, R. Muralidhar and R. H. Stote, Time correlation function approach to vibrational energy relaxation in liquids: revised results for monoatomic solvents and a comparison with the isolated binary collision model, *J. Chem. Phys.,* 1991, **95,** 2783-2751.

[47] J. K. Brown, C. B. Harris and J. C. Tully, Studies of chemical reactivity in the condensed phase IV. Density dependent molecular dynamics simulations on vibrational relaxation in simple liquids, *J. Chem. Phys.,* 1988, **89,** 6687-6696.

[48] D. J. Nesbitt and J. T. Hynes, Vibrational energy transfer from highly excited anharmonic oscillators. Dependence on quantum state and interaction potential, *J. Chem. Phys.,* 1982, **76,** 6002-6014.

[49] R. H. Stote and S. A. Adelman, Theory of vibrational energy relaxation in liquids: diatomic solutes in monoatomic solvents, *J. Chem. Phys.,* 1988, **88,** 4415-4420.

[50] R. E. Larsen and R. M. Stratt, Instantaneous pair theory for high-frequency vibrational energy relaxation in fluids, *J. Chem. Phys.,* 1999, **110,** 1036-1052.

[51] A. Bastida, C. Cruz, J. Zúniga, A. Requena and B. Miguel, Surface hopping simulation of the vibrational relaxation of I_2 in líquid xenon using the collective probabilities algorithm, *J. Chem. Phys.,* 2004, **121,** 10611-10622.

[52] M. E. Paige, D. J. Russell and C. B. Harris, Studies of chemical reactivity in the condensed phase II, Vibrational relaxation of iodine in liquid xenon following geminate recombination, *J. Chem. Phys.,* 1986, **85,** 3699-3700.

[53] M. E. Paige and C. B. Harris, Ultrafast studies of chemical reactions in liquids: validity of gas phase vibrational relaxation models and density dependence of bound electronic state lifetimes, *J. Chem. Phys.,* 1990, **149,** 37-62.

[54] K. Nauta and R. E. Miller, Solvent mediated vibrational relaxation: superfluid helium droplet spectroscopy of HCN dimer, *J. Chem. Phys.,* 1990, **111,** 3426-3433.

[55] S. Grebenev, M. Havenith, F. Madeja, J. P. Toennies and A. F. Vilesov, Microwave-infrared double resonance spectroscopy of an OCS molecule inside a ^{4}He droplet, *J. Chem. Phys.,* 2000, **113,** 9060-9066.

[56] K. Nauta and R. E. Miller, Metastable vibrationally excited HF ($v = 1$) in helium nanodroplets, *J. Chem. Phys.,* 2000, **113,** 9466-0469.

[57] K. Nauta and R. E. Miller, Vibrational relaxation of Ne, Ar, Kr-HF ($v = 1$) binary complexes in helium nanodroplets, *J. Chem. Phys.,* 2001, **115,** 4508-4514.

[58] B. Grüner, M. Schlesinger, P. Heister, W. T. Strunz, F. Stienkemeier and M. Mudrich, Vibrational relaxation and dephasing of Rb2 attached to helium nanodroplets, *Phys. Chem. Chem. Phys.,* 2011, **13,** 6816-6826.

[59] P. Claas, G. Droppelmann, C. P. Schulz, M. Mudrich and F. Stienkemeier, Wave packet dynamics on triplet states of Na_2 attached to helium nanodroplets, *J. Phys. Chem. A,* 2007, **111,** 7537-7541.

[60] M. Schlesinger, M. Mudrich, F. Stienkemeier and W. T. Strunz, Dissipative vibrational wave packet dynamics of alkali dimers attached to helium nanodroplets, *Chem. Phys. Lett.,* 2010, **490,** 245-248.

[61] J. H. Reho, J. Higgins, M. Nooijen, K. K. Lehmann, G. Scoles and M. Gutowski, Photoinduced nonadiabatic dynamics in quartet Na_3 and K_3 formed using helium nanodroplet isolation. *J. Chem. Phys.,* 2001, **115,** 10265-10274.

[62] B. Shepperson, A. A. Søndergaard, L. Christiansen, J. Kaczmarczyk, R. E. Zillich, M. Lemeshko and H. Stapelfeldt, Laser-induced rotation of iodine molecules in helium nanodroplets: revivals and breaking free, *Phys. Rev. Lett.,* 2017, **118,** 203203.

[63] D. Mateo, A. Hernando, M. Barranco, E. Loginov, M. Drabbels and M. Pi, Translational dynamics of photoexcited atoms in ^{4}He nanodroplets: the case of silver, *Phys. Chem. Chem. Phys.,* 2013, **15,** 18388-18400.

[64] N. B. Brauer, S. Smolarek, E. Loginov, D. Mateo, A. Hernando, M. Pi, M. Barranco, W. J. Bruma and M. Drabbels, Critical Landau velocity in helium nanodroplets, *Phys. Rev. Lett.,* 2013, **111,** 153002.

[65] A. Leal, D. Mateo, A. Hernando, M. Pi and M. Barranco, Capture of heliophobic atoms by ^{4}He nanodroplets: the case of cesium, Phys. *Chem. Chem. Phys.,* 2014, **16,** 23206-23213.

[66] D. Mateo, F. Gonzalez and J. Eloranta, Rotational superfluidity in small helium nanodroplets, *J. Phys. Chem. A,* 2015, **119,** 2262-2270.

[67] F. Dalfovo, A. Lastri, L. Pricaupenko, S. Stringari and J. Treiner, Structural and dynamical properties of superfluid helium: a density-functional approach, *Phys. Rev. B: Condens. Matter. Phys.,* 1995, **52,** 1193-1209.

[68] F. Ancilotto, M. Barranco, F. Caupin, R. Mayol and M. Pi, Freezing of ^{4}He and its liquid-solid interface from density functional theory, *Phys. Rev. B: Condens. Matter Mater. Phys.,* 2005, **72,** 214522.

[69] L. Delgado-Tellez, A. Valdés, R. Prosmiti, P. Villarreal and G. Delgado-Barrio, HeI_2 interaction potential based on an interpolation scheme, *Int. J. Quantum Chem.,* 2012, **112,** 2971-2975.

[70] M. Frigo and S. G. Johnson, The design and implementation of FFTW3, *IEE Proceedings,* 2005, **93,** 216-231.

[71] A. Ralston, in *Mathematical Methods for Digital Computers,* ed. A. Ralston and H.S. Wilf, John Wiley & Sons, New York, 1960, vol. 1, pp. 95-109.

[72] R. J. Thompson, Improving round-off in Runge-Kutta computations with Gill's method, *Commun. ACM,* 1970, *13,* 739-740.

[73] A. Vibók and G. G. Balint-Kurti, Parametrization of complex absorbing potentials for time-dependent quantum Dynamics, *J. Phys. Chem.,* 1992, **96,** 8712-8719.

[74] G. C. Schatz and M. A. Ratner, Quantum mechanics in chemistry, Dover, Mineola, 2002, pp. 70-74.

7. Conclusions

The main conclusions obtained from the results of the studies performed in this thesis are the following:

1. For the capture of a Ne atom by a HeND at zero angular momentum, the comparison between the quantum and classical descriptions of Ne shows that quantum effects are not important under the initial conditions explored in this work.
2. The capture occurs below a certain maximum impact parameter, which decreases as the initial velocity of Ne increases, and it follows elliptical rotating trajectories inside the nanodroplet reaching the Landau's critical velocity.
3. Even though the maximum impact parameter can be similar to the geometric HeND radius, significantly higher values can be obtained for low atom initial velocities.
4. Major energy and angular momentum exchanges occur when the Ne atom collides with the nanodroplet and the excitation energy of the HeND is released by evaporation of some ^{4}He atoms through the excitation of its surface modes.
5. Angular momentum introduces smoothness into the overall capture process but the general trends are similar to the zero angular momentum case (b=0 Å): energy exchange and variations are softer with increasing impact parameter, while angular momentum exchange and variations are stronger.
6. The Ne atom ($b\neq$0 Å) induces a certain amount of angular momentum to the HeND surface so that both tend to rotate solidarily after the capture.
7. If the initial angular momentum of neon is high enough it can induce vortex nucleation during the capture, which arises from the collapse of surface excitations, and the vortex can be long-lived.

---

8. For zero angular momentum the quantum and classical descriptions of the Ne atoms used to describe the Ne + Ne@HeND reaction lead to similar results for intermediate-high initial incoming Ne atom velocities, where the Ne_2 dimer is formed. For lower initial velocities a Ne-Ne adduct is formed using the classical treatment (which can lead to the formation of a "quantum gel"/"quantum foam" if more Ne atoms are captured), while the Ne_2 dimer is always formed using a standard quantum approach.
9. There are important energy and angular momentum exchanges in Ne + Ne@HeND during the incoming Ne atom capture. Moreover, in the case of the Ne_2 dimer formation some additional energy is released to the nanodroplet (much less energy is released in the Ne-Ne adduct formation). The HeND is excited by both processes and relaxed by evaporation of some ^{4}He atoms.
10. Once the dimer/adduct is formed both Ne atoms travel together and their velocity reaches the Landau's critical velocity.
11. Angular momentum does not help the Ne_2 dimer formation to occur since it makes the removal of the liquid helium located between the Ne atoms more difficult.
12. Vortex formation is more difficult for Ne + Ne@HeND than for Ne + HeND owing to the liquid helium wave interferences induced by the solvation layers of the Ne atom initially placed inside the nanodroplet.

---

13. The HeND structure essentially does not change during the rotational energy relaxation (RER) of the H_2 isotopes (fast rotors) and the superfluid liquid helium efficiently removes from the nanodroplet the energy released by the molecule.
14. The rotational relaxation time of D_2, T_2, … is of the order of nanoseconds and the process approximately occurs following sequential transitions between two "consecutive" rotational levels (cascade mechanism): $j \rightarrow j$-2; j-2 $\rightarrow j$-4; … 4 $\rightarrow$ 2; 2 $\rightarrow$ 0 and m_j is conserved (the decrease of two units in j and the conservation of m_j are due to the nuclear symmetry).

15. The lifetime of an excited rotational state of D_2, T_2, … increases when: (a) the rotational constant increases; (b) the quantum number j increases; (c) the nanodroplet size decreases (above N=100 there is a small influence of N on the relaxation time properties).
16. RER results suggest that the inverse of the relaxation time properties increases approximately linearly with the coupling term $\langle V_{20}^2 \rangle$ between both states, while their dependence with respect to the angular velocity (which makes transition more difficult as it increases) is not so simple and plays a dominant role.
17. While both the rotational energy relaxation and vibrational energy relaxation (VER) processes take place following a cascade mechanism, the lifetime of the excited vibrational states decreases as excitation increases, differing from what happens for the rotational case. This has been interpreted on the basis of the very different types of motion/degrees of freedom involved. Moreover, in VER metastability has been found for intermediate excited states in contrast to RER.
18. Studying the rotational energy relaxation of heavy diatomic molecules such as the halogens is particularly difficult, as their ground state in HeND corresponds to a superposition of rotational states of the free molecule.

---

19. The HeND structure is essentially unchanged during VER but it has small fluctuations during the transitions.
20. The HeND size has a very small effect on VER once the first solvation layer is fully formed (which happens for nanodroplets with a small number of He atoms for systems with strong molecule-helium interactions).
21. As the molecule-helium interaction becomes stronger VER is faster. The same happens as the energy gap between vibrational levels decreases.
22. VER results suggest that the inverse of the relaxation time properties increases approximately linearly with the coupling term $\langle V_{10}^2 \rangle$ between both states, while no information on the dependence with respect to the oscillator velocity (which makes transition more difficult as it increases) can be deduced. Nevertheless, it seems that the oscillator velocity plays a dominant role. These results are analogous to those obtained for RER.

We hope that these studies will contribute to encourage both theoretical and experimental research on the dynamics of the processes investigated here, about which we still have a quite limited knowledge.

8. Resum en català

8.1. Introducció

L'estudi de les propietats de l'heli superfluid ha estat realitzat principalment per físics durant molts anys. En els darrers anys, aprofitant les potencialitats que presenten les nanogotes d'heli superfluid (HeND) com a matriu inert a temperatura molt baixa (0.37 K), la comunitat química es va implicar en la seva aplicació a l'estudi de l'espectroscòpia d'alta resolució de molècules. Més recentment (principis dels anys 2000), després de comprovar que les HeNDs també podien ser bons nanoreactors, la comunitat química va començar a estar involucrada en investigacions amb HeNDs per investigar la reactivitat química en aquest dissolvent quàntic. L'interès d'aquesta comunitat per les aplicacions de les HeNDs ha estat creixent des d'aleshores i, probablement, ha crescut més després de descobrir que aquests sistemes també poden ser útils en síntesi química. Pel que fa als estudis teòrics sobre la dinàmica dels processos fisicoquímics en HeNDs, aquests han estat possibles des de fa uns cinc anys i fins ara el nombre d'aquests estudis realitzats en el context químic, malgrat el seu interès, és molt escàs. L'objectiu principal d'aquesta tesi és contribuir al desenvolupament de la recerca en aquest àmbit.

Aquesta tesi està estructurada en set capítols i un capítol final amb un resum en català. El primer capítol dona una introducció al camp d'estudi i el segon presenta la metodologia teòrica emprada per realitzar els estudis detallats als capítols següents. Els Capítols 3 i 4 reporten dos estudis (captura atòmica i reacció de formació d'un dímer/adducte, respectivament) on es descriuen les impureses (àtoms) mitjançant la mecànica clàssica. A més, els Capítols 5 i 6 reporten els estudis de dos tipus de relaxació d'energia molecular (rotacional i vibracional, respectivament), i les principals

conclusions obtingudes es presenten al Capítol 7. Finalment, com ja s'ha indicat, s'inclou un resum en català (Capítol 8).

Per tal d'introduir al lector en el tema, el Capítol 1 es divideix en quatre seccions: la primera descriu les propietats de l'heli, la segona considera la història del descobriment i la recerca realitzada sobre el fenomen de la superfluidesa, la tercera descriu les propietats de les nanogotes d'heli superfluid i l'última dona una visió general de les aplicacions i camps d'estudi que utilitzen HeNDs.

Després, per entendre com s'han realitzat els càlculs, els mètodes teòrics i numèrics emprats per descriure l'heli líquid superfluid es detallen al Capítol 2. En la primera secció s'ha posat especial atenció en la teoria funcional de densitat (DFT) i la seva extensió per a simulacions en temps real (DFT dependent de temps (TDDFT)). La segona secció descriu el principals funcionals de la densitat utilitzats en aquest context. La tercera secció està dirigida a presentar els mètodes numèrics utilitzats per realitzar els càlculs TDDFT.

Els capítols següents contenen els estudis originals realitzats en aquesta tesi. L'estudi del procés de captura d'un àtom de Ne per una HeND (Ne + HeND → Ne@HeND ...) es pot trobar al Capítol 3. Aquí es descriu l'àtom mitjançant la mecànica clàssica i s'examina la influència de l'energia i el moment angular considerant un ampli conjunt de condicions inicials. S'ha analitzat àmpliament el mecanisme microscòpic, els intercanvis d'energia i moment angular i la formació de vòrtexs. Aquest treball complementa i amplia un estudi previ del nostre grup on es va tractar l'àtom de Ne utilitzant la mecànica quàntica estàndard amb moment angular igual a zero. A més, la present contribució correspon al primer anàlisi sistemàtic sobre la influència del moment angular en el procés de captura i formació de vòrtexs.

El Capítol 4 representa una evolució natural a partir del Capítol 3 i en ell s'analitza què succeeix si s'introdueix un segon àtom de Ne en una nanogota dopada (Ne@HeND). Així, descriu la formació d'un dímer o adducte de neó dins d'una nanogota d'heli superfluid, tractant clàssicament els dos àtoms. Anàlogament, com en el capítol anterior, també s'ha tingut en compte el moment angular i s'ha analitzat el mecanisme, l'intercanvi d'energia i moment angular i la formació de vòrtexs. Aquest treball complementa i amplia una investigació prèvia del nostre grup on es van tractar els àtoms de neó utilitzant un mètode mecano-quàntic estàndard i amb moment angular zero. D'altra banda, el

contingut d'aquest capítol correspon a la segona investigació teòrica de la dinàmica de reaccions bimoleculars en nanogotes d'heli superfluid.

Els capítols següents utilitzen un enfoc híbrid quàntic per explorar les dinàmiques de relaxació energètica rotacional i vibracional. El Capítol 5 es correspon amb el primer estudi teòric reportat fins ara sobre la dinàmica de relaxació rotacional en les HeNDs. Aquest procés s'ha estudiat utilitzant diversos isòtops de la molècula H_2 (rotors ràpids) i considerant diverses excitacions inicials i mides de la nanogota.

L'última investigació (Capítol 6) està centrada en l'estudi de la relaxació vibracional en les HeNDs. Així, s'ha analitzat la influència de la separació d'energia entre els nivells vibracionals, energia d'interacció molècula-heli i mida de nanodroplet en la dinàmica de relaxació vibracional, prenent com a referència la nanogota dopada $I_2@(^4He)_{100}$, que ha estat estudiada recentment en el nostre grup. Segons el que sabem aquesta és la primera vegada que s'ha examinat l'efecte d'aquests factors en la dinàmica.

Com s'ha indicat anteriorment, als Capítols 7 i 8 es presenten les conclusions principals i un resum en català, respectivament.

Del treball aquí desenvolupat s'han publicat dos articles:

- M. Blancafort-Jorquera, A. Vilà i M. González, Quantum-classical dynamics of the capture of neon atoms by superfluid helium nanodroplets, *Phys. Chem. Chem. Phys.*, 2018, **20**, 29737-29753. DOI: 10.1039 / c8cp05140b.

- M. Blancafort-Jorquera, A. Vilà i M. González, Rotational energy relaxation quantum dynamics of a diatomic molecule in a superfluid helium nanodroplet and study of the hydrogen isotopes case, *Phys. Chem. Chem. Phys.*, 2019 (disponible en línia). DOI: 10.1039 / c9cp00952c.

A més, s'ha sotmès per la seva publicació un article corresponent al Capítol 4 (16 d'agost): M. Blancafort-Jorquera, A. Vilà i M. González, Quantum-classical approach to the reaction dynamics in a superfluid helium nanodroplet. The Ne_2 dimer and Ne-Ne adduct formation reaction $Ne + Ne@(^4He)_N$. I també s'està preparant un article sobre la relaxació vibracional (Capítol 6).

8.2. Dinàmica quàntica-clàssica de la captura d'un àtom de neó per una nanogota d'heli superfluid

La captura d'un àtom de neó per una nanogotes d'heli superfluid, [(^{4}He)$_{500}$; T=0.37 K)], és a dir, el procés Ne + (^{4}He)$_N$ → Ne@(^{4}He)$_{N'}$ + (N-N') ^{4}He ha estat investigada fent servir un enfoc quàntic-clàssic tenint en compte el moment angular. En el mètode híbrid QM-CM considerat l'heli líquid s'ha tractat quànticament (mètode TDDFT i funcional de la densitat Orsay-Trento (OT)) i s'ha fet servir una descripció clàssica per l'àtom de neó. Aquest treball complementa i amplia substancialment un treball dinàmic quàntic del nostre grup sobre el mateix procés de captura però amb moment angular igual a zero (*Phys. Chem. Chem. Phys,* 2016, **18,** 2006-2014). La present contribució es centra especialment en el mecanisme microscòpic, els bescanvis d'energia i moment angular entre l'àtom de neó i la nanogota d'heli (HeND) i la formació de vòrtexs.

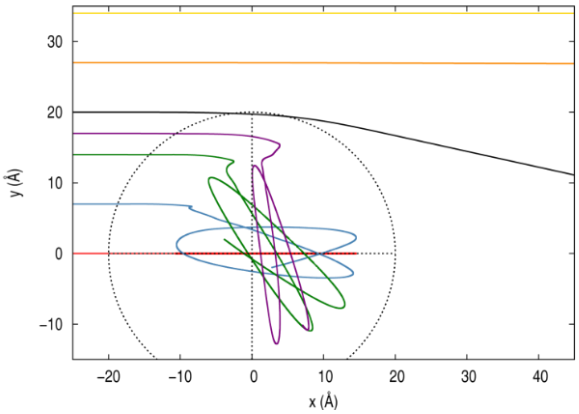

Figura 8.1 Trajectòries de l'àtom de Ne per v_0=500 m s^{-1} i paràmetre d'impacte b=0 (vermell), 7 (blau), 14 (verd), 17 (lila), 20 (negre), 27 (taronja) i 34 Å (groc).

La captura de l'àtom de neó succeeix quan el paràmetre d'impacte (b) està per sota d'un cert valor (b_{max}), que disminueix quan augmenta la velocitat inicial de l'àtom. Un cop a dins de la nanogota aquest segueix trajectòries el·líptiques i amb una velocitat que acaba arribant a la velocitat crítica de Landau. Els bescanvis d'energia i moment angular més importants es produeixen quan l'àtom col·lisiona amb la superfície de la nanogota i l'energia d'excitació de la nanogota i part del moment angular inicial s'alliberen mitjançant l'evaporació d'alguns àtoms d'heli resultat de l'excitació de modes superficials de la nanogota.

El moment angular aporta "suavitat" al procés però, en general, els comportaments observats són semblants al cas amb moment angular igual a zero. Mentre que els

bescanvis d'energia i les variacions són més suaus quan el paràmetre d'impacte augmenta, els intercanvis i variacions de moment angular són més accentuats. El moment angular que l'àtom indueix a la nanogota es tradueix principalment en rotació de la superfície de la gota.

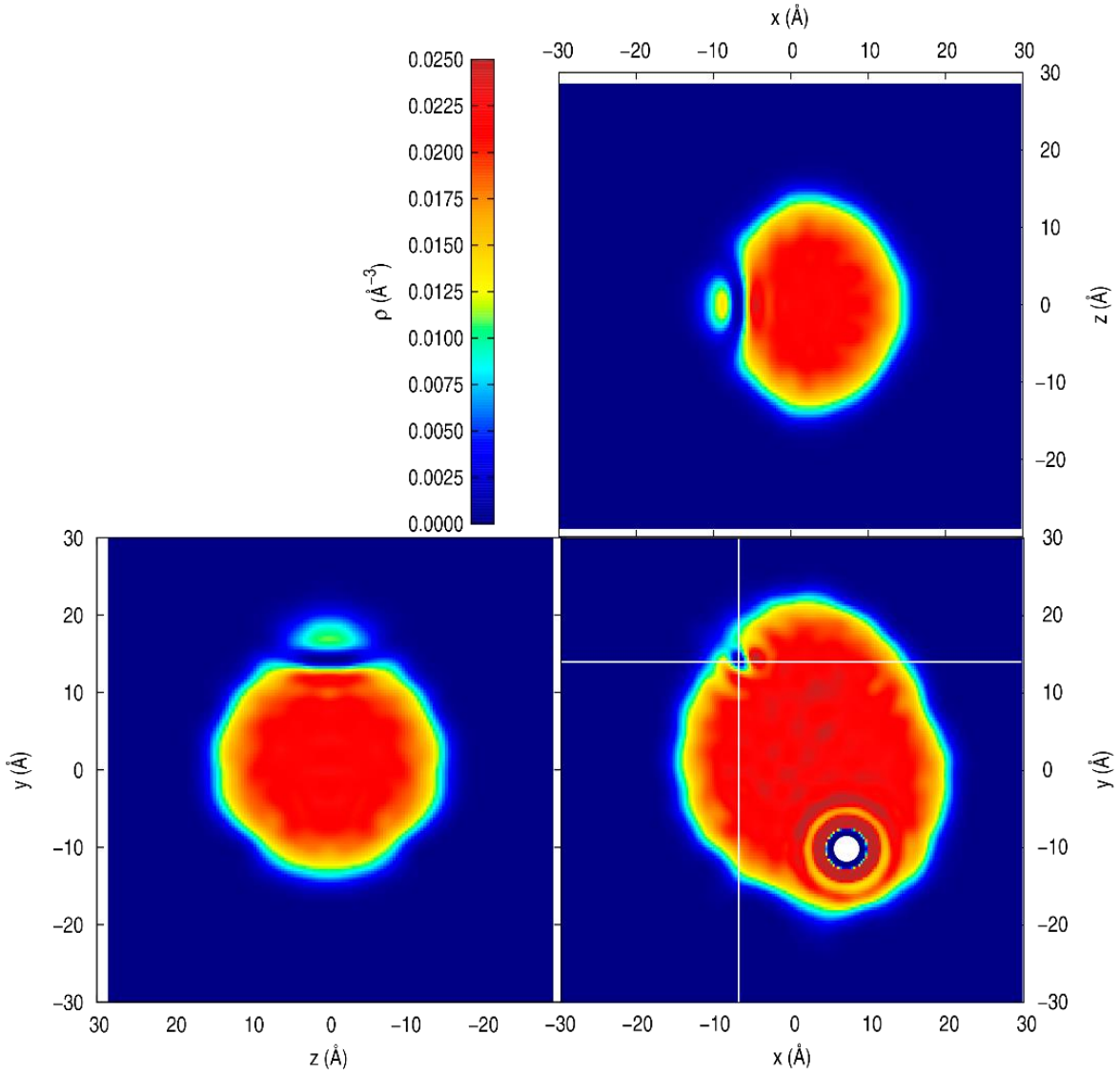

Figura 8.2 Densitat de l'heli en el pla xy i dues seccions perpendicular a través del vòrtex lineal per v_0=500 m s-1 i b=17 Å al temps final de la simulació (171.2 ps). El vòrtex dibuixa un forat lineal lleugerament corbat perpendicular al pla xy.

Un fenomen especialment interessant que sorgeix de la transferència de moment angular de l'àtom a la nanogota és la formació de vòrtex quantitzats, quan el moment angular inicial de l'àtom és prou gran. Aquests vòrtexs provenen del col·lapse de les excitacions superficials (riplons) i poden ser de llarga durada (és a dir, típicament existeixen durant tres o quatre rebots de l'àtom de neó contra la superfície de la

nanogota). Cal destacar, també, que s'han comparat els resultats d'aquest estudi pel cas de moment angular igual a zero amb els de l'estudi previ del nostre grup on l'àtom de neó es va tractar quànticament, i s'ha vist que els efectes quàntics no són importants per a les condicions inicials estudiades (condicions rellevants en experiments de captura on els àtoms de Ne estan a 300 K).

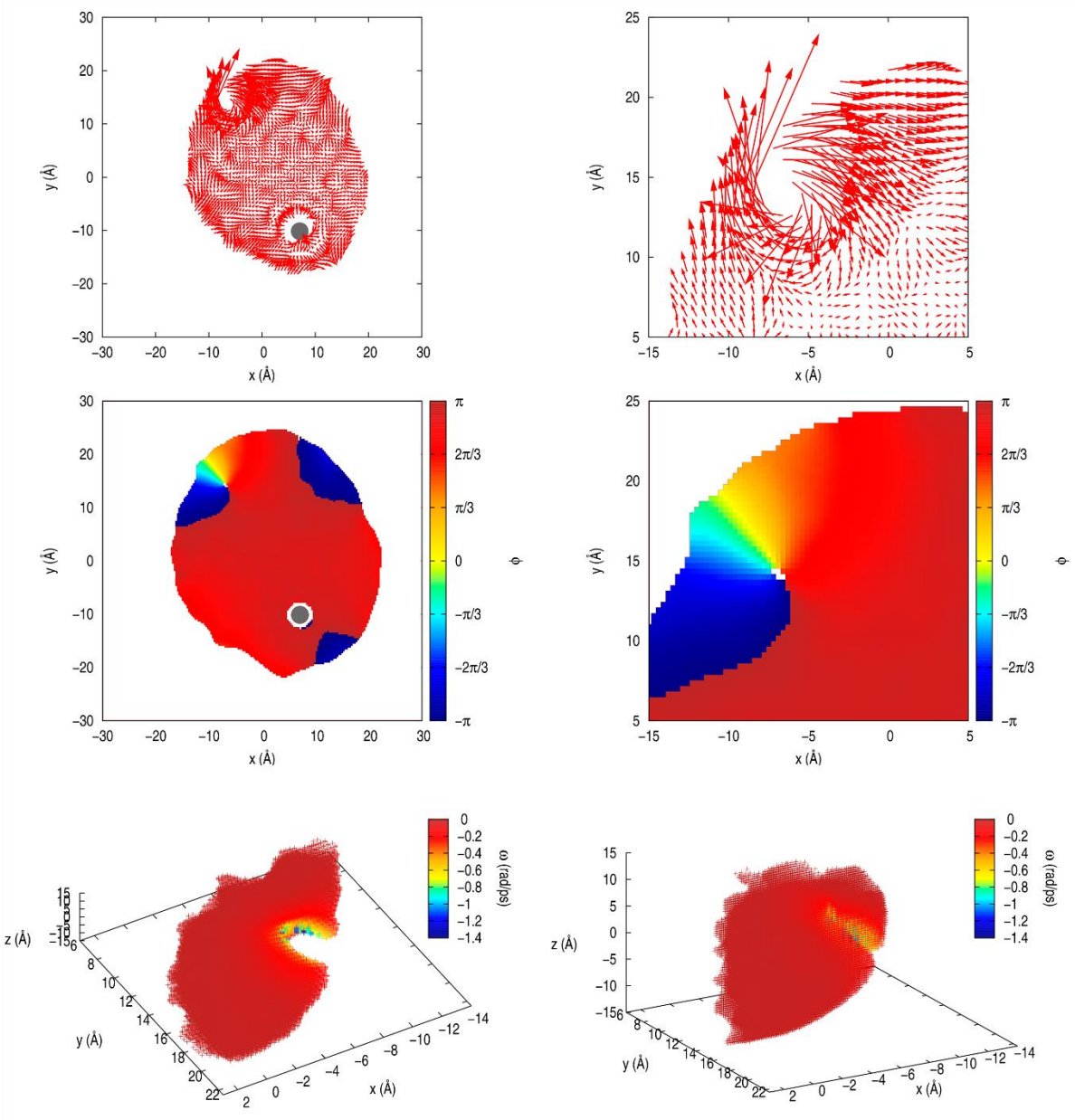

Figura 8.3 Vòrtex lineal per v_0=500 m s-1 i b=17 Å al temps final de la simulació (171.2 ps) des de diferents perpectives: camp de velocitats de la HeND i vòrtex lineal (superior); fase de la funció d'ona de la HeND i vòrtex lineal (centre); volum d'heli associat al vòrtex lineal des de dos punts de vista (inferior).

Tot i l'escassa informació disponible, també s'ha pogut fer una comparativa sobre la solvatació d'impureses en nanogotes d'heli superfluid. S'han comparat les espècies Ne, Ar, Xe, Rb^+, Cs^+ i Ba^+ com a dopants, considerant diferents condicions inicials, i s'ha observat una gran diversitat de comportaments durant el procés de solvatació

L'estudi teòric que s'acaba de descriure correspon al primer en el que s'han analitzat de manera sistemàtica la influència del moment angular en el procés de captura d'àtoms per nanogotes d'heli superfluid.

8.3. Dinàmica quàntica-clàssica de reaccions en nanogotes d'heli superfluid. Reacció de formació del dímer Ne_2 i l'adducte Ne-Ne.

L'estudi de la dinàmica de la reacció de formació del dímer Ne_2/adducte Ne-Ne dins de nanogotes d'heli [$(^4He)_{500}$; T=0.37 K], Ne + Ne@$(^4He)_N$ → Ne_2@$(^4He)_{N'}$/Ne-Ne@$(^4He)_{N''}$ + (N-N')^{4}He/(N-N'')^{4}He, s'ha realitzat fent servir un mètode híbrid QM-CM: enfoc quàntic per a l'heli (DFT dependent del temps i funcional OT) i tractament mecànico clàssic per als àtoms de neó. Pel que sabem aquest estudi correspon a la segona investigació teòrica disponible sobre la dinàmica de reaccions bimoleculars en $(^4He)_N$ i la primera on s'examina l'efecte del moment angular. Per investigar la influència de la velocitat inicial i el moment angular de l'àtom atacant en la dinàmica, s'ha examinat un conjunt de condicions de velocitat inicial i paràmetre d'impacte representatives per la captura de neó a 300 K.

Els resultats obtinguts per a moment al angular igual a zero s'han comparat amb els resultats quàntics d'un treball anterior del nostre grup (*Phys. Chem. Chem. Phys.,* 2016, **18,** 31869-31880) i s'ha trobat que aquests són similars per velocitats inicials iguals o superiors a v_0=500 (velocitat més probable del neó a 300 K) i la formació del dímer Ne_2 (r_e=3.09 Å) té lloc en tots els casos. En canvi hi ha diferències evidents per a velocitats inferiors, perquè en la dinàmica QM-CM, en comptes de la formació del dímer, es forma l'adducte Ne-Ne (r_e=5.45 Å). Els bescanvis d'energia i moment angular són similars al cas de la captura per la gota no dopada. Una vegada s'ha format el dímer o adducte ambdós àtoms viatgen junts i la seva velocitat arriba a la velocitat crítica de Landau.

Els intercanvis d'energia són més suaus quan augmenta el paràmetre d'impacte. El principal intercanvi de moment angular succeeix durant el procés de captura. L'àtom de neó atacant transfereix gran part del seu moment angular a la gota i als àtoms d'heli evaporats. A més, quan el moment angular s'incrementa no s'afavoreix la formació del dímer, ja que dificulta l'eliminació de l'heli líquid situat entre els dos àtoms. Per tant, la formació de l'adducte Ne-Ne domina la reactivitat del sistema. La formació preferent d'aquest adducte suggereix la formació d'un "gel quàntic"/"escuma quàntica" (els àtoms de neó mantenen essencialment la seva identitat dins la nanogota) quan s'addicionen més àtoms de Ne. Addicionalment, per v_0=800 m s^{-1} i b=4 Å es pot veure un comportament particular on també s'hi observa un altre adducte, en aquest cas molt dèbilment enllaçat i amb r_e=9.14 Å.

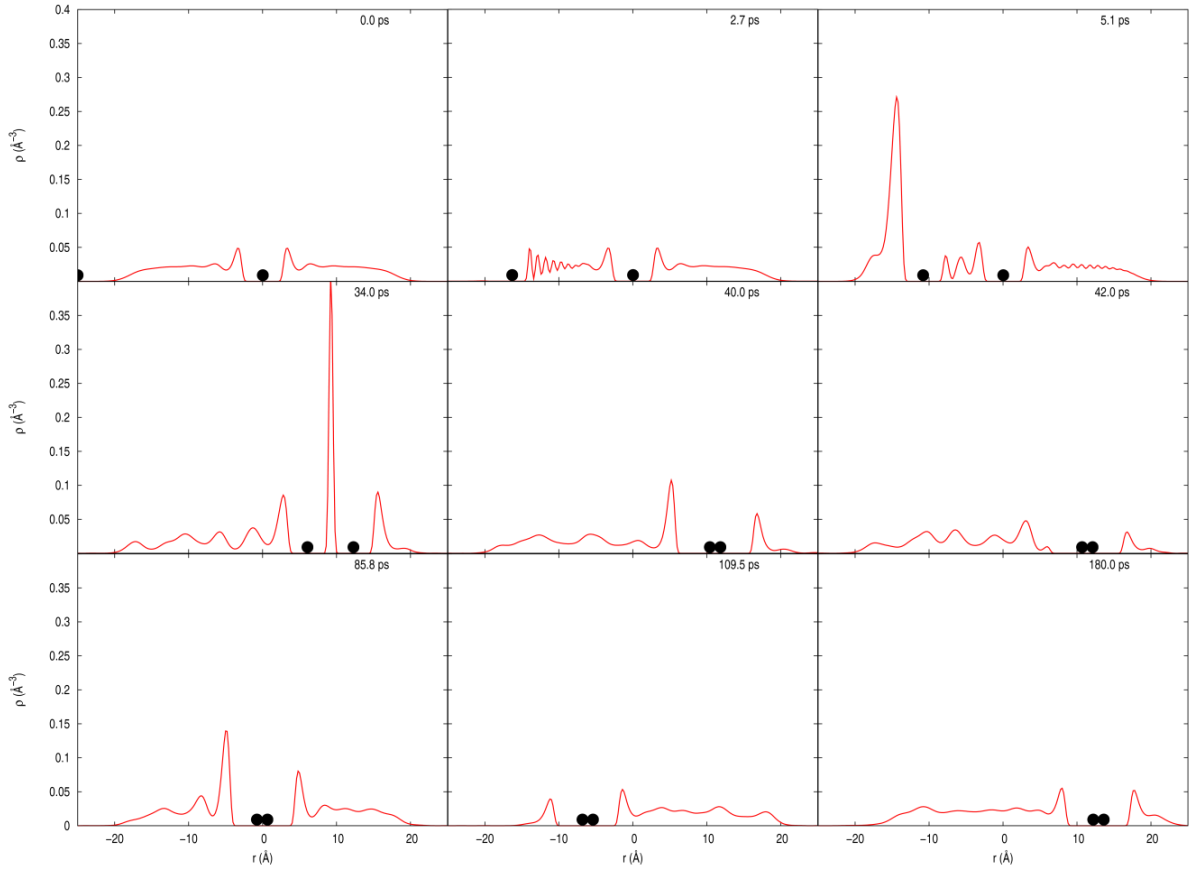

Figura 8.4 Evolució temporal de la densitat d'heli al llarg de l'eix x per v_0=500 m s^{-1} i b=0 Å a temps representatius. Les posicions dels àtoms de Ne estan indicades mitjançant cercles negres.

Si el moment angular inicial és prou gran es creen vòrtex lineals de curta durada. Aquests apareixen pel col·lapse de les excitacions superficials de la nanogota (riplons) i es generen amb més dificultat que pel procés de captura considerat a la secció anterior.

Això és degut a la interferència d'ones que es produeixen en el líquid induïdes per les capes de solvatació de l'àtom que es troba inicialment dins de la gota.

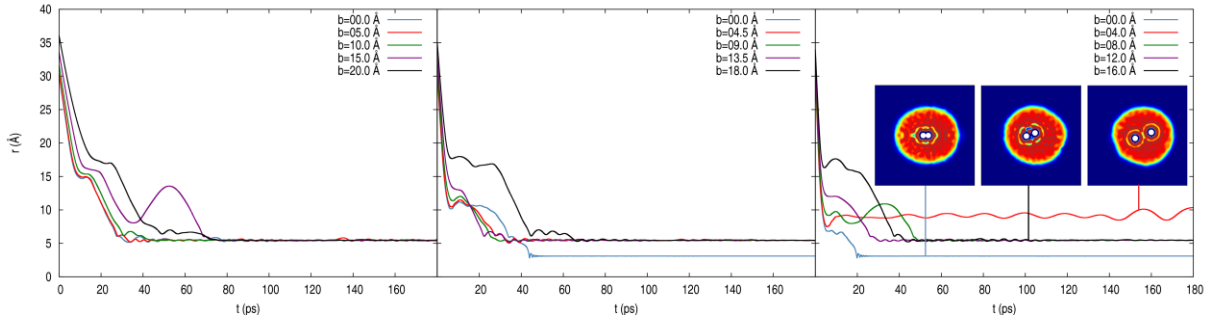

Figura 8.5 Distància internuclear Ne-Ne en funció del temps per v_0=210, 500 i v_0=800 m s^{-1} d'esquerra a dreta a diferents paràmetres d'impacte. La última subfigura mostra la densitat de l'heli en en pla xy i les posicions dels àtoms de neó per tres casos representatius.

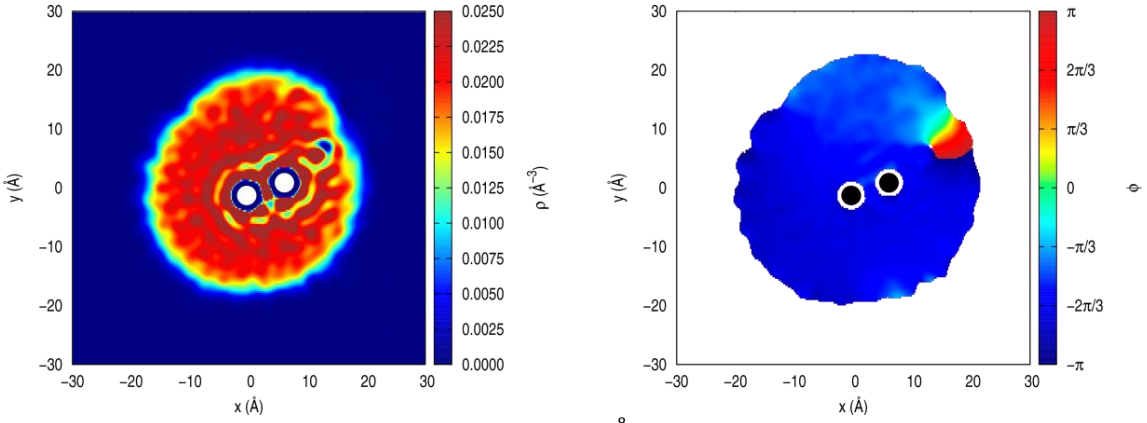

Figura 8.6 Vòrtex lineal per v_0=500 ms^{-1} i b=18 Å a t=46.7 ps: densitat d'heli en el pla xy (esquerra) i fase de la funció d'ona de l'heli (dreta).

9.4 Dinàmica quàntica de la relaxació rotacional d'una molècula diatòmica en un nanogota d'heli líquid superfluid i estudi del cas dels isòtops de l'hidrogen

La relaxació rotacional d'una molècula diatòmica homonuclear dins d'una nanogota d'heli superfluid s'ha investigat fent servir un enfoc teòric híbrid anàleg al proposat pel nostre grup en l'estudi de la relaxació vibracional d'una molècula diatòmica en una HeND (*Phys. Chem. Chem. Phys.,* 2018, **20,** 118-130). La dinàmica de l'heli i la molècula s'han descrit amb TDDFT (funcional OT) i mètodes quàntics estàndards, respectivament. Es tracta del primer estudi teòric disponible sobre la relaxació rotacional de molècules en nanogotes d'heli superfluid.

Varis isòtops reals (D_2 and T_2) i hipotètics (Qa_2, Qi_2 and Sx_2) del H_2 s'han examinat per facilitar aquest estudi inicial, aprofitant les constants rotacionals (B_e) altes dels sistemes seleccionats (rotors ràpids) i per investigar la influència d'aquesta constant en la dinàmica de relaxació. Per a tots aquests isòtops s'ha estudiat la relaxació rotacional des de l'estat $(j = 2, m_j = 0)$ i a més s'han fet servir les molècules Sx_2 i el T_2 per determinar la influència de l'estat rotacional excitat inicial i la mida de la nanogota en la dinàmica de la relaxació, respectivament.

Els resultats mostren que l'estructura de la nanogota quasi no canvia durant la relaxació rotacional i que l'heli líquid superfluid allibera energia eficientment per a que la gota es relaxi (tot i que el número d'àtoms que s'evaporen és inferior al que, en principi, s'esperaria). A més, el procés de relaxació rotacional funciona de manera seqüencial entre dos nivells rotacionals (mecanisme de cascada): $j \rightarrow j$-2; j-2 $\rightarrow j$-4; ... 4 $\rightarrow$ 2; 2 $\rightarrow$ 0 i m_j es conserva (el decrement en dues unitats en j i la conservació de m_j és degut a la simetria nuclear). El temps de relaxació $(j = 0, m_j = 0) \leftarrow (j = 2, m_j = 0)$ és de l'ordre dels nanosegons (des de 1.3 a 5.3 ns per a Sx_2 i D_2, respectivament).

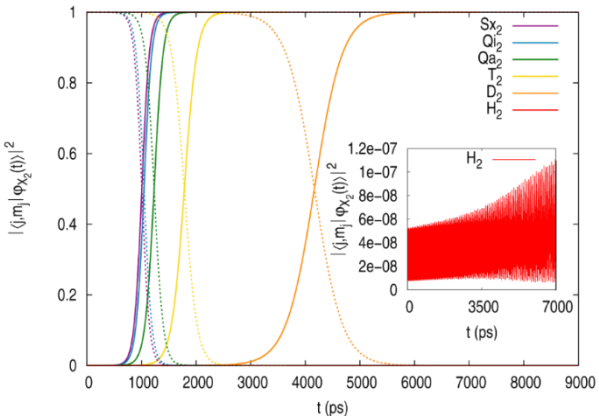

Figura 8.7 Poblacions dels estats rotacionals (j=0, m_j=0) (línies contínues) i (j=2, m_j=0) (línies discontínues) de les molècules en funció del temps.

Pel que fa al temps de vida d'un estat rotacional excitat, aquest augmenta quan: (a) la constant rotacional augmenta; (b) el nombre quàntic j augmenta; (c) la mida de la nanogota disminueix (per sobre de N=100 hi ha una influència molt petita de N sobre temps de vida de l'estat rotacional excitat). L'anàlisi de la dependència dels temps de relaxació amb els acoblaments entre els estats implicats, $\langle V_{ij}^2 \rangle$, i la velocitat angular de la diatòmica aporten força informació sobre la dinàmica. Els resultats suggereixen que

l'invers del temps de transició augmenta linealment amb l'acoblament, mentre que la dependència amb la velocitat angular (que fa la transició més difícil a mesura que augmenta) no és senzilla. El mateix comportament es pot trobar també en la resta de propietats temporals de la relaxació.

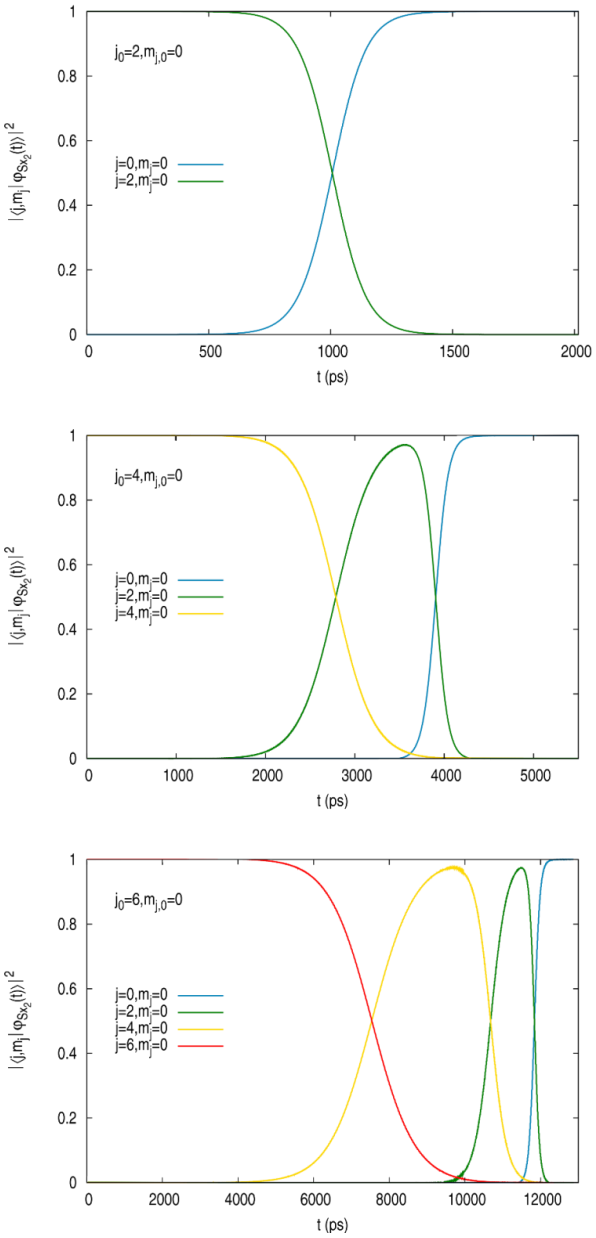

Figura 8.8 Poblacions dels estats rotacionals de $Sx_2(j, m_j=0)$ per tres excitacions inicials diferents (j_o, $m_{jo}=0$), en funció del temps: (2, 0), (4, 0) i (6, 0), de dalt a baix, respectivament.

També és interessant comparar la relaxació rotacional amb la vibracional. Tot i que els dos processos segueixen el mecanisme de cascada, a diferència del que passa amb la rotació, el temps de vida dels estats vibracionals excitats disminueix a mesura que

l'excitació augmenta. Aquesta diferència s'interpreta partint del fet que els dos tipus de moviments/graus de llibertat són molt diferents. D'altra banda, la metaestabilitat que s'observa en el cas dels estats excitats intermedis en la relaxació vibracional no succeeix en la relaxació rotacional.

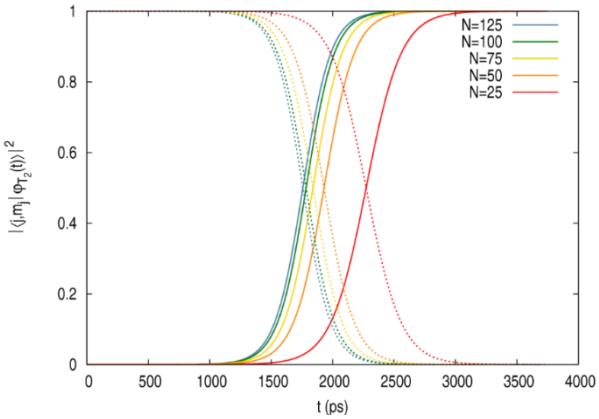

Figura 8.9 Poblacions dels estats rotacionals $T_2(j=0, m_j=0)$ (línies contínues) i $(j=2, m_j=0)$ (línies discontínues) per cinc mides de la nanogota en funció del temps.

8.4. Efecte de la mida de la nanogota, interacció molècula-nanogota i separació energètica en la dinàmica quàntica de relaxació vibracional d'una molècula diatòmica en una nanogota d'heli líquid superfluid

S'ha estudiat l'efecte de la mida de la nanogota (N=50, 100, 150 i 200), l'energia potencial d'interacció ($V = V_{I_2-He}$ amb x=1.50, 1.25, 1.00, 0.75 i 0.50) i la separació energètica entre nivells vibracionals ($\nu_e = x\nu_{e,I_2}$ amb x=1.50, 1.25, 1.00 i 0.75) en la dinàmica de relaxació de l'energia vibracional molecular en una nanogota d'heli superfluid, prenent com a referència la relaxació vibracional de la molècula I_2 en una nanogota de 100 àtoms de ^{4}He i els estats vibracionals v=1 i v=0. Això s'ha investigat mitjançant un mètode quàntic híbrid on l'evolució temporal de l'heli i de la molècula diatòmica homonuclear s'han descrit fent servir TDDFT (funcional OT) i mètodes estàndards de la mecànica quàntica, respectivament.

Aquest estudi complementa i amplia un treball previ desenvolupat al nostre grup (*Phys. Chem. Chem. Phys.,* 2018, **20,** 118-130) amb l'objectiu de poder entendre millor la dinàmica de la relaxació vibracional. Es tracta del segon treball teòric desenvolupat en

aquest context, i el primer on s'estudia la influència de les variables essencials abans esmentades sobre la dinàmica.

Els resultats mostren que la mida de la nanogota afecta molt poc a la relaxació, ja que la interacció entre la molècula i l'heli líquid essencialment és deguda a la primera capa de solvatació. Aquesta capa està totalment formada per a totes les mides de nanogota estudiades, donat que la interacció I_2-He és relativament forta.

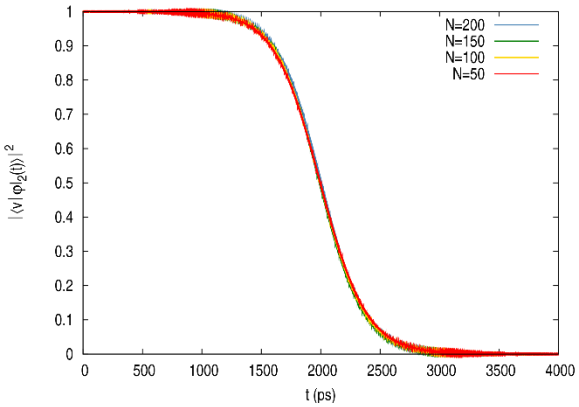

Figura 8.10 Població de l'estat vibracional inicial (v=1) en funció del temps per a N=50, 100, 150 i 200.

D'altra banda, per a interaccions "I_2-He" més fortes la relaxació vibracional és més ràpida perquè els acoblaments entre els dos estats vibracionals, $\langle V_{10}^2 \rangle$, són més grans. La inversa dels temps de relaxació presenta una dependència aproximadament lineal amb $\langle V_{10}^2 \rangle$. Separacions energètiques més petites entre els dos nivells vibracionals també generen relaxacions vibracionals més ràpides, amb un comportament lineal de la inversa dels temps de relaxació amb la separació energètica.

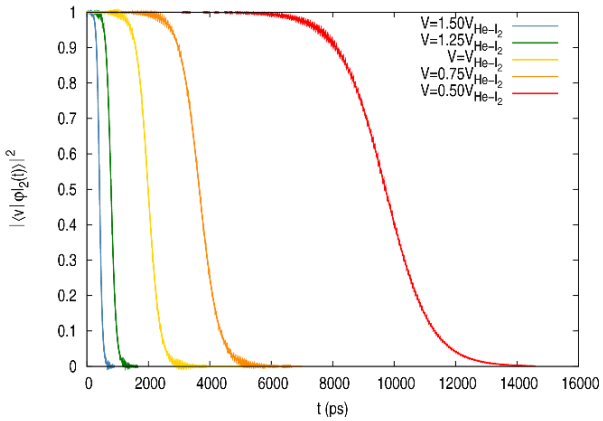

Figura 8.11 Població de l'estat vibracional inicial (v=1) en funció del temps per a V=$xV_{I_2\text{-}He}$ amb x=1.50, 1.25, 1.00, 0.75 i 0.50.

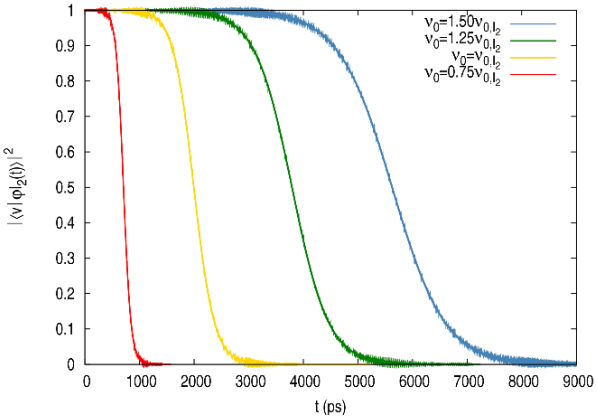

Figura 8.12 Poblacions vibracionals per a l'excitació inicial (v=1) en funció del temps per $\nu_e = x\ \nu_{e,I_2}$ amb x=1.50, 1.25, 1.00 i 0.75.

8.5. Conclusions

Les principals conclusions que s'obtenen dels estudis desenvolupats en aquesta tesi són les següents:

1. Per la captura d'un àtom de Ne en una HeND a moment angular zero, la comparació entre les descripcions quàntica i clàssica del Ne mostra que els efectes quàntics no són importants per a les condicions inicials explorades en aquest treball.
2. La captura es dona per sota d'un cert paràmetre d'impacte màxim, que disminueix quan augmenta la velocitat inicial del Ne, i un cop dins de la HeND segueix trajectòries el·líptiques que van rotant amb velocitats que arriben a la velocitat crítica de Landau.
3. Tot i que el paràmetre d'impacte màxim pot ser similar al radi de la HeND, es poden obtenir valors significativament superiors per a velocitats inicials baixes del Ne.
4. Es produeixen intercanvis d'energia i moment angular particularment important quan l'àtom de Ne xoca amb la nanogota i l'energia d'excitació de la HeND s'allibera mitjançant l'evaporació d'alguns àtoms de ^{4}He deguda a l'excitació de modes superficials.
5. El moment angular indueix "suavitat" al procés de captura, però en general, les tendències són similars a les del cas amb moment angular zero (b=0 Å): l'intercanvi i les variacions d'energia són més suaus quan el paràmetre d'impacte augmenta, mentre que l'intercanvi i variacions de moment angular són més forts.

6. L'àtom de Ne ($b \neq 0$ Å) indueix moment angular a la superfície de la HeND, de manera que ambdós tendeixen a rotar solidàriament després de la captura.
7. Si el moment angular inicial és prou gran pot provocar la nucleació de vòrtexs durant la captura, que provenen del col·lapse de les excitacions superficials de la nanogota i els vòrtex poden ser de llarga durada.

---

8. Per moment angular zero les descripcions quàntica i clàssica dels àtoms de Ne per descriure la reacció Ne + Ne@HeND condueixen a resultats similars per a velocitats inicials de l'àtom entrant mitjanes-altes, quan el dímer Ne_2 es forma. Per velocitats inicials de l'àtom de Ne més petites es forma un adducte Ne-Ne fent servir el tractament clàssic (que pot donar lloc a la formació d'un "gel quàntic" o "escuma quàntica" si es capturen més àtoms de Ne), mentre que el dímer Ne_2 sempre es forma amb la descripció quàntica.
9. S'observen importants intercanvis d'energia i moment angular en Ne + Ne@HeND durant la captura de l'àtom de Ne entrant. A més, pel cas de la formació del dímer Ne_2 s'allibera una quantitat d'energia addicional (per a la formació de l'adducte Ne-Ne l'energia alliberada és molt inferior). La HeND s'excita degut a ambdós processos i es relaxa mitjançant l'evaporació d'alguns àtoms de ^4He.
10. Quan es forma el dímer o l'adducte els dos àtoms viatgen junts i la seva velocitat arriba a la velocitat crítica de Landau.
11. El moment angular dificulta la formació del dímer Ne_2 ja que fa que l'eliminació de l'heli líquid situat entre els dos àtoms sigui més difícil.
12. La formació de vòrtex és una mica més difícil per Ne + Ne@HeND que per Ne + HeND degut a la interferència de les ones en l'heli líquid induïdes per les capes de solvatació de l'àtom de Ne present inicialment a la nanogota.

---

13. L'estructura de la HeND es manté essencialment constant durant la relaxació d'energia rotacional (RER) dels isòtops de H_2 (rotors ràpids) i l'heli superfluid allibera eficientment l'energia transferida per les molècules.
14. Els temps de relaxació rotacional de D_2, T_2, … és de l'ordre dels nanosegons i el procés succeeix seguint un mecanisme seqüencial entre dos nivells rotacionals "consecutius"

(mecanisme de cascada): $j \rightarrow j$-2; j-2 $\rightarrow j$-4; ... 4 $\rightarrow$ 2; 2 $\rightarrow$ 0 i m_j es conserva (el decrement en dues unitats en j i la conservació de m_j és degut a la simetria nuclear).

15. El temps de vida d'un estat rotacional excitat de D_2, T_2, ... augmenta quan: (a) la constant rotacional augmenta; (b) el nombre quàntic j augmenta; (c) la mida de la nanogota disminueix (per sobre de N=100 la influencia de N sobre les propietats temporals de la RER és molt petita).
16. Els resultats de la RER suggereixen que l'invers de les propietats temporals de la relaxació augmenta aproximadament linealment amb el terme d'acoblament $\langle V_{20}^2 \rangle$ entre els dos estats, mentre que la seva dependència amb la velocitat angular (que fa que la transició sigui més difícil quan augmenta) no és tan senzilla i hi juga un paper dominant.
17. Mentre que tant la relaxació d'energia rotacional com la relaxació d'energia vibracional (VER) tenen lloc seguint un mecanisme de cascada, el temps de vida d'un estat vibracional excitat disminueix a mesura que l'excitació augmenta, a diferència del que passa amb la rotació. Aquest fet ha estat interpretat tenint en compte que els moviments/graus de llibertat implicats són molt diferents. A més, en la VER s'ha trobat metaestabilitat per als estats excitats intermedis en contrast amb el que succeeix en la RER.
18. L'estudi de la relaxació d'energia rotacional de molècules diatòmiques pesants com, p. ex., els halògens, és particularment difícil ja que el seu estat fonamental en HeND correspon a la superposició dels estats rotacionals de la molècula lliure.

---

19. L'estructura de la HeND és essencialment constant durant la VER tot i que experiments petits fluctuacions durant la transició.
20. La mida de la HeND té un efecte molt petit sobre la VER quan la primera capa de solvatació està completament formada (fet que succeeix per a nanogotes amb un nombre d'àtoms d'heli petit en sistemes amb interaccions molècula-heli fortes).
21. Quan la interacció molècula-heli esdevé més forta la VER és més ràpida. El mateix passa quan la diferència d'energia entre nivells vibracionals disminueix.
22. Els resultats de la VER suggereixen que l'invers de les propietats temporals de la relaxació augmenten aproximadament linealment amb el terme d'acoblament $\langle V_{10}^2 \rangle$

entre els dos estats implicats, mentre que no es pot deduir informació sobre la dependència amb la velocitat de l'oscil·lador (que fa que la transició sigui més difícil quan aquesta augmenta). D'altra banda, sembla que la velocitat de l'oscil·lador juga un paper dominant. Aquest resultats són anàlegs als que s'han obtingut per la RER.

Confiem en que aquests estudis teòrics contribueixin a incentivar la recerca, tant teòrica com experimental, sobre la dinàmica dels processos investigats en aquesta tesi sobre els quals, tot i el seu interès, encara tenim un coneixement força limitat.